HIGH-SPEED CONVENTIONAL AND MUTUALLY COUPLED TOROIDAL-WINDING SWITCHED RELUCTANCE MACHINES: DESIGN AND COMPARISON

HIGH-SPEED CONVENTIONAL AND MUTUALLY COUPLED TOROIDAL-WINDING SWITCHED RELUCTANCE MACHINES: DESIGN AND COMPARISON

By

JIANING LIN, M.A.Sc.

A Thesis Submitted to the School of Graduate Studies in Partial Fulfillment of the Requirements for

the Degree of Doctor of Philosophy

Doctor of Philosophy (2019) McMaster University

(Electrical & Computer Engineering) Hamilton, Ontario, Canada

TITLE: High-Speed Conventional and Mutually Coupled Toroidal-Winding Switched Reluctance Machines: Design and Comparison

AUTHOR: Jianing Lin

SUPERVISORS: Dr. Ali Emadi & Dr. Nigel Schofield

NUMBER OF PAGES: xxv, 260

To My Husband & Parents

ABSTRACT

Switched reluctance machines (SRMs) are well known for their simple and robust structure, facilitating their increasing application in many sectors, for example vacuum cleaners, where domestic machines operate at high-speed, 50,000 RPM being typical. Conventional SRMs (CSRMs) use a decoupled concentrated phase winding so that torque is predominantly only generated due to the self-inductance, which limits utilization of the machine electrical circuits.

In this thesis, the toroidal winding SRM (TSRM) is introduced, which operates based on the variation of mutual inductance between different phases. The toroidal winding introduces additional winding space, and the winding is practically easy to implement, both features that lead to a relatively higher copper filling factor. The toroidal winding also benefits the machine thermal performance, as the winding is directly exposed on the machine periphery and thus accessible to cooling. All these make TSRMs interesting and meaningful for further study.

Following a comprehensive comparison of CSRM and TSRM characteristics, a general torque equation is presented that is applicable to both CSRM and TSRM. Two 12-switch converters are proposed to drive three-phase TSRMs. Moreover, sinusoidal current excitation with a commercial three-phase half-bridge converter has been suggested as an alternative converter solution for TSRMs.

Accordingly, a three-phase six-stator-pole, four-rotor-pole CSRM is designed and optimized with a speed of up to 50,000 rpm in this thesis. A TSRM is resized to achieve

the same envelope dimension as a benchmark CSRM. Thus, a comparative study between high-speed CSRM and TSRMs has been carried out. They have both been prototyped and tested. The findings suggest that the TSRM is superior, considering machine mass and wire temperature management. The TSRM has a better torque output at lower speeds because copper losses are dominant. However, the CSRM has more advantages at higher speeds due to lower iron losses and lower DC voltage requirements.

ACKNOWLEDGEMENTS

First and foremost, I would like to express my sincere gratitude to my supervisors, Dr. Ali Emadi and Dr. Nigel Schofield. This work could not have been carried out without their expert supervision and guidance. Dr. Emadi's great enthusiasm and extensive work in electric-hybrid vehicular research opened a door for me to the electric transportation world. Throughout my graduate studies, his continuous trust and support have given me the opportunity to truly explore the research world. My sincere gratitude also goes to Dr. Nigel Schofield. His precious time and valuable suggestions were educational, enlightening, and uplifting, especially on the hard days. His profound knowledge and rigorous academic attitude made him my role model as a researcher.

I am grateful to all my colleagues in the Canada Excellence Research Chair in Hybrid Powertrain Program. Special thanks go to Dr. Berker Bilgin. He has played an important role in guiding me in the world of switched reluctance machines. My thanks also go to Mr. Jianbin Liang, Dr. Brock Howey, Dr. Alan Callegaro, Ms. Romina Rodriguez, Mr. Robert Lau, Ms. Elizabeth Rowan, Mr. Jack Gillies, Dr. Le Sun, Dr. Jianning Dong, Dr. James Jiang, Dr. Yinye Yang, Dr. Nan Zhao, Dr. Sandra Castano, Dr. Pira Suntharalingam, and Mr. Haoding Li. They all play important roles during my Ph.D. study. I will never forget the great times that we have shared together.

In addition, I express my thanks to Dr. Fei Peng, Dr. Wei Hua, Mr. Weiguo Zheng, and Mr. Hongpei Li from Southeast University. Dr. Peng gave me valuable suggestions and he also supported with converter setup and machine control during the validation tests. Dr.

Wei Hua is always supportive to his students. He gave me very useful advices regarding SRMs. The practical suggestions from Mr. Weiguo Zheng, and Mr. Hongpei Li during the test bench setup is very important for the completion of the validation test.

Last but not the least, I owe a special debt of gratitude to my family. Their love has continuously supported me in hard times. Without their spiritual and material support, the completion of this thesis would not have been possible.

This research was undertaken, in part, thanks to funding from the Canada Excellence Research Chairs Program.

TABLE OF CONTENTS

LIST OF FIGURES

LIST OF TABLES

Chapter 1 Introduction

1.1. Motivations and Applications.

The majority of home appliances are powered by electricity nowadays. Electric motors can be found abundant in a variety of home applications, totaling up to approximately 30-50% energy consumption in residential homes [1][2]. Among them, high-performance, lightweight, and low-cost vacuum cleaners are attracting great attention from the market. A review of the best-selling air vacuum cleaners shows the electric motor they use generally operate at 20,000-35,000 rpm, with a few designs even reaching over 100,000 rpm [3][4][5][6][7]. Switched reluctance motors (SRMs) are well-known for their simple and robust structure, facilitating their applications in vacuum cleaner applications at this high-speed of operation [8][9].

Meanwhile, with the development of power electronics and low-lost lamination material, as well as the rapidly increasing market demand, there is a great opportunity for high-speed electric machines, especially for those with low cost.

Switched reluctance machines (SRM) are brushless, doubly salient, and free of windings, permanent magnet (PM) materials or squirrel coils on the rotor. With the advantages of simple structure and high reliability, SRM is a strong candidate for wide varieties of rotation applications. However, the problem of its high torque ripple and acoustic noise still constraining widespread application take-up. On the contrary, the vacuum cleaner is a very suitable application for SRM as acoustic noise is given a wide acceptable range. At

high-speed operation, the speed change caused by motor torque ripple would be less appreciable.

Given the above, the high-speed SRM is a promising candidate technology for vacuum cleaner applications.

1.2. Background of High-Speed Electric Machines.

Although it's well-known that system can be made smaller and lighter at the same power level by increasing the operating speed of the system, high-speed and super-high-speed drives are only becoming popular and realizable in the last few decades, benefiting from the development of power electronic switching devices, converter topologies, control methodologies, advanced materials and computer analysis and simulation technologies in design processes. New solutions like bearing-less and sensor-less, etc. also solve the mechanical difficulties along with such drive systems. In the meantime, there have been significant strides forward of transport systems electrifications during the last ten years. This trend shows a large demand of high-speed technologies. Furthermore, the advancing technologies, notably fly-wheel energy storage, cellular medical equipment, and precision machining, high-speed computer information storage, and compressors, pumps, spindle drives, also requires the support of high-speed electric machine development. Consequently, considerable worldwide researches on high-speed and super high-speed electric machines have been conducted in the last decade.

For high-speed, currently, there is no uniformity in its definition. Theoretically, a comprehensive definition requires the considerations of electrical, thermal and mechanical constraints of the machine. However, all these constrain has a huge dependence on their applications. Dealing with this topic, literature like [10][11][12] are all based on particular examples. In [13], it proposes a numerical borderline to distinguish high-speed and super-high-speed based on notable examples of high-speed motors and generators. But more generally, motors with a rotor surface linear velocity over 100 m/sec are referred to as high-speed motors [14][15]. This gives a more straightforward definition of high-speed electric machine.

Worldwide, there is a great number of researches conducted on high-speed electric motors. In [16], a 40 kW, 40,500 rpm surface permanent magnet synchronous machine (PMSM) with a 1:26 reduction magnetic gear and water cooling system is study and verified by finite element analysis (FEA) for an electric vehicle (EV) application. The efficiency of the whole powertrain can achieve up to 96.75%. The advantages of magnetic gear reduced maintenance cost, improved reliability, reduced acoustic noise, and inherent overload protection makes PMSMs quite attractive for high-speed powertrain [17]. A 300 kW, 60,000 rpm, three-phase induction motors (IMs) have been investigated for air compressor in [18]. A solid rotor made of mild steel instead of a cage rotor is used, which has been approved with the advantages of high-power density, high efficiency, and high starting torque-to-starting current ratio. In [15], a more-electrified engine with a family of four high-speed electrical machines is discussed, which emphasize the advantages of the high-speed machine on EVs and hybrid EVs. A high-

speed SRM with conical magnetic bearings is designed for electric aircraft application to start a gas turbine engine in [19]. The continuous power is 30 kW while peak power equals 45 kW, rated speed 14,000 rpm and maximum speed 30,000 rpm, efficiency higher than 85% at rated speed. In [20], it studies increasing motor drive speed for machine tooling, which demonstrates unavoidable demand to increase the speed limits up to 300,000 rpm and over. Paper [21] addresses the challenge to design a 200 kW, 100,000 rpm PM machine for micro-turbo generators application and it also gives the solution of nanotechnologies.

More high-speed electric machines and their application environment are available in [22][23][24][25]. As can be seen, the induction machine and permanent magnetic machine still dominates among high-speed electric machines in both industry and academia. The comparison between IM, PM, and SRM has been studied by an abundance of literature like [19][20][21]. It is well known that the IM has the problem of lower efficiency, while high-efficiency IMs are usually at a high expense of material or manufacturing complexity. As for the PM machines, the cost has a significant dependence on the rare earth material price. It's well-known that, in 2011, rare earth material costs increased sharply to a peak, almost 50 times higher than the costs in 2005 [26] as presented in Figure 1.1. Demand for the rare-earth magnet is forecasted to continue growing, reaching an estimated value of $6.07 billion by 2025 [27]. Those growing demand from clean energy markets such as EVs and wind turbines alongside a tight supply chain has put the rare earths market at an even higher risk for a supply deficit.

With no windings, permanent magnet materials or squirrel coils on the rotor, the laminated rotor structure of SRMs is quite simple and rigid, and of low cost, high reliability. more rugged, more easily maintained, and equally light and compact And the advantages make SRM particularly suitable for high-speed operation, high temperature, and other harsh environments [28][29].

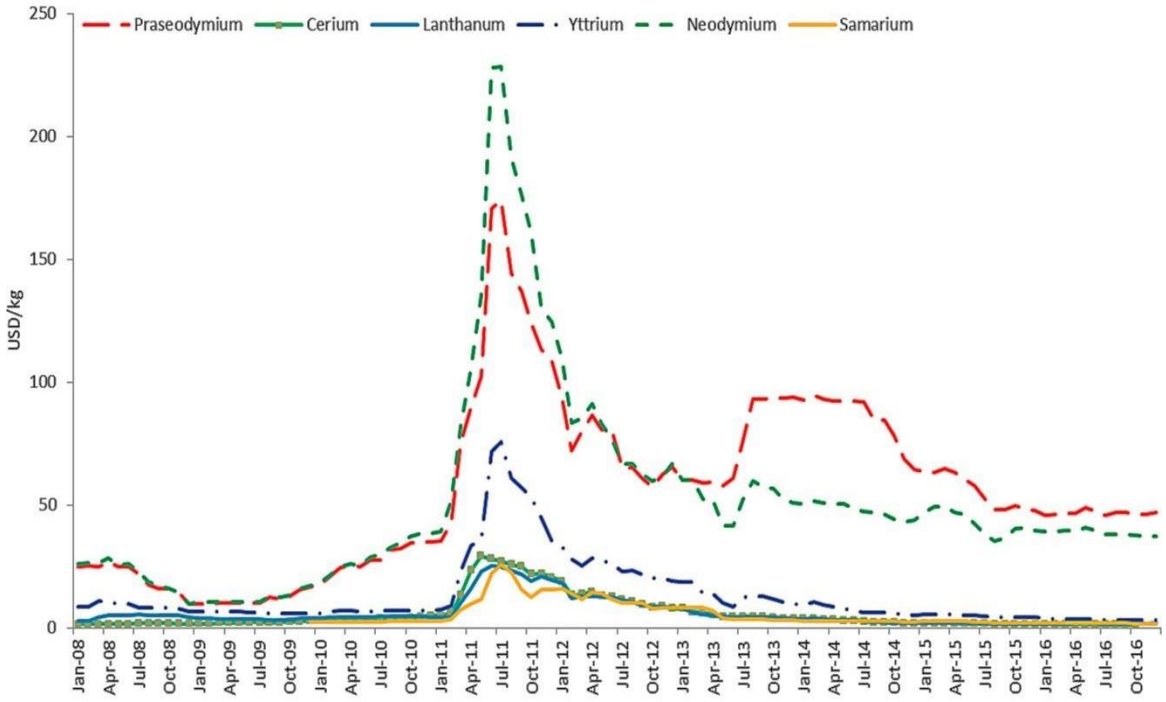

Figure 1.1. Shanghai Steel home nominal price of rare-earth oxides (REO): January 2008–December 2016 [30].

1.3. High-Speed Switched Reluctance Machines.

SRMs are simpler, more rugged, more easily maintained, and equally light and compact. They're also more flexibly controllable, more heat-tolerant, and cheaper for the same torque and production volume. However, the development of SRM also has big

challenges because of its high torque ripple, vibration, and noise. Meanwhile, SRM has limited superiority than PM machine for the power density comparison, since there is only one energizing source, the windings, for SRM, However, this weakness is reduced for the high-speed working condition.

In [31], an 18/12 SRM with 10JNEX900 material and a filling factor of 0.57 is designed and test competing the popular Toyota Prius IPMSM. In [32], an even higher power density SRM is designed compared to the Toyota Prius IPMSM. Compared with the designed 18/12 SRM in [31], this machine in [32] is of higher speed but lower torque, which definitely reduces the machine size and increase its power density. In 2009, Adura Systems incorporated SRMs in its bus and truck power train and achieved sales in China [33]. In 2011, John Deere and LeTourneau fitted SRMs to their heavy-duty electric vehicle models [34]. At EV Japan in January 2012, Nidec exhibited a prototyped SRM [35]. As exhibited in Figure 1.2, it is 177mm in diameter, 234mm in length and 26.5kg in weight. Its maximum torque and rotational speed is 86Nm and 12,000 rpm, respectively.

Figure 1.2. Nidec's 12,000 rpm switched reluctance motor for EVs and HEVs at EV Japan in January 2012 [35].

Compared with low-speed SRMs, high-speed SRM has more challenges. Despite regular electromagnetic design process, a multi-parameter integrated design method is needed for a high-speed SRM design. Based on the literature review of the outcomes in the past, the most important challenge has been listed. A multi-domain design procedure for the high-speed SRM machine is necessary.

1.3.1. Electromagnetic Design and Optimization for High-Speed SRMs.

Considering the heavy nonlinearity of SRM, traditional SRM design is usually based on FEA [36]. Many research work has been done on optimizing the geometries, especially pole shapes, to achieve like higher average torque or lower torque ripple as it has been proved that the stator and rotor poles have a significant influence on machine torque performance [37] [38], and [39]. With the development of computer technology and new numerical analysis methods, different optimization theories have been developed and applied to SRMs designs. It gains great popularity because of their accuracy in derivative calculation and efficiency in terms of computation time [40]. The most popular optimization method is the genetic algorithm, neural networks, and sensitivity analysis technology, which typically couple with the FEA and Matlab/Simulink to propose an optimal solution given a certain design boundary and with a particular optimization target [41] [42]. Papers [43] and [44] have applied sensitivity analysis together with FEA for machine optimization, dealing with both electromagnetic and mechanical analysis. Swarm Optimization is a particular genetic algorithm widely used for SRM optimization design [45][46]. B-spline parameterization is another popular neural network approach applied to SRM optimization [47]. In [48], the level set method is combined with FEA to

optimize rotor geometry for a high-speed SRM. The material distribution and density are studied for the rotor.

1.3.2. Iron Loss Estimation and Reduction for High-Speed SRMs.

Accurate iron losses estimation is one of the most important issues related to high-speed machine study. For the most widely used method of predicting SRM iron losses, the spatial flux density distribution is considered to be uniform through the cross-section of the iron core. The non-sinusoidal waveform is expanded into a Fourier series of harmonics, and then the iron losses for each harmonic is calculated and summed for the total losses. Now thanks to the development of fast computer calculation, FEA approach is widely used for accurate iron losses calculation. Well-meshed element is used as the calculation unit to eliminate the assumption of uniform flux distribution for different machine parts. More research is conducted by investigating the harmonics components of the measured flux waveforms and the iron losses coefficients in [49].

For iron losses reduction, one way is to develop low-loss lamination material, feno-magnetic material [50]. In [51], a novel Co-based soft magnetic material is used as electrical steel on a 10kw PM material, which achieved a size reduction of 70% when compared with the conventional M-19 G29 electrical steel lamination. Its reduction of PM material usage is up to 83%. The material also has good performance at high temperature, up to 300ºC. An amorphous soft magnetic material is applied on the stator of a 1 kW 70 000 rpm BLDC motor, and it leads to stator iron losses even less than 7 W, this may eliminate the need of using additional cooling systems [52].

Besides iron losses, AC copper losses are another issue for a high-speed machine. Because AC copper losses are frequency-dependent and this influence increases significantly for high-speed operation because of the increasing eddy current loss in stator coils and the proximity and skin effect. Usually, to avoid the extra copper losses, the radius of the copper wire has to be limited. In [53], rectangular transposed coils and optimized slot shape are applied on a 5.0 MW 15,000 rpm PM machine with form-wound winding to reduce the dynamic copper losses for the high-speed machine.

1.3.3. Mechanical Concerns Related to High-Speed SRMs.

Mechanics analysis is significantly important for high-speed SRM. First, the critical speed has to be estimated at the initial design status. The critical speed is the maximum speed for the machine rotor to run safely. If it's over this speed, the stress will break the machine. Usually, it's determined by the rotor geometry and material distribution. FEA stress analysis model can be set up to discover the stress distribution at a certain speed [54]. The maximum stress usually happens on the transition part between the rotor pole and yoke. This stress must be made sure lower than the yield strength of the applied material.

SRM salient pole rotor rotating at high speed will bring significant windage losses, making the total mechanical loss increases greatly. In order to reduce windage loss at high speeds, typically rotor shape is analyzed and specially designed to increase the arc length and reduce the tooth height. In [55], it proposed a cylindrical rotor structure, which has been proved with much lower windage losses than a conventional rotor shape.

The skewed rotor/stator SRM is also approved to have a significant reduction on the abrupt change of radial magnetic force without any decrease of efficiency or torque production. Therefore this skew structure can be used for the reduction of vibration and acoustic noise [56]. There are also lots of papers dealing with the possibility of replacing a mechanical gear system by a magnetic gearbox. The magnetic planetary gearbox has many advantages such as contact-free, no gear lubrication, high-speed-reduction ratio, and high durability.

1.4. Winding Topologies for Switched Reluctance Machines.

For high-speed SRM, there have been many prior works on geometry optimization, iron, and windage losses estimation and reduction, etc. However, there is not much attempt to study the possible winding topologies on high-speed SRMs.

The conventional SRMs (CSRMs) use a decoupled concentrated phase winding so that torque is generated due to the rate of change of the self-inductance of the excitation phase only, which limits the utilization rate of the electrical circuits [57]. By reversing the polarity of geometric opposite stator poles, CSRM can be modified to mutual-coupled SRMs (MSRMs). MSRM operates based on the variation of mutual-inductance between different phases [58]. Previous research [59][60] have shown that MSRM is less sensitive to saturation than the CSRM and has better thermal performance [61]. Multiphysics numerical modeling and experiments also show that the MSRM has lower vibrations and sound power levels [62]. The torque ripple of the MSRM is found to be relatively higher,

which can be reduced by using a single-layer full-pitched winding [63]. It also increases the winding failure due to the overlap of different phase windings. Given above, only the concentrated winding is to be studied in this thesis.

Therefore, the toroidal winding SRM (TSRM) is proposed in this thesis as it offers additional winding space while retaining the benefits of mutual coupling excitation [64][65]. For the toroidal winding, practically, it's easier for winding, therefore leading to a higher filling factor. At the same time, the toroidal winding benefits machine thermal performance as the winding is directly exposed [64]. Both these two characteristics will have a direct impact on machine output performance. However, for the electromagnetic performance comparison, the published information is still limited, especially for high-speed SRM. In toroidal winding literature [66][67], the machines are all operating under 5000 rpm. Publication [68] has developed a 50,000 rpm SRM with toroidal winding, which can produce almost the same electromagnetic performance as conventional SRM, but with higher copper losses.

1.5. Thesis Contributions and Structure.

Considering SRM's advantage of solid robust rotor structure on high-speed applications and the toroidal-winding stator benefit, this thesis combines these advantages together and apply it on high-speed applications. The electromagnetic theory of the mutually coupled toroidal-winding SRM has been comprehensively studied. Control strategies and two converter topologies have been developed to drive the proposed TSRM. Accurate

dynamic models have been built for TSRM's accurate torque estimation. The experimental work is another contribution, considering the test and measurement difficulties at high-speed low-torque operation. Two machines are prototyped and tested. Control difficulties arising from the high-speed operation are also overcome during the test.

In this thesis, the fundamental operational principles of CSRM are first discussed in Chapter 2, followed by an introduction of two proposed TSRMs. As illuminated in Figure 1.3(b), the first TSRM replaces the conventional winding around CSRM stator pole with two coils wounded around the yoke beside the pole. As a result, it is called double-layer TSRM (DLTSRM). The second TSRM is modified based on the first TSRM. For TSRM-2 shown in Figure 1.3(c), the two coils inside one slot are parallel connected as one. Thus, there will be 6 coils wounded in the 6 stator slots. So TSRM-2 is named as single-layer TSRM (SLTSRM). A general torque equation applicable for both CSRM and TSRMs has also been developed and stated in Chapter 2.

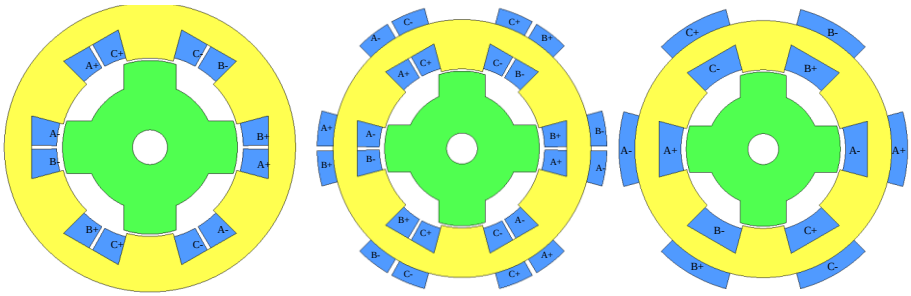

(a) (b)

Figure 1.3 Winding schemes: (a) CSRM, (b) DLTSRM, and (c) SLTSRM.

In Chapter 3, static characterization has been compared between CSRM and TSRMs, with emphasis on their self/mutual inductance profile together with torque contribution of each inductance. After comparison, SLTSRM is proved with superiority over DLTSRM and therefore selected for further analysis in this thesis. From there on, TSRM will only mean SLTSM in this thesis.

Following that, the dynamic performance of both CSRM and TSRM has been analyzed in Chapter 4. The control methods, as well as converter topologies, has been researched. Two 12-switch inverters have been proposed for the three-phase TSRM. After comparison, the full bridge one is used for further discussion. Moreover, sinusoidal current excitation with commercial three-phase half-bridge converter has been proposed as an alternative solution for TSRM.

Based on the analysis discussed in preceding Chapters, a three-phase six-stator-pole, four-rotor-pole CSRM is designed and optimized with speed up to 50,000 rpm in Chapter 5. The TSRM is resized based on the CSRM constraints to achieve the same envelope dimensions. A comparative study has been made between high-speed CSRM and TSRMs. The CSRM and TSRM are then prototyped in Chapter 6. All of their steady characteristics are tested and compared. Dynamic performances at three typical speeds, namely 10,000 rpm, 30,000 rpm, and 50,000 rpm have been tested and compared. Conclusions and future works are then stressed based on the test results in Chapter 7.

Chapter 2 Fundamental Theories of Conventional and Toroidal-Winding Mutually-Coupled Switched Reluctance Machines

2.1. Introduction.

The CSRM torque is purely reluctance torque, which is under the minimum magnetic reluctance principle so that the operating direction and speed of the machine is only determined by the sequence of the energized phases and the switching frequency. The asymmetric bridge is applied to its converter structure [ref]. All these features make highly fault tolerant. This is particularly suitable for high-speed operation, high temperature and harsh environments [69][70]. CSRM uses a decoupled concentrated phase winding so that torque is generated due to the rate of change of the self-inductance of the excitation phase only, which limits the utilization rate of the electrical circuits. Moreover, the pulsed excitation based on self-inductance leads to significant torque ripple and vibration. These problems can be partially eliminated by involving mutual-inductance between different phases and using multi-phase excitation on SRMs. Mutual-inductance can be introduced by toroidal-winding structure [57]. TSRM is proposed, also because it offers additional winding space while retaining the benefits of mutual coupling excitation.

In this chapter, the operation principle of CSRM is first presented. Following that, two toroidal winding topologies are discussed. As inductance is the determination of machine output performance, a comparative study has been made on flux distribution and inductances of these three types of machines. For purposes of illustration and explanation,

the following study used lamination geometry of a three-phase six-stator-pole four-rotor-pole SRM. Following that, the general torque equation for three-phase SRMs is presented.

2.2. Operation Principle of Conventional SRMs.

CSRM's operation is relatively simple. When the stator coils are excited, the machine has the tendency to move from a position with a larger magnetic reluctance to a position with a smaller one, i.e., the rotor moves to minimize the magnetic circuit reluctance.

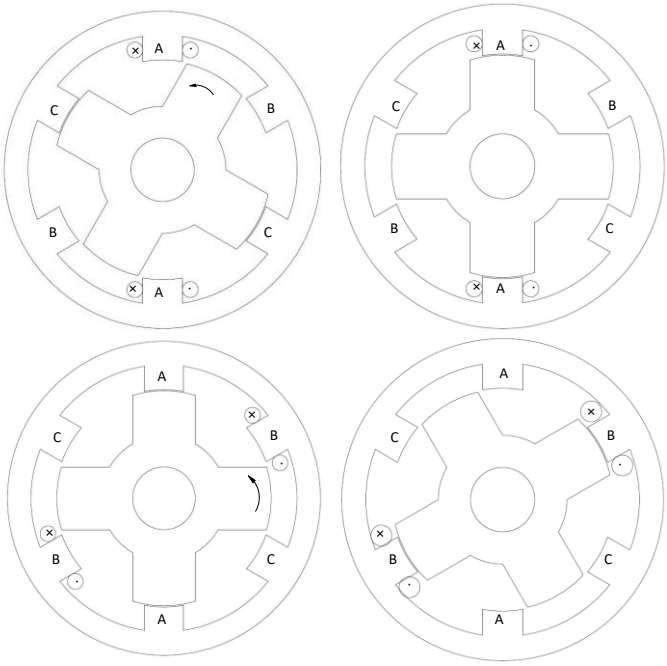

Figure 2.1 CSRM's operating principle.

Since the soft magnetic material has a much smaller magnetic reluctance than that of air, if phase A in Figure 2.1 is energized, rotor pole will move from the unaligned commutation position, Figure 2.1(a), to the aligned commutation position, Figure 2.1 (b).

After that, phase A is de-energized, while at the same time, phase B is energized, the rotor poles will thus continue to move from the unaligned position of phase B, Figure 2.1(c), to the aligned position of phase B, Figure 2.1(d). Similarly for phase C, hence the rotor will rotate counterclockwise. However, if the phases are energized BAC instead of ABC, the rotor will rotate clockwise. Consideration of this basic operation highlights that the operating direction has nothing to do with the current polarity. Rotation direction is determined by the sequence of the energized phases, and the frequency of this switching sequence dictates the speed of the rotor.

2.2.1. Mathematic Model of Conventional SRMs.

CSRM's operation is an electromagnetic process; hence, it follows that the laws of electromagnetic induction, Kirchhoff's current law and the law of conservation of energy. Based on the laws, CSRM mathematics model is developed, as illustrated schematically by the simplified equivalent circuit in Figure 2.2. It also shows the energy conservation process of the CSRM. The left part represents the electrical circuit of the SRM, while the right part indicates the mechanical operation process, with the middle part detailing the electromagnetic transfer process.

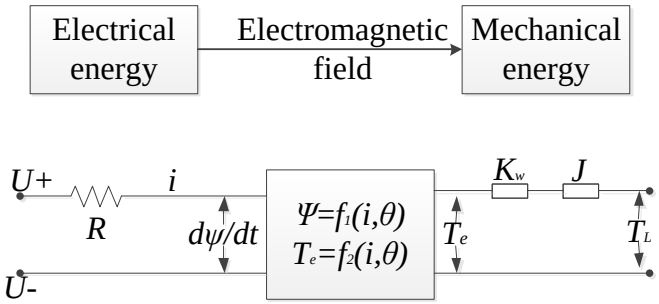

Figure 2.2 Simulation diagram of CSRM.

Firstly, the voltage equation of one phase of CSRM can be written from first principles as Equation 2-1:

$$u_k = i_k R_k + \frac{d\psi_k}{dt} \qquad \text{Equation 2-1}$$

where u_k, i_k, R_k and ψ_k are the voltage, current, resistance, and flux-linkage of phase k. Equation 2-1 shows that the voltage drop has two components: one is due to the electrical resistance of the phase winding, while the other due to the flux-linkage variation in the phase winding. The phase coil flux-linkage is produced not only by coil self-induction but also by mutual induction with other coils. However, for CSRM, mutual inductance is much lower compared to self-inductance. In the meantime, it's usually under single-phase energization; thus, mutual induction is ignored in CSRM. To simplify the process, flux-leakage is not considered. Since $\psi_k = i_k L_k$, Equation 2-2 can be derived.

$$\frac{d\psi_k}{dt} = L_k \frac{\partial i_k}{\partial t} + i_k \frac{\partial L_k}{\partial t} \qquad \text{Equation 2-2}$$

The voltage Equation 2-2 can be rewritten to Equation 2-3, by mathematical decomposition:

$$u_k = i_k R_k + \left(L_k + \frac{1}{2} i_k \frac{\partial L_k}{\partial i_k} \right) \frac{\partial i_k}{\partial t} + \frac{1}{2} i_k \frac{\partial L_k}{\partial \theta} w \qquad \text{Equation 2-3}$$

where L_k is the induction of phase k. Equation 2-3 shows that the flux variation is caused by two mechanisms: one is the current changing in the coil, and the other is the

rotation of the rotor. The input voltage is thus finally divided into three parts: the resistive voltage drop, the inductive voltage drop and the back-EMF.

When an electromagnetic machine works as an electric motor, it converts electrical energy to mechanical energy. To simplify the process, it's assumed that the whole process is within CSRM's unsaturated condition. Then flux-linkage-current characteristic of the process switching conditions are shown in Figure 2.1(a) and Figure 2.1(b) can be represented on the system flux-linkage versus phase current diagram, as shown in Figure 2.3.

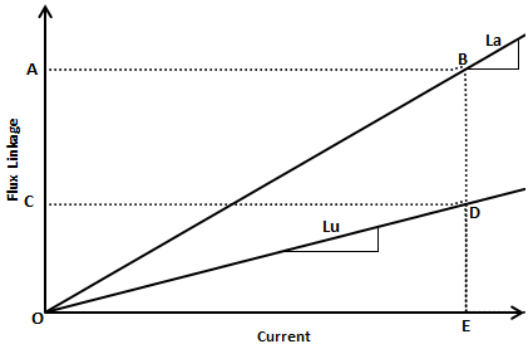

Figure 2.3 Ideal flux-linkage versus phase current profiles at rotor aligned and unaligned commutation positions.

For motoring operation, part of the electrical input energy W_e is stored in the phase magnetic circuit as W_f and the other part is converted to mechanical energy as W_m. Thus, the electrical input energy can be expressed as Equation 2-4.

$$W_e = W_f + W_m \qquad \text{Equation 2-4}$$

For an assumed unsaturated condition, the energy stored in the phase coils can be expressed by Equation 2-5:

$$W_f = \int i\,d\lambda = \int i\,d(i\cdot L) = \frac{1}{2}L\cdot i^2 + \int i^2 dL \qquad \text{Equation 2-5}$$

where λ is the phase coil flux-linkage, L is the self-inductance of the phase coils, and i is the exciting current. The motor status moves from point D to B in Figure 2.3, when a CSRM rotates from unaligned commutation position to the aligned commutation position with a constant current i_c. Then, the second part of Equation 2-5 can be resolved as Equation 2-6:

$$\int i^2 dL = i^2\cdot(L_a - L_u) = i_c\cdot(\lambda_a - \lambda_u) \qquad \text{Equation 2-6}$$

where L_a is the inductance value at the aligned commutation position, and L_u the inductance value at unaligned commutation position. During this same period, the electrical input energy changes from area OCDEO to area OABEO. The electrical input energy is related to the excitation and the flux-linkage at different positions, which can be expressed as Equation 2-7:

$$W_e = F_c\cdot(\phi_a - \phi_u) \qquad \text{Equation 2-7}$$

where $F_c = N\cdot i_c$ and $\phi = \frac{1}{N}\lambda$. The second part of the stored energy in Equation 2-6 equals the electrical input energy in Equation 2-7. From Equation 2-4 to Equation 2-7, Equation 2-8 is derived. This indicates the converted mechanical energy comes from the first part of the stored energy in coils.

$$W_m = \frac{1}{2} L \cdot i^2 \qquad \text{Equation 2-8}$$

For the motoring energy conversion system, the decreasing energy means an increasing output of mechanical energy. Thus,

$$W_m = \frac{1}{2} L \cdot i^2 = T_e \cdot \delta\theta \qquad \text{Equation 2-9}$$

If phase current is assumed constant, the electromagnetic torque for each phase can be derived as Equation 2-10.

$$T_e = \frac{1}{2} \cdot \frac{dL}{d\theta} \cdot i^2 \qquad \text{Equation 2-10}$$

The electrical energy is converted to mechanical energy via the dynamic electromagnetic field. As the excited phases switch sequentially, energy conversion will be continuous, and the rotor will rotate as required. From Equation 2-10, it can be seen that CSRM's torque is not related to the polarity of phase current; and direction and speed of rotation are only determined by the sequence of the excited phases and the switching frequency. To increase the area for energy conversion, CSRM usually operated outside the linear magnetic characteristics, and therefore magnetic saturation is usually considered. This can be a problem for machine design and control. In the meantime, the saturated field will also significantly increase iron losses.

Machine electromagnetic torque is used to overcome friction torque and to provide system acceleration torque and the required external load torque, as represented in Equation 2-11:

$$T_e = J\frac{d^2\theta}{dt^2} + K_w\frac{d\theta}{dt} + T_L \qquad \text{Equation 2-11}$$

where J is the machine rotor and system moment of inertia, K_w is the machine viscous friction constant and T_L is the torque applied to the rotor by an external load.

2.2.2. Control Method and Converter Configuration of CSRMs.

From Equation 2-10, a net positive motoring toque is achieved while the phase is excited when the inductance increases. As discussed previously, the cyclic switching characteristic of CSRM, where all phase current profiles repeat at every rotor pole pitch, allows the analysis of only one rotor pole pitch to represent complete rotation. The nonlinear characteristic introduces complexity in analysis. Thus a linear, simplified model of phase inductance variation can be applied to explain the torque generation process of the CSRM, as illustrated in Figure 2.4.

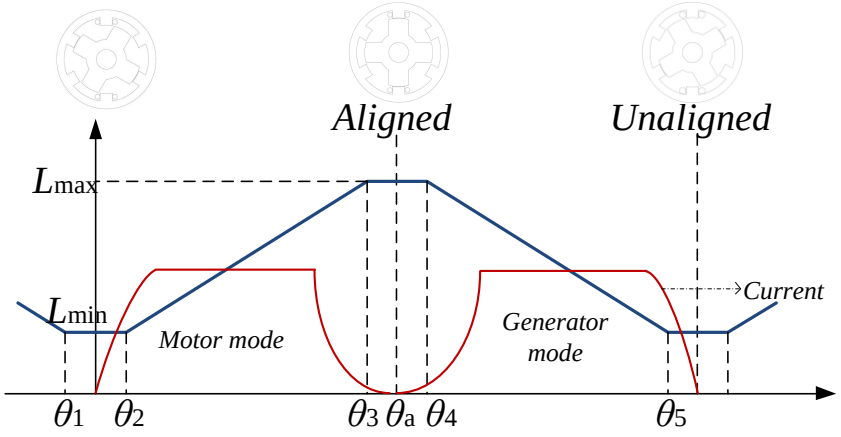

Figure 2.4 Phase inductance characteristics of CSRM versus rotor position, at motor and generator modes.

From Figure 2.4, the following position relationships hold:

$$\begin{aligned} \theta_2 &= \frac{1}{2}\left[\frac{2\pi}{P_r} - (\beta_s + \beta_r)\right] \\ \theta_3 &= \theta_2 + \beta_s \\ \theta_4 &= \theta_3 + (\beta_r - \beta_s) \\ \theta_5 &= \theta_4 + \beta_s \end{aligned} \qquad \text{Equation 2-12}$$

where β_s, β_r are the stator pole arc and rotor pole arc respectively and P_r is the rotor pole number.

As Figure 2.4 shows, if the phase current is excited at the inductance increasing positions, the machine operates at a motor mode, but a generator mode if at the decreasing inductance range. To avoid negative torque generation, the turn-on and turn-off angles have to be specified. For this nonlinear model, the inductance profile of which is not only a function of the rotor position but also of current. It requires more complex analysis to figure out the right turn-on and turn-off. This analysis is called CSRM's control strategies. A controller has motor's dynamic parameter and position information as input, using its control strategy to generate signals to control the inverter to turn on or turn off under a certain condition, as shown in Figure 2.5.

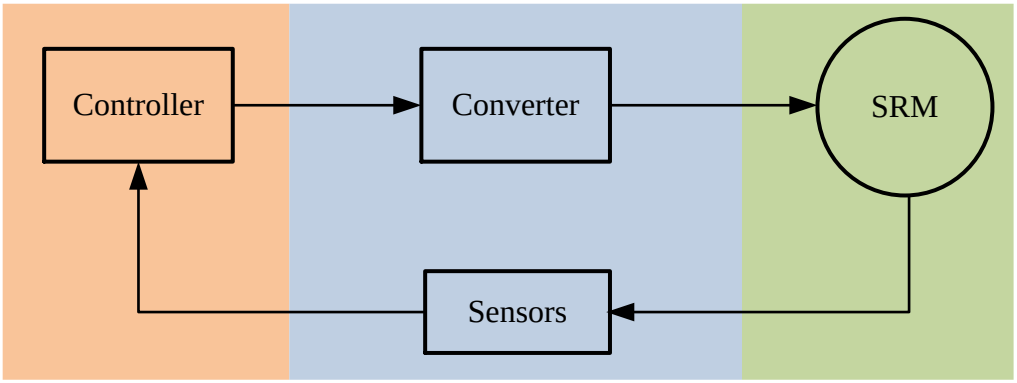

Figure 2.5 Diagram of a typical CSRM drive.

Different control strategies can be used to generate phase energizing sequence signals. To apply these sequences to a CSRM requires an electronic commutation connected with a DC power source, which is also called converter. For the power converters of CSRM, an asymmetric 2-switch-per-phase converter is used. Asymmetric bridge converter has the advantage of a simple concept, flexibility in control, as well as better faults tolerance. Figure 2.6 shows the asymmetric bridge converter of three-phase CSRM, and there are two switches for each phase, an upper one and a lower one.

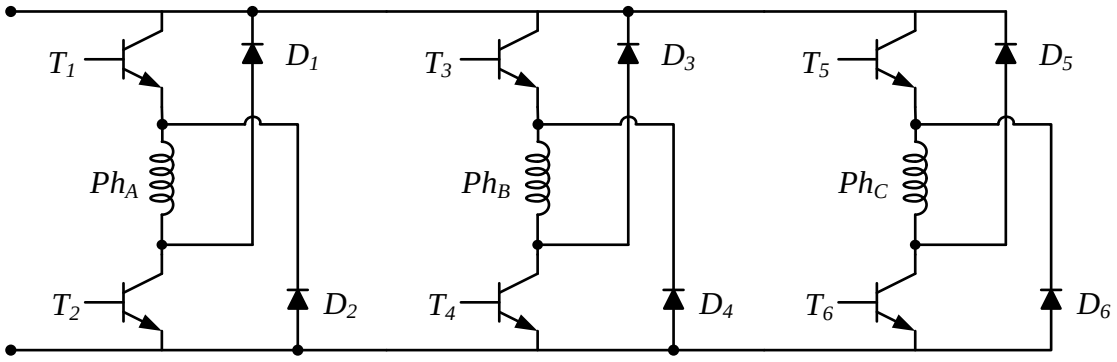

Figure 2.6 Configuration of an asymmetric bridge converter for a three-phase CSRM.

2.3. Toroidal-Winding SRMs.

For toroidal winding, it still maintains the high failure tolerance and low resistance advantages as concentrated winding. In addition, toroidal winding introduces additional winding space outside the stator lamination. Moreover, practically, it has a higher filling factor since it's easier for manufacturing. Especially for single layer TSRM, as it doesn't need extra space in the slot for winding needles as well as the insulation purpose afterwards, it results in a relatively higher filling factor. Last but not the least, toroidal winding benefits machine's thermal performance as the winding is directly exposed for cooling. All these characteristics have a direct impact on machine output performance.

2.3.1. Double Layer Toroidal-Winding SRM (DLTSRM).

CSRM uses decoupled concentrated phase winding so that torque is generated due to the rate of change of the self-inductance of the excited phase. Based on CSRM, the first toroidal winding switched reluctance motor is derived and presented in Figure 2.7. To replace the conventional concentrate winding round single stator pole, two coils are wound around the yoke beside this pole. As there are double layers of winding in each stator slot which belongs to two different phases, this type machine is named as double-layer toroidal winding SRM. For a consistency comparison, the number of turns per coil is the same, which is also applied to the other winding scheme discussed later. All of the three machines have concentrated winding. "-" represents that the current go into the paper, while "+" represents the currents coming out from paper.

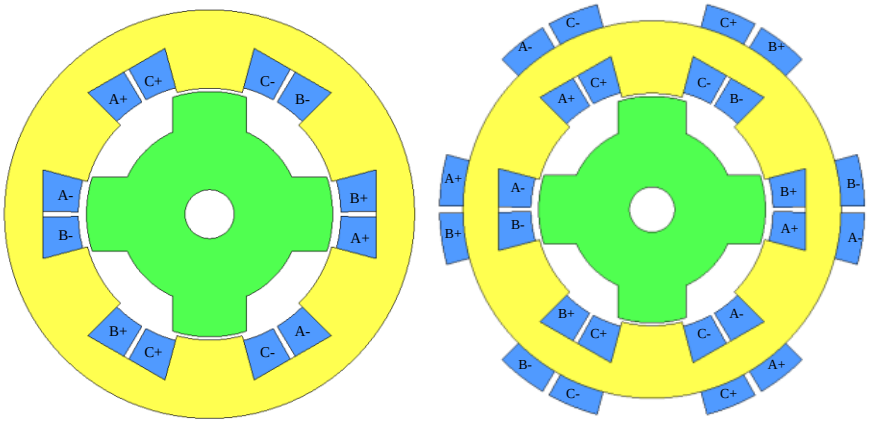

(a) (b)

Figure 2.7 Winding schemes: (a) CSRM, (b) DLTSRM.

From the magnetic point of view, these two coils around the yoke beside a certain stator pole have the same function as the conventional coil around the pole. This could be seen clearly from their flux distribution at unaligned (active stator pole is aligned with the middle line between two rotor poles) and aligned (active stator pole is fully aligned with one rotor pole) positions in Figure 2.8, in which phase A is injected with a constant DC current.

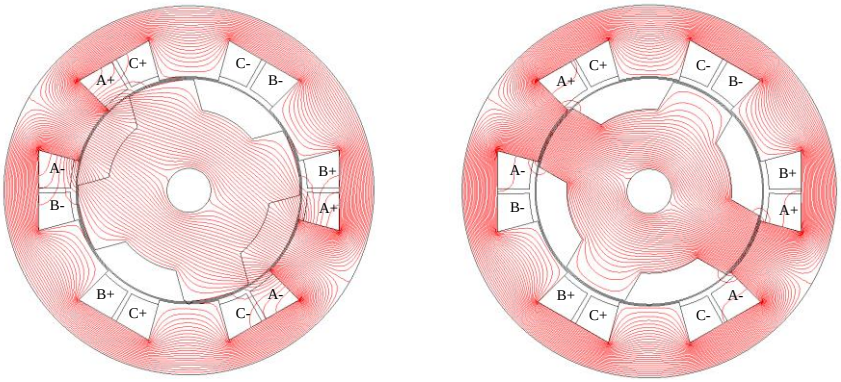

(a) (b)

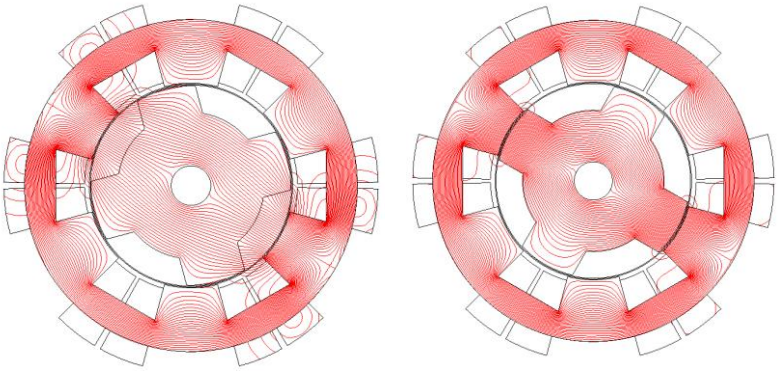

(c) (d)

Figure 2.8 Flux distribution: (a) CSRM at unaligned position, (b) CSRM at aligned position, (c) DLTSRM at unaligned position, (d) DLTSRM at aligned position.

The flux distribution of these two machines is almost the same, not only on the stator and rotor cores; but also in the air region between the rotor and stator. From this, it can be predicted that these two types of machines would have the same electromagnetic performance. From Figure 2.8, it's obvious for CSRM, that there is no flux generated by the active phase-A coupling with any other phases. However, for the specific toroidal winding, the flux by phase-A goes into one coil of phase-B, but the same amount into another coil of phase-B. Because these two coils are connected in opposite polarity, these flux coupling will be cancelled with each other, leading to a decoupled phase winding between A and B. The same manner can also be applied between phase A and C. Thus, the mutual coupling is also very limited in this DLTSRM.

The simplified equivalent magnetic circuits of CSRM and DLTSRM are presented in Figure 2.9, while it is assumed that phase A is active. In the equivalent magnetic circuits, *NI* represents the *MMF* of a single active coil of phase A. Φ_1 is the flux across the air gap,

linking the stator and rotor poles. R_1 includes reluctance of the air between the to-be-aligned / partially aligned/aligned stator and rotor poles, these stator and rotor poles, as well as the rotor yoke. This flux is divided into two parts: Φ_2 goes to the upper part of the stator yoke while Φ_3 to the bottom part. R_2 is the magnetic reluctance for half of the stator yoke, R_3 the other half.

The self-inductance of phase A is proportional to Φ_1, which depends on the equivalent total reluctance of the magnetic circuit. If saturation and flux leakage can be ignored, R_2 and R_3 are then almost constant, position-dependent overlap angle between the stator and rotor poles leads to varying $R_1$with respect to position.

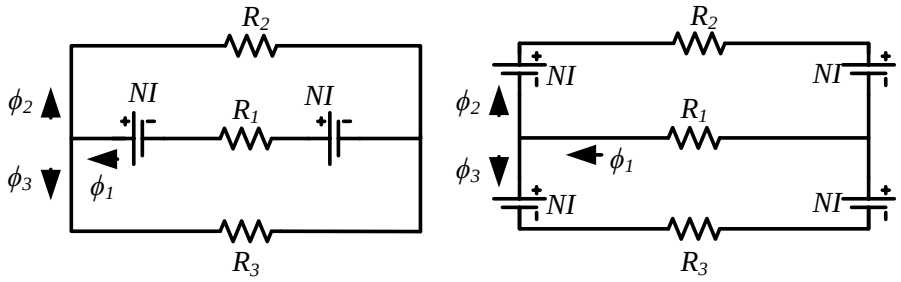

Figure 2.9 Simplified magnetic circuits: (a) CSRM, (b) DLTSRM.

Referring to Fig. 2.10, if the permeability of lamination is infinity compared to air, R_2 and R_3 are both equal to zero, the maximum inductances at *p4* of these two types of machine can be developed as:

$$\begin{aligned} \boldsymbol{L}_a &= \frac{4N^2}{R_g} = \frac{4N^2\mu_0 A}{g} = \frac{4N^2\mu_0 L_{stk} D_r}{g}\alpha \\ \boldsymbol{L}_b(\theta_e) &= \boldsymbol{L}_a(\theta_e - 120°) \\ \boldsymbol{L}_c(\theta_e) &= \boldsymbol{L}_a(\theta_e + 120°) \\ \boldsymbol{M}_{ab} &\approx 0; \quad \boldsymbol{M}_{bc} \approx 0; \quad \boldsymbol{M}_{ac} \approx 0. \end{aligned}$$

Equation 2-13

where N is the number of turns per coil for both CSRM and DLTSRM, R_g is the reluctance of air gap, μ_0 is the permeability of the air gap, L_{stk} is the stack length of the core, D_r is the diameter of the rotor pole, g is the air-gap length, and α is overlap angle of active stator poles with the rotor poles.

Subscript a, b, and c represent the three phases, and θ_e is the electrical degree. By defining θ_e as the electrical degree regarding the magnetic poles, we can see that $\theta_e = P_r \cdot \theta_m$ with that θ_m is the mechanical degree, P_r is the number of magnetic pole pairs, which is 2 for this three-phase 6-4 machine. Based on Equation 2-13, the simplified linear self-inductance of phase-A is presented in Figure 2.10.

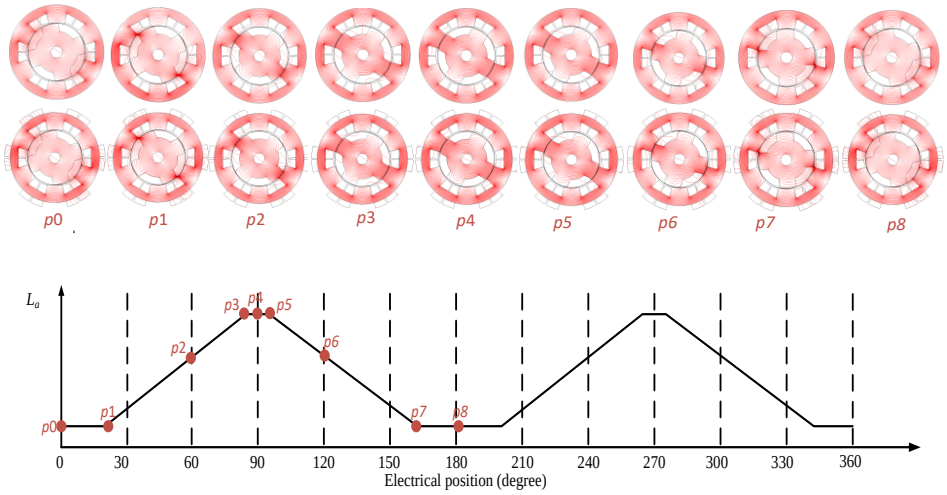

Figure 2.10 Self-inductance variation of the 6/4 CSRM and DLTSRM according to the rotor positions.

Rotor position *p*0 is the unaligned position, the flux flows through the largest air region, leading to a minimum value of the inductance. Position *p*1 represents the position where the stator and rotor poles start to overlap. Because of the assumption that permeability of lamination is infinity compared to air and no saturation and flux leakage, L_a stays as the minimum value from *p0* to *p1*. From *p1*, inductance starts increasing, continuing at *p2* and ending at *p3*. In the region between *p3* and *p5,* 100% overlap is achieved; thus, the inductance stays constant at the maximum value, while *p4* is the aligned rotor position. As the rotation continues, symmetry with respect to *p4* is achieved.

This prediction is then verified by FEA as shown in Figure 2.11. Flux leakage and saturation are both considered in this analysis, and the inductance profile is a nonlinear function of rotor position. The mutual inductance of both the CSRM and DLTSRM is at an ignorable level compared with self-inductance; the magnitude of self-inductance is 100 times that of mutual inductance. Therefore DLTSRM can also apply the conventional asymmetric converter and the same switching sequence as CSRM.

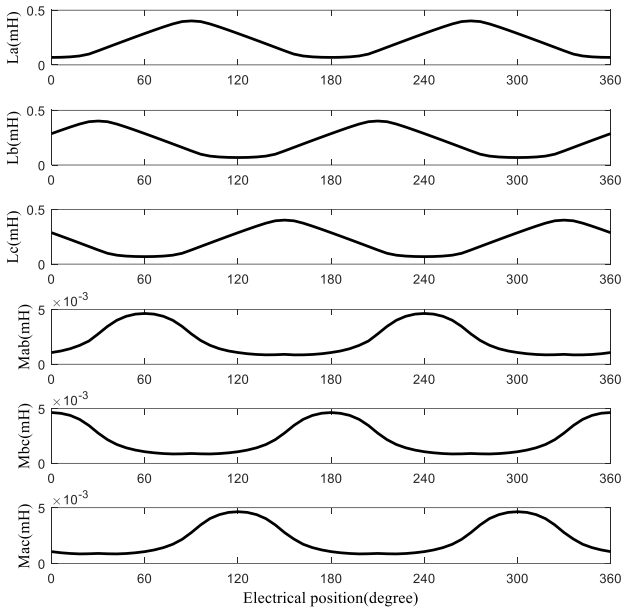

(a)

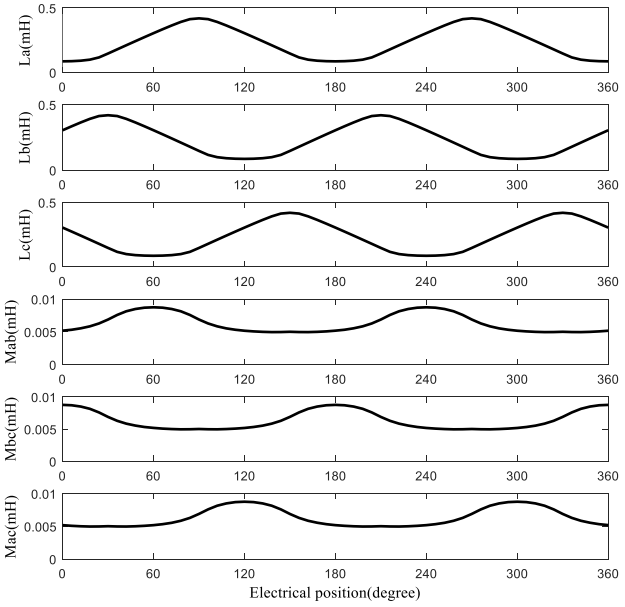

(b)

Figure 2.11 Inductance profile with saturation and flux leakage considered: (a) CSRM, (b) DLTSRM.

From Figure 2.10 and Figure 2.11, it shows only the self-inductance contributes to the torque generation. One phase winding can only contribute to positive torque for at most one half of the period, which limits the utilization rate of the electrical circuits. It also needs high volt-ampere and reactive power to drive a motor. Meanwhile, the single-phase excitation of CSRM leads to full magnetization and demagnetization during the torque generation, which introduces attractions and rebounding of the magnetic circuits. All this increases the torque ripple. Therefore, another winding topology has been proposed with the utilization of mutual inductance. Single-layer toroidal-winding SRM is studied below with enhanced the mutual effects between phases.

2.3.2. Single Layer Toroidal-Winding SRM (SLTSRM).

Here, another type of toroidal winding is presented, of which the mutual inductance is also an important component for torque generation. The winding scheme of this SLTSRM is compared against CSRM in Figure 2.12.

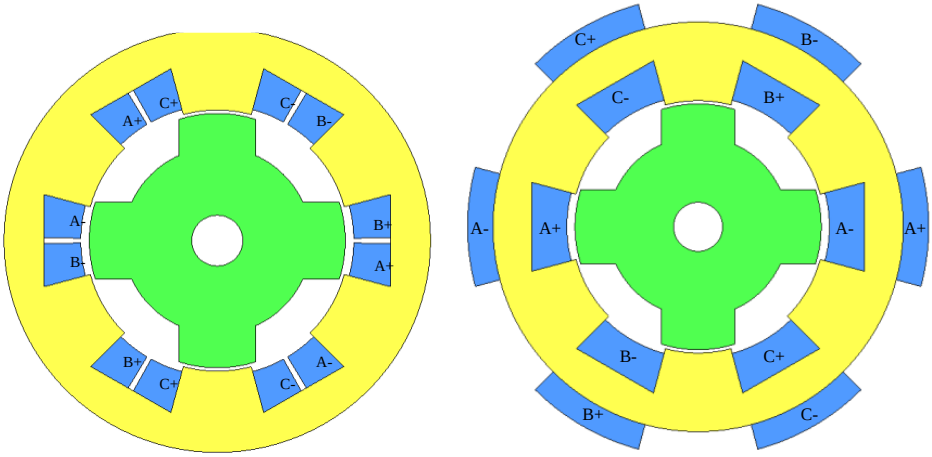

(a) (b)

Figure 2.12 Winding schemes: (a) CSRM, (b) SLTSRM.

As shown in Figure 2.12, SLTSRM is modified based on the double layer TSRM in Figure 2.7, both with toroidal winding. As introduced above, there will be two coils in each slot in DLTSRM. In the SLTSRM, these two coils are parallel connected as one. Thus, there will be 6 coils wounded in the 6 stator slots. The term ‘single-layer’ indicates one coil in each slot for this type of machine. The polarity of two coils of one single phase is opposite. This type of machine has relatively similar electromagnetic performance as the single-layer full-pitch winding introduced by B.C. Mecrow [63]. The full-pitch winding topology can help reduce the torque ripple. However, its extensively long end-windings result in large overall axial rotor length and make it unsuitable for compact or high-speed operating conditions. However, the SLTSRM use the toroidal winding to overcome this while keeping the merits of the full-pitched mutual coupled SRMs. The thermal and electrical isolation between the three phases also increases reliability and the slot filling factor.

The flux distribution at different positions of SLTSRM is presented in Figure 2.13, in which a constant DC current is injected into phase A. Because of the special winding topology, the magnetized pole is upper and bottom poles as shown in Figure 2.13 when only phase A energized. Therefore, the aligned and unaligned rotor position is completely different from that of Figure 2.8. For consistency, the initial position (0 electrical degrees) and 90 electrical degrees stay like that in Figure 2.13(a) and (b), which are the unaligned and aligned position for CSRM, and DLTSRM. Now for SLTSRM, the rotor fully unaligned with the magnetized stator pole at 60 electrical degrees ((c) in Figure 2.13) and completely aligned at 150 electrical degrees ((d) in Figure 2.13).

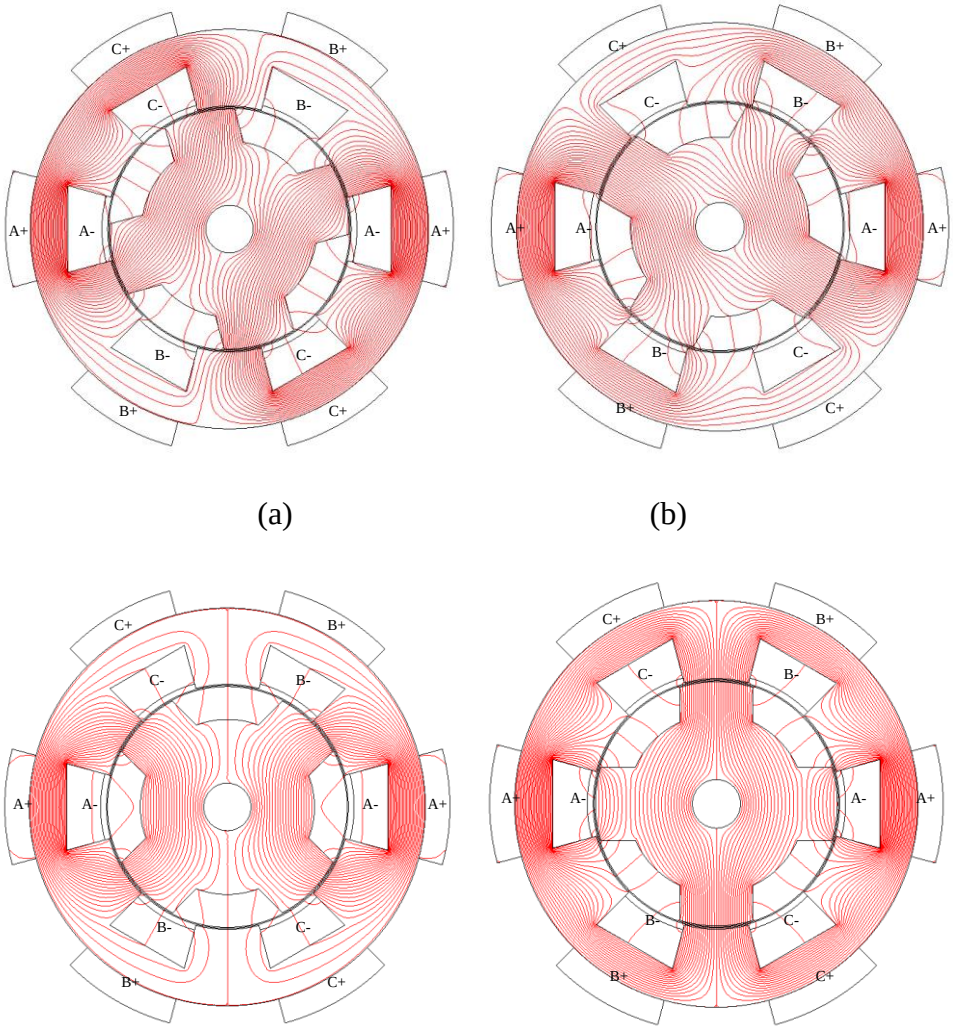

Figure 2.13 Flux distribution of SLTSRM: (a) 0 electrical degree, (b) 90 electrical degree, (c) 60 electrical degree, (d) 150 electrical degree.

The simplified magnetic circuit of the whole machine is presented in Figure 2.14, for clear demonstration, the poles are numbered. In this equivalent magnetic circuit, saturation and flux leakage are neglected. In Figure 2.14, R_1, R_2, and R_3 are the reluctance of the corresponding stator pole, overlap air gap between this stator pole and rotor pole or

air region between this stator pole and rotor core, as well as rotor pole if necessary. For example, R_1 is for the stator pole numbered as 1 which is in the vertical direction; R_2 is for the two 60 degree off from the vertical direction in clockwise; R_3 is for the other two stator poles. R4 is the reluctance of the rotor yoke. From this magnetic circuit and the winding location, φ_{ab} represents the flux coupling with phase B, and φ_{ab} coupling with phase C. *NI* represents the *MMF* of the single active coil of phase A.

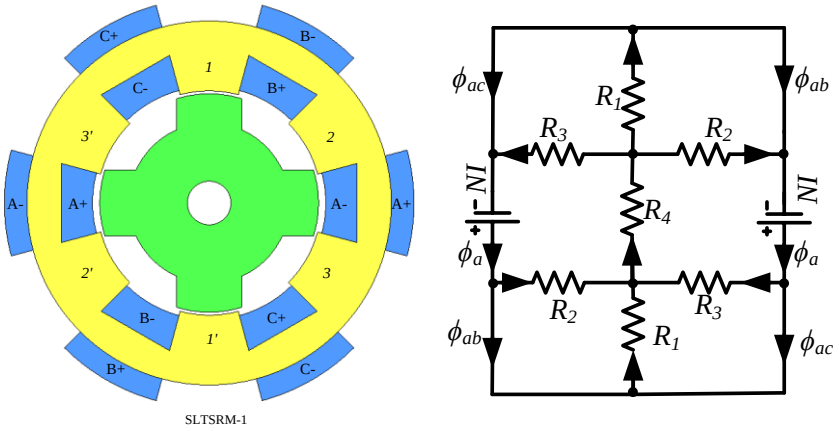

Figure 2.14 Machine layout with pole numbered, and simplified equivalent magnetic circuit of SLTSRM.

If similarly assumed as before that permeability of lamination is infinity compared to air, then the overlapped angle between the rotor pole and the corresponding stator pole will dominate the reluctance values. And the reluctance of the rotor yoke will be much lower compared with others, so $R_4 \approx 0$.

$$R_1 = \frac{g}{\mu_0 L_{stk} D_r \alpha}$$
$$R_2 = \frac{g}{\mu_0 L_{stk} D_r \beta} \qquad \text{Equation 2-14}$$
$$R_3 = \frac{g}{\mu_0 L_{stk} D_r \gamma}$$

where α, β, and, γ are the overlap angle of pole pair #1 with the rotor poles, pole pair #2 with rotor pole and pole pair #3 with rotor pole. It's now that, α, β, and, γ are in a complementary relationship, which means that $\alpha + \beta + \gamma$ = constant.

Solving the above equivalent magnetic circuit, the fluxes are shown in Equation 2-15. From the flux, the self and mutual inductances can be derived as in Equation 2-16.

$$\phi_a = \frac{NI}{4}\left(\frac{1}{R_1} + \frac{1}{R_2} + \frac{1}{R_3}\right)$$
$$\phi_{ab} = \frac{NI}{4}\left(\frac{1}{R_1} + \frac{1}{R_3} - \frac{1}{R_2}\right) \qquad \text{Equation 2-15}$$

$$\boldsymbol{L}_a = \frac{N^2}{2}\left(\frac{1}{R_1} + \frac{1}{R_2} + \frac{1}{R_3}\right)$$
$$\boldsymbol{L}_b(\theta_e) = \boldsymbol{L}_a(\theta_e - 120°)$$
$$\boldsymbol{L}_c(\theta_e) = \boldsymbol{L}_a(\theta_e + 120°)$$

Equation 2-16

$$\boldsymbol{M}_{ab} = \frac{N^2}{2}\left(\frac{1}{R_1} + \frac{1}{R_3} - \frac{1}{R_2}\right)$$
$$\boldsymbol{M}_{bc}(\theta_e) = \boldsymbol{M}_{ab}(\theta_e - 120°)$$
$$\boldsymbol{M}_{ac}(\theta_e) = \boldsymbol{M}_{ab}(\theta_e + 120°)$$

Substituting the relationship ($\alpha + \beta + \gamma$ = constant) and Equation 2-14 into Equation 2-16, it shows that if saturation and flux leakage is neglected, the self-inductance of this machine is constant as shown in Equation 2-17 which doesn't vary with the rotor position.

$$\boldsymbol{L}_a = \boldsymbol{L}_b = \boldsymbol{L}_c = const. \qquad \text{Equation 2-17}$$

But the mutual inductance is still a function of rotor position. The torque generation of this SLTSRM will totally rely on the rate of change of mutual inductance against rotor position.

The simplified mutual inductance between phase A and B is presented in Figure 2.15, neglecting the effect of saturation and flux leakage. At the initial position *p*0, the overlapping angles α and β are equal with each other, the magnetic reluctance of air region between pole #3 and the rotor yoke determines the mutual inductance between phase A and B. Therefore, the value is small. As rotating, α decreases while β increases. This difference cancels the coupled inductance caused by the air region between pole #3 and the rotor yoke. The magnitude decreases until the mutual coupling cross zero. From then, the mutually coupled flux between phase A and B changes direction and starts to rise as the difference between α and β continues rising. However, this rising would continue long until the overlapping angle between stator pole #1 and rotor pole becomes zero, while is indicated as *p2* in Figure 2.15. From *p2* the magnitude begins to reduce back to zero until position *p3*. Then the flux changes direction again and starts rising in the opposite direction until *p4*. From *p4* till p5, the overlapping angle between stator pole pair #2 and rotor poles β is zeros. However, at the same time, α is reducing while γ

increases the same amount as α has reduced. These two cancels with each other, leading to a constant region for the M_{ab}.

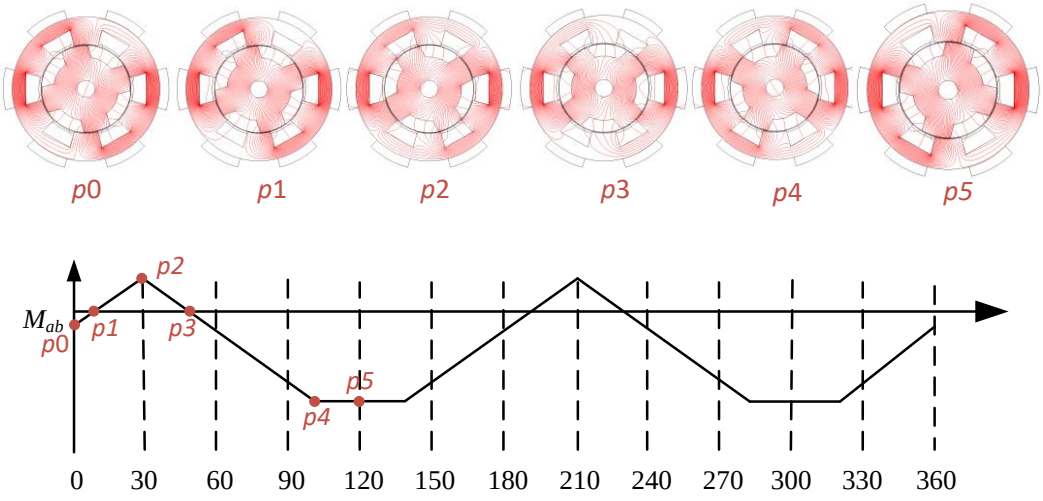

Figure 2.15 M_{ab} variation of the 6/4 SLTSRM according to the rotor positions.

The actual inductances are presented in Figure 2.16, considering saturation and flux leakage. Because of the saturation and flux leakage, the self-inductances are not constant anymore. It shows that the self-inductance is about 2 times the magnitude of the mutual inductance. Theoretically, the flux linkage generated by the active phase A is divided into two other phases. Thus, each of the mutually coupled flux will be roughly half that of the self-generated flux in phase A. However, the variation of self-inductance is much smaller.

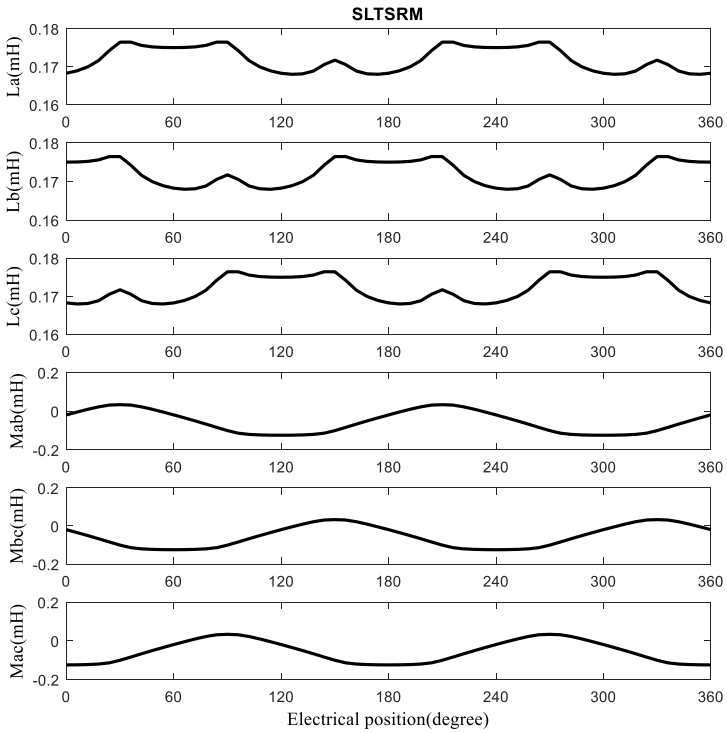

Figure 2.16 Inductance profile of the SLTSRM with saturation and flux leakage considered.

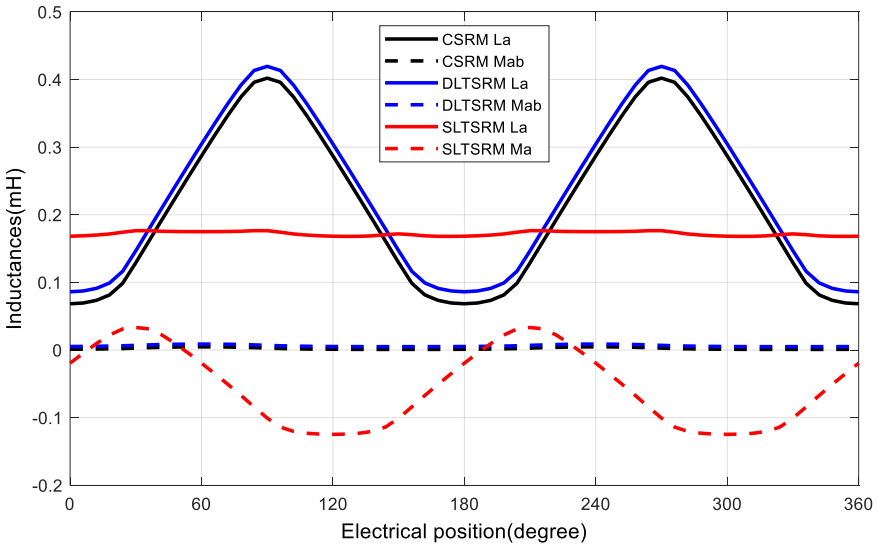

Figure 2.17 Inductance comparison between CSRM, DLTSRM, and SLTSRM.

Finally, the inductance profiles of CSRM, DLTSRM, and SLTSRM are shown and compared in Figure 2.17, from which not only the relative magnitude but also the variation can be seen clearly. From the comparison, it shows for CSRM and DLTSRM has almost the same inductance profile. Not only the mean value but also the changes of self-inductance are both very significant compared with others. However, for SLTSRM, self –inductance is almost constant, but the mutual inductance variation is more significant.

2.4. General Torque Equations for SRMs.

The voltage for any types of SRM can be expressed by a general equation in Equation 2-18:

$$\begin{aligned}\mathbf{V} &= R\mathbf{I} + \frac{\mathrm{d}\boldsymbol{\Psi}}{\mathrm{d}t} = R\mathbf{I} + \omega_m \frac{\mathrm{d}\boldsymbol{\Psi}}{\mathrm{d}\theta_m} \\ &= R\mathbf{I} + \omega_m \frac{\mathrm{d}\mathbf{L}\mathbf{I}}{\mathrm{d}\theta_m} \\ &= R\mathbf{I} + \mathbf{L}\frac{\mathrm{d}\mathbf{I}}{\mathrm{d}t} + \omega_m \left(\frac{\mathrm{d}\mathbf{L}}{\mathrm{d}\theta_m}\right)\mathbf{I}\end{aligned} \qquad \text{Equation 2-18}$$

where R is the phase resistance, $\mathrm{V} = [v_a, v_b, v_c]^{\mathrm{T}}$ is the voltage vector of the three phases, $\mathbf{I} = [i_a, i_b, i_c]^{\mathrm{T}}$ is the current vector, ω_m is the mechanical rotation speed, and $\boldsymbol{\Psi}$ is the flux linkage vector, which is solved from the current vector and the inductance matrix $\mathbf{L}$ in Equation 2-19.

$$\mathbf{L} = \begin{bmatrix} L_u & M_{uv} & M_{wu} \\ M_{uv} & L_v & M_{vw} \\ M_{wu} & M_{vw} & L_w \end{bmatrix}. \qquad \text{Equation 2-19}$$

Then the energy absorbed from the electrical source is stated in Equation 2-20.

$$\begin{aligned} \frac{\mathrm{d}W_{in}}{\mathrm{d}t} &= \mathbf{I}^{\mathrm{T}}\mathbf{V} = \mathbf{I}^{\mathrm{T}}R\mathbf{I} + \mathbf{I}^{\mathrm{T}}\frac{\mathrm{d}\boldsymbol{\Psi}}{\mathrm{d}t} = \mathbf{I}^{\mathrm{T}}R\mathbf{I} + \mathbf{I}^{\mathrm{T}}\omega_m\frac{\mathrm{d}\boldsymbol{\Psi}}{\mathrm{d}\theta_m} \\ &= R\mathbf{I}^{\mathrm{T}}\mathbf{I} + \omega_m\mathbf{I}^{\mathrm{T}}\frac{\mathrm{d}\mathbf{L}\mathbf{I}}{\mathrm{d}\theta_m} \\ &= R\mathbf{I}^{\mathrm{T}}\mathbf{I} + \mathbf{I}^{\mathrm{T}}\mathbf{L}\frac{\mathrm{d}\mathbf{I}}{\mathrm{d}t} + \omega_m\mathbf{I}^{\mathrm{T}}\left(\frac{\mathrm{d}\mathbf{L}}{\mathrm{d}\theta_m}\right)\mathbf{I} \end{aligned} \qquad \text{Equation 2-20}$$

If the magnetic nonlinearity and loss are ignored, the rate of change of the magnetic stored energy is presented in Equation 2-21.

$$\begin{aligned} \frac{\mathrm{d}W_{mag}}{\mathrm{d}t} &= \frac{\mathrm{d}}{\mathrm{d}t}\left(\frac{1}{2}\mathbf{I}^{\mathrm{T}}\mathbf{L}\mathbf{I}\right) = \frac{1}{2}\mathbf{I}^{\mathrm{T}}\frac{\mathrm{d}\mathbf{L}}{\mathrm{d}t}\mathbf{I} + \left(\frac{\mathrm{d}\mathbf{I}}{\mathrm{d}t}\right)^{\mathrm{T}}\mathbf{L}\mathbf{I} \\ &= \frac{1}{2}\omega_m\mathbf{I}^{\mathrm{T}}\frac{\mathrm{d}\mathbf{L}}{\mathrm{d}\theta_m}\mathbf{I} + \left(\frac{\mathrm{d}\mathbf{I}}{\mathrm{d}t}\right)^{\mathrm{T}}\mathbf{L}\mathbf{I} \end{aligned} \qquad \text{Equation 2-21}$$

According to the law of conservation of energy, the power relationship is shown in Equation 2-22.

$$\frac{\mathrm{d}W_{in}}{\mathrm{d}t} = \frac{\mathrm{d}W_{mag}}{\mathrm{d}t} + \frac{\mathrm{d}W_{mec}}{\mathrm{d}t} \qquad \text{Equation 2-22}$$

The converted mechanical power W_{mec} is the absorbed electrical power subtracted by the loss of the resistance and the rate of change of magnetic stored energy, as shown in Equation 2-23.

$$\frac{\mathrm{d}W_{mec}}{\mathrm{d}t} = p_{mec} = \frac{1}{2}\omega_m \mathbf{I}^{\mathrm{T}} \frac{\mathrm{d}\mathbf{L}}{\mathrm{d}\theta_m}\mathbf{I} \qquad \text{Equation 2-23}$$

Then the instantaneous electromagnetic torque can be solved by Equation 2-24.

$$T_e = \frac{p_{mec}}{\omega_m} = \frac{1}{2}\mathbf{I}^{\mathrm{T}} \frac{\mathrm{d}\mathbf{L}}{\mathrm{d}\theta_m}\mathbf{I} \qquad \text{Equation 2-24}$$

Substituted the current vector and inductance matrix into Equation 2-24, the torque equation can be rewritten as Equation 2-25.

$$T_e = \frac{1}{2}\left(\frac{\mathrm{d}L_a}{\mathrm{d}\theta_m} I_a^{\,2} + \frac{\mathrm{d}L_b}{\mathrm{d}\theta_m} I_a^{\,2} + \frac{\mathrm{d}L_c}{\mathrm{d}\theta_m} I_a^{\,2}\right) + \frac{\mathrm{d}M_{ab}}{\mathrm{d}\theta_m} I_a I_b + \frac{\mathrm{d}M_{bc}}{\mathrm{d}\theta_m} I_b I_c + \frac{\mathrm{d}M_{ac}}{\mathrm{d}\theta_m} I_a I_c$$

Equation 2-25

From the general torque equation in Equation 2-25, it's obvious that the torque is actually a function of the rate of change of both the self and mutual inductances. However, for CSRM, the last three items are omitted as the mutual inductance is almost zero. This is the same condition for the double layer SRM presented in this chapter. As for the SLTSRM, the mutual inductance plays a significantly important role in the torque generation. Benefiting from the mutual-inductance, more than one-phase could contribute the torque generation at each moment. This could potentially increase the torque density.

2.5. Conclusions.

For electrical machines, winding topology has essential effects. This is especially true for SRMs as windings are the sole MMF source. There could be various winding topologies,

resulting in different inductance coupling and different performance. In this chapter, the operation principles of three types of SRMs are presented and compared. The general voltage and torque equation are stated. All of the analysis is based on the most popular internal rotor 6-4 machine with identical lamination.

Considering the enhanced cooling, the toroidal winding attracts more attention for this thesis over CSRM. In the meantime, for DLSRM, it replaces the conventional winding around the pole. Two coils are wounded around the yoke beside the pole. From the magnetic point of view, these two coils have the same function as the conventional pole coil. Therefore, it still applies the conventional asymmetric converter and the same switching sequence, and the mutual inductance is ignorable compared with self-inductance, which is the same as CSRM. However, this winding topology significantly increases the copper material as well as the copper losses. Taking all the above into consideration, the SLTSRMs will be the focus of further study in this thesis and compared against CSRM.

Chapter 3 Static Characteristics Comparison between Conventional and Toroidal-Winding SRMs

3.1. Introduction.

As discussed in Chapter 2, DLTSRM generates the same electromagnetic field as CSRM. In DLTSRM, mutual inductance is at an ignorable level compared to self-inductance. The conventional asymmetric converter can still be used with the same control method as CSRM. As shown in Figure 3.1(b), the two coils are wounded around the stator yoke beside a stator pole. It uses these two coils to produce the same flux distribution as one of the conventional coils on the stator pole. In Figure 3.1(c), the SLTSRM is modified based on the DLTSRM. As introduced in Chapter 2, there will be two coils in each slot for the DLTSRM. However, in the SLTSRM, these two coils are parallel connected to one coil. This proposes a new winding topology as SLTSRM, but it requires a totally different converter and control method from CSRM or DLTSRM.

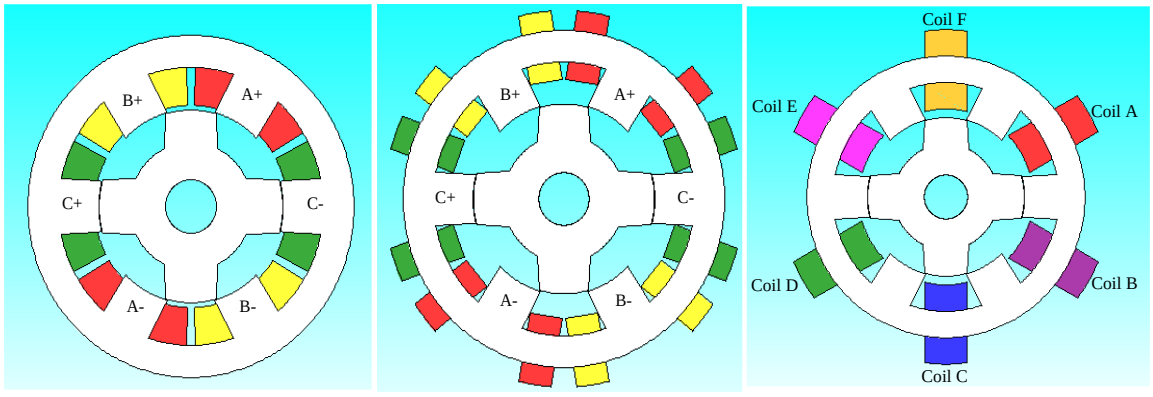

(a) CSRM (b) DLTSRM (c) SLTSRM

Figure 3.1 Winding schemes of CSRM, DLTSRM, and SLTSRMs.

For purposes of illustration and explanation, the following study still uses lamination geometry of a three-phase six-stator-pole four-rotor-pole SRM with key dimensions indicated in Table 3-I. The TSRMs and CSRM share the same lamination during the comparison; only the winding topologies are different.

Table 3-I Key geometry information for comparison.

Parameters	Values
Number of phases	3
Number of poles	Stator 6, Rotor 4
Stator outer diameter	50 mm
Bore diameter	30 mm
Stack length	50 mm
Air gap	0.4 mm
Stator pole arc	30º
Rotor pole arc	35º
Lamination steel	29 GA M15 C5

The comparison conducted in this chapter is only on the static state. In this chapter, the torque per unit copper losses suggests the DLTSRM will not be a good choice considering the increased copper losses and weight. Thus, latter in this chapter, it focuses more on the comparison between SLTSRM and CSRM. The roles of self and mutual inductance during torque generation is developed. To better understand the toroidal winding, a method to project the coil flux to pole flux is proposed. With the projection method, the difference between CSRM and TSRMs will be more straightforward to understand. As the last part of the static analysis, the reason for the torque difference between CSRM and SLTSRM is figured out. The conclusion is drawn that SLTSRM presented is a strong competitor to CSRM, considering the torque per unit copper losses.

All this bring the author a great interest to design a SLTRM for a special high-speed application.

3.2. Potential Power Density Differences.

Compared to CSRM, TSRMs have the obvious difference of winding directly exposed. The enhanced cooling capability will have a direct impact on machine output power. Meanwhile, the ease of toroidal-winding manufacture will significantly increase the copper filling factor since TSRM doesn't require such slot space for the wounding needles as shown in Figure 3.2. Therefore, it leads to a higher power density of TSRM. Both of those characteristics propose a great attraction to apply toroidal winding on SRMs.

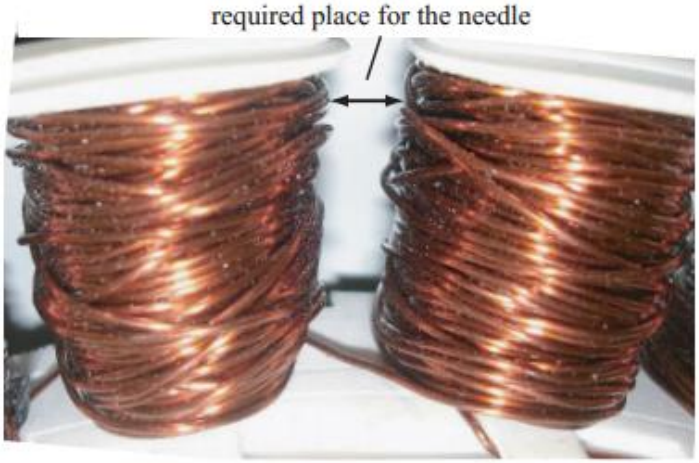

Figure 3.2 Slot space required for CSRM wounding.

3.3. Static Torque Comparison at Unit Copper losses.

As discussed in Chapter 2, DLTSRM, as shown in Figure 3.3(b) uses four coils to produce the same electromagnetic field as CSRM in Figure 3.3(a). As for SLTSRM in Figure 3.3(c)-(d), there will be 6 coils wounded in the 6 stator slots, and it requires at least 4 coils to be active at each moment to generate useful and balanced torque. In the previews publication of TSRM [58][66][67], it prefers 4 of 6 coils active at each moment. In [58], the author claimed that if the other two coils are active, it will lead to negative torque. However, the following analysis suggested that it's better for all the 6 coils to be active all the time to generate the optimal torque at unit copper losses.

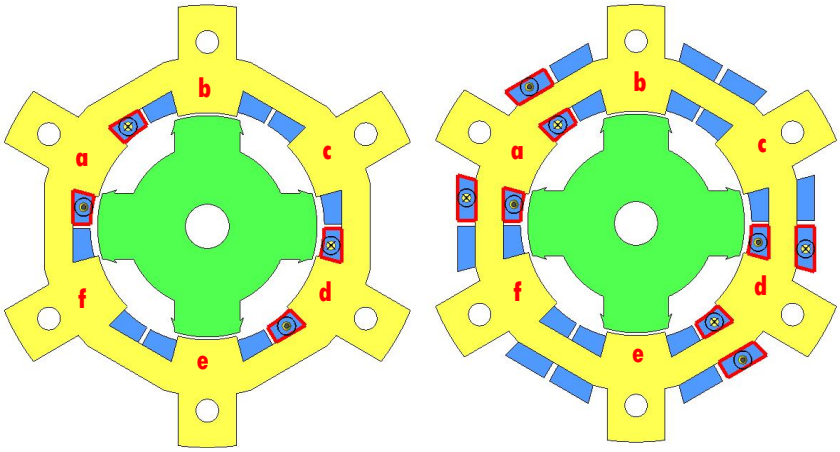

(a) CSRM (b) DLTSRM

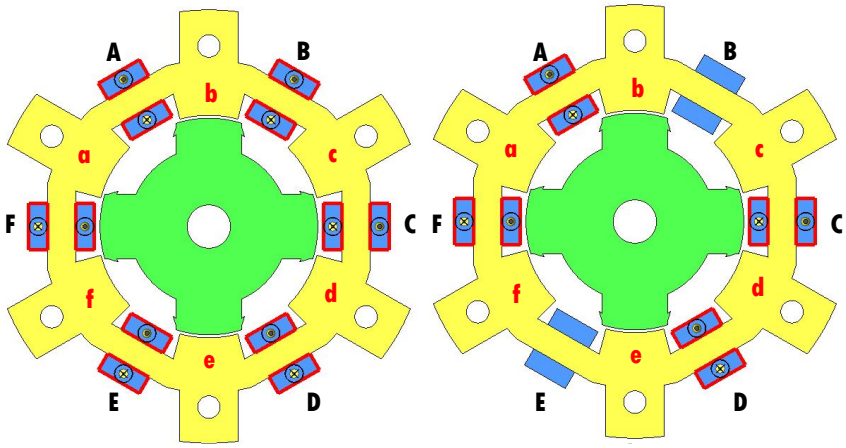

(c) SLTSRM-6coils (d) SLTSRM-4 coils

Figure 3.3 Active coils of the four different SRMs at the same position.

The same number of turns per coil is applied for a consistent comparison among motors. To keep the same filling factor for each slot, it requires the copper cross-sectional area of SLTSRM to double that used in CSRM and DLTSRM. To produce the equivalent electromagnetic field, the coil/phase current magnitude of 6-coil SLTSRM only needs to be 2/3 of the current per coil in CSRM, DLTSRM and 4-coil SLTSRM. For a consistent comparison, SRMs with the same lamination geometry but the different winding location is studied, and its flux distribution at typical steady states is shown in Figure 3.4. As presented already in Chapter 2, DLTSRM produces almost the same electromagnetic torque as conventional SRM, but with double copper losses. The following analysis will only focus on CSRM and SLTSRMs.

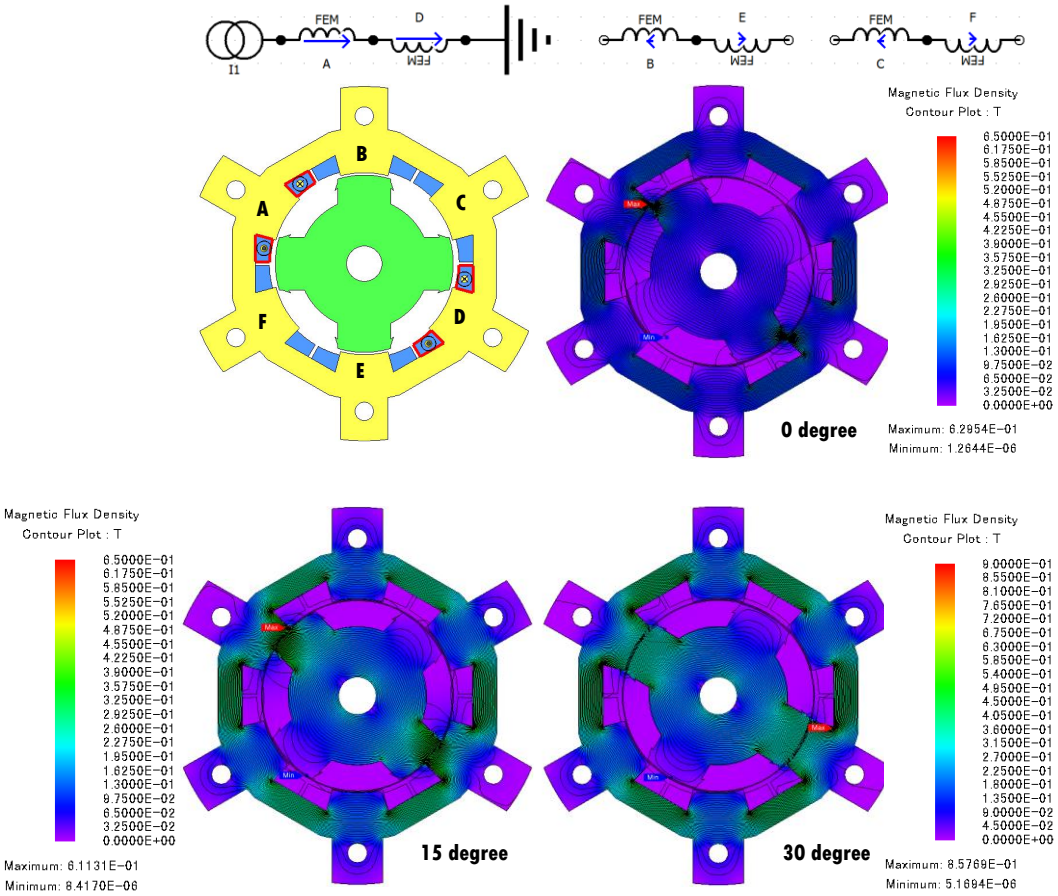

Figure 3.4 Coils location and flux distribution of CSRM with $I_A = -I_D = 10A$; $I_B = I_C = I_E = I_F = 0A$.

Compared to CSRM, the same number of turns per coil is used in SLTSRM for a consistent comparison. The geometrically opposite two coils, for example, coil A and coil D, are in series connected as one phase. At the same time, the corresponding SLTSRM with 4 coils active and 6 coils active are studied with their flux distribution presented in Figure 3.5 and Figure 3.6. To start, the simplified linear magnetic material is applied. By applying the material with a constant relative permeability of 1000, it's assumed no saturation happens at any part of the machine.

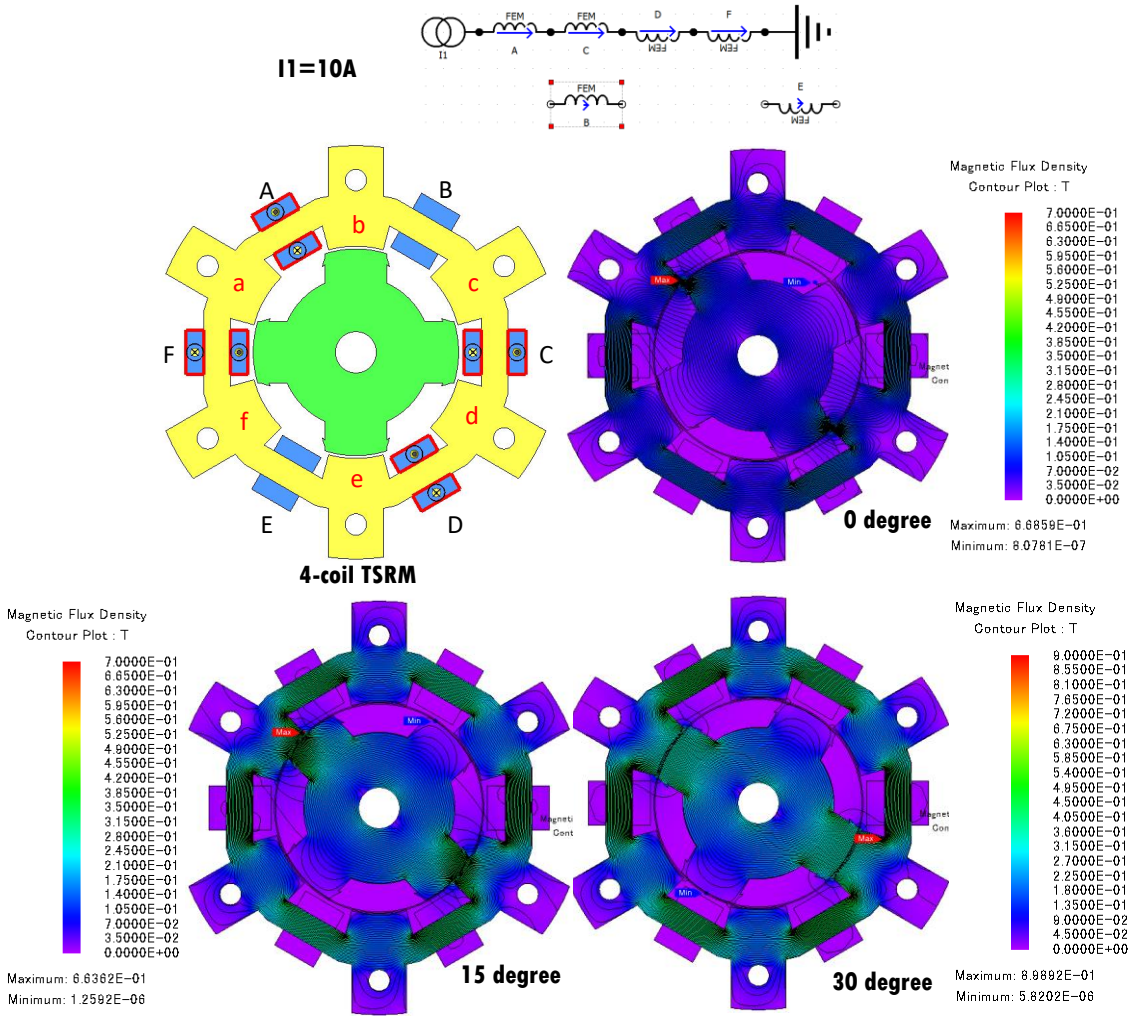

Figure 3.5 Coils location and flux distribution of 4-coil SLTSRM with $I_A = I_C = -I_D = -I_F = 10A$; $I_B = I_E = 0A$.

In the 4-coil SLTSRM of Figure 3.5, at each position, only four coils located around the excited poles conduct current, while the other two coils are at open circuit. Figure 3.6 is represented below for 6-coil SLTSRM. Flux linkage in coil A is the sum of self-flux linkage as well as mutual flux linkage contributed by all the other five coils. As for 4-coil SLTSRM, $flux_{B\to A}$ and $flux_{E\to A}$ are both zero, since there is no current in coil-B and

coil-E. Therefore, 4-coil SLTSRM requires a higher coil current than that in 6-coil SLTSRM. Electromagnetically, it requires only two-third of coil current in 6-coil SLTSRM to produce the equivalent electromagnetic field as 4-coil SLTSRM.

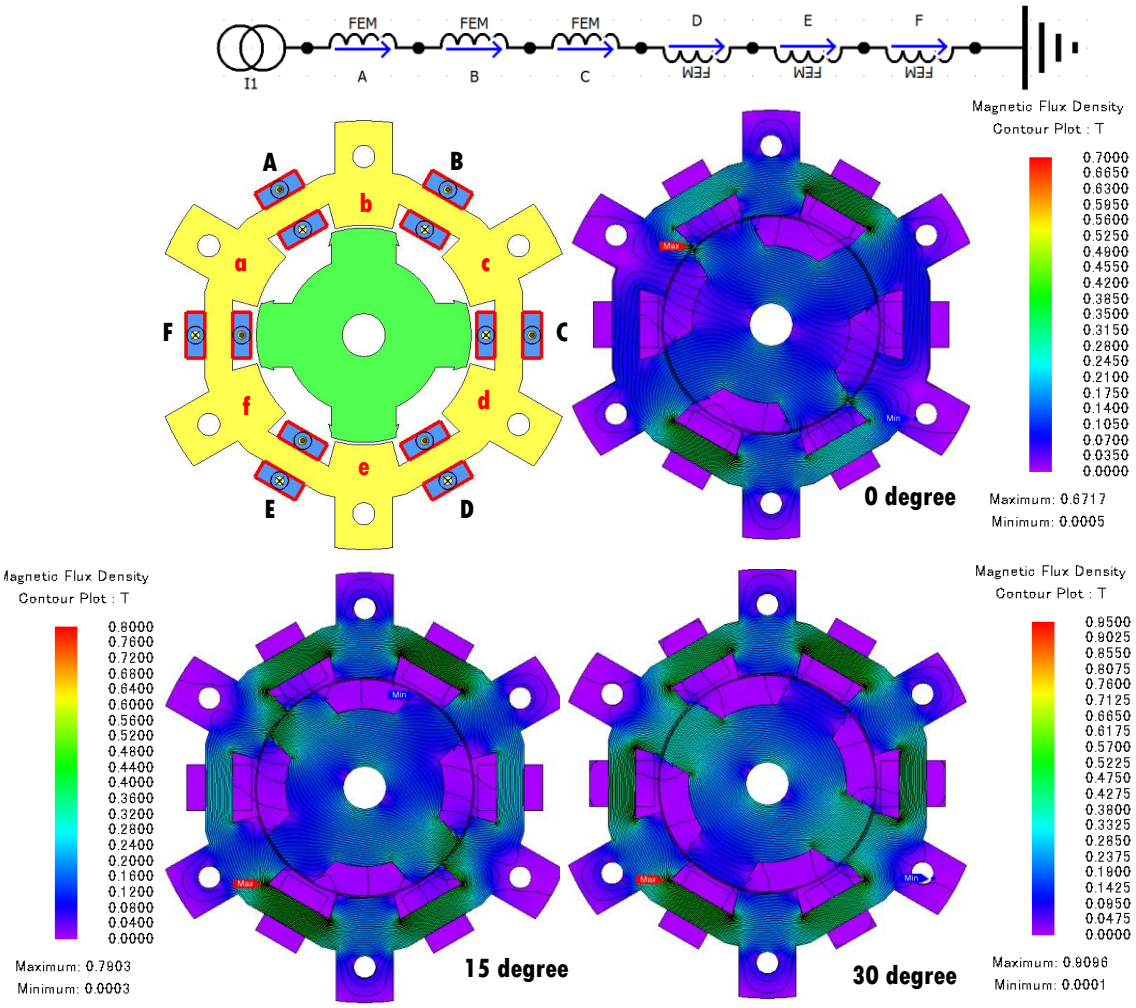

Figure 3.6 Coils location and flux distribution of 6-coil SLTSRM with $I_A=I_B=I_C=6.7A$; $I_D=I_E=I_F=-6.7A$.

Ideally, the electromagnetic field in Figure 3.4, Figure 3.5, and Figure 3.6 will be the same. As compared in Figure 3.7, with the equivalent MMF for each magnetic loop, very

similar electromagnetic torque is produced. As for difference at the region (0-20 deg.), it is caused by flux leakage, which is will be studied in detail in Section 3.4.

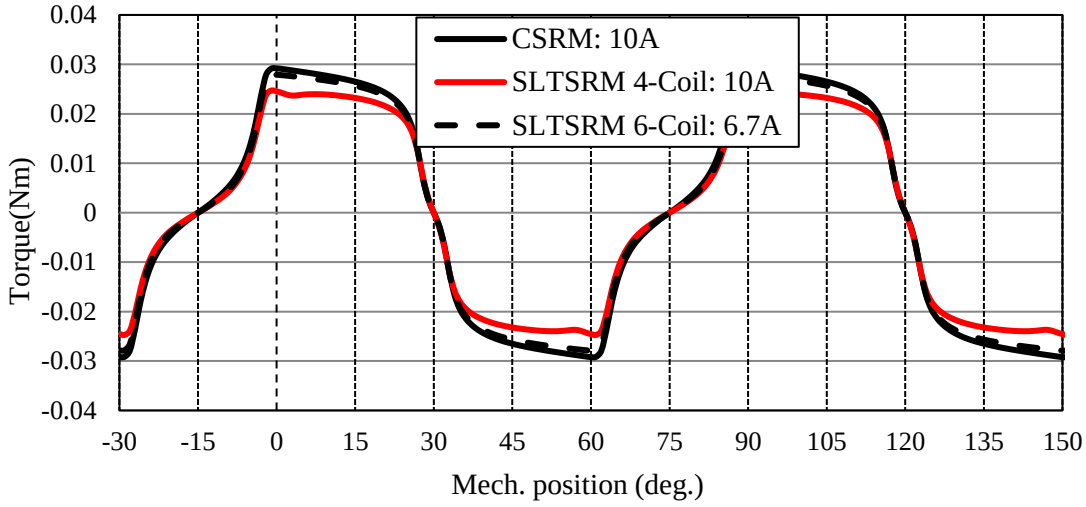

Figure 3.7. Static torque comparisons at constant currents.

Table 3-II Ideal static comparison between CSRM, and TSRMs.

	CSRM	DLTSRM	SLTSRM-6coil	SLTSRM-4coil
Objective torque	$1 \cdot T_e$	$1 \cdot T_e$	$1 \cdot T_e$	$1 \cdot T_e$
Number of conducted coils	2	4	6	4
Rated current per coil	$1 \cdot I$	$1 \cdot I$	$2 \cdot I / 3$	$1 \cdot I$
Resistance per coil	$1 \cdot R$	$1 \cdot R$	$1 \cdot R / 2$	$1 \cdot R / 2$
Copper losses	$2\ I^2\ R$	$4\ I^2\ R$	$4\ I^2\ R / 3$	$2\ I^2\ R$

Taking into consideration of the active coil number and coil resistance difference, these typical steady-state conditions hold different copper losses as already discussed in Table 3-II. Therefore, the 6-coil SLTSRM has an obvious advantage over CSRM and 4-coil SLTSRM regarding the output torque per unit copper losses. Thus, the following thesis

will only focus on the comparison between CSRM and 6-coil SLTSRM. To avoid confusion, TSRM is only referring 6-coil SLTSRM from now on.

3.4. Torque Generation Comparison between CSRM and TSRM.

As discussed in Chapter 2, in CSRM, its mutual inductance is at a very low level compared with self-inductance. Moreover, there is typically only single-phase of CSRM active at each moment. Thus, mutual inductance is usually ignored during its analysis. However, as for the proposed TSRM, all the 6 coils are active all the time; the mutual inductance is very high and plays an important role during torque generation.

3.4.1. Relationships between SRM Coil-Flux and Pole-Flux.

Figure 3.8 shows a flux linkage relationship between CSRM and TSRM, in which the blue line is for flux linkage in coil A of CSRM at $I_A = -I_D = 10A$; $I_B = I_C = I_E = I_F = 0A$; while the red line is for flux linkage in coil A minus that of coil F of TSRM at $I_A = I_B = I_C = 6.7A$; $I_D = I_E = I_F = -6.7A$, labeled as TSRM_AF in the figure. It shows that these two curves are very close to each other.

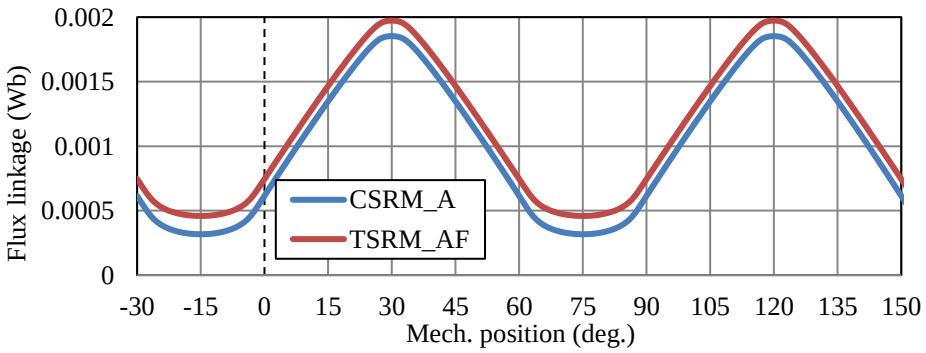

Figure 3.8. Flux linkage relationship between CSRM and TSRM.

Besides the coil flux, here introduces another concept stator pole flux to assist the analysis of this relationship. As for the torque generation, it is more directly linked with the stator pole flux. In Figure 3.9, capital back letters represent coils while red lower-case letters are for stator poles. Considering the magnetic circuit, the surface of each stator pole is a node for flux portions (yokes and pole). Based on Gauss's law, the flux in a stator pole should be the difference of its adjacent yoke flux. Therefore, the stator pole flux can be derived from coil flux for both machines, as shown in Table 3-III.

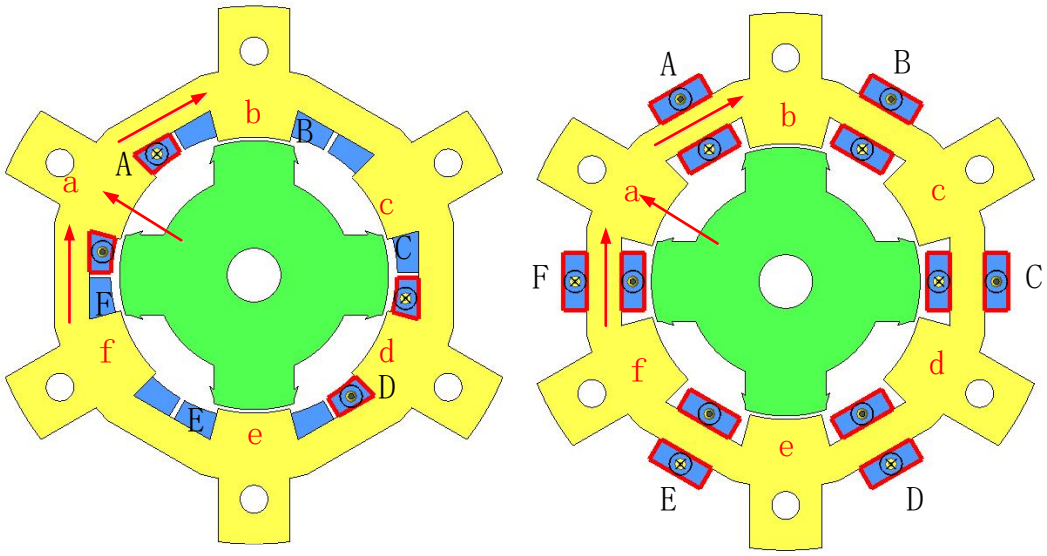

(a) CSRM (b) TSRM

Figure 3.9. Coil and pole configuration of CSRM and TSRM.

Table 3-III Coil and pole flux relationship for CSRM and TSRM.

TSRM	CSRM
$Flux_a = Flux_A - Flux_F$	$Flux_a = Flux_A$
$Flux_b = Flux_B - Flux_A$	$Flux_b = Flux_B$
$Flux_c = Flux_C - Flux_B$	$Flux_c = Flux_C$
$Flux_d = Flux_D - Flux_C$	$Flux_d = Flux_D$
$Flux_e = Flux_E - Flux_D$	$Flux_e = Flux_E$
$Flux_f = Flux_F - Flux_E$	$Flux_f = Flux_F$

The equation set for CSRM is straight forward; based on its coil location, its pole flux is the same of its coil flux. For TSRM's pole flux, it's validated through FEA as shown in Figure 3.10 with the analytical value calculated based Table 3-III and FEA valued on stator pole using commercial FEA software, JMAG. However, in Figure 3.10, it also shows that the magnitude of the real pole flux linkage is always smaller than the predicted from its coil flux. The reason is that the relationship presented in TABLE ideally assumes there is no flux leakage happens. However, resulting from the specific coil location, there is flux leakage happens, as shown in Figure 3.11.

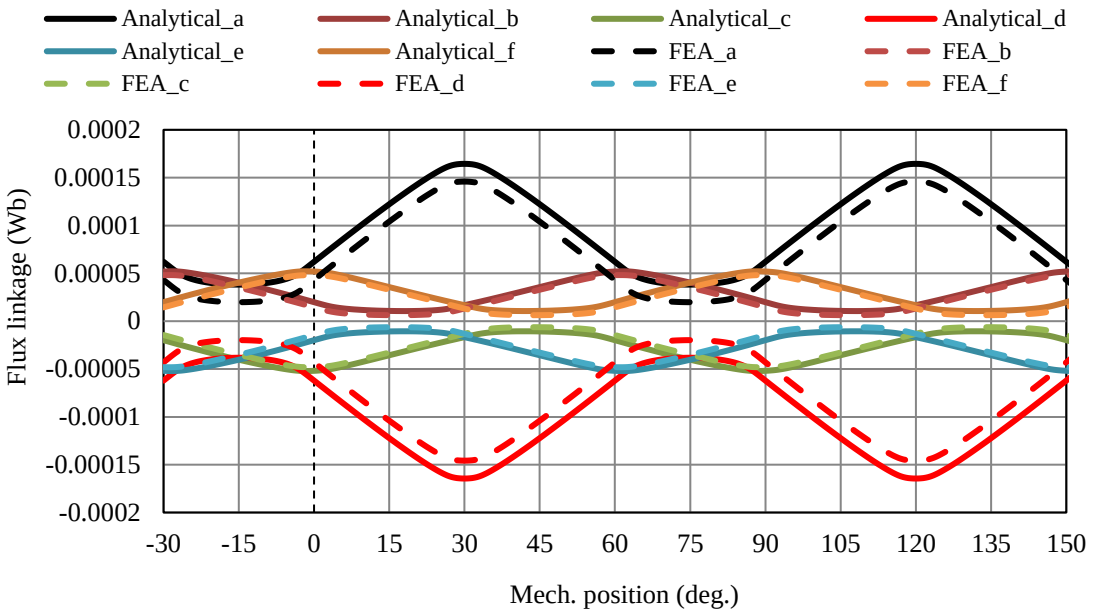

Figure 3.10. Validation of coil and pole flux relationship of TSRM.

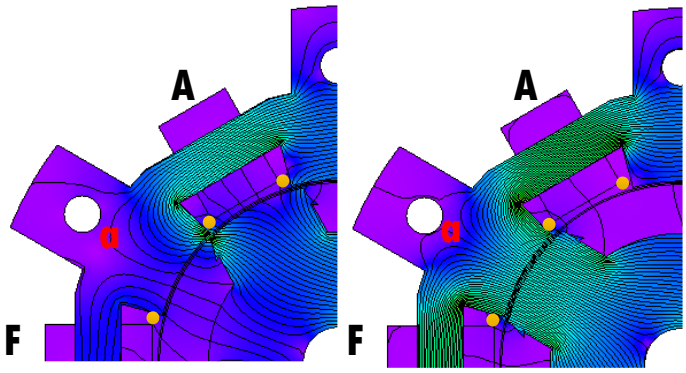

Figure 3.11. Flux leakage happens in TSRM.

This also answers this question of why the steady-state torque is slightly different in Figure 3.7. The similar flux in the energized stator poles is the necessary reason for a

similar torque generation of these two machines. Pole fluxes during static torque generation of CSRM and TSRM are presented and compared in Figure 3.12. They are measured value from FEA. For the two typical steady states with electromagnetically equivalent currents in each of the two machines, pole-a and pole-d are the energized poles regarding torque generation which are called primary coils, while the other poles are called secondary coils. In Figure 3.13, it summarizes the torque generation process of the TSRM.

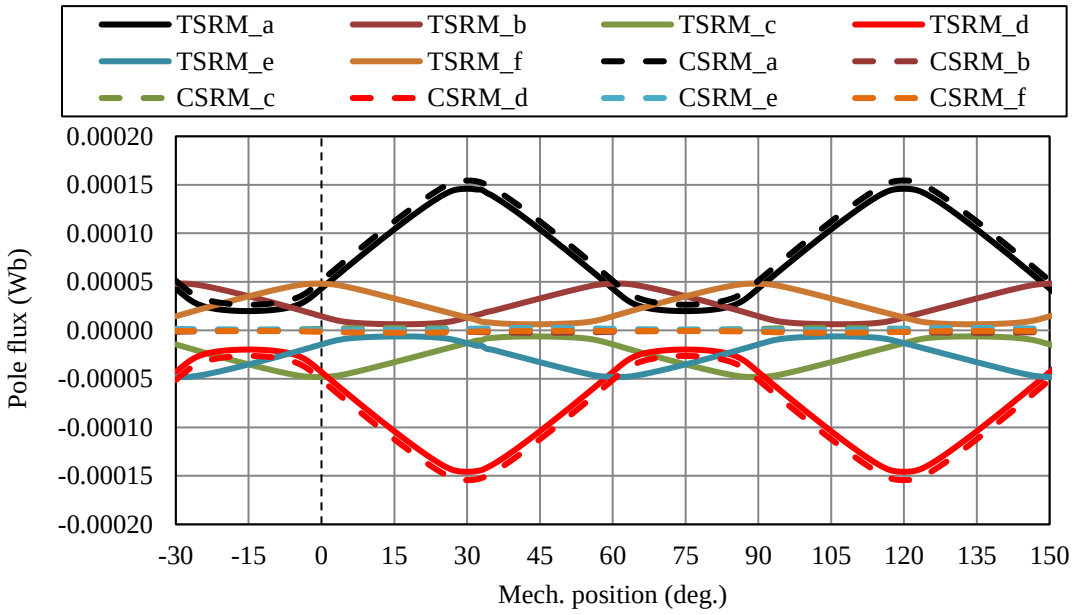

Figure 3.12. Pole flux profiles comparison of CSRM and TSRM.

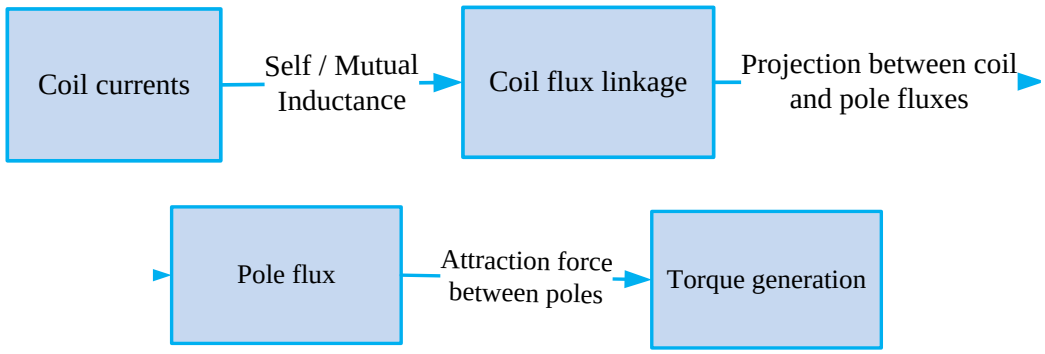

Figure 3.13. Flowchart of TSRM torque generation.

3.4.2. Roles of Primary and Secondary Stator Poles regarding Torque Generation.

As for CSRM, it's obvious that the secondary coil/pole has a very limit effect on its torque generation. Its primary pole torque is compared with its total torque in Figure 3.14. They match with each other almost exactly. This proves that only the primary poles in CSRM contribute to torque generation. This also indicates, for CSRM, its torque generation only relies on self-inductance.

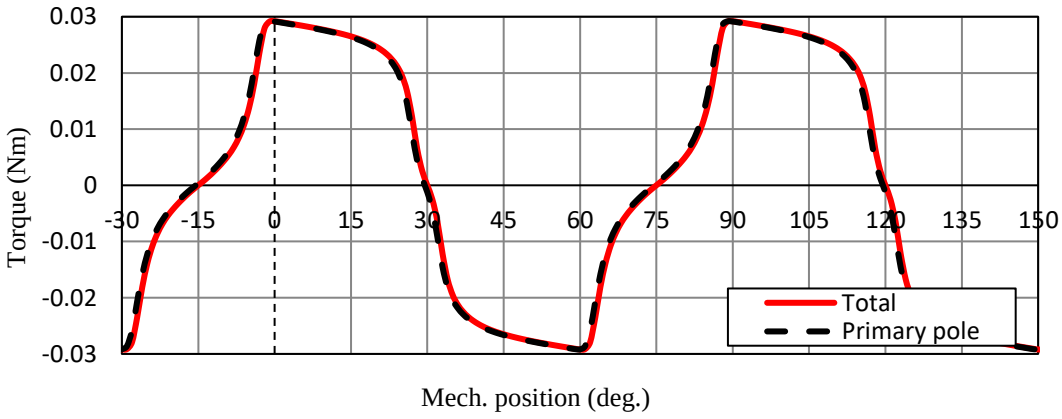

Figure 3.14. Primary pole torque and total torque comparison of CSRM.

For the TSRM, as for symmetric geometry of 6-4 machine, the torque direction of the opposite pole is always the same; therefore, they are combined together as a pole pair. In Figure 3.15, the torque direction of each pole pair at different positions is presented together with their pole fluxes. For example, T_{ab}=1, it means that in this region this pole pair (a & d) generate positive torque, while -1 for negative torque. Since the geometrically opposite two poles always have the same-magnitude opposite-direction flux, only pole fluxes of a, b and c are studied for simplification. It shows for each pole pair (opposite poles), there are certain positions the flux on them will provide positive torque, which is from unaligned commutation position to aligned. But this torque generation has nothing to do with the flux direction but only the amount of flux on them. For the region of (-15~30 degree) where the primary pole pair generate positive torque, the first 15 degree, the torque direction of secondary pole pair b-e is negative, while positive for c-f, while the direction is opposite for the third 15 degree in this region. As for the second 15 degree, both secondary pole pairs contribute to negative torque. To conclude qualitatively, the flux in the secondary pole pairs canceling the torque generated by the primary pole pair. Together with the flux leakage, it claims the reason why 6-coil SLTSRM generate a little bit less torque than CSRM with equivalent MMF.

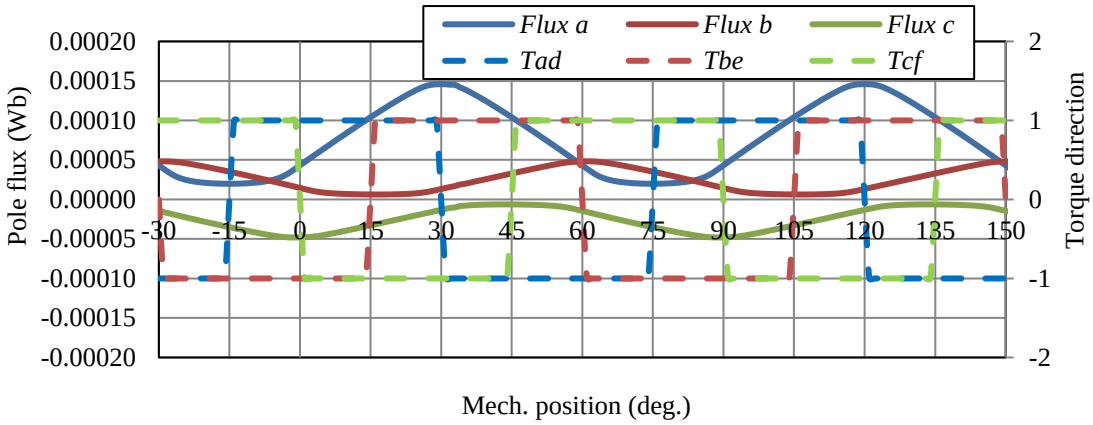

Figure 3.15. Torque contribution of primary and secondary poles on TSRM.

However, to figure out how much the cancellation happens on the flux leakage of the primary poles, and secondary poles, it requires a quantitative analysis. Figure 3.16 shows the nodal force vectors of the primary stator pole (pole a in the context), with Figure 3.16(a) at the unaligned position and Figure 3.16(b) at the aligned position. Only tangential nodal force produces torque between rotor and stator. However, differently from other machine topology, the salient stator pole structure will lead torque not only come from pole arc, but also from the two edges. Therefore, accurate torque estimation from nodal forces will require integration along the red vectors as shown in Figure 3.16(a), taking into account both the vectors along the arc and vectors along the pole edge.

During the analysis on nodal forces, it is found out that the tangential forces mainly concentrates on the tap of stator pole. For example, four points are chosen along the stator pole arc, as shown in Figure 3.17(a), and their corresponding nodal force is presented in Figure 3.17(b). As seen, compared with points at the corners, the forces on other points

along the arc can be neglected since they are almost zero. This conclusion is true for all the poles.

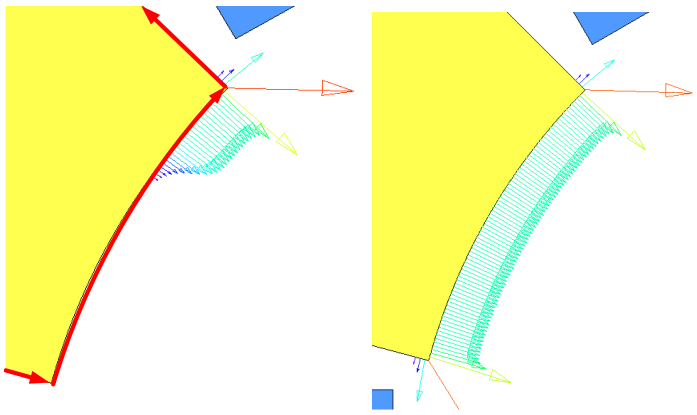

(a) Unaligned (b) Aligned

Figure 3.16. Nodal force distribution of a single stator pole at the unaligned and aligned positions for TSRM.

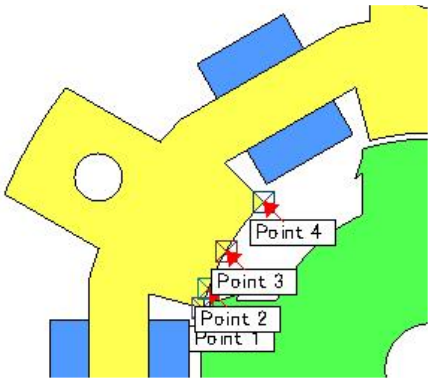

(a) Location of the analysis points.

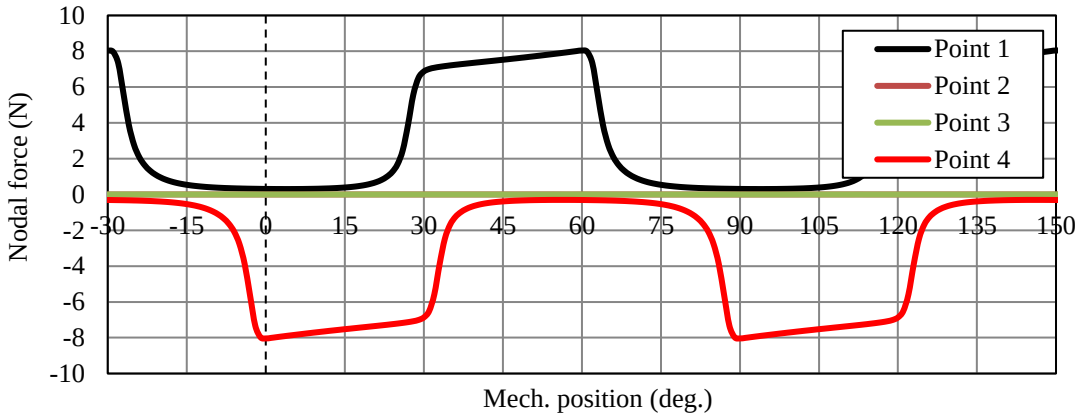

(b) Nodal force variation.

Figure 3.17. Nodal force variation v.s. rotor rotation position for different points on the stator pole of TSRM.

To calculate the total torque of a single pole, the force will be integrated along this single pole edges and arc and multiply their corresponding radians. The torque contribution of each pole is shown and compared in Figure 3.18. It shows that the secondary poles contribute less than the primary ones. However, they function as canceling the torque of the primary poles.

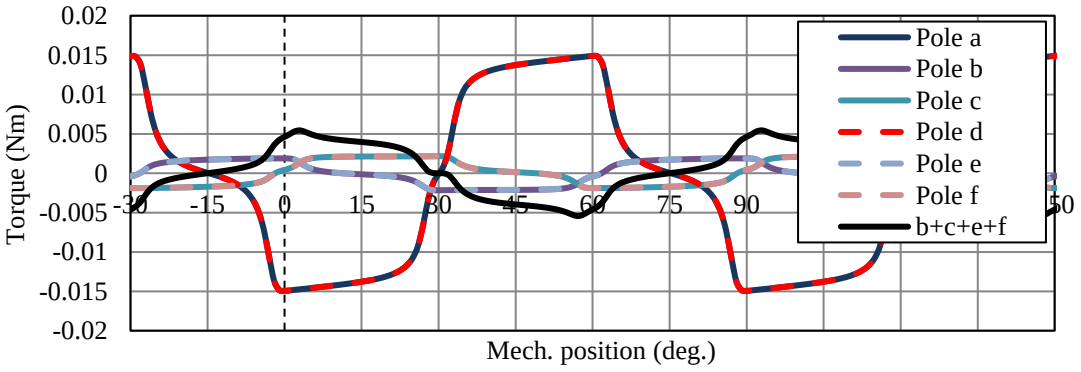

Figure 3.18. Torque contribution of each TSRM stator pole.

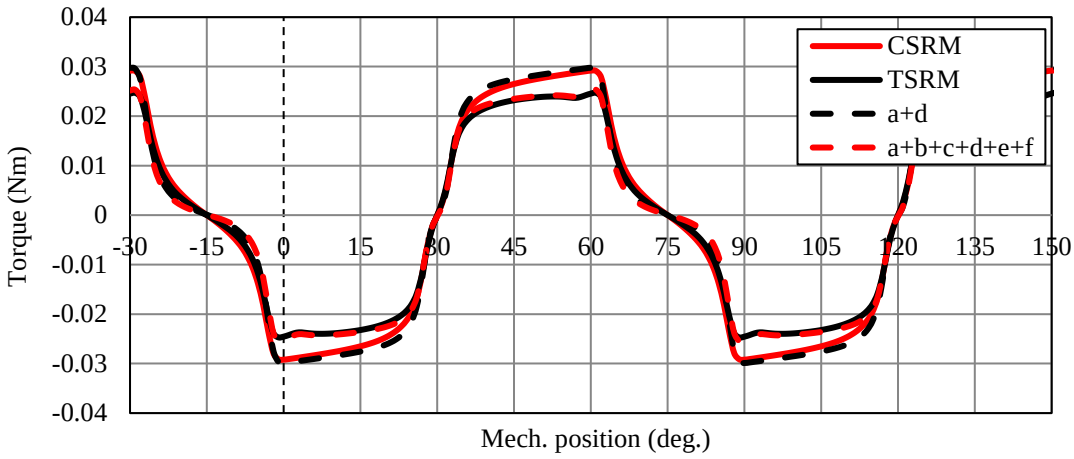

Figure 3.19. Torque comparison of CSRM, TSRM, and TSRM's torque components.

The comparison between the pole torques and CSRM and SLTSRM total torques in Figure 3.19 shows that the torque difference between CSRM and SLTSRM mainly comes from the cancelation function of the secondary poles. In other words, the toroidal winding topology results in more flux leaked to the secondary poles, and those flux in the secondary poles cancel the torque of the primary poles.

3.5. Conclusions.

In this chapter, it mainly discussed the static characteristics difference between CSRM and TSRMs. First of all, the coil location of TSRM makes the wounding process, and motor cooling significantly improved. This will cause TSRM capable of high-power density. Secondly, this chapter compares the torque generation of CSRM and TSRM, considering unit copper losses. As known, most of the time, an electric machine is limited by its heat generation of copper. It concludes that the SLTSRM with 6 coils active all the

time will make the best torque per unit copper losses among CSRM, DLTSRM, 4-coil SLTSRM, and 6-coil SLTSRM. It only requires 2/3 coil current in 6-coil SLTSRM to generate the equivalent electromagnetic torque compared to all the other three options. However, there is a small difference on the static torque profile between the CSRM and 6-coil SLTSRM. The reason is studied in Section 3.4. It indicated that, with the benefit of higher torque-per-copper losses in 6-coil SLTSRM, however it also suffers higher flux leakage. The torque difference between CSRM and SLTSRM mainly comes from the cancelation function of the secondary poles of SLTSRM. To avoid confusion, TSRM is only referring 6-coil SLTSRM in the following study.

Chapter 4 Control Strategies and Converter Topologies

4.1. Introduction.

The CSRM uses a decoupled concentrated phase winding so that torque is generated due to the rate of change of the self-inductance of the excitation phase. Therefore, one phase winding can only contribute to positive torque for a maximum of half period, which limits the utilization rate of the electrical circuits. Following the fundamental theories of CSRM discussed in Chapter 2, Chapter 4 first presents a deep and close look into the control theories and converter topologies of CSRM. Its dynamic performance is discussed in detail.

Previous researches have shown that TSRM is less sensitive to saturation than the CSRM and has better thermal performance[57]. Multiphysics numerical modeling and experiments show that the TSRM has lower vibrations and sound power levels. TSRM also offers additional winding space, while retaining the benefits of mutual coupling excitation. Thus, Chapter 4 then presents a dynamic analysis of the single-layer TSRM. The required rotation magnetic field is first presented for TSRM, followed by its corresponding current sequence to achieve the required rotation sequence. Then it's a comparison between difference current sequences. Two TSRM converter topologies are then introduced, and the dynamic operation of the whole driving system is studied including both the machine and the converter.

After that, it also proposes to use sinusoidal currents control for TSRM with widely available commercial three-phase half-bridge inverter. Decoupling between phases is achieved by using the DQ transformation.

4.2. Dynamic Drive of CSRMs.

As indicated in Chapter 2, CSRM requires asymmetric bridge converter to synchronize the energization of the motor phases based on rotor position input. Figure 4.1 is an expansion of a typical CSRM control diagram, in which green represents the motor, blue represents the hardware, and orange represents the control method in software.

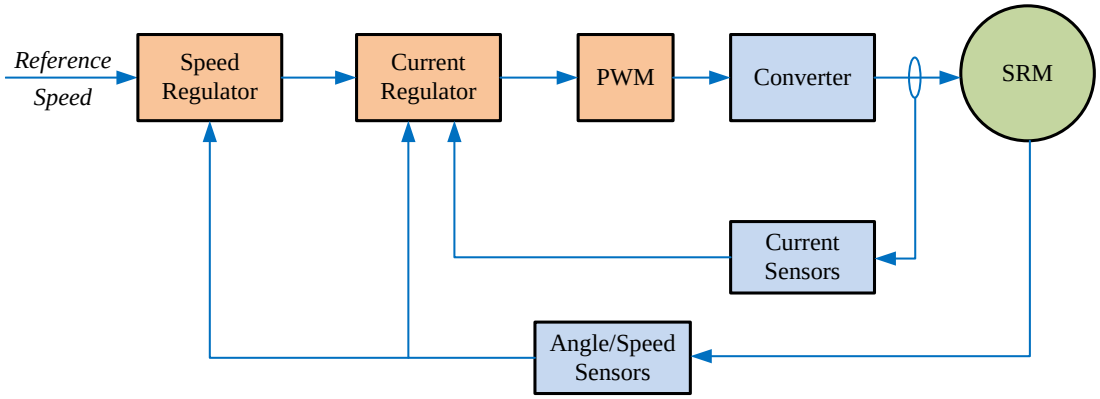

Figure 4.1 Typical control diagram for CSRMs.

As shown, the first loop is for the speed control regulator. Usually, the PI controller is enough for SRM's speed control. The difference between the measured speed and desired speed is the input for a PI controller, which generates the desired torque to overcome this speed difference. The reason for choosing a PI controller instead of a PID controller is to

minimize the tuning complexity. At the same time, PI controller is more widely used on motors as it can keep a good track on the required speed; however, the D parameter will increase the noise of the system. Based on the torque ripple reduction consideration, PI controller is more suitable for SRMs.

The inner loop, the current regulator, aims to generate the proper switch signals for the converter to regulate the phase current. As discussed in Chapter 2, for each phase of CSRM, there is a certain range of positions, which can generate positive output torque. Controlling the phase to be energized only at those positions can avoid negative torque. To control torque ripple, the controller requires even more specific turn-on and turn-off angle at a different current magnitude and different positions. This angular position control is one of the most classic control strategies for CSRM. Normally, single phase is energized at each time, which is very simple and easy. However, it suffers bigger torque ripple as there is no overlap between phases. For torque improvement, it applies multi-phase energizing angular control. A potential issue associated with multi-phase angular control is mutual inductance, which is ignored during analysis. According to Chapter 2, CSRM is famous for its smaller mutual inductance. So, each phase is independent with others.

Given conduction angle and reference current for CSRM, normally, hysteresis current or PWM voltage controls is applied to generate switch signal for the converter. Hysteresis current control is firstly used on CSRM due to hysteresis control’s easy implementation and fast dynamic response. However, hysteresis control suffers higher switching losses and current noise. This is because to maintain constant hysteresis current band, it needs higher

and varied switching frequency, which also limited its current control capability. Thus, to solve this, PWM becomes more and more popular.

As shown in Figure 4.2, in a classic CSRM control, certain turn-on, θ_{on}, and turn-off, θ_{off}, positions are chose for each phase to conduct current. Phase current is limited within a current band during this conduction region to avoid over-heating. At rotor position of θ_{on}, both the switches on the certain controlled phase are turned on. A positive full DC voltage is supplied on the particular phase winding. Phase current increases and generate torque. According to Equation 4-1, positive torque is generated only when the phase self-inductance rises. To take full use of the positive inductance slope, θ_{on} is typically around the unaligned position.

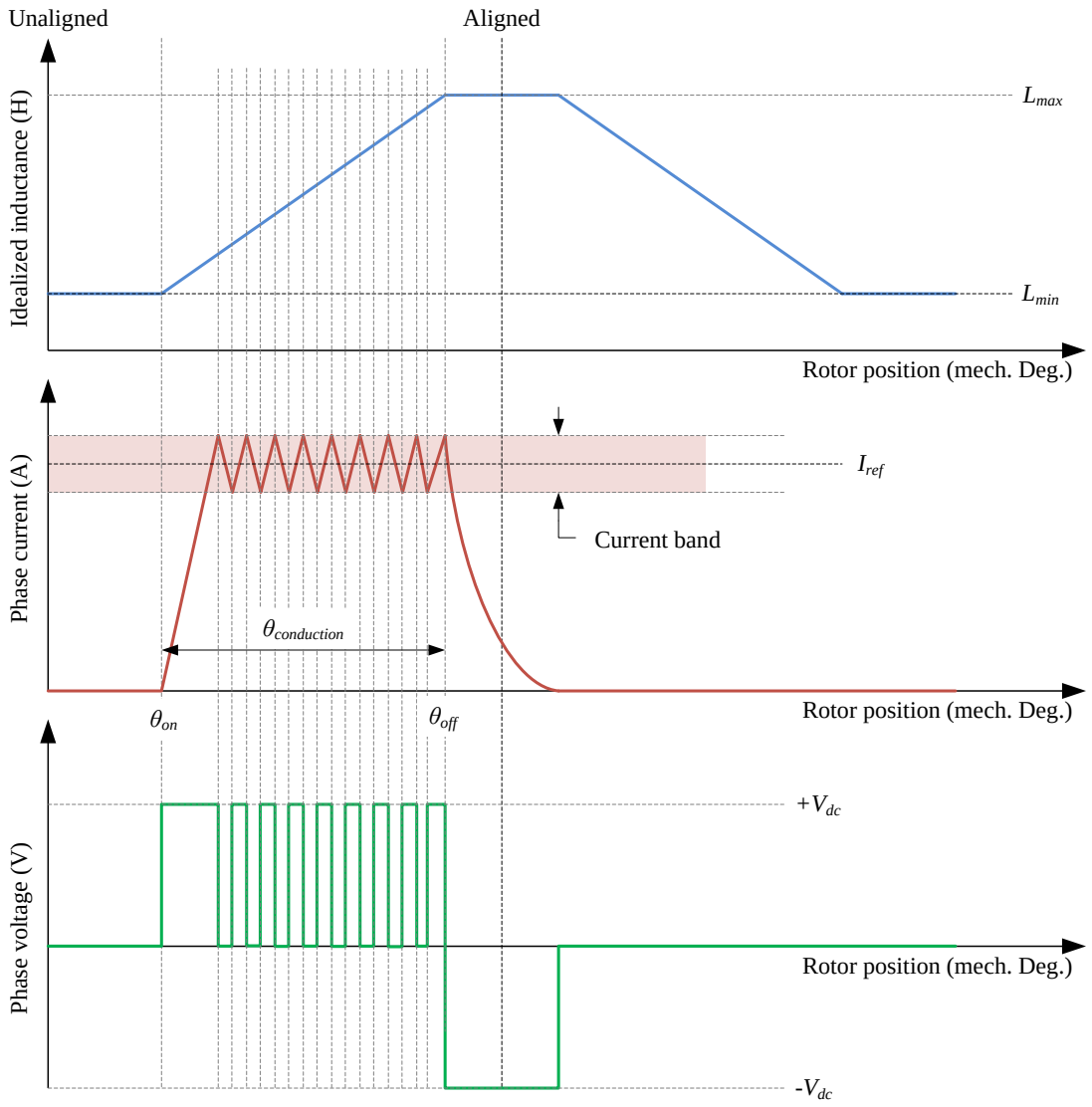

Figure 4.2. Dynamic phase current and voltage v.s. inductance variation in CSRM.

$$T_{ave} = \frac{1}{2} i^2 \frac{dL}{dt} \qquad \text{Equation 4-1}$$

The current sensor on hardware measures and reports the actual current to the controller. After sensoring the current reaches the maximal, the bottom switch is set off to avoid

current rising. The phase voltage becomes zeros. This bottom switch responds on and off accordingly to maintain the phase current without the defined allowance until the rotor position reaches θ_{off}. Both switches are set off and force full negative DC voltage on phase wire to clear the phase current. θ_{off} needs to be properly defined and is usually before aligned to avoid negative torque.

Figure 4.3 illustrates the phase voltage and current flow on the single phase-leg circuit. The voltage across the phase winding is V_{bus}, when both T_1 and T_2 are on, as shown in Figure 4.3(a). In Figure 4.3(b), T_2 is off, and the phase current is forced through D_1 to close the circuit. The voltage across the phase winding is now zero. When both T_1 and T_2 are off as shown in Figure 4.3(c), the circuit can only close through D_1 and D_2. The reversed voltage is then across the phase winding guarantees that the flux linkage is returned to zero.

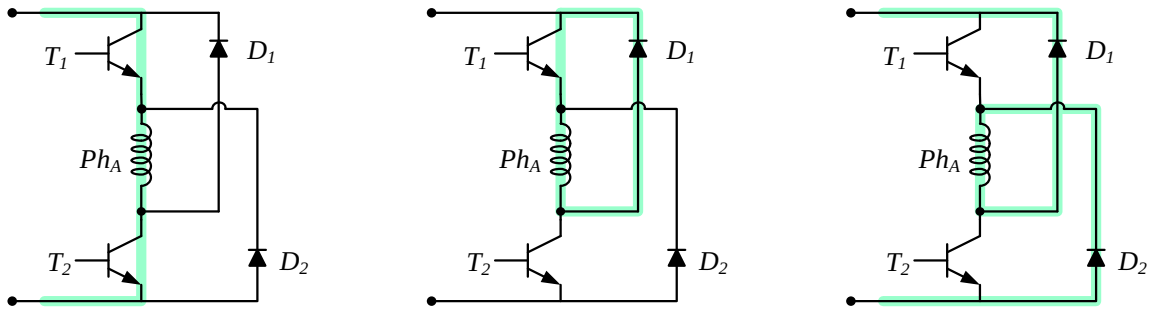

Figure 4.3 Current flow controlled by switches: (a) both T_1 and T_2 on, (b) T_1 on and T_2 off, and (c) both T_1 and T_2 off.

The idea of angular position control phase current simply by defining the turn-on/turn-off angles and reference current. If the position is within this range, this phase will be turned

on; otherwise, it is off. Control performance is limited since there are only three control degrees of freedom. More CSRM control strategies have been developed.

Torque-sharing function control uses multiple phases to generate the desired total torque following a sharing function. The idea is explained through Equation 4-2 to Equation 4-4. If T_d is the desired total torque, the sharing function $f(\theta)_i$ for the phase i should meet the following constraints:

$$T_i = T_d \cdot f(\theta)_i \qquad \text{Equation 4-2}$$

$$\sum_{i=1}^{m} f(\theta)_i = 1 \qquad \text{Equation 4-3}$$

$$0 \leq f(\theta)_i \leq 1 \qquad \text{Equation 4-4}$$

where T_i is the desired torque for phase i. It is shown that there is more than one unique solution for the equations of Equation 4-2 to Equation 4-4. Actually, many functions of $f(\theta)_i$ can satisfy the constraints. However, there are usually a few factors to consider when choosing a TS function. One is the copper losses. The torque sharing function may assign one phase to generate torque at a position of a small rate of change of phase inductance. The required current will be big, but the copper losses will increase significantly. Therefore, one of the optimizing objectives to decide the proper torque sharing function is to reduce the copper losses. Another is to maximize the speed range of a certain TS function. The last but not the least is to evaluate its torque ripple reduction ability. Torque ripple reduction ability is always one of the most important factors to evaluate the TS functions. But there is always a trade-off between the three factors.

Linearization and decoupling control (LDC) is first proposed by Martija Ilic'-Spong in [71]. It used a state feedback control algorithm, which compensated for all the nonlinearities by matching the model with experimental data. By translating the coupled nonlinear model into a simple decoupled linear system, traditional control techniques will be valid to generate a high-quality performance in SRM. However, to realize this state control technique requires that all the state variables are testable, like current, position, and velocity, which definitely increase its cost.

Sliding mode control (SMC) [72] is also a state feedback control strategy, which forces the system to slide along a special cross-section of the system's state and finally get stable. SMC is more robust, better dynamic response-ability and easy to implement, compared with LDC. However, it will introduce high-frequency chatter and therefore increase CSRM's torque ripple.

As for CSRM's control strategies, it must be able to reduce its torque ripple and noise, as these are the biggest problems hindering CSRM's development. At the same time, it should have better dynamic performance, easy implementation, and robustness. Thus, some intelligent control algorithms, like fuzzy-logic-based [73] and neural-network-based techniques [74][75], are also studied on CSRM. They both have good self-learning and adaptive capability. However, they are still time and money-costing. Further developments are still required to apply these intelligent control strategies in real industry.

4.3. Dynamic Drive Development for TSRMs.

The static profile comparison in Chapter 3 concludes that the six-coil single-layer TSRM is a good competitor compared to CSRM, double-layer TSRM, and 4-coil single-layer TSRM. Thus, the study is followed by the dynamic analysis of the six-coil single-layer TSRM.

The basic diagram of dynamic analysis is shown in Figure 2.1. To rotate the rotor, it first requires the stator to generated correct rotation field, which can make the rotor rotation in the required direction consequently. To generate the required rotation field, the corresponding current sequences in the stator coils need to be properly controlled. Different converters are studied to achieve the require stator sequence.

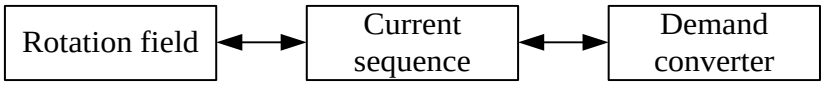

Figure 4.4 Diagram of dynamic analysis.

4.3.1. Rotation of Magnetic Field and Current Excitation Sequences

For the typical three-phase six-stator-pole four-rotor-pole CSRM, there are six possible magnetic fields, as shown in Figure 4.5. The magnetic field is mainly generated by stator poles. As known for reluctance machine, to rotate anti-clockwise, the magnetic field sequences should be as:

V1/V4→V2/V5→V3/V6→ V1/V4→V2/V5→V3/V6

This leads to mathematically 64 possibilities. However, considering the system balance, the following three conditions are studied in this thesis:

Case 1: V1 →V2 → V3→ V4 →V5 → V6

Case 2: V1 →V2 → V3→ V1 →V2 → V3

Case 3: V1 →V5 → V3→ V1 →V5 → V3

Similarly, this stator generated magnetic field is also applicable to TSRM to properly rotate its rotor.

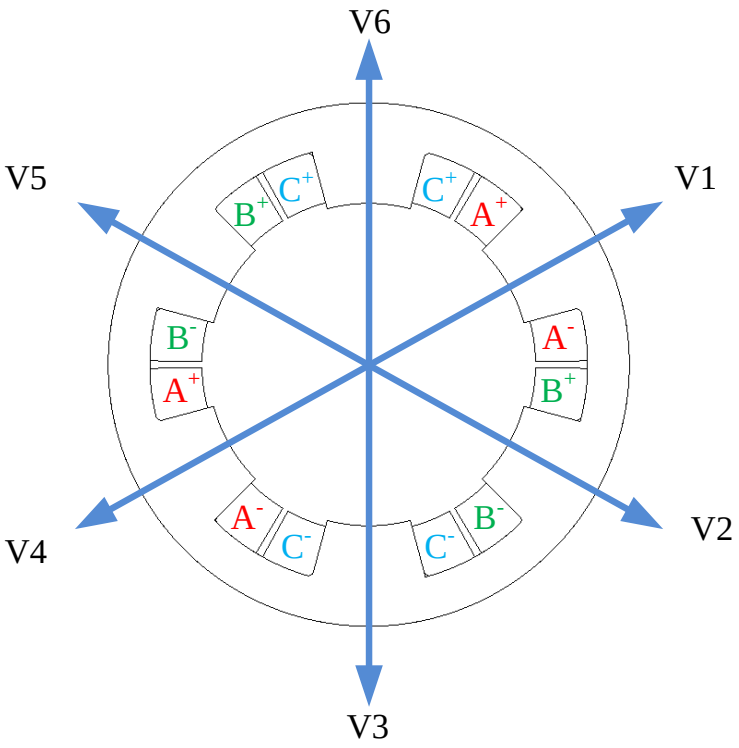

Figure 4.5 Magnetic field vectors and winding pattern in CSRM.

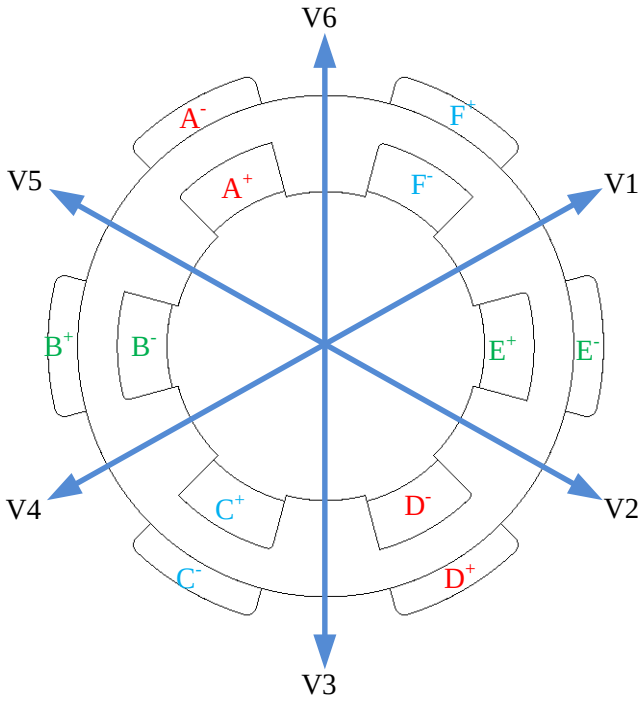

Figure 4.6 Magnetic field vectors and winding pattern in TSRM.

With the winding pattern is shown in Figure 4.6, to generate the rotating magnetic field, with all six coils active all the time, the following current sequences are required for TSRM as shown in Figure 4.7. Obviously, different current sequences will result in a different magnetic field on both stator and rotor. Clearly, this will potentially affect the dynamic torque response as well as iron core loses, which has also been studied in [76].

To initiate the comparison, the ideal square-wave currents are injected to TSRM FEA model, in which the flux variation influence will be included. The TSRM geometry follows the same as CSRM. Both choose a typical three-phase six-stator four-rotor. Detail of an optimal solution will be discussed in Chapter 5.

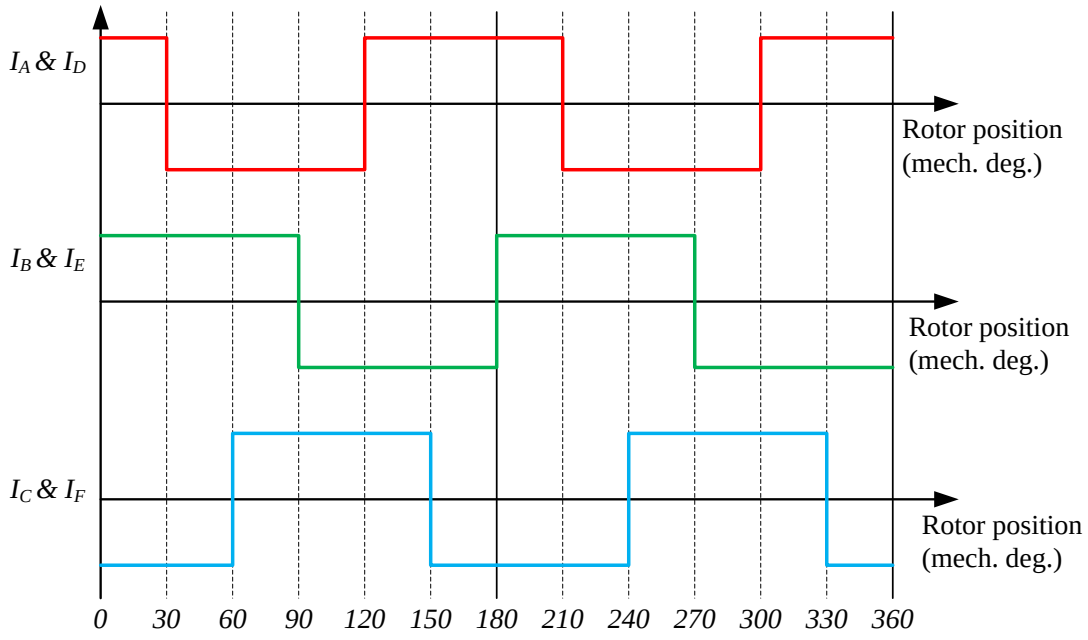
I_A & I_D
Rotor position (mech. deg.)
I_B & I_E
Rotor position (mech. deg.)
I_C & I_F
Rotor position (mech. deg.)
0 30 60 90 120 150 180 210 240 270 300 330 360

(a)

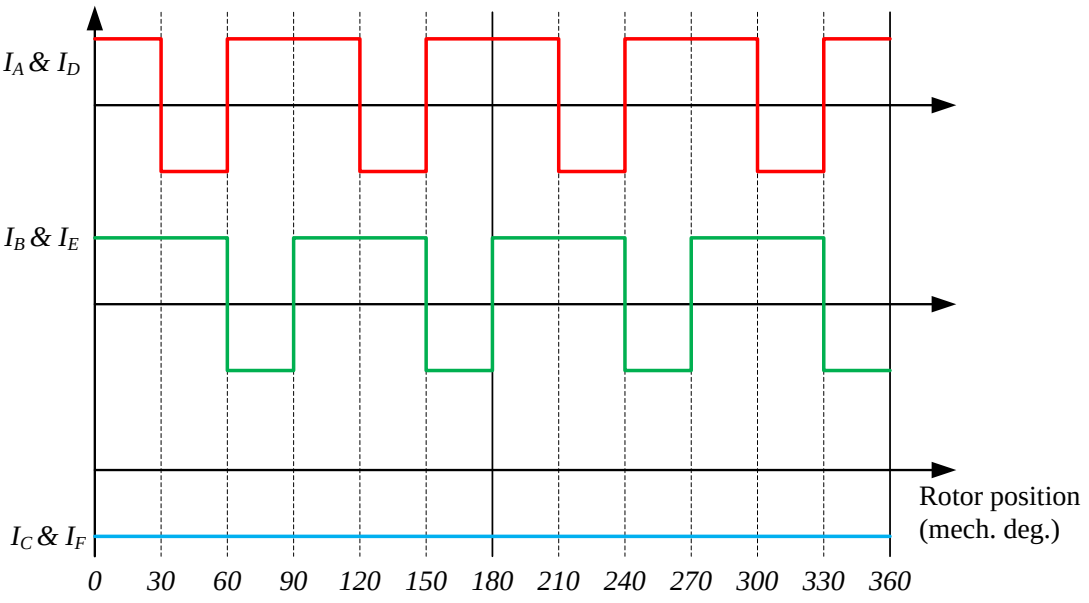
I_A & I_D
I_B & I_E
Rotor position (mech. deg.)
I_C & I_F
0 30 60 90 120 150 180 210 240 270 300 330 360

(b)

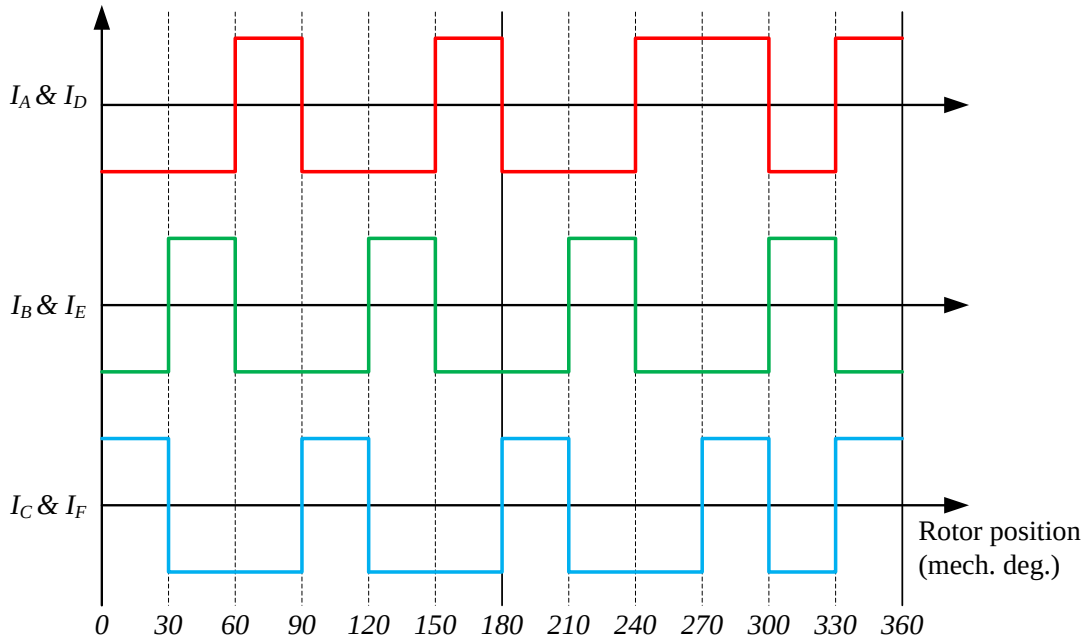

(c)

Figure 4.7 Current sequences options in TSRM.

The dynamic torques of the three current sequences presented are very close with each as the same as zoomed and compared in Figure 4.8. This torque is only for illumination purpose, which is not optimized.

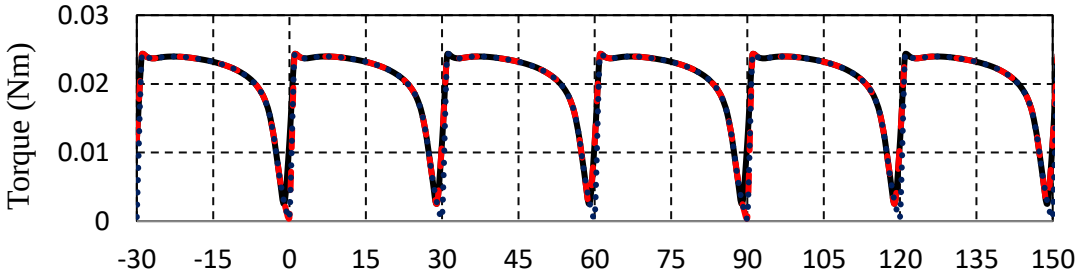

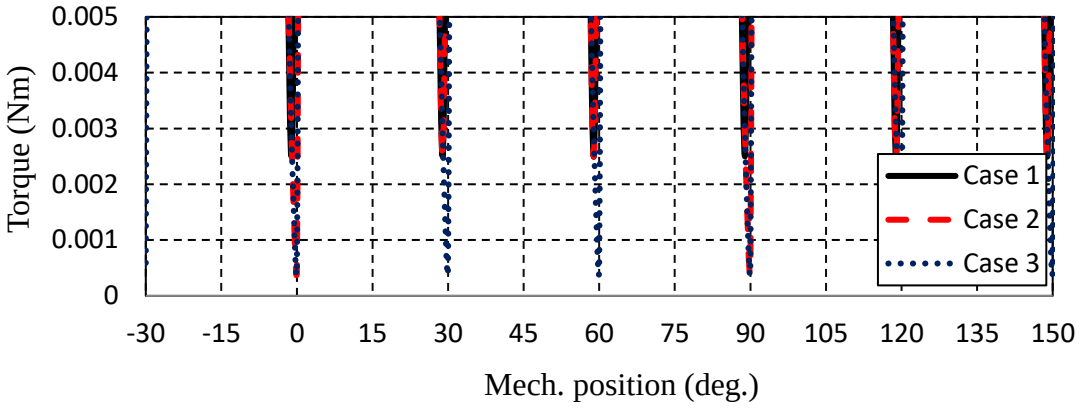

Figure 4.8 Torque comparisons with three different current sequences.

Equation 4-5 presents the general machine core losses equation, which is known as the Steinmetiz equation [77][78][79].

$$P_{iron} = k \cdot f^{\alpha} \cdot B^{\beta} \qquad \text{Equation 4-5}$$

where B is the peak flux density, f is the excitation frequency, and k, α, and β are coefficients. Through this, conventional equations are used with the assumption that magnetic flux density is almost sinusoidal, and it's applicable only for the simple condition. However, it can still conclude that iron core lose is determined by flux magnitude and variation frequency on the motor core. To better understand the current sequence influence on iron losses of the three cases, flux variation is measured via FEA during the torque simulation in Figure 4.8. Six positions on stator and four positions on rotor have been selected for comparison, as shown in Figure 4.9.

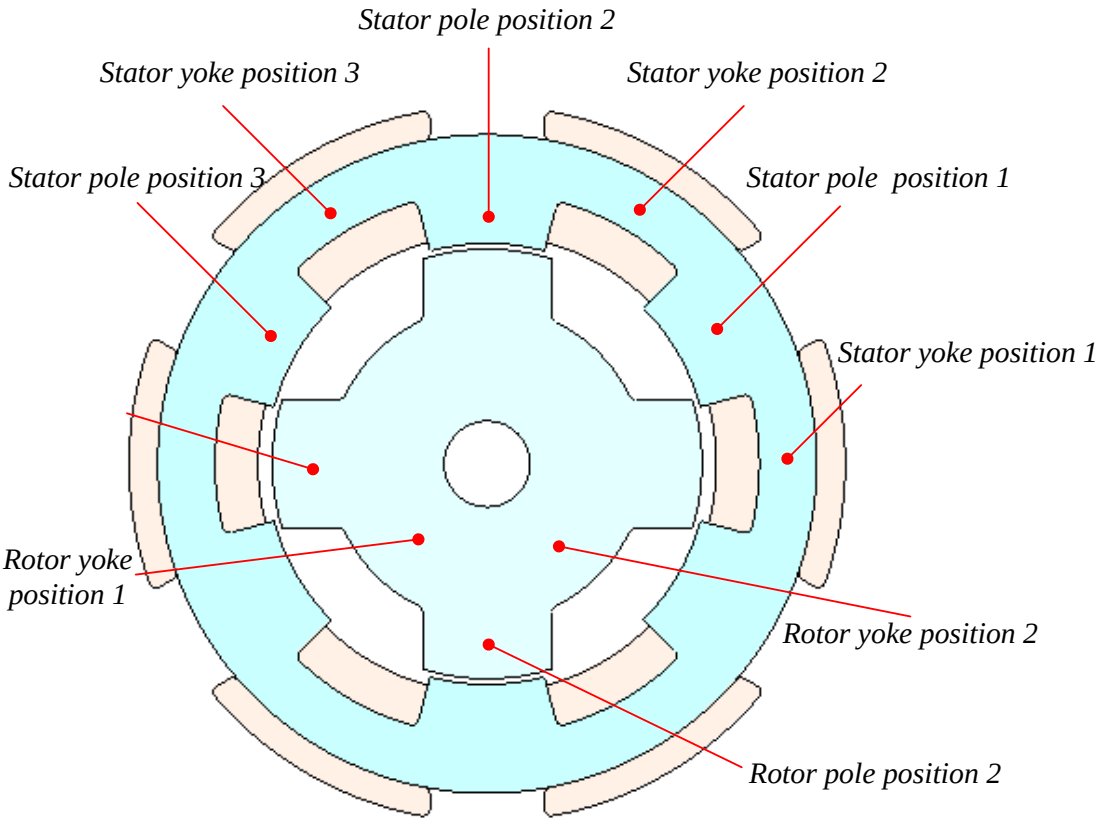

Figure 4.9 Flux measurement locations on TSRM.

Figure 4.10 compares the flux variation in different parts with different current sequences cases. It is clarified that the flux waveform on the machine poles only concentrates on the radial component, but only the tangential component for the flux on the yoke. Therefore, the frequency difference between cases will be clearer.

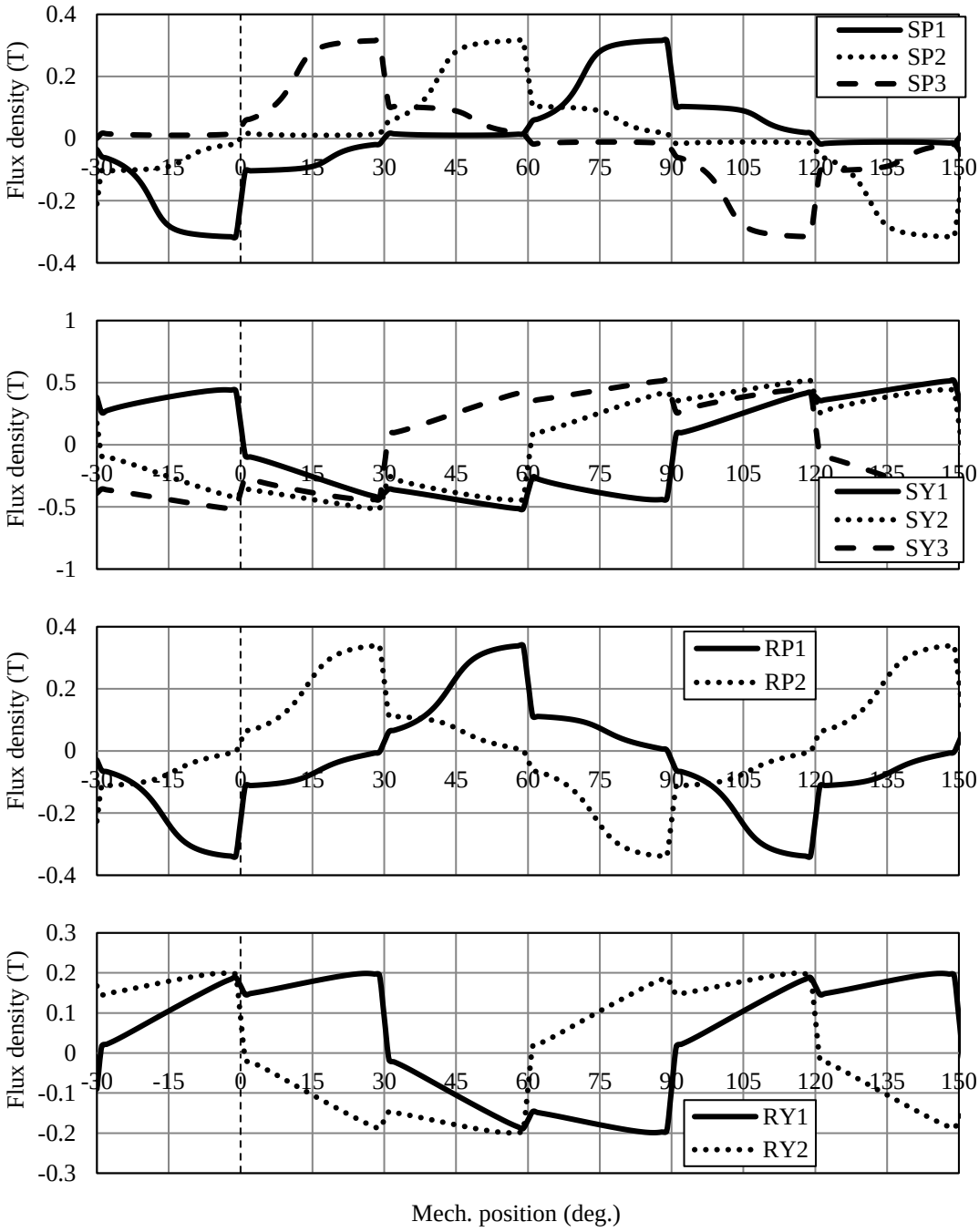

(a) Current sequence 1

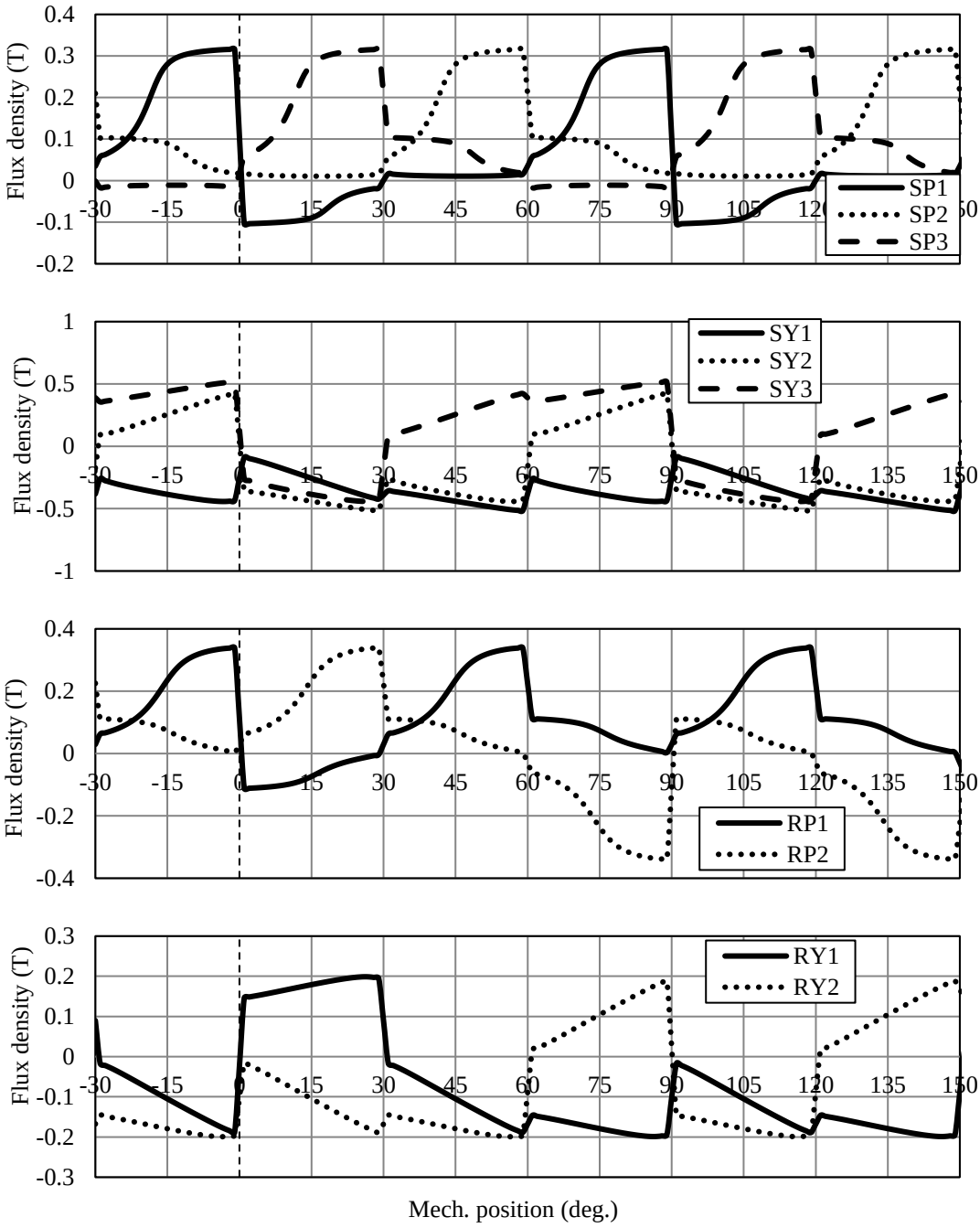

(b) Current sequence 2

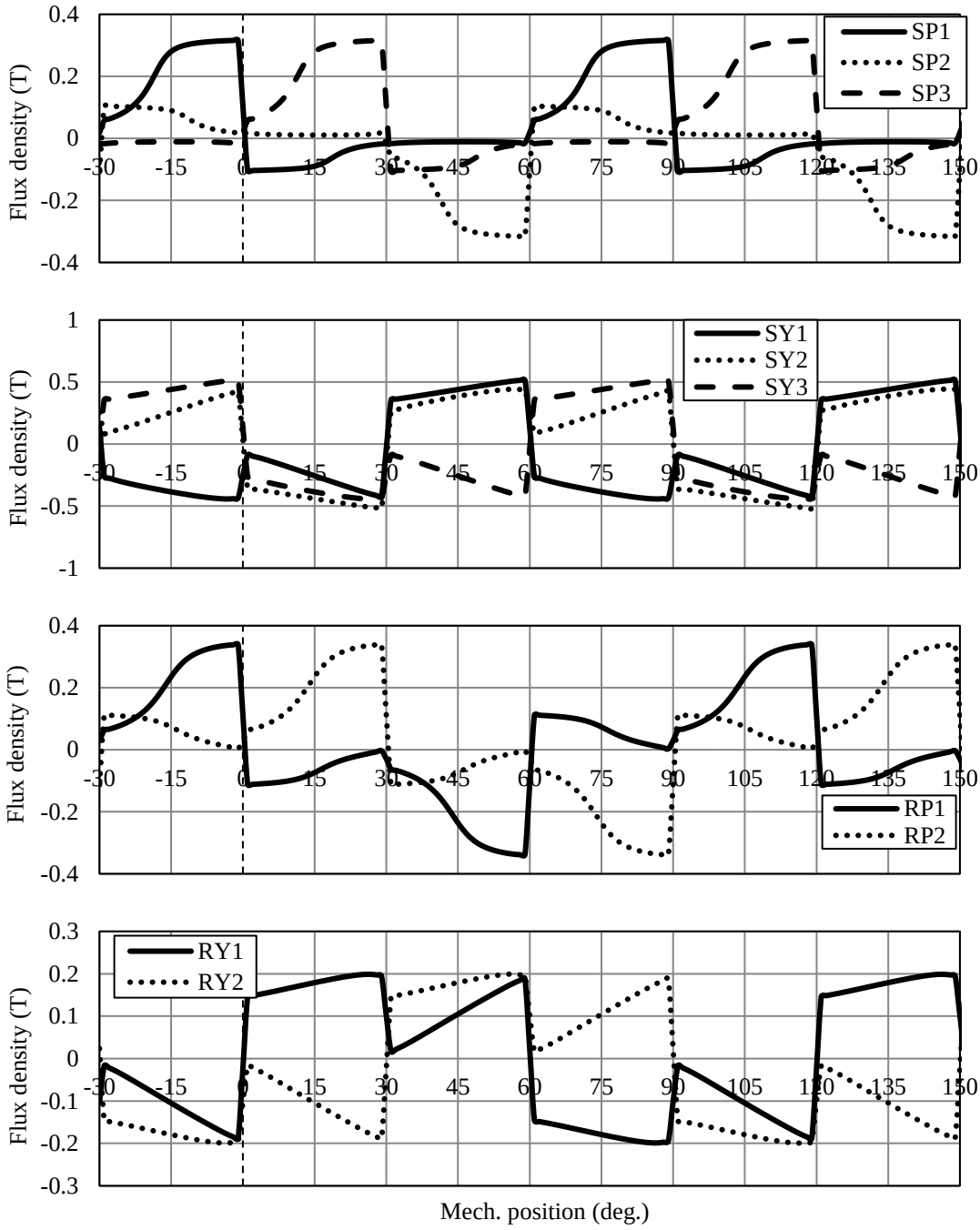

(c) Current sequence 3

Figure 4.10. Flux variations at different positions with different current sequences on TSRM.

Table 4-I Frequency and iron losses comparison among three TSRM current sequences.

	Sequence 1	Sequence 2	Sequence 3
Power electronic			
Current frequency	6 coils × f_1	4 coils × 2 f_1	6 coils × 2 f_1
Switching frequency*	12 switches × $k f_1$	8 switches × 2$k f_1$	12 switches × 2$k f_1$
Field frequency			
Stator yoke	6 yokes × f_1	2 yokes × 0 + 4 yokes × 2 f_1	6 yokes × 2 f_1
Stator pole	6 poles × f_1	6 poles × 2 f_1	6 poles × 2 f_1
Rotor yoke	4 poles × 3 f_1 /2	4 poles × f_1 /2	4 poles × 3 f_1 /2
Rotor pole	4 poles × 3 f_1 /2	4 poles × f_1 /2	4 poles × 3 f_1 /2
Iron losses			
Stator (Watt)	63.54	132.14	259.96
Rotor (Watt)	27.68	25.86	79.69

* Switching frequency also depends on converters, here is approximately estimation.

Flux variation frequency is the focus of the comparison since the flux magnitude is the same among different current sequence, which is the necessary condition for equivalent torque performance. This is also proved in Figure 4.10. Table 4-I compares the current/switching frequency and filed frequency of each part when the motor rotates at the speed of 50,000 rpm, f_1 is the base frequency defined in Equation 4-6 with N_r as rotor pole number, rpm as rotation speed.

$$f_1 = \frac{N_r / 2 \cdot rpm}{60} \qquad \text{Equation 4-6}$$

The iron losses are calculated via FEA in JMAG, using the field solutions in each material element, and material loss information from the manufacturer's specifications.

It's concluded qualitatively, but not quantitatively, that current sequence 1 has the most advantage in term of stator field frequency, and therefore benefits stator iron losses. But current sequence 2 is better if the rotor iron losses are the most important issue to consider. In the end, current sequence 1 is chosen considering the torque balance and iron losses as stator dominate the machine mass in particular internal rotor SRMs. Additionally, current sequence 1 has the best symmetricity for the whole system.

4.3.2. Proposal of Two Inverter Topologies for TSRMs

To achieve the current sequence 1, as shown in Figure 4.7(a), there can be more than one type of converter topologies. As seen for this current sequence, at each moment, there are three coils share the same currents and the other three conduct exactly the opposite currents. Thus, this chapter proposes two typical connections among these 6 coils as shown in Figure 4.11.

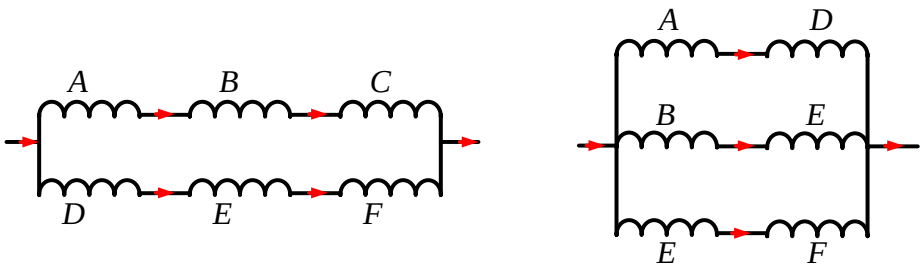

Figure 4.11. Connections between the stator coils, with the winding pattern in Figure 4.6.

To achieve the current sequence, two converter topologies are studied based on the different connection in Figure 4.11. As shown in Figure 4.12, these two converters both require 12 switches to achieve the bipolar current in each coil. For converter 1, there is one pair of switches is turned on at each moment, one from the upper and the other from the bottom. As for converter topology 2, it uses three typical H-bridge converter parallel connected for '3 phases'. At each moment there are one pair of each H-bridge is on; therefore, 3 pairs are turned on for the '3 phases'.

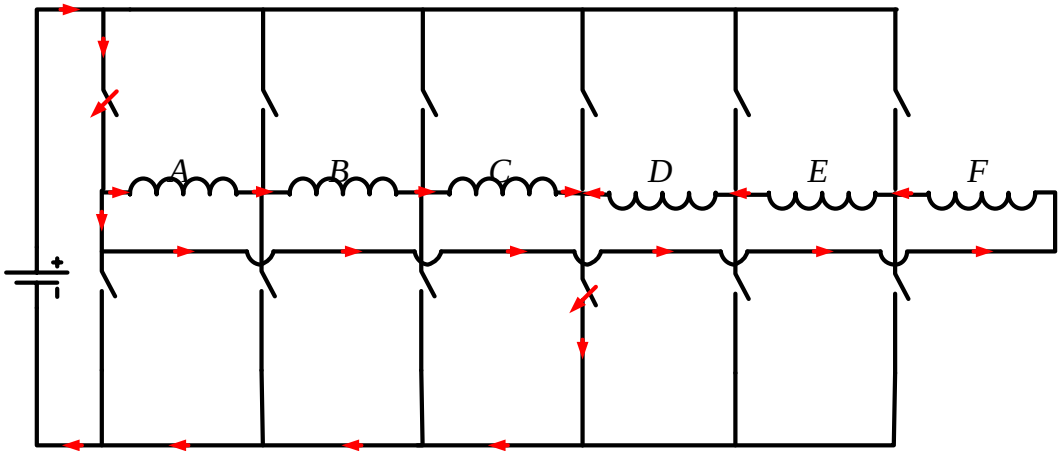

(a) Converter topology 1

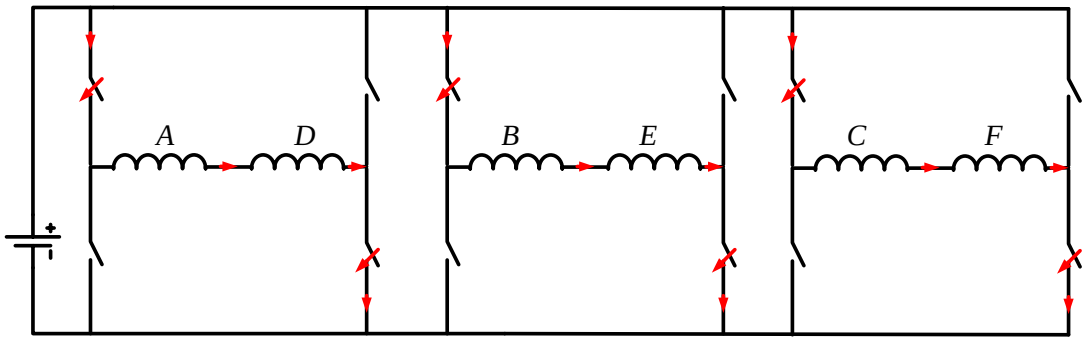

(b) Converter topology 2

Figure 4.12. Two proposed converter topologies for 6-coil single-layer TSRM.

4.3.3. Converter Comparisons for TSRMs.

To validate these two converters can both achieve required control performance, the dynamic system, motor together with the converter is set up in FEA and tested. As indicated in Table 3-I, a typical 6-4 geometry and typical material from commercial FEA software, JMAG, is used. Same control parameters are applied.

The results are presented in Figure 4.13. It shows that these two converters have a relatively similar dynamic performance for the 6-coil SLTSRM. For both the two converters, advanced switching angle would benefit machine performance at high speed. Below it shows the average torque/torque ripple variation regarding different switching angle.

Since the average torque is the main consideration for the high-speed application performance evaluation. The switching angle of -10 degree is selected for both these two inverters. Detail comparison of these two inverters is conducted in Table 4-II. From the comparison, it shows that Converter-2(full-bridge inverter) leads to relatively high output at the expense of higher copper and iron losses than Converter-2(ring-inverter). The electrical efficiencies are very close to each other at 83%. The comparison is also conducted regarding DC current waveforms in

Table 4-III. It clearly presents that the ring inverter results in a relatively lower DC current ripple. However, considering the reduced output power, this benefit is not obvious enough.

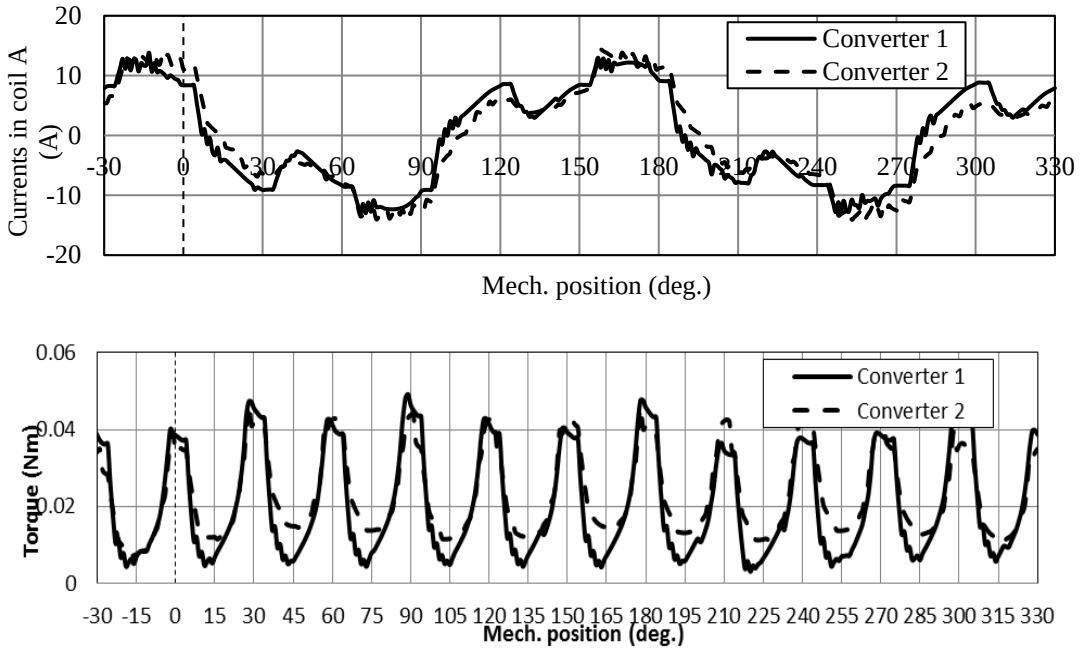

Figure 4.13. Dynamic current and torque comparison between the two converters results come from FEA.

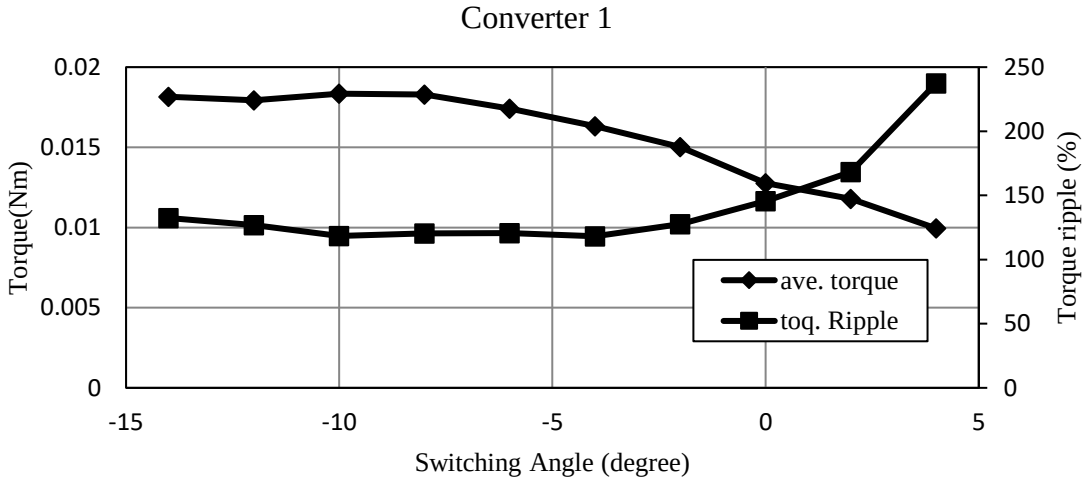

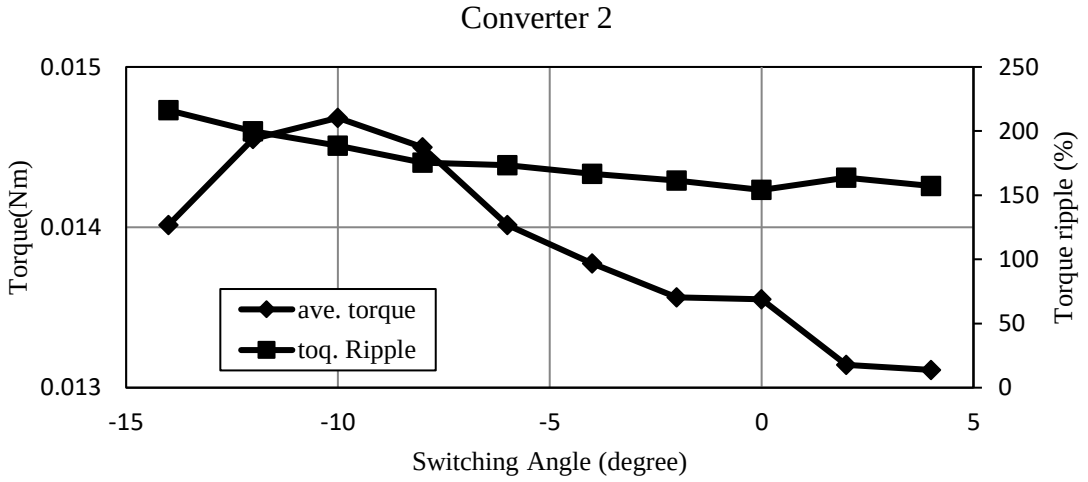

Figure 4.14. Dynamic torque comparison between the two converters, results from FEA.

Table 4-II Dynamic torque performance comparison among two TSRM converters at 50,000 rpm (switch angle = -10deg.).

	Torque (Nm)	Mech. Power(W)	Losses(W)		Eff.(%)
			Copper	Iron	
Converter 1	0.0143	74.87	11.87	37.20	60.41
Converter 2	0.0183	95.81	14.77	46.30	61.07

Table 4-III DC bus currents comparison among two TSRM converters at 50,000 rpm (switch angle = -10deg.).

	Converter 1 Ring-inverter	Converter-2 Full-bridge
Average	14.29A	17.35A
RMS	29.68	33.21
Max.	39.29A	61.32A
Min.	-39.16A	-55.74A
Ripple	548.84%	674.85%

Additionally, the semiconductor device rating is another important character considering the evaluation of the two converter topologies. Semiconductor device rating is constrained and determined by their electrical, material, mechanical, and thermal properties, design, and manufacture processes, etc., among which the thermal properties are comparatively dominant on the rating restrictions. Thermal performances of a device are determined by its power loss and heat transfer characteristics. Power losses in a semiconductor device include conduction losses, switching losses, diodes recovery and gate terminal losses.

For the full-bridge inverter, as it shows in Figure 4.15, the diode only works when the switches are off for current chopping. The switches and diode work together to shape the coil current as required. For all the switches and diodes, their peak current would be limited by the current controller. In the ring topology inverter, the switches conducted for an only one-third time of the switched in the full-bridge inverter. The diodes are conducted when the current in coils switches, or it chops. The switches during the transient time conduct the required current for the next moment as well as compensating the current change. Therefore, it doubles the current in the coil. Table 4-IV summarizes the currents value in the power electronics devices.

From Table 4-IV, it shows that the ring-inverter has higher current requirement on the switches and diodes because of the transient coil current. Also taking the torque output also into consideration, the full-bride inverter yields better overall performance compared than the ring-inverter because of its higher output torque and lower device requirement. In

addition, the modeling of the full-bridge inverter is much simpler than ring-inverter. Therefore, the full-bridge inverter is chosen for TSRM comparison in the following study.

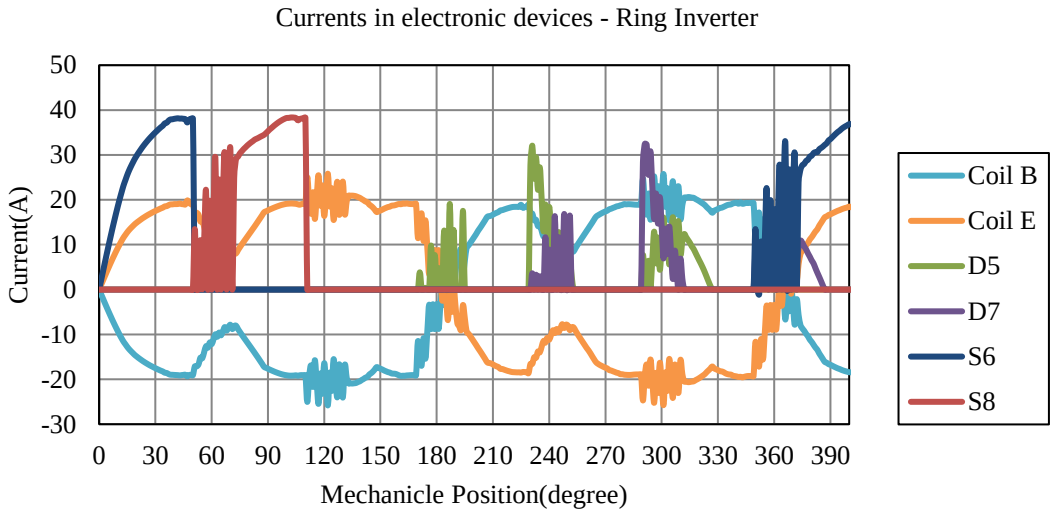

(a)

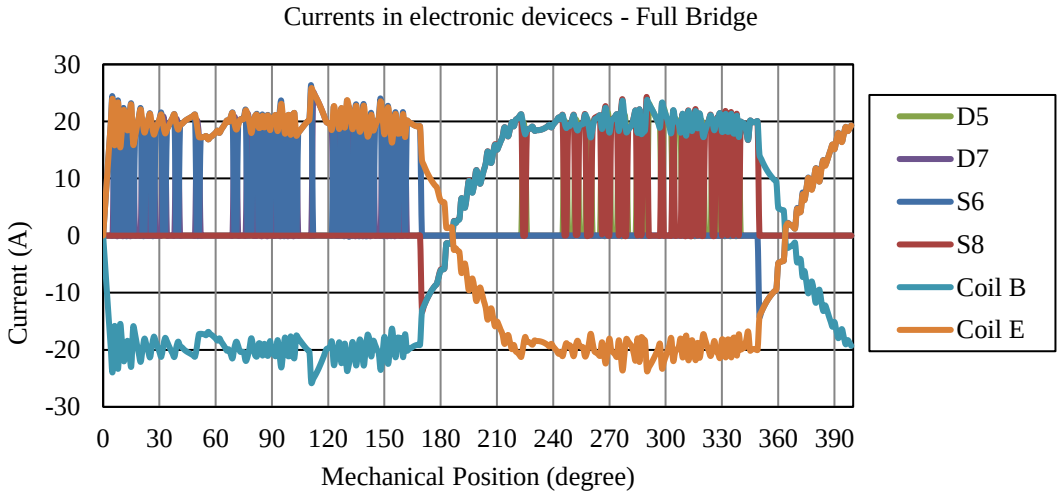

(b)

Figure 4.15. Current waveforms comparison in semiconductor devices.

Table 4-IV Semiconductor devices comparison among two TSRM converters at 50,000 rpm (switch angle = -10deg.).

	Full-Bridge	Ring-Inverter
Switch peak voltage (V)	31.90	30.38
Switch RMS voltage (V)	17.19	15.90
Switch peak current(A)	25.78	38.16
Switch RMS current(A)	10.66	11.77
Diode peak current (A)	23.08	32.08
Diode RMS current(A)	6.98	5.52

4.4. Sinusoidal Excitation and DQ Modeling of TSRMs.

For a three-phase mutual-coupled TSRM with balanced excitation and without third and other harmonics, the three-phase state variables (flux linkage ψ, current i, and voltage u) can be fully mapped into the static α-β reference system by using the Clarke Transformation. If expressed in space vectors, the voltage equation in the α-β reference system is

$$\boldsymbol{u}_{\alpha\beta} = R_s \boldsymbol{i}_{\alpha\beta} + \frac{\mathrm{d}\boldsymbol{\psi}_{\alpha\beta}}{\mathrm{d}t} \qquad \text{Equation 4-7}$$

where $\boldsymbol{u}_{\alpha\beta}$, $\boldsymbol{i}_{\alpha\beta}$ and $\boldsymbol{\psi}_{\alpha\beta}$ are space vectors of the voltage, current, and flux linkage in the α-β reference system respectively. R_s is the phase resistance, and t is time. The relationship between the values in the static α-β reference system and those in the synchronous rotating DQ reference system is

$$\boldsymbol{\psi}_{\alpha\beta} = \boldsymbol{\psi}_{dq} e^{j\theta} \qquad \text{Equation 4-8}$$

where $\boldsymbol{\psi}_{dq}$ is the flux linkage space vector in the *DQ* reference system, θ is the rotor position in electrical angles.

If nonlinearity of the magnetic circuit is neglected for clarity, the flux linkage equation in the static *ABC* reference system is

$$\boldsymbol{\psi}_{abc} = \boldsymbol{L}_{abc}\, \boldsymbol{i}_{abc} \qquad \text{Equation 4-9}$$

where $\boldsymbol{\psi}_{abc}$ and $\boldsymbol{i}_{abc}$ are the column vector of the three-phase flux linkage and current respectively, $\boldsymbol{L}_{abc}$ is the inductance matrix. For the TSRM with symmetric salient rotor pole structures, the inductance contains only even spatial harmonics. By applying the amplitude invariant Park's Transformation **K** to Equation 4-9, the flux linkage equation in the *DQ* reference system becomes

$$\begin{aligned} \boldsymbol{\psi}_{dq} &= \mathbf{K}\boldsymbol{L}_{abc}\mathbf{K}^{-1}\mathbf{K}\boldsymbol{i}_{abc} \\ &= \boldsymbol{L}_{dq}\boldsymbol{i}_{dq} \end{aligned} \qquad \text{Equation 4-10}$$

where $\boldsymbol{L}_{dq}$ is the inductance matrix in the *DQ* reference system. $\boldsymbol{L}_{dq}$ will only contain special harmonics whose orders are multiples of 6 for the TSRM. However, only the surface spanned by the fundamental component vector is of key importance to the electromechanical energy conversion function of the machine. The electromagnetic torque equation in the *DQ* reference system is

$$T = \frac{3}{2} p\boldsymbol{\psi}_{dq} \times \boldsymbol{i}_{dq} + p\frac{\partial W_{co}}{\partial \theta} \qquad \text{Equation 4-11}$$

where p is the number of rotor pole pairs of the TSRM, W_{co} is the magnetic coenergy. The first term of Equation 4-11 is labeled as T_{dq} and is produced by the *DQ* axis alignment,

while the second term is labeled as T_{co} and is produced by the magnetic coenergy. For the linear case, W_{co} can be computed as

$$W_{co} = \frac{1}{2}\boldsymbol{i}_{dq}{}^{T}\boldsymbol{L}_{dq}\boldsymbol{i}_{dq} \qquad \text{Equation 4-12}$$

Obviously, for specific current excitation T_{co} also contains the same harmonic orders of those of L_{dq}.

From Equation 4-7 to Equation 4-12, we can come up with a dynamic DQ model of the TSRM. However, even though the spatial harmonics and the cross-coupling are included, the nonlinearity of the magnetic circuit is ignored. When saturation is included, the interpretation of inductances becomes complex since now they depend on both $\mathbf{i}_{dq}$ and $\boldsymbol{\theta}$. For calculation considering circuit switching, the incremental inductance makes matters even more complicated. Therefore, the look-up-table (LUT) approach, which gives the flux-current relationship, is more commonly used. The DQ dynamic model can be built directly based on the flux linkage LUT. Then the currents are used as the inputs while the voltages and torque are the outputs. The voltage space vector $\boldsymbol{u}_{\alpha\beta}$ is solved from the differential of $\boldsymbol{\psi}_{\alpha\beta}$ as is expressed in Equation 4-7. This kind of dynamic model is called an "incremental inductance" model, which is direct but the differential coefficients in it can amplify errors. Moreover, it is more convenient to use the voltage as inputs when considering the voltage source inverter. Therefore, a dynamic model based on the inverted current LUT is presented in Figure 4.16. This dynamic model contains only one integrator but no differentiator, which increases the accuracy when compared to the

conventional incremental inductance model. In the meantime, all the inductance harmonics are also included in the model.

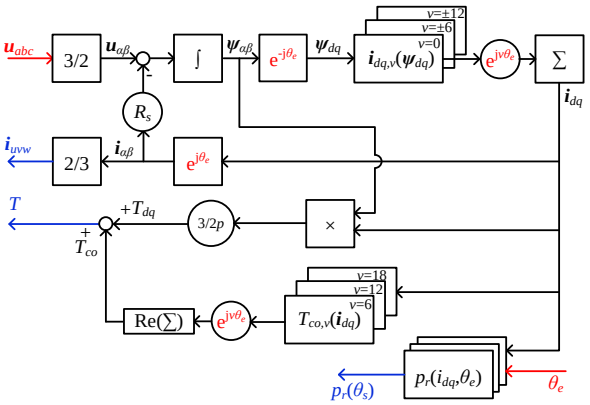

Figure 4.16. The dynamic model of the TSRM based on current LUT.

4.5. Conclusions.

This Chapter discussed the dynamic modeling, control method, and converter topologies of CSRM and TSRM. CSRM uses a decoupled concentrated phase winding so that torque is generated due to the rate of change of the self-inductance of the excitation phase. The asymmetric inverter is typically used on CSRM with popular angular position control.

Chapter 4 also presents the dynamic analysis of the TSRM. The required rotation magnetic field is first developed for TSRM, followed by its corresponding current sequence to achieve the required rotation sequence. Two TSRM converter topologies are introduced to obtain the required control flexibility, and the dynamic operation of the whole driving system is studied, including both the machine and the converter. The two

converters have been compared in detail regarding torque performance, iron losses, DC current requirement as well as semiconductor device rate and its heat generation.

In addition, three-phase sinusoidal current excitation is also proposed as a control option for TSRM. DQ modeling is discussed in this chapter, which is built based on the current LUTs which can consider the magnetic nonlinearity, spatial harmonics, and switching effects.

Chapter 5 Design of High-Speed CSRM and Mutually-Coupled TSRM

5.1. Introduction.

For higher speed machines, to reduce the frequency and number of semiconductor devices as well as the iron losses, lower stator and rotor pole numbers are preferred. However, to avoid extra mechanical difficulties caused by the no self-starting ability and one-direction drive, conventional three-phase six-stator-pole and four-rotor-pole topology is usually chosen as a standard in all types of SRM study. Thus, the comparison of CSRM and TSRM is also conducted on three-phase six-stator-pole and four-rotor-pole geometry.

To initiate the design, the out diameter, and stack length is usually fixed at the beginning because, for a certain application, there is limited space for the electric machine. For a certain output power/torque level, the outer diameter of the air gap is also available based on the well-known SRM output power equation.

Considering the typical nonlinearity of SRM, commercial FEA software coupled with Matlab/Simulink is used to propose an optimal solution. An optimization design based on engineering tuning without specific optimization theory is introduced. The comparison for different phase number, pole number as well as geometry has been addressed systematically. Considering the limited slot area for the winding and the limitation of the current density without any extra cooling system, the stator geometry can be decided usually. Thus, lots of machine design optimization problem will focus on optimizing the rotor topology a fixed the stator geometry. Paper [76] has proved that the rotor geometry has significant influence on the machine output performance. As the required torque and

stator structure is known already, the target of this Chapter is to find out the optimal rotor geometry. However, it's known, the output torque is generally proportional with the square of phase current. Without a constraint on the phase current, the optimal results will be of no practical meaning. At the same time, a higher phase current will lead to higher copper losses, which will affect not only thermal stress but also the drive efficiency of the designed SRM. In addition, the iron losses will be a significant issue for high-speed machine design. Thus, a multi-objective optimization as shown in Figure 5.1 is necessary to maximize the output performance at the same time limit the losses.

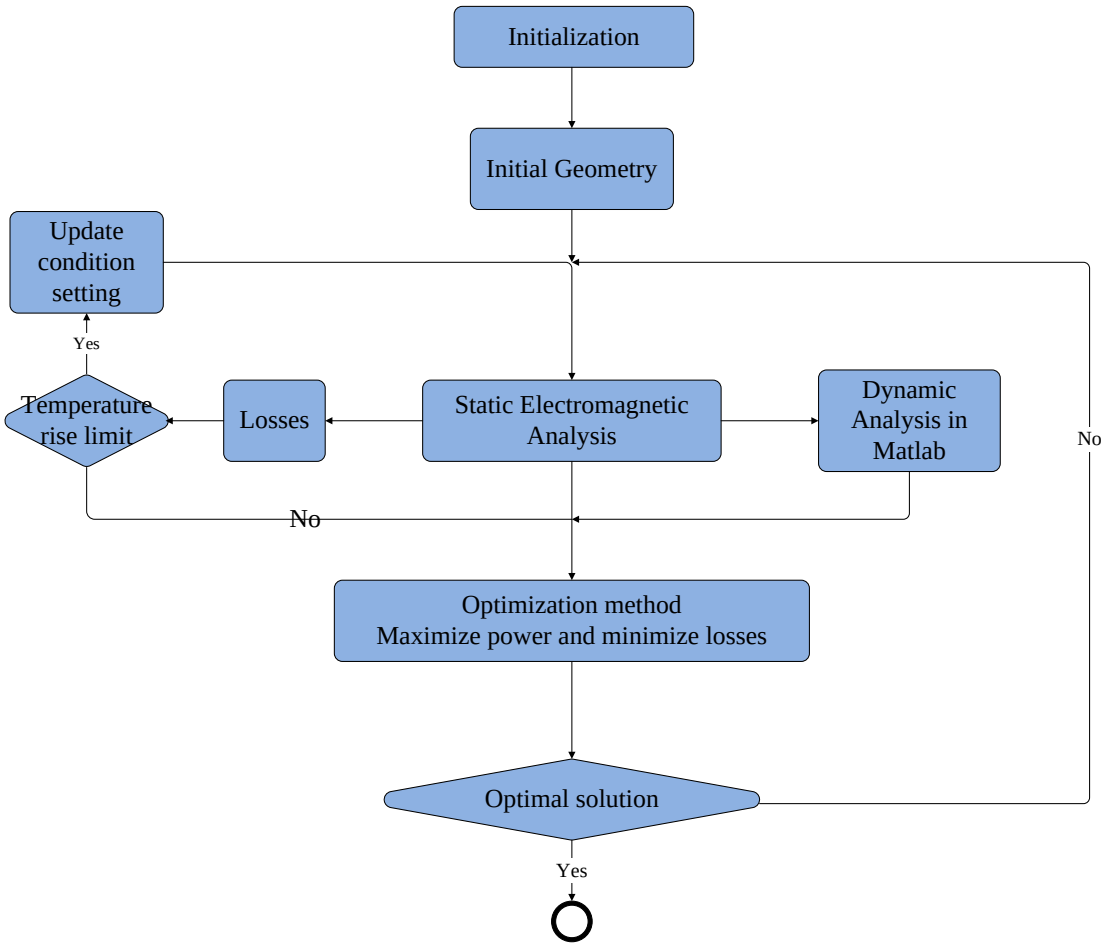

Figure 5.1 Procedure diagram of SRM design.

For the electromagnetic design and optimization process, this chapter will conduct a multi-objective optimization method coupling with FEA and mathematic dynamic simulation. The performances of CSRM and TSRM are then studied and compared.

5.2. Design of a Low-Cost High-Speed CSRM.

The objective is to maximize the output torque and efficiency. The geometry parameters to be determined are phase/pole numbers, shaft and rotor diameters, pole length/width, air gap, together with winding specifications. Their effect on motor performance will be discussed throughout Section 5.2.

A widely used approach is to start with the SRM output equation. Output power can be derived from the input power, as shown in Equation 5-1.

$$P_{out} = k_e \cdot k_d \cdot V_{DC} \cdot i \cdot m \qquad \text{Equation 5-1}$$

where k_e and k_d are efficiency and duty cycle ratio, V_{DC} is the input voltage, i is phase current, and m is the phase number.

$$V_{DC} = R_s \cdot i + \frac{d\lambda}{dt} \approx \frac{d\lambda}{dt} \qquad \text{Equation 5-2}$$

As for the motoring operation, which can be seen as the repeat of the process from unaligned position to aligned position, V_{DC} then can be expressed in Equation 5-3.

$$V_{DC} \cong \frac{d\lambda}{dt} = \frac{\lambda_a - \lambda_u}{\beta_s / w_m} \qquad \text{Equation 5-3}$$

where λ_a and λ_u are flux-linkage at aligned and unaligned commutation positions and β_s is stator pole arc. w_m is the angular speed, which can be derived by revolutions per minute N_{rpm}.

$$w_m = \frac{N_{rpm} \cdot 2\pi}{60} \qquad \text{Equation 5-4}$$

At the aligned position, flux-linkage can be implied from Equation 5-5.

$$\lambda_a = \phi \cdot T_{ph} = B_s \cdot \frac{D_r}{2} \cdot \beta_s \cdot L \cdot T_{ph} \qquad \text{Equation 5-5}$$

B_s is the stator pole flux density at the aligned position, which is usually chosen as the material saturated flux density to fully use of the core material. L is the stack length, D_r is the outer diameter of the rotor, and T_{ph} is the number of turns per phase. Summarizing equation Equation 5-1 to Equation 5-5, the output power is then expressed in Equation 5-6.

$$P_{out} = k_e \cdot k_d \cdot \frac{\pi}{60} \cdot (1 - \frac{\lambda_u}{\lambda_a}) \cdot B_s \cdot D_r \cdot L \cdot T_{ph} \cdot N_{rpm} \cdot i \cdot m \qquad \text{Equation 5-6}$$

Introducing $k_1 = \pi^2/120$ as a constant coefficient, and $k_2 = 1 - \lambda_u / \lambda_a$ a variable dependent on the operating point, which is usually chosen between 0.65 to 0.75, practically, A_s the specific electric loading, which is related to the system's cooling capability, Equation 5-6 can be reorganized as Equation 5-7. The conservative estimation has a range of $25000 < A_s < 50000$ [69][70].

$$P_{out} = k_e \cdot k_d \cdot k_1 \cdot k_2 \cdot B_s \cdot A_s \cdot L \cdot N_{rpm} \cdot D_r^2 \qquad \text{Equation 5-7}$$

The following specification is given to limit the machines competitive to commercial high-speed motors. Moreover, the designed machines are naturally cooled. All material used on machine is required to be commonly available in the market to reduce cost. Copper filling factor is highly dependent on the winding technique. In practice, it's usually between 35% and 60%. In this chapter, it's limited to 30% to avoid extra wounding difficulty and manufacture cost.

Table 5-I Design requirements.

Parameters	Value
OD of outer stator: D_s	50 mm
Stack length: L	50 mm
Rated speed: N_{rpm}	50,000 rpm
OD of Shaft	6 mm

As for a higher speed machine to reduce the frequency and number of switches as well as the iron losses, lower stator and rotor pole numbers are preferred. And to avoid extra mechanical difficulties caused by the no self-starting ability and one-direction drive, finally, a common industry used phase/pole configuration is chosen. A three-phase six-stator-pole and four-rotor-pole SRM is will be designed in this chapter.

5.2.1. The Outer Diameter of the Rotor.

Rotor outer diameter is one of the most important parameters in SRM design. Equation 5-7 indicates the simplified proportional relationship between rotor volume and output

torque. However, with the limitation of total space, a larger rotor will reduce stator size. This will consequently lower the winding space and system efficiency. Considering the balance between these tradeoffs, calculation suggests the rotor diameter around half of the stator diameter.

5.2.2. Airgap Selection.

Switched reluctance machines performance is more sensitive to airgap selection. As indicated in Chapter 2, electromagnetic torque is proportional to inductance variation. A smaller air gap will enhance aligned inductance as well as inductance variation between unaligned and aligned position.

However, the air gap size is dictated by the available manufacturing and assembly tolerances. A smaller airgap will significantly increase manufacturing cost and difficulty. Moreover, for this high-speed machine, one of the most important issues limit the machine's output power is the current drop time. To decrease this, a lower inductance at the aligned position is necessary.

In literature review shows, airgap between 0.15mm and 0.35mm is very popular for high-speed SRM design. The design finally set the air gap to 0.4 mm, considering the cost reduction and prototype difficulty.

5.2.3. Stator Pole Arc.

Considering the ability to start the machine at any rotor position, one should avoid dead zones, which have no inductance variation for any phase, leading to a zero torque region. That is to say that, the following constraints need to be satisfied.

$$\begin{cases} \min(\beta_s, \beta_r) \geq \dfrac{4\pi}{P_r P_s} \\ \beta_s + \beta_r < \dfrac{2\pi}{P_r} \end{cases} \qquad \text{Equation 5-8}$$

where β_s is stator pole arc and β_r is rotor pole arc. For the three-phase, 6-4 motor, this equates to:

$$\min(\beta_s, \beta_r) \geq 30^{\circ}, \quad \beta_s + \beta_r < 90^{\circ} \qquad \text{Equation 5-9}$$

$\beta_s < \beta_r$ is preferred for this design because a smaller β_s provides a larger slot for the stator winding. Considering the winding difficulty and thermal issue for this smaller high-speed machine, lower current density and filling factor are suggested, which require an ev en smaller stator pole arc. Thus, the minimum value for the stator pole arc is chosen as $\beta s = 30^{o}$.

5.2.4. Rotor Pole Arc.

It has been approved with many advantages for a larger rotor pole arc. First of all, a greater rotor pole increases the average torque contribution of each phase. At the same time, it gives more time for the winding current dropping to zero before generation a negative torque. A larger rotor pole arc is preferred for this high-speed machine design. However, a higher rotor pole will also increase the current drop time. Thus, there is a trade-off for choosing the rotor pole arc. For this machine design, Figure 5.2 shows a trendy for the contribution of an increasing rotor pole arc on its output power. It first increases with the rotor pole arc increases, but it then reaches a constant value, after that it drops quickly. Therefore, the rotor pole arc is chosen $\beta r = 35^{o}$, considering both the output power benefit and the material cost.

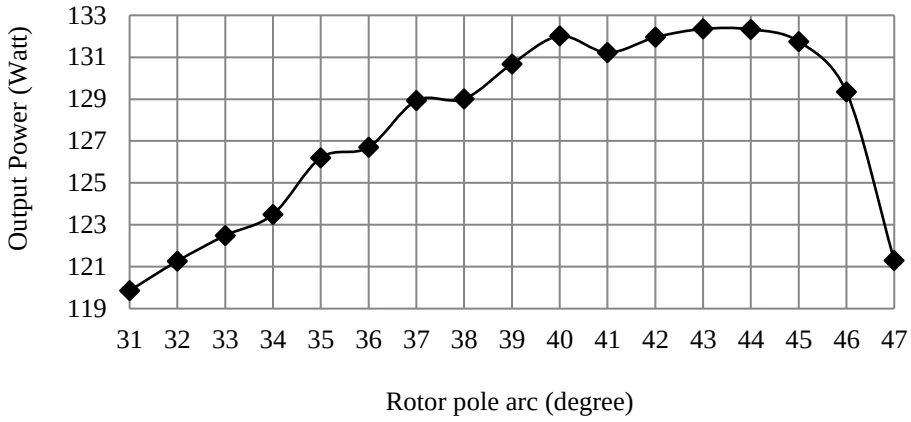

Figure 5.2 Tendency of simulated output power with rotor pole arcs in the CSRM at 50,000 rpm.

5.2.5. Other Dimensions.

The stator/rotor yoke thickness, *b*, is calculated from their pole width, *w*, by Equation 5-10.

$$b = k\frac{w}{2} \qquad \text{Equation 5-10}$$

A higher *k* value on stator will reduce the iron loss on the yoke but leads to shorter stator pole which limited winding slot area. Thus, *k* is usually chosen one for stator based on engineering experiences. As for rotor, the selection of k is more dependent on torque performance. Considering both torque performance and iron losses, *k = 1* is also used for rotor yoke thickness. With all the stator/rotor information above, their pole height is determined.

5.2.6. Winding Design.

Concentrated winding electrically isolates phases from each other, leading to higher fault tolerance than conventional AC machines. Besides, the concentrated winding also has the advantages of shorter and fewer complex end-windings. This has the advantage of lower copper losses and higher efficiency. However, it also brings the problem of bigger torque ripples than distributed winding. For the high-speed small-size and low-cost machine design, losses and efficiency have higher priority than torque ripple. Figure 5.3 shows the structures of the conventional concentrated winding.

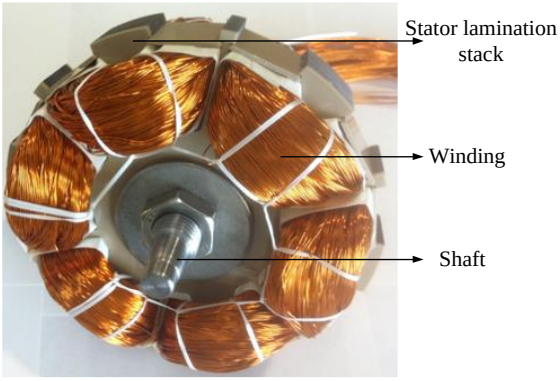

Figure 5.3 Physical view of concentrated winding on an external-rotor CSRM [76].

The relationship between the current density and stator slot is stated in Equation 5-11.

$$I_{rms} \cdot T_p = J_{rms} \cdot S_{fill} \cdot A_{slot} \qquad \text{Equation 5-11}$$

where I_{rms} is the RMS value of the phase current, T_p is the winding turns per pole, S_{fill} is filling factor, and A_{slot} is the area of single stator slot.

Typical continuous allowable current densities for induction machine by T.A. Lipo in Table 5-II, is used as a reference for current density limitation. For this naturally cooled small-size machine, the current density, J_{rms}, is better to be within 6 A/mm^2 based on engineering experience.

Table 5-II Continuous allowable current density in induction machines [80].

totally enclosed machines with no external cooling (4.5 to 5.5 A/mm2)
forced air cooling over stator surface (7.5 to 9.5A/mm2)
air cooling through stator ducts/vents (axial or radial) (14 to 15.5A/mm2)
liquid cooling in ducts (23 to 31A/mm2)

The slot area is determined by stator geometry, with S_{fill} of 30%, and J_{rms} of 6 A/mm^2, the right side of the equation is fixed. The relationship finally becomes a limitation of the current and the winding turns. At the same time, it's known that inductance is proportional to the square of phase winding turns. With the limited slot area, the phase resistance is also proportional to the square of phase winding turns. A higher inductance requires higher longer current response time with a limited DC bus voltage, which is difficult for high-speed machine control. An *n*-time winding number of turns requires only *1/n* of the previous phase current for equivalent static magnetic field generation. However, as voltage drops on the inductance and resistance are both proportional to the square of winding number of turns, achieve the required dynamic current response; a*n*-time DC voltage is needed. Considering this high-speed low-power machine is to be

applied on home applications, the most popular DC voltage of 12V. The peak current is selected to 20A, and the number of turns per coil is 6.

5.2.7. CSRM Design Solution.

Finally, a 50,000 rpm 6/4 SRM has been designed in Table 5-III. The analysis shows that the designed machine operates at the unsaturated magnetic condition. Thus, the nonlinearity of this machine is not that significant, which make the analysis much easier.

Table 5-III Solution of the CSRM design.

Parameters	Values
Number of phases	3
Number of poles	Stator 6, Rotor 4
Winding topologies	Conventional Concentrate
Stator outer diameter	50 mm
Bore diameter	30 mm
Stack length	50 mm
Air gap	0.4 mm
Stator pole arc	30º
Rotor pole arc	35º
Input voltage	12 V
Current	20 A
Turns per pole	6
Rated speed	50,000 rpm
Lamination steel	29 GA M15 C5
Coil gauge	AWG 16 (OD = 1.29mm)

5.3. Design of a Low-Cost High-Speed TSRM.

For toroidal-winding, coils are wounded around the stator yoke beside the stator pole. As proposed in Chapter 2, the double layer TSRM, it uses these two coils to produce the same flux distribution as the one conventional coil on the stator pole. To generate the equivalent magnetic field, it requires the same magnetic motive force (*MMF = number of turns × current*) for each magnetic circuit. Therefore, the number of turns per coil will be the same between CSRM and DLTSRM, but the number of turns per phase will be twice in DLTSRM compared with CSRM. That's to say, for the same rotor/stator geometry, to achieve equivalent performance, DLTSRM needs double copper material and losses of CSRM.

Obviously, DLTSRM has a bare advantage over CSRM, especially if copper losses and weight is taken as high priority. The two coils in each slot of DLSRM are then parallel connected as one coil for SLTSRM. With a double copper cross-section area and 6-coil current control, SLTSRM has a significant benefit on copper losses reduction.

All the six coils are active and contribute to torque generation at any time. By changing the current direction in all these six coils, the flux field will rotate at demand speed and generate required torque. However, to achieve bi-direction current in each coil, 12-switch are needed for this three-phase machine, two power electronic converters have been proposed in Chapter 4. In this thesis, the study will only focus on the three-phase full-bridge converter. Resized Single Layer TSRM

However, compared to CSRM, the envelope dimension of both DLTSRM and SLTSRM is enlarged since the windings are wounded outside the lamination, as shown in Figure 5.4. To make the same volumetric comparison between CSRM and SLTSRM, SLTSRM is modified with a resized stator.

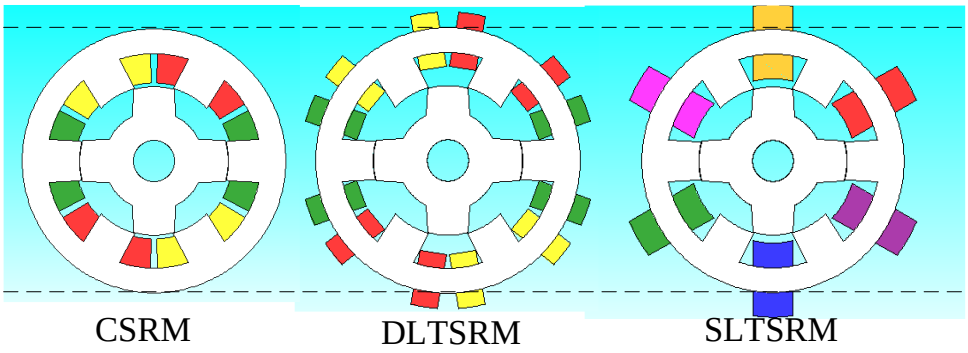

Figure 5.4. Same stator/rotor geometry among CSRM, DLTSRM, and SLTSRM.

In this new version of SLTSRM, the stator pole height is reduced by 2 mm. But all the other dimensions, like the stator yoke thickness, stay the same. That's to say, the outer diameter of lamination is reduced of 4 mm, leaving space for the toroidal winding outside the stator yoke. This can achieve the same envelope dimension as CSRM. Figure 5.5 shows the changes in 2D.

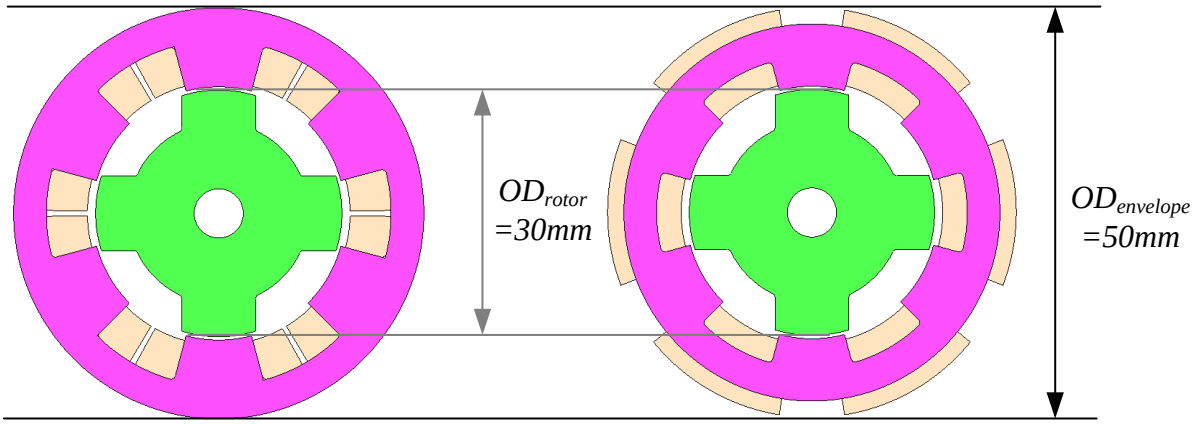

Figure 5.5. Geometry comparison between CSRM and resized SLTSRM.

Because the stator pole height is reduced, the slot area is reduced. As a sequence, it leads the filling factor will increase if the same conductor cross-sectional area is kept, resulting in difficulties during manufacturing. Even though the achievable filling factor of TSRMs should be higher, considering the manufacturing process that toroidal winding doesn't need any specific space between the poles for the winding tool to go through. To make the comparison consistent, the same filling factor will be maintained which requires lower conductor cross-sectional area. The winding parameters of CSRM and SLTSRMs are presented and compared in Table 5-IV. Because the slot area is reduced in the resized SLTSRM, it is using fewer strands. As a sequence, the filling factors of these three machines are almost the same. Moreover, the resized SLTSRM has phase resistance in between CSRM and original SLTSRM.

Table 5-IV Winding specification comparison between CSRM and SLTSRMs.

	CSRM	SLTSRM	Resized SLTSRM
Location	Stator pole	Stator yoke	Stator yoke
Number of turns per coil	6	6	6
AWG#	16	13	15
Filling factor	30.6%	30.6%	30.3%
Phase resistance	0.0227Ω	0.0108Ω	0.0153Ω

In Table 5-V, it summarizes volume and mess difference of active parts. The weight comparison shows that the three machines are sharing the same rotor. The original SLTSRM almost double the copper weight of CSRM. But this is improved via fewer strands in the resized SLTSRM. Moreover, resized SLTSRM is lighter than the CSRM because of its smaller stator lamination. The resized stator also makes the TSRM have the same envelope OD as the CSRM.

It concludes the stator resizing achieves the same envelope dimension between CSRM and TSRM. Moreover, TSRM is about 55g lighter than CSRM because of the resizing of stator lamination.

Table 5-V Size and mess comparison between CSRM and SLTSRMs.

	CSRM	SLTSRM	Resized SLTSRM
Stator OD (mm)	50	50	46
Envelope OD (mm)	50	54	50
Rotor lamination(g)	186.0	186.0	186.0
Stator lamination(g)	334.6	334.6	269.2
Copper(g)	52.1	98.6	62.5
Total mess(g)	572.7	619.2	517.7

5.4. Static Characterization.

As discussed in Chapter 2, TSRMs use all six coils wounded around stator yoke to generate an equivalent magnetic field as CSRM. To validate this, magnetic flux distribution at two typical rotor positions, aligned and unaligned commutation positions, is calculated via 2D FEA and compared in Figure 5.6.

During the static magnetic field check, Phase-A of CSRM is injected with constant DC current of 20A. For a consistent comparison, in both single-layer TSRMs, it only needs 14A, about two-third of 20A, to produce a similar field since all three phases, six coils contribute to flux generation. In Figure 5.6(c) to (d), Phase-A, Phase-B, and Phase-C are all with constant DC current of 14A. Agreeing with previously stated, all these high-speed machines are under unsaturation condition to avoid extremely high iron losses. It’s

seen that the two TSRMs generate all most the same magnetic field. The comparison between CSRM and TSRMs shows that TSRMs have relatively higher maximal flux density which indicated higher flux localization in TSRM. Thus, it will be more sensitive to saturation when currents are pushed higher. Moreover, TSRMs are at the risk of high iron losses. All the three machines have similar flux path at the aligned position, where their flux distribution is similar to each other. However, because of the decentralization of the magneto-motive force in TSRMs, it has more flux leakage. This is especially obvious at the unaligned position as shown in Figure 5.6.

However, because of the cancellation function of those flux leakage in TSRM, their influence on torque production is very little, as shown in Figure 5.7. It shows all the three machines generate almost the same static torque at every rotor position, but with different DC current and different magneto-motive force distribution. It also shows that the static torque can reach 0.03Nm at its peak. The static torque has a period of 90 degrees. In the region between 60 degree and 80 degree, the static torque variation is very small; this is a good feature for torque ripple control during the dynamic drive.

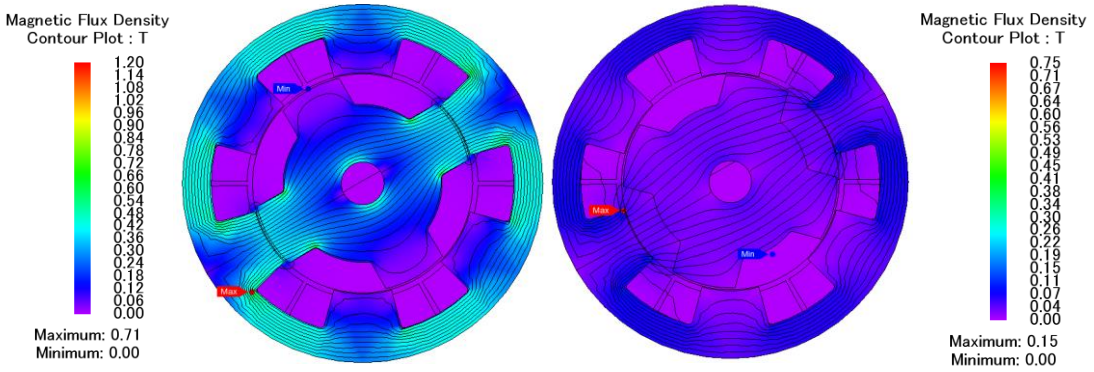

(a) (b)

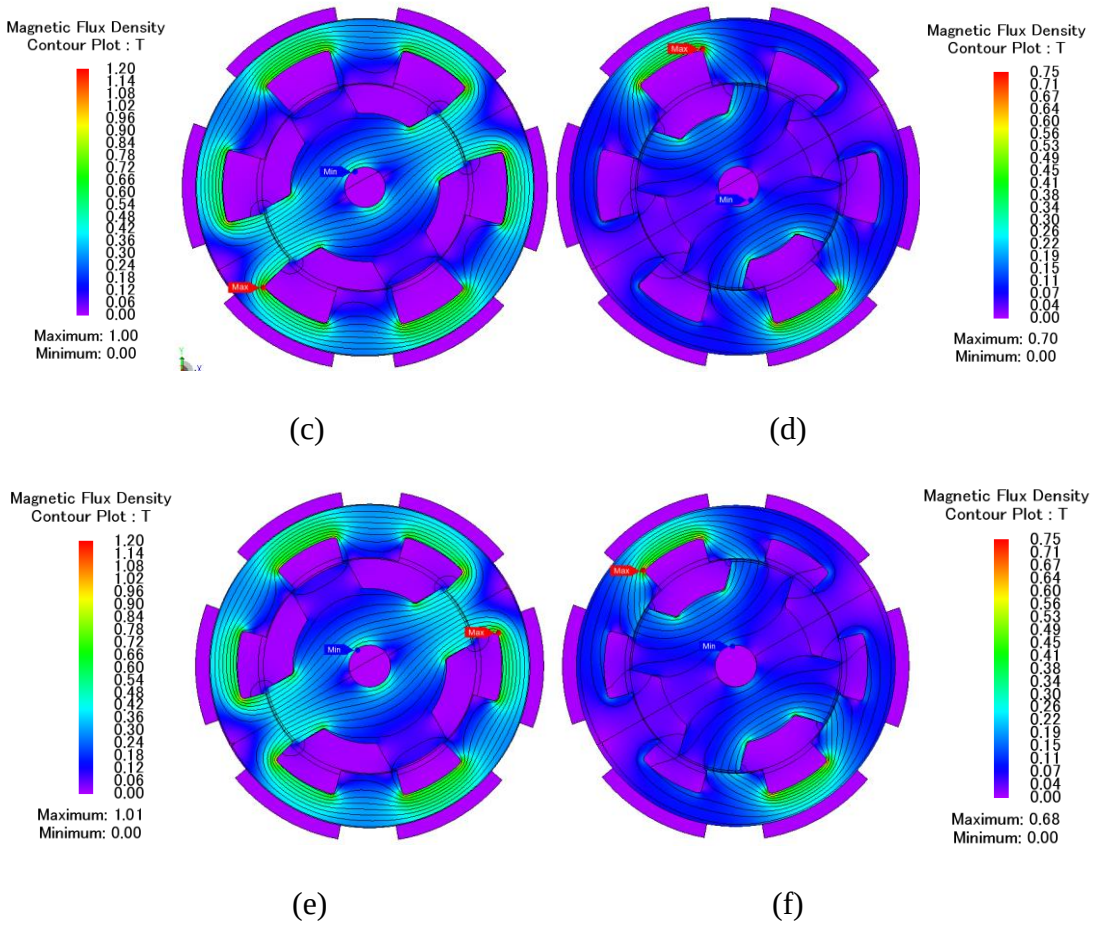

Figure 5.6. Magnetic flux distribution at aligned and unaligned position in the three 6-4 SRMs: (a) CSRM at aligned position, (b) CSRM at unaligned position, (c) original TSRM at aligned position, (d) original TSRM at unaligned position, (e) resized TSRM at aligned position, (f) resized TSRM at unaligned position.

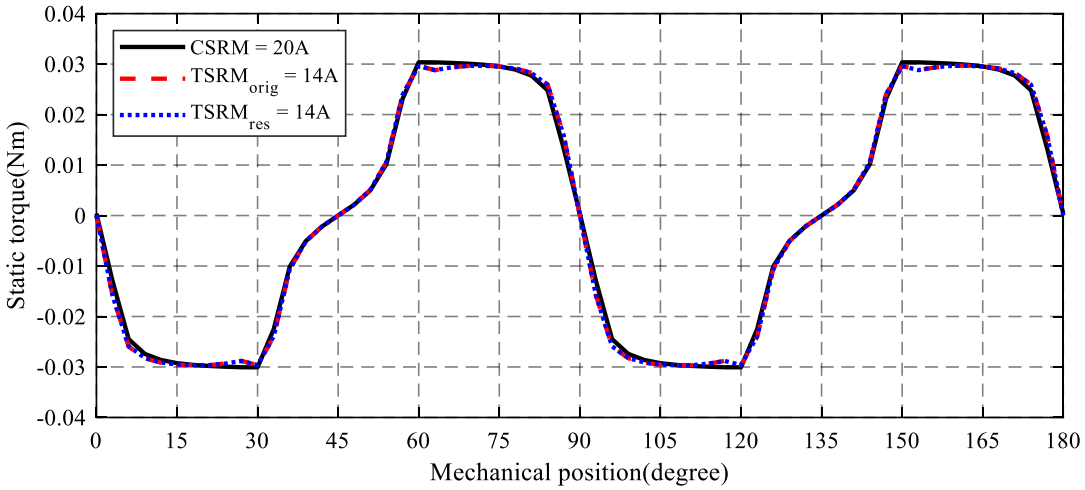

Figure 5.7. Static torque comparison among the three 6-4 SRMs.

Another importance characterization is the inductance profiles of all the three machines, as stated in Figure 5.8. It clearly shows that the stator pole height reduction doesn't have any down-effect on its electromagnetic performance. The two TSRMs share almost the same inductance profiles, but different phase resistance indicated in Table 5-IV. That's to say, if copper losses are not considered, the two TSRM will generate exactly the same output performance, including output torque as well as dynamic current response. However, this assumption will barely be true since copper losses always play one of the most important roles in machine design and drive. It shows mutual inductance is almost constant of zero in CSRM. Oppositely, self-inductance in TSRM doesn't change much and maintains around 40mH. On the other hand, self-inductance of CSRM has about 80mH variation. But mutual-inductance slope of TSRM is only half that of CSRM. But both the two mutual inductances contribute to torque generation in TSRMs.

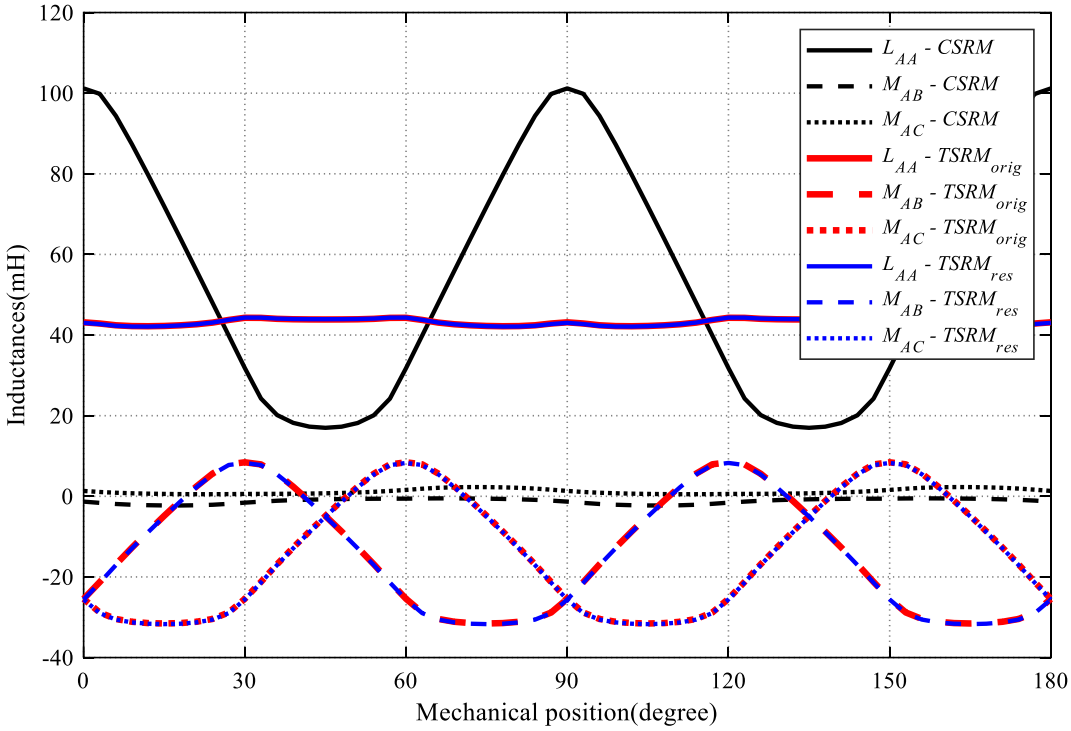

Figure 5.8. Inductance profiles of the three 6-4 SRMs.

5.5. Dynamic Analysis and Performance Comparison between CSRM and TSRMs.

5.5.1. Dynamic Simulation Modeling.

As known from Chapter 4, the commutation angle will affect the stator field significantly and, in a sequence, it affects motor output torque. In the meantime, those commutation angles are also related to the motor operating speed. The voltage forcing current variation is the difference between DC voltage and back EMF. A higher speed introduces significantly high back EMF, leading current change slows down. Therefore, to produce required torque, an advancing angle is usually needed for all the machines.

In order to efficiently study the commutation angle's effect on all three machines, and to obtain optimal commutation angle at a different speed, dynamic CSRM/TSRM MATLAB is built as Figure 5.9. Their inductance and torque profiles are generated via FEA for both CSRM and TSRMs. As stated in Section 0, all the three motors are under unsaturated condition, which means the look-up-tables are only dependent on position. Both the inductance and torque profiles are only 2-dimensional. However, in CSRM, only self-inductance is considered in the model, while in TSRMs, mutual-inductance and self-inductance all need to be taken into consideration. The same applied to torque look-up-tables.

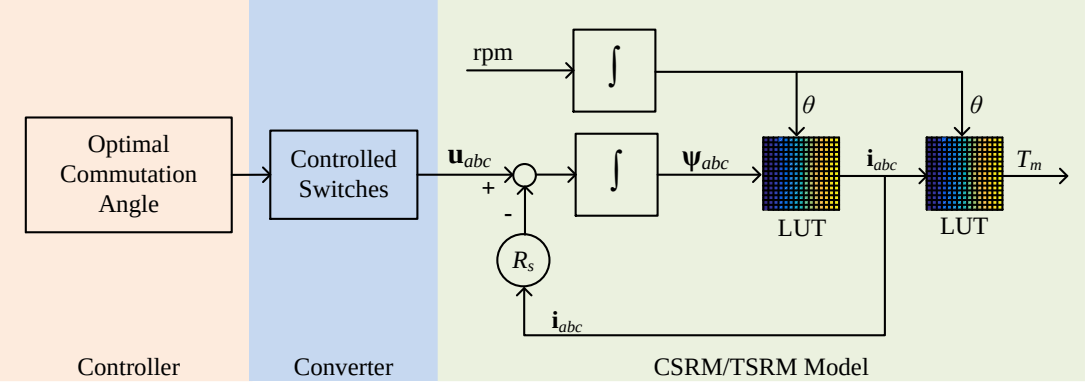

Figure 5.9. Diagram of the CSRM/TSRMs drive model.

As for the inverter models and control theories, they are both different between CSRM and TSRM. Figure 5.10 and Figure 5.11 state their different inverter topologies and current control sequences. Obviously, CSRM only needs six switches for this three-phase machine. However, because it requires an asymmetric inverter, which is not popular in the market, customizing this particular inverter usually requires more cost. The current

sequences show that CSRM usually has only one-phase conducted while TSRMs always have all three phases active. CSRM simply controls the active stator pole by activating/de-activating it associated phase. However, TSRM makes use of all three phases to produce a rotational magnetic field. The field changes status of its stator poles.

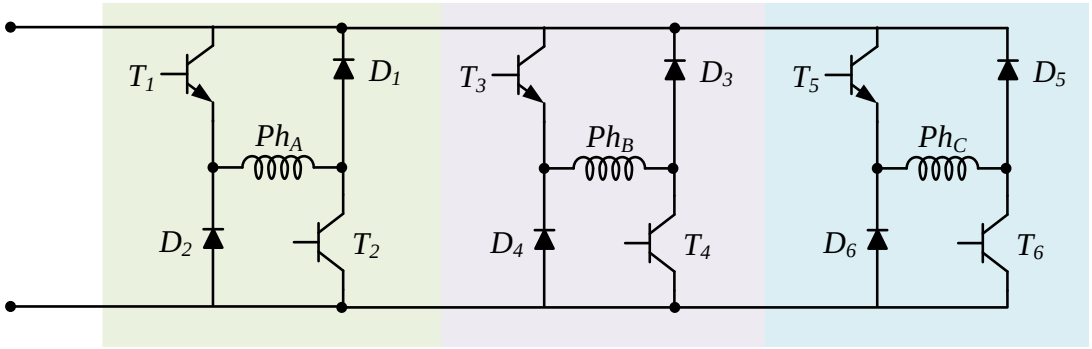

(a) Inverter

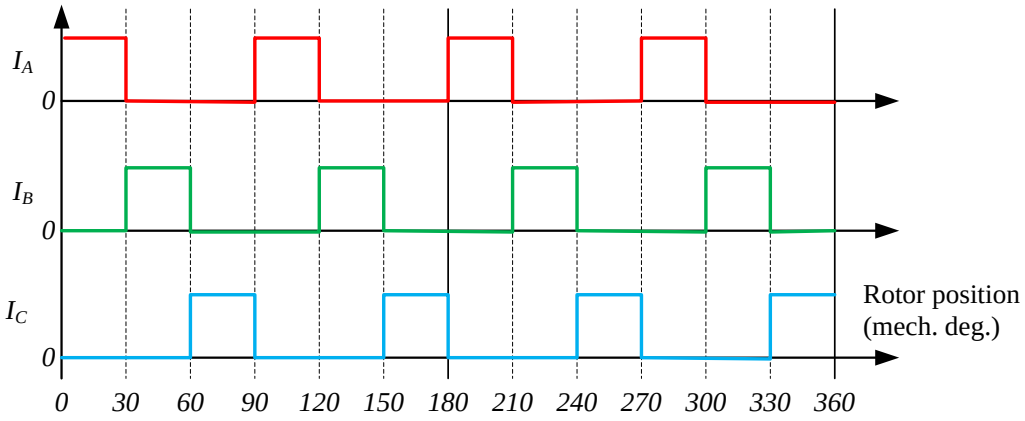

(b) Ideal current sequences

Figure 5.10. Inverters topology and current sequences of CSRM.

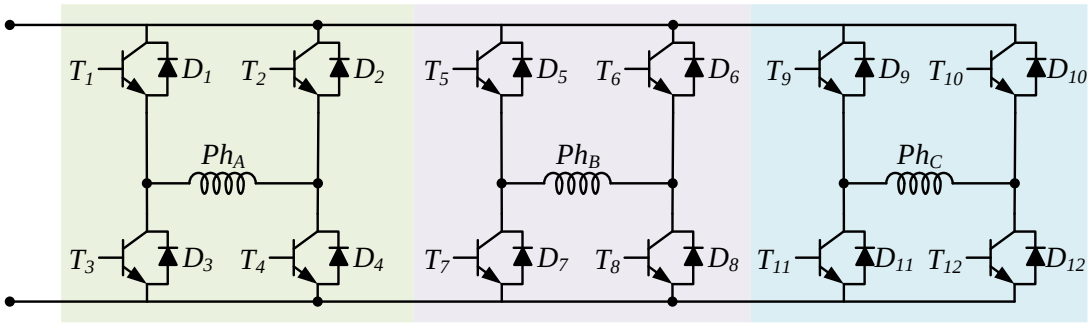

(a) Inverter

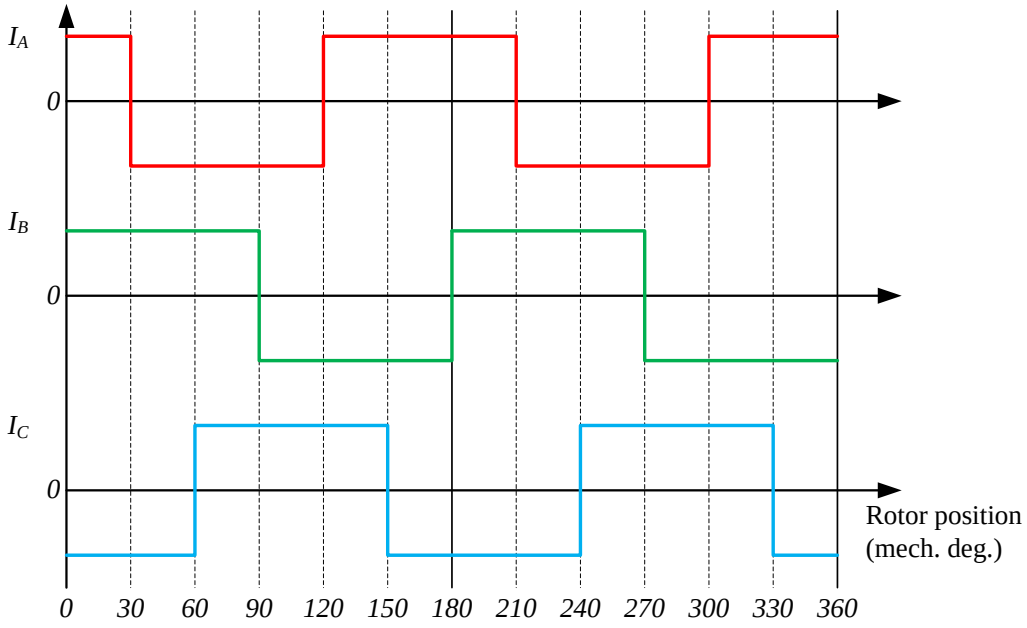

(b) Current sequences

Figure 5.11. Inverters topology and current sequences of TSRMs.

5.5.2. Optimization of Current Commutation Angles.

As indicated previously, the commutation angles need to be optimized at a different speed. Obviously, maximal torque is always preferred. However, in a certain condition, a higher average torque will be at the high expense of torque ripples and copper losses. In the

meantime, the requirement at different speed varies. It requires higher value for initial torque. Moreover, the system is more sensitive to torque ripple at lower speed, while copper losses are with larger threshold since the operation time for acceleration is usually short. Thus, the optimization problem has been divided into three speed regions as shown in Figure 5.12. The objectives of these three regions are listed below:

- region 1: maximize $T_{ave}/\Delta T$,
- region 2: maximize T_{ave}, but limiting $\Delta T < 200\%$,
- region 3: maximize T_{ave}, with no torque ripple limitation.

Average torque and torque ripple are defined in Equation 5-12 and Equation 5-13. In lower speed region from zero to 20,000 rpm, both average torque and torque ripple needs to be optimized. A higher average torque is needed for proper start, which the torque ripple needs to be minimized to avoid extra vibration. Thus, the objective is defined as the division of average torque and torque ripple. In the middle-speed region of 20,000 rpm to 50,000 rpm, the system is less sensitive to torque ripple, but extremely high ripple is still unacceptable. Therefore, in the region, the objective is to maximize average torque while in the meantime, limiting torque ripple within 200%. After speed of 50,000 rpm, the system only needs to achieve the maximal torque while torque ripple is not considered since its influence is even less in this speed region.

$$T_{ave} = \frac{1}{\theta_{cycle}} \int T(\theta) \cdot d\theta \qquad \text{Equation 5-12}$$

$$\Delta T = \frac{T_{\max} - T_{\min}}{T_{ave}} \times 100\% \qquad \text{Equation 5-13}$$

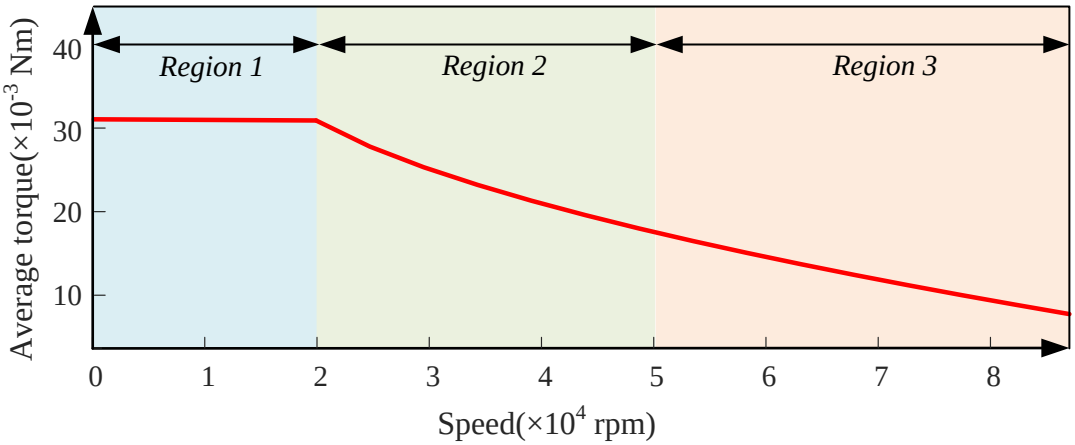

Figure 5.12. Optimization regions defined in the torque-speed curve.

Table 5-VI Optimization constraints of the torque-speed curve.

Parameters	Constraints
DC voltage	= 12V
Peak phase current	= 20A
Current band	= 1A
Current sample rate	= 1MHz
Switching frequency	= 100kHz
Maximal copper losses	<12W

The constraints for this optimization are limited by the inverter capability and system heat capability. They are listed in Table 5-VI for all three studied machines. The same constraints are applied for consistent comparison.

5.5.3. Dynamic Performance Comparisons.

The optimization results are presented and compared in Figure 5.13. Obviously, the original TSRM has the best torque performance at speed up to 50,000 rpm. This difference is more significant at a lower speed. Because in this region DC voltage is enough to control required current waveform for optimal torque, the output performance is more limited by the maximal bearable copper losses of 12W. As stated in Table 5-IV, the phase resistance ratio between CSRM, original TSRM and resized TSRM are *4:3:2*, the low-speed torque follows an inversed proportion ratio of *2:3:4*.

As the speed rises, the current dynamic response is limited by its voltage as well as the switching frequency. Because of the same boundary, the torque performance trends to be the same among each other at the speed of 60,000 rpm. After this speed, it seems CSRM has better output torque than both TSRMs. Because the self-inductance in TSRMs is relatively high but has a bare contribution to torque generation, this disadvantage becomes significant at higher speed.

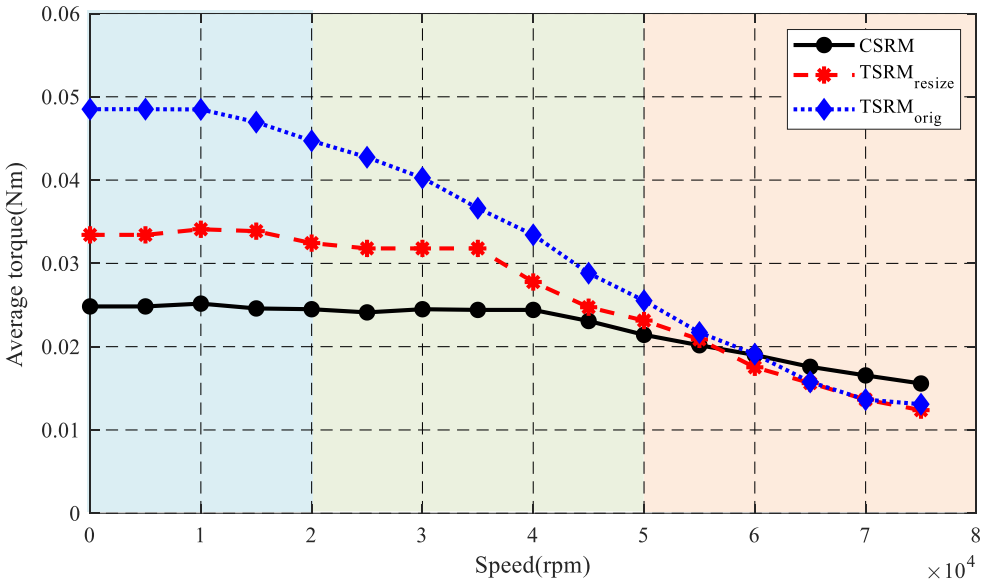

Figure 5.13. Optimization torque-speed curve comparison.

The performance at 10,000 rpm, 30,000 rpm, and 50,000 rpm are presented and compared in detail. The dynamic simulation models for CSRM and TSRMs are first validated via FEA. During the FEA validation, the same switch-controlled voltages are applied to the FEA windings. Its corresponding current and torque waveforms are compared against Matlab/Simulink results. All those dynamic simulation results are presented in Table

5-XIV to Table 5-IX, and Figure 5.14 to Figure 5.25, while their power distribution indicated in Figure 5.26.

Table 5-VII Dynamic performance comparison at 10,000 rpm.

	CSRM	Original TSRM	Resized TSRM
DC voltage(V)	12	12	12
Peak current(A)	20	20	17
Commutation angle (mech. deg.)	45 to 77	-24	-24
Average torque(mNm)	25.17	48.48	34.10
Torque ripple (%)	136.95	111.43	135.96
Copper losses (W)	11.66	11.15	11.21
Iron losses (W)	2.80	8.15	6.20
Motor efficiency (%)	64.57	72.46	67.22

The comparison in Table 5-VII shows all three motors produce about the same amount of copper losses, but output torques are at the ratio of 2:4:3 among CSRM, original TSRM and resized TSRM. In the meantime, the simulated iron losses are the lowest in CSRM. Both TSRMs produce more than twice iron losses than CSRM. However, as copper losses still dominate all the losses, the original TSRM still have the highest efficiency, followed by resized TSRM, and then CSRM.

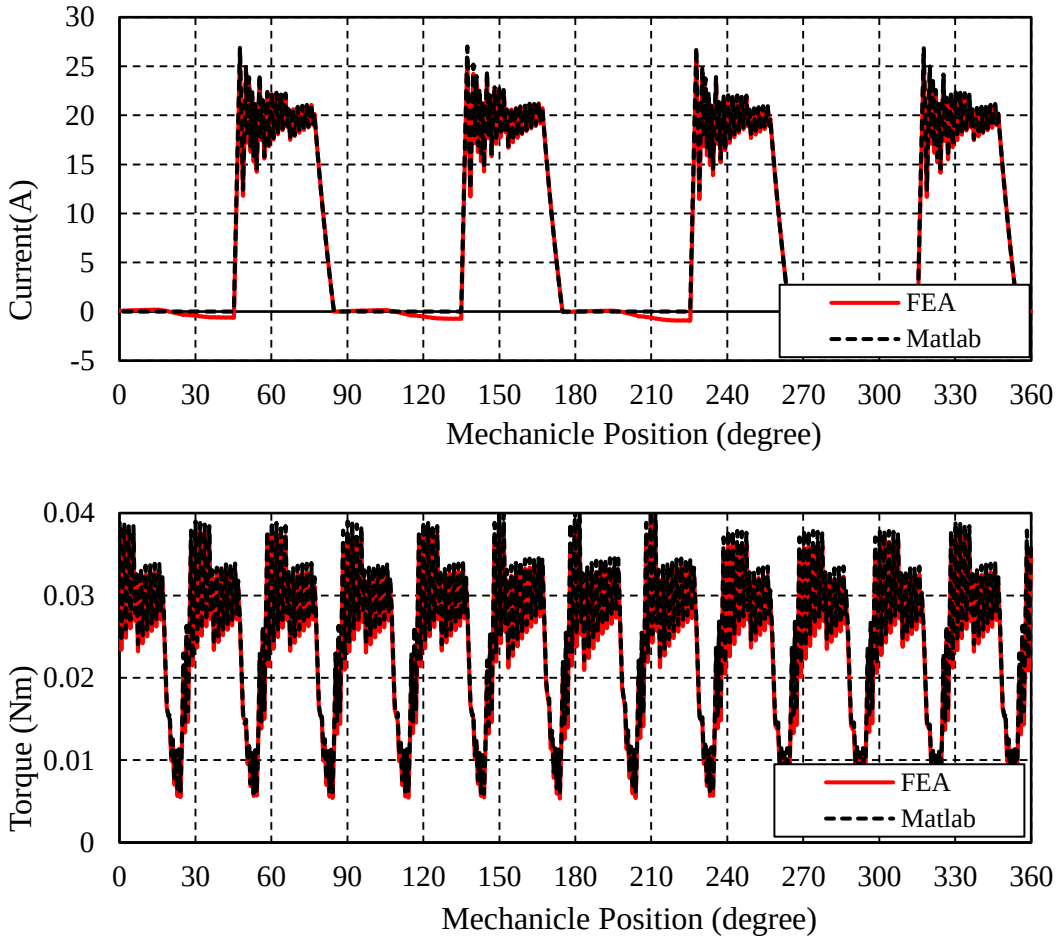

Figure 5.14. CSRM phase current and total torque waveform with optimal commutation angle at 10,000 rpm.

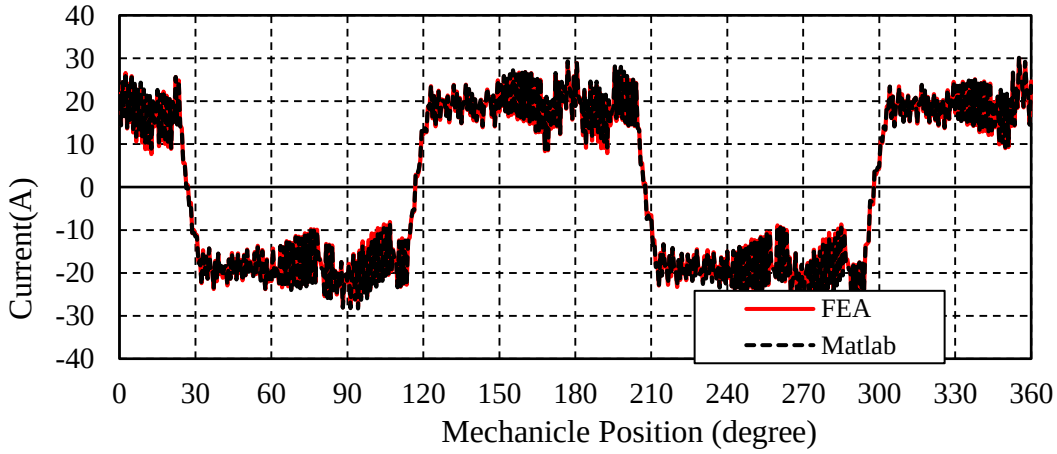

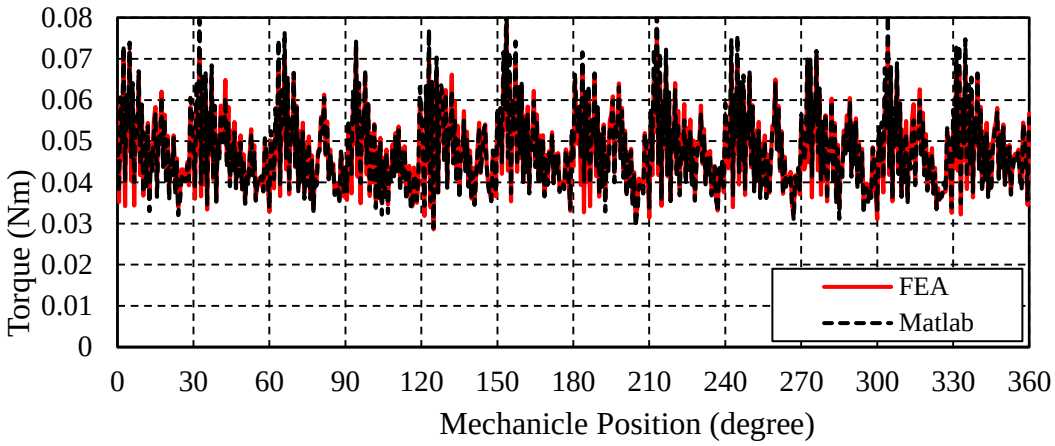

Figure 5.15. Original TSRM phase current and total torque waveform with optimal commutation angle at 10,000 rpm.

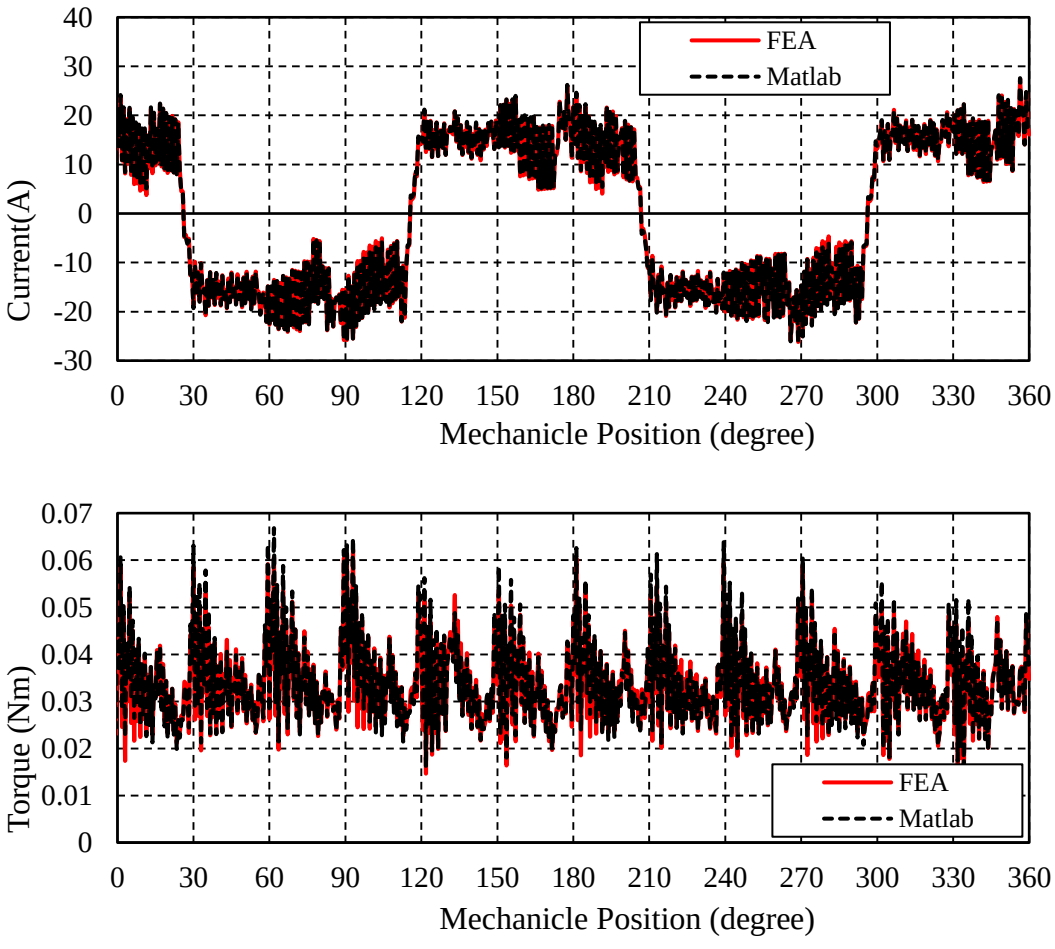

Figure 5.16. Resized TSRM phase current and total torque waveform with optimal commutation angle at 10,000 rpm.

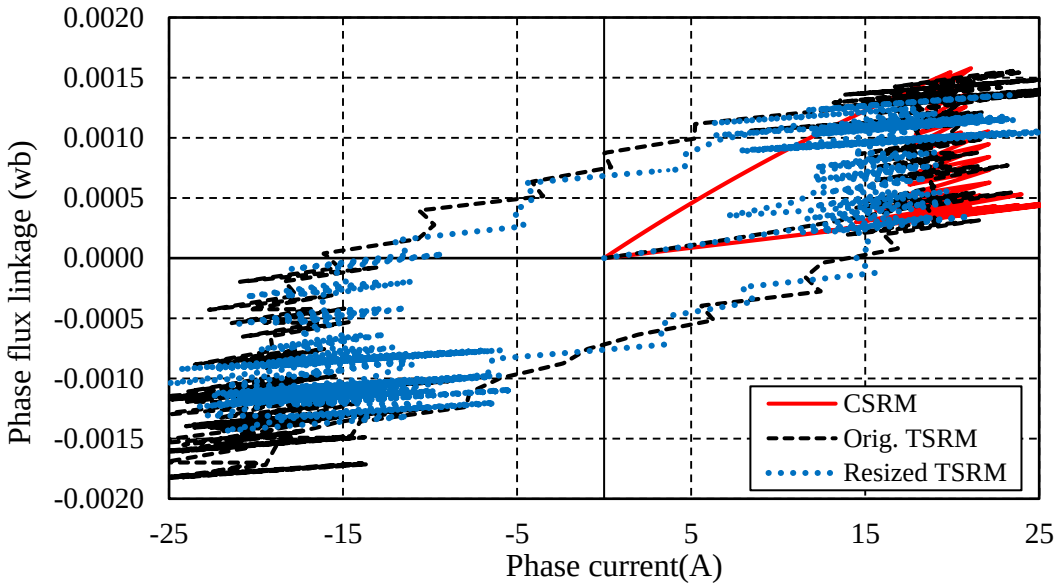

Figure 5.17. Phase flux linkage-current curves of each motor at speed of 10,000 rpm.

The dynamic current/torque waveforms show great agreement between FEA and Matlab/Simulink. This validates the Matlab/Simulink model accuracy. In the meantime, the current waveforms are all well controlled among the three machines at 10,000 rpm. It suggests that not only the DC voltage but also the switching frequency are plentiful. The energy conversion curves also indicate the higher energy conversion in TSRMs.

Table 5-VIII Dynamic performance comparison at 30,000 rpm.

	CSRM	Original TSRM	Resized TSRM
DC voltage(V)	12	12	12
Peak current(A)	20	20	17
Commutation angle (mech. deg.)	45 to 78	-11	-14
Average torque(Nm)	24.50	40.36	31.80
Torque ripple (%)	77.35	94.01	123.34
Copper losses (W)	11.74	10.18	10.53
Iron losses (W)	4.30	10.95	8.07
Motor efficiency (%)	82.75	85.72	84.30

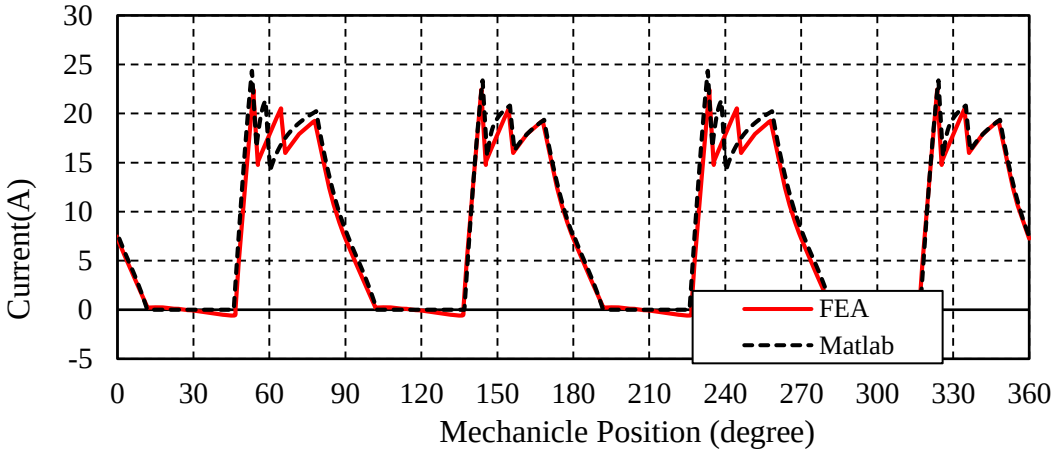

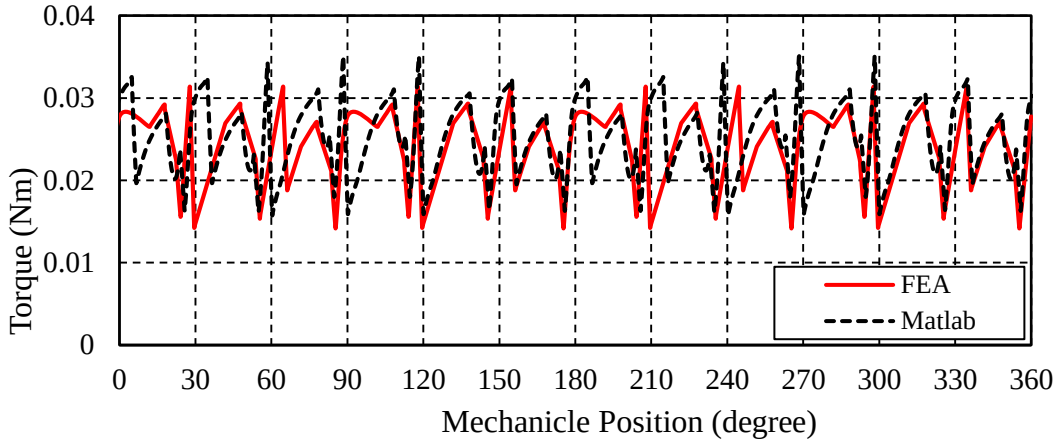

Figure 5.18. CSRM phase current and total torque waveform with optimal commutation angle at 30,000 rpm.

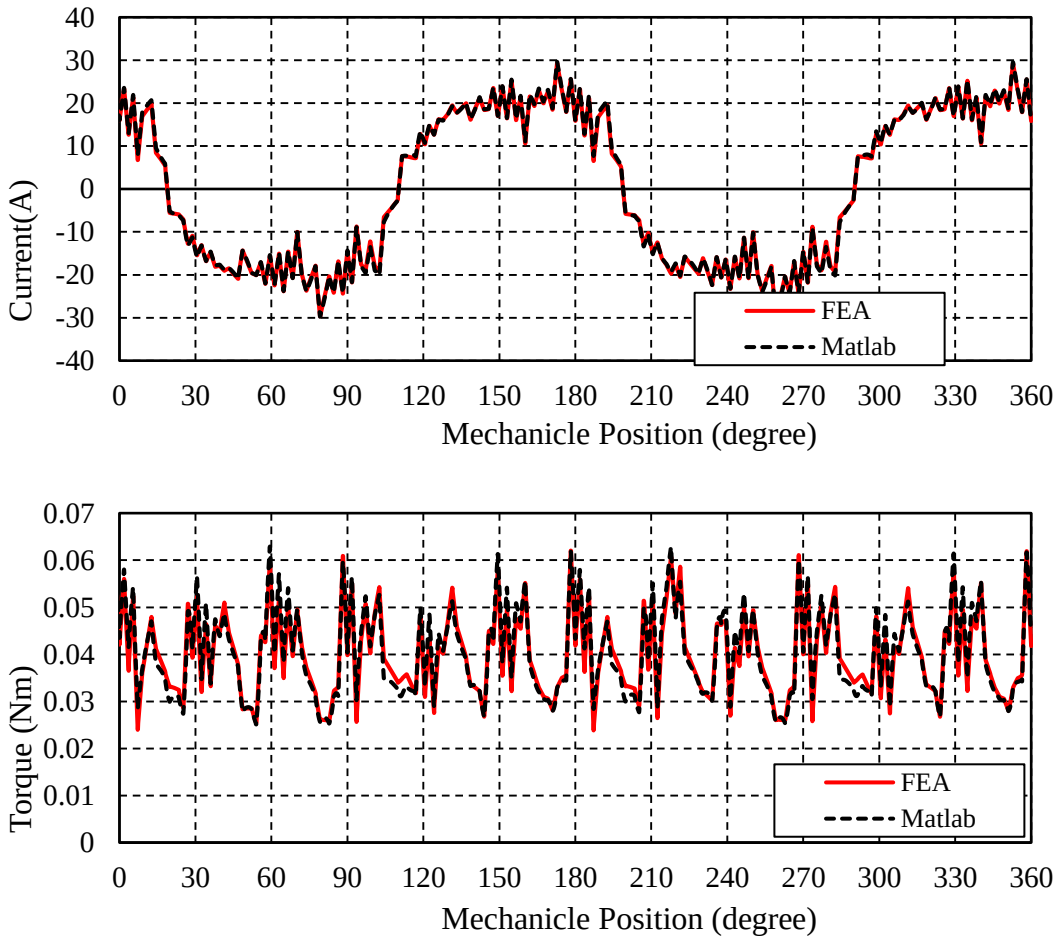

Figure 5.19. Original TSRM phase current and total torque waveform with optimal commutation angle at 30,000 rpm.

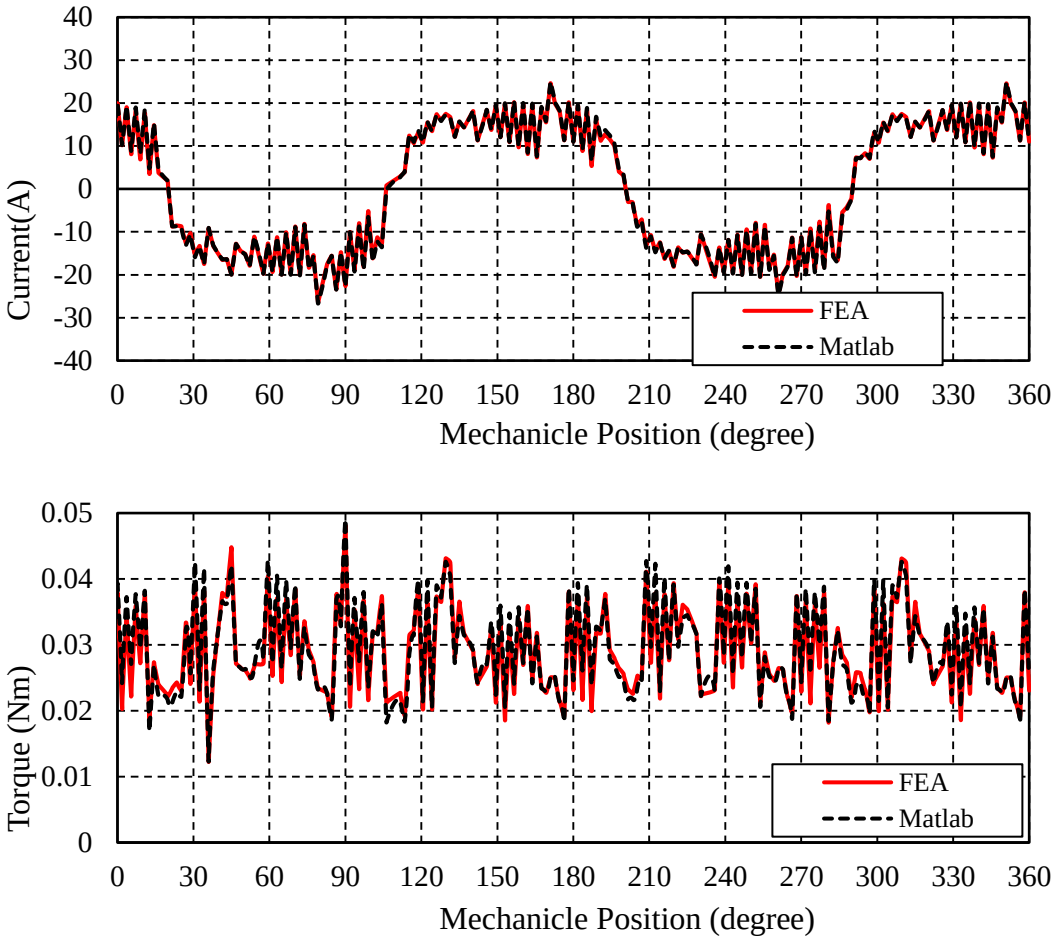

Figure 5.20. Resized TSRM phase current and total torque waveform with optimal commutation angle at 30,000 rpm.

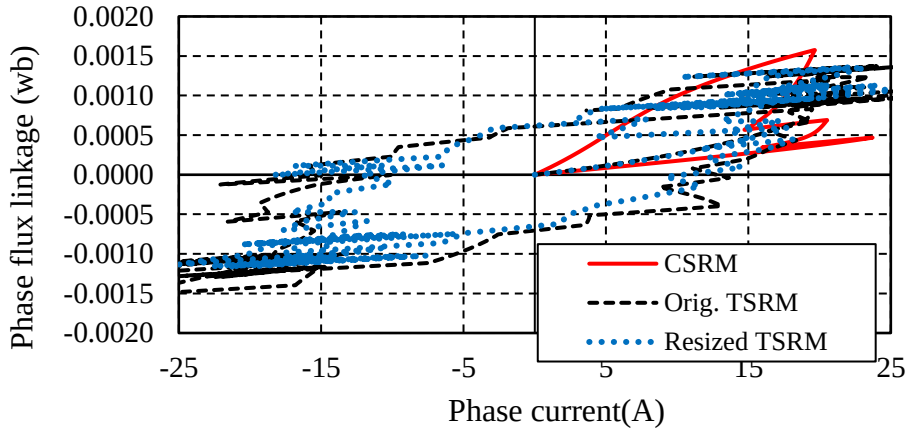

Figure 5.21. Phase flux linkage-current curves of each motor at a speed of 30,000 rpm.

The comparison in Table 5-VIII and Table 5-IX shows similar conclusions as Table 5-VII. However, it's noticed that both the two TSRMs have more torque drops compared with that at 10,000 rpm. It states that TSRMs are more sensitive with voltage supply at a higher speed. In the meantime, the iron losses also increase with the operation speed. Because of the limited switch frequency, the current waveform suffers higher ripples. So are the torque ripples. Additionally, there is a slightly higher error on the torque waveform comparison at higher speed. This is caused by that the torque estimation involves differential calculation which causes higher error at higher speed.

Table 5-IX Dynamic performance comparison at 50,000 rpm.

	CSRM	Original TSRM	Resized TSRM
DC voltage(V)	12	12	12
Peak current(A)	20	20	19
Commutation angle (mech. deg.)	38 to 85	-6	-6
Average torque(Nm)	21.42	25.52	24.05
Torque ripple (%)	77.41	167.17	141.83
Copper losses (W)	11.69	7.35	10.75
Iron losses (W)	8.51	13.69	11.01
Motor efficiency (%)	84.74	86.40	85.27

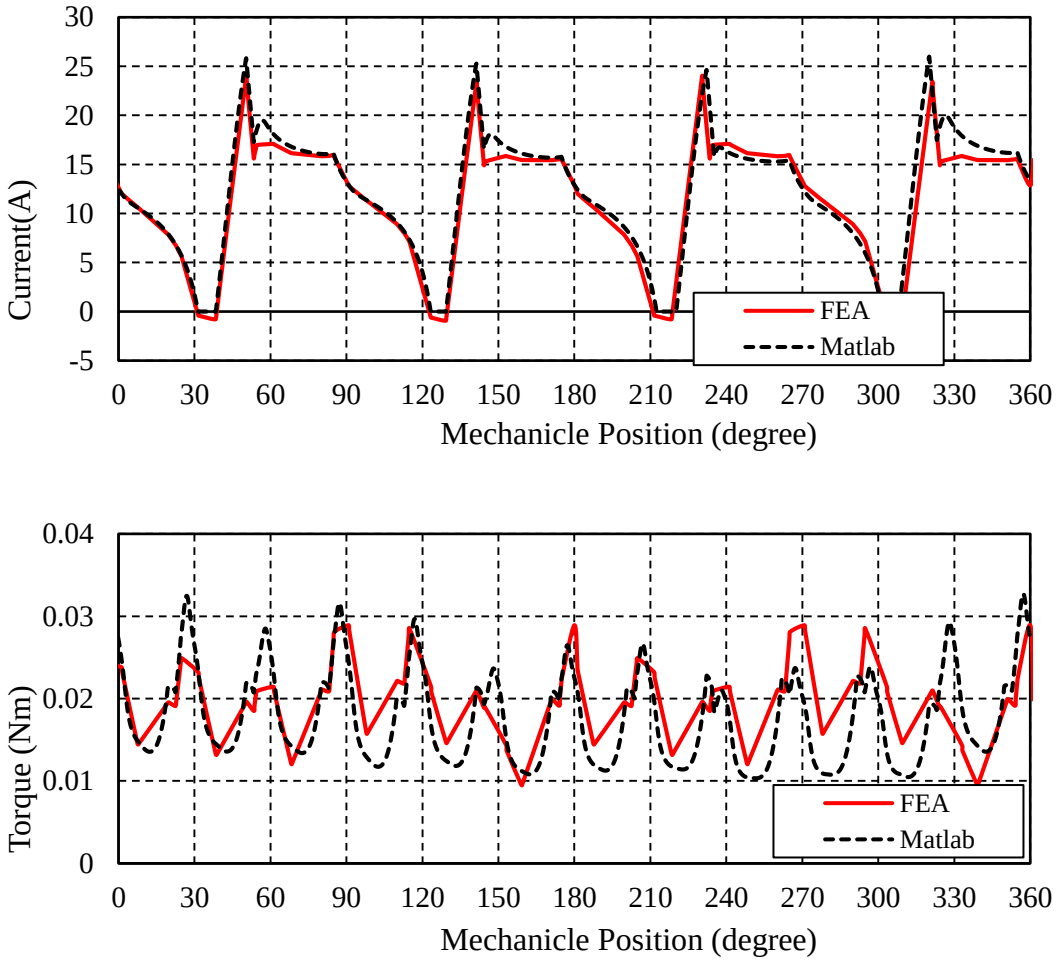

Figure 5.22. CSRM phase current and total torque waveform with optimal commutation angle at 50,000 rpm.

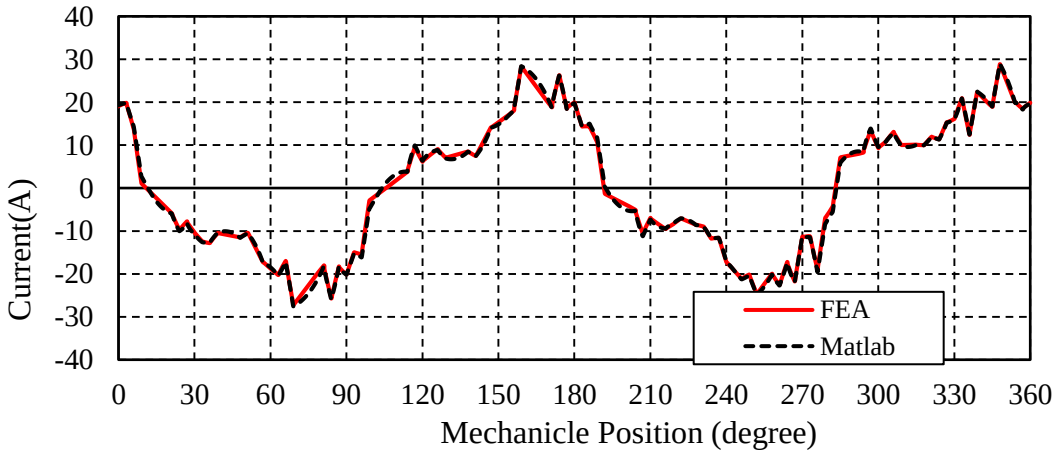

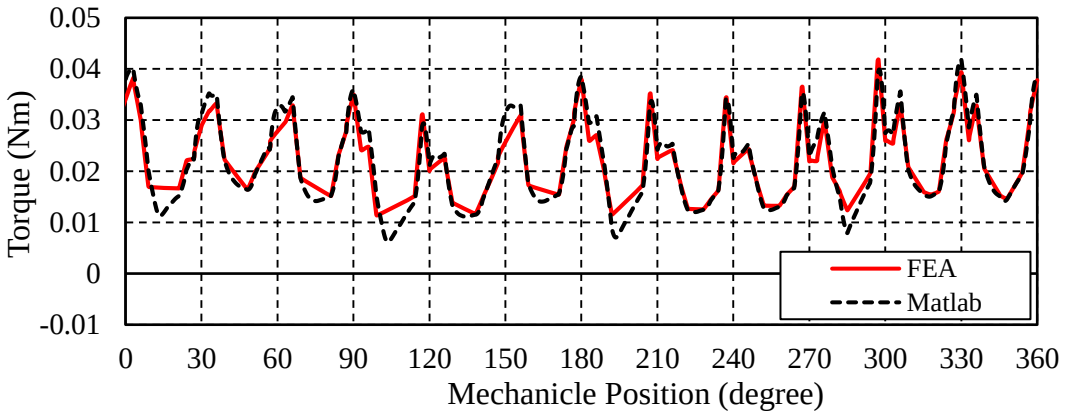

Figure 5.23. Original TSRM phase current and total torque waveform with optimal commutation angle at 50,000 rpm.

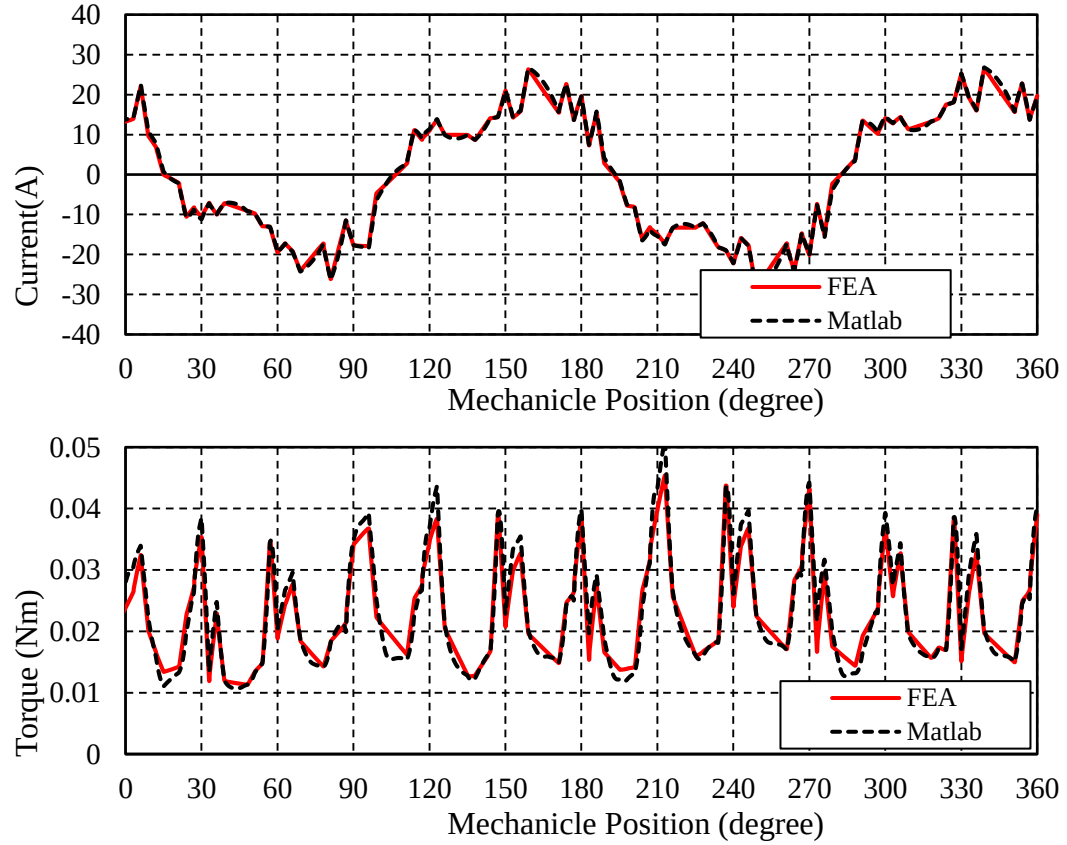

Figure 5.24. Resized TSRM phase current and total torque waveform with optimal commutation angle at 50,000 rpm.

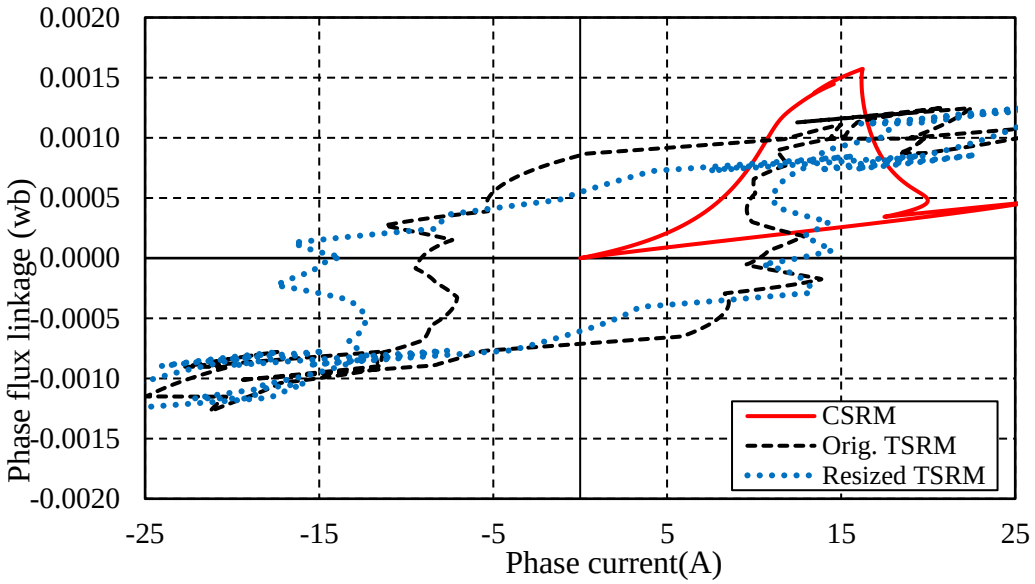

Figure 5.25. Phase flux linkage-current curves of each motor at a speed of 50,000 rpm.

At higher speed operation, the system control ability has been limited not only by DC bus voltage but also by the switching frequency. Thus, all the waveforms deviate from desired square shape. But all three machines are able to produce more than 0.02Nm up to 50,000 rpm with required boundary. The original TSRM has the best efficiency at 50,000 rpm of 86% benefitting from its relatively lower copper losses. Both resized TSRM and CSRM can reach the efficiency of 85% at 50,000 rpm based on the simulation results. The power distributions are stated in Figure 5.26. In the meantime, the power density is also compared in Table 5-X, which indicated the resized TSRM has about 24% improvement compared to CSRM.

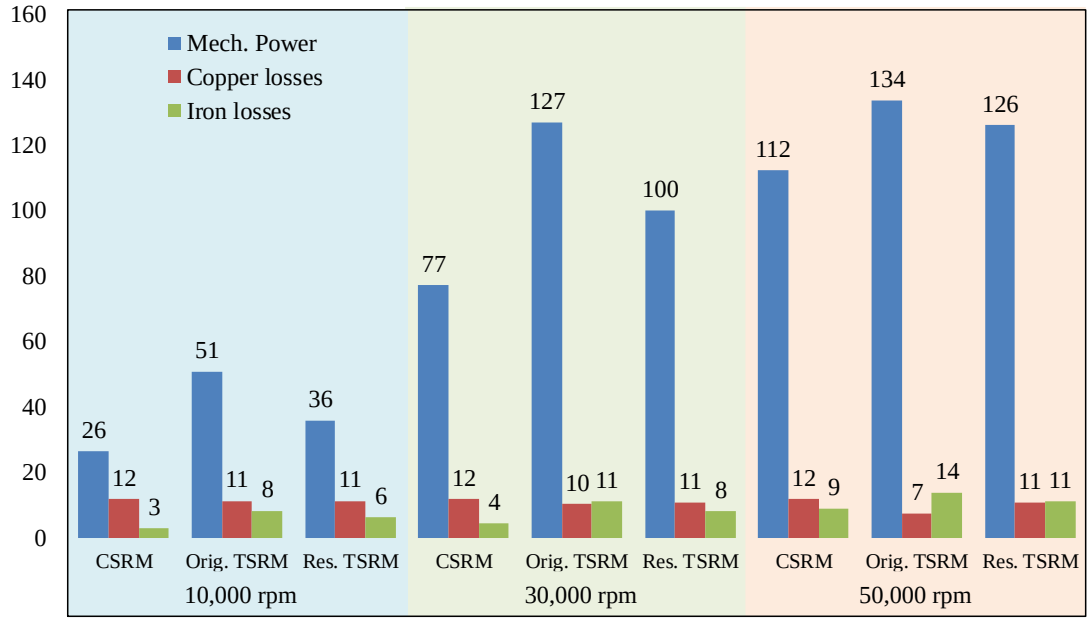

Figure 5.26. Power distribution among three machines iron losses distribution at different speeds.

Table 5-X Power density comparison at rated speed of 50,000 rpm.

	CSRM	Original TSRM	Resized TSRM
Maximal power (W)	112.2	133.6	125.9
Total mess(g)	572.7	619.2	517.7
Power Density (W/g)	0.196	0.216	0.243

5.6. Sinusoidal Current Control with Conventional Three-phase Half-Bridge Inverters.

In Section 5.5, both the TSRMs are controlled by 12-switch full-bridge inverter. In this section, conventional three-phase half-bridge inverter in Figure 5.27 will be applied on resized TSRMs. Its control performance will be evaluated against CSRM and resized TSRM with 12-switch full-bridge inverter.

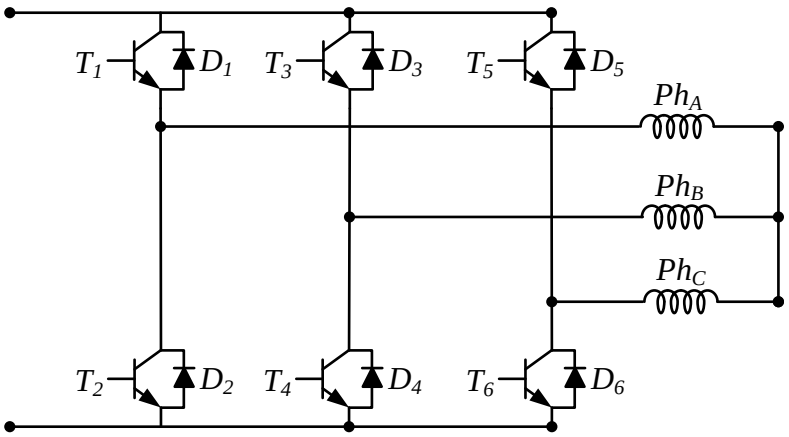

Figure 5.27. Conventional a three-phase half-bridge inverter for TSRMs.

5.6.1. Optimal Currents in Sinusoidal Waveforms.

As shown in Figure 5.8, the two TSRMs share the same inductance profiles. All the inductances of TSRMs are presented in Figure 5.28 for clarification. As presented, for the specific TSRM, its mutual inductance variation is significantly higher than the variation of its self-inductances. All the inductance waves have four periods during one mechanical cycle.

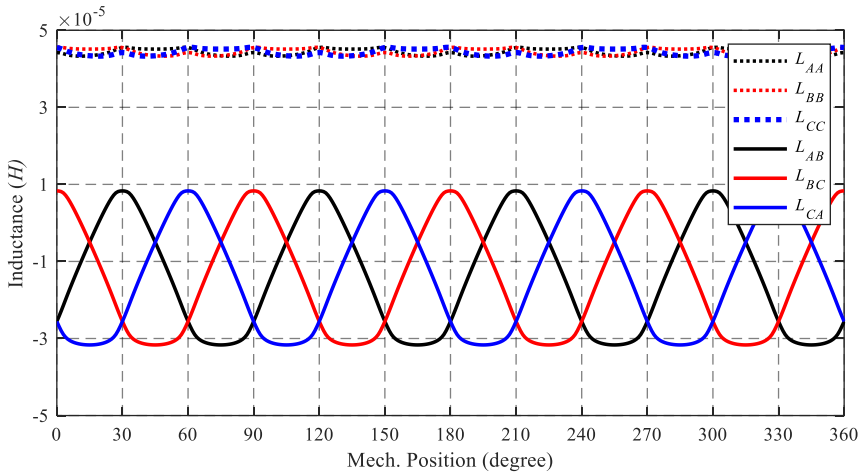

Figure 5.28. Self and mutual inductances of TSRMs.

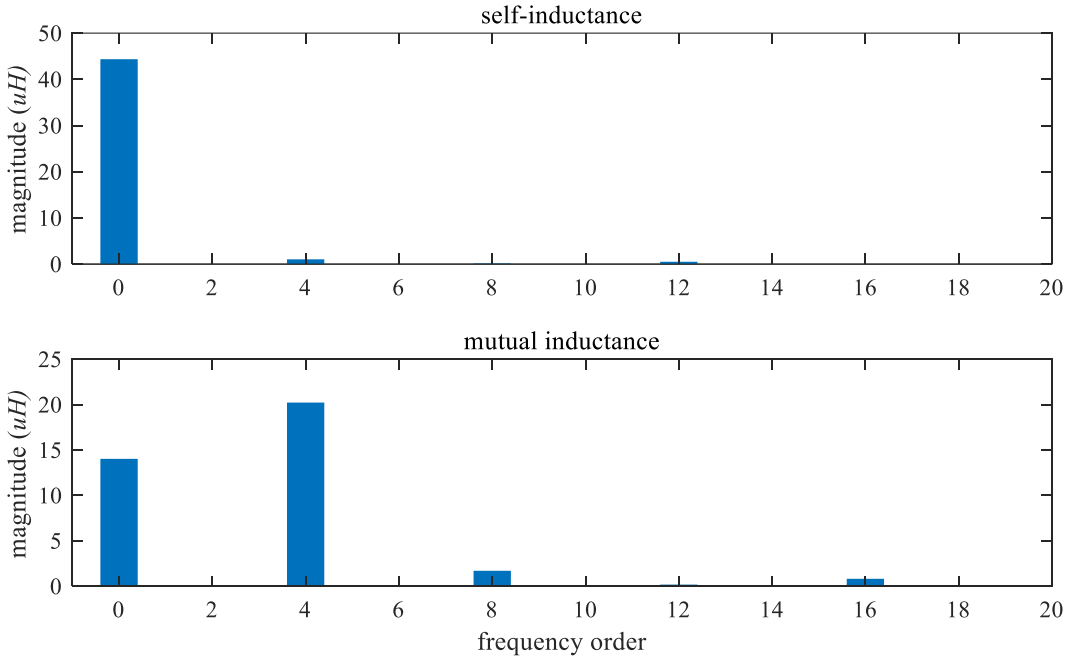

Figure 5.29. Fourier analysis of TSRM inductances.

Figure 5.29 shows the magnitude of each component after the FFT of both self-inductance and mutual-inductance. The base frequency (2.67 kHz) is the mechanical frequency for this 6-4 system at 50krpm. For the inductance waveforms converted into

Fourier series, it shows harmonics orders are only of multiples of four for this four-rotor pole system. Since the DC components don't contribute to torque generation, the FFT in Table 5-XI further proves that the mutual-inductance dominate its torque generation.

Table 5-XI TSRM inductances frequency distributions

Frequency Order	Magnitude(μH)	
	Self	Mutual
0	44.356	14.023
1	0.000	0.002
2	0.000	0.003
3	0.000	0.006
4	1.036	20.219
5	0.000	0.007
6	0.000	0.004
7	0.000	0.003
8	0.151	1.697

If ignoring the harmonics if their magnitude is lower than 2μH, the self-inductances and mutual inductances can be written as Equation 5-14.

$$\begin{cases} L_{AA} = L_{BB} = L_{CC} = L_0 \\ L_{AB} = M_0 + M_4 \cos\left(4\theta_m + \varphi\right) \\ L_{BC} = M_0 + M_4 \cos\left(4\theta_m + \varphi + 120°\right) \\ L_{AC} = M_0 + M_4 \cos\left(4\theta_m + \varphi - 120°\right) \end{cases} \quad \text{Equation 5-14}$$

where L_0 = 44.356μH, M_0 = -14.023μH, M_4 = -20.219μH and φ = 60 degree and θ_m is the mechanical position. The general torque Equation 2-25 in Chapter 2 can be simplified as Equation 5-15.

$$\begin{aligned} T_e &= \frac{1}{2}\left(\frac{\mathrm{d}L_a}{\mathrm{d}\theta_m} I_a^{\,2} + \frac{\mathrm{d}L_b}{\mathrm{d}\theta_m} I_a^{\,2} + \frac{\mathrm{d}L_c}{\mathrm{d}\theta_m} I_a^{\,2}\right) \\ &\quad + \frac{\mathrm{d}M_{ab}}{\mathrm{d}\theta_m} I_a I_b + \frac{\mathrm{d}M_{bc}}{\mathrm{d}\theta_m} I_b I_c + \frac{\mathrm{d}M_{ac}}{\mathrm{d}\theta_m} I_a I_c \\ &= \frac{\mathrm{d}M_{ab}}{\mathrm{d}\theta_m} I_a I_b + \frac{\mathrm{d}M_{bc}}{\mathrm{d}\theta_m} I_b I_c + \frac{\mathrm{d}M_{ac}}{\mathrm{d}\theta_m} I_a I_c \end{aligned}$$

Equation 5-15

$$\text{with} \begin{bmatrix} \frac{\mathrm{d}M_{ab}}{\mathrm{d}\theta_m} \\ \frac{\mathrm{d}M_{bc}}{\mathrm{d}\theta_m} \\ \frac{\mathrm{d}M_{ac}}{\mathrm{d}\theta_m} \end{bmatrix} = \begin{bmatrix} -4M_4 \sin\left(4\theta_m + \varphi\right) \\ -4M_4 \sin\left(4\theta_m + \varphi + 120°\right) \\ -4M_4 \sin\left(4\theta_m + \varphi - 120°\right) \end{bmatrix}.$$

For simplification, $\theta = 4\theta_m + \varphi$ is applied to the inductance profiles. The inductance will be shortened to Equation 5-16.

$$\begin{cases} L_{AA} = L_{BB} = L_{CC} = L_0 \\ L_{AB} = M_0 + M_4 \cos\theta \\ L_{BC} = M_0 + M_4 \cos\left(\theta + 120°\right) \\ L_{AC} = M_0 + M_4 \cos\left(\theta - 120°\right) \end{cases}$$

Equation 5-16

To be able to make the time-dependent inductance to a constant value for easier analysis, Park transformation is applied with Park's matrix shown in Equation 5-17.

$$K = \frac{2}{3}\begin{bmatrix} \cos\theta & \cos\left(\theta + 120°\right) & \cos\left(\theta - 120°\right) \\ -\sin\theta & -\sin\left(\theta + 120°\right) & -\sin\left(\theta - 120°\right) \\ \frac{1}{2} & \frac{1}{2} & \frac{1}{2} \end{bmatrix}$$

Equation 5-17

$$K^{-1} = \begin{bmatrix} \cos\theta & -\sin\theta & 1 \\ \cos(\theta + 120°) & -\sin(\theta + 120°) & 1 \\ \cos(\theta - 120°) & -\sin(\theta - 120°) & 1 \end{bmatrix}$$

$$T_e = \begin{bmatrix} \frac{dM_{ab}}{d\theta_m} \\ \frac{dM_{bc}}{d\theta_m} \\ \frac{dM_{ac}}{d\theta_m} \end{bmatrix}^T \begin{bmatrix} I_a I_b & I_b I_c & I_c I_a \end{bmatrix}^T$$

$$= \left(K^{-1} K \begin{bmatrix} \frac{dM_{ab}}{d\theta_m} \\ \frac{dM_{bc}}{d\theta_m} \\ \frac{dM_{ac}}{d\theta_m} \end{bmatrix} \right)^T \begin{bmatrix} I_a I_b & I_b I_c & I_c I_a \end{bmatrix}^T \qquad \text{Equation 5-18}$$

$$T_e = \left(K \begin{bmatrix} \frac{dM_{ab}}{d\theta_m} \\ \frac{dM_{bc}}{d\theta_m} \\ \frac{dM_{ac}}{d\theta_m} \end{bmatrix} \right)^T \left(\begin{bmatrix} I_a I_b & I_b I_c & I_c I_a \end{bmatrix} K^{-1} \right)^T \qquad \text{Equation 5-19}$$

$$T_e = \begin{bmatrix} L_d & L_q & L_0 \end{bmatrix} \cdot \left(\begin{bmatrix} I_a I_b & I_b I_c & I_c I_a \end{bmatrix} K^{-1} \right)^T \qquad \text{Equation 5-20}$$

where $\begin{cases} L_d = 0 \\ L_q = 4M_4 = -80.88 \times 10^{-6} \\ L_0 = 0 \end{cases}$.

If the translated current products are assigned to x, y, and z, only y contribute to torque generation in this analysis.

$$\begin{bmatrix} x \\ y \\ z \end{bmatrix} = \begin{bmatrix} I_a I_b & I_b I_c & I_c I_a \end{bmatrix} K^{-1} \qquad \text{Equation 5-21}$$

$$y = -I_a I_b \sin\theta - I_b I_c \sin(\theta + 120°) - I_c I_a \sin(\theta - 120°) \qquad \text{Equation 5-22}$$

$$T_e = -L_q \left(I_a I_b \sin\theta + I_b I_c \sin(\theta + 120°) + I_c I_a \sin(\theta - 120°) \right) \qquad \text{Equation 5-23}$$

Obviously, the optimal current should generate maximal and constant T_e with the least copper losses. The optimization becomes to maximize the following equation which the restrains that I_a, I_b, and I_c are 120 electrical degree shifted as shown Equation 5-24. $\theta_e = 2\theta_m$ for this two-pole-pair machine.

$$\max: \quad \frac{T_e}{-L_q \left(I_a^{\,2} + I_b^{\,2} + I_c^{\,2} \right)} = \frac{\left(I_a I_b \sin\theta + I_b I_c \sin(\theta + 120°) + I_c I_a \sin(\theta - 120°) \right)}{I_a^{\,2} + I_b^{\,2} + I_c^{\,2}} \qquad \text{Equation 5-24}$$

$$\textit{with} \quad \begin{cases} I_a = f(\theta_e) \\ I_b = f(\theta_e - 120°) \\ I_c = f(\theta_e + 120°) \end{cases}$$

Superimposition could be applied to this system since nonlinearity is not considered in the inductances of this machine. $f(\theta_e)$ could be expressed in the Fourier series as Equation 5-25.

$$f(\theta_e) = \frac{A_0}{2} + \sum_{n=1}^{\infty}\left[A_n \sin(n\theta_e + \phi_n)\right] \qquad \text{Equation 5-25}$$

Trigonometry theories indicate that only current in the frequency of second-order will contribute to torque generation. The optimal phase current sequence should be

$$\begin{bmatrix} I_{peak}\cos(2\theta_m + 45°) \\ I_{peak}\cos(2\theta_m + 45° - 120°) \\ I_{peak}\cos(2\theta_m + 45° + 120°) \end{bmatrix} \qquad \text{Equation 5-26}$$

The maximal ideal average torque can be by Equation 5-27 with M_4 = -20.219×10^{-6}.

$$T_{\max} = -\frac{3}{4}L_q I_{peak}^2 = -3M_4 I_{peak}^2 \qquad \text{Equation 5-27}$$

For the same RMS current of 20A, the ideal optimal current waveforms are presented in Figure 5.30. Its analytical torque is compared with Matlab simulation in Table 5-XII and Figure 5.31. It shows that the simplified analytical model considers only the fourth-order component in the inductance variation. It gives an accurate estimation of average torque. But it loses the information of torque ripples.

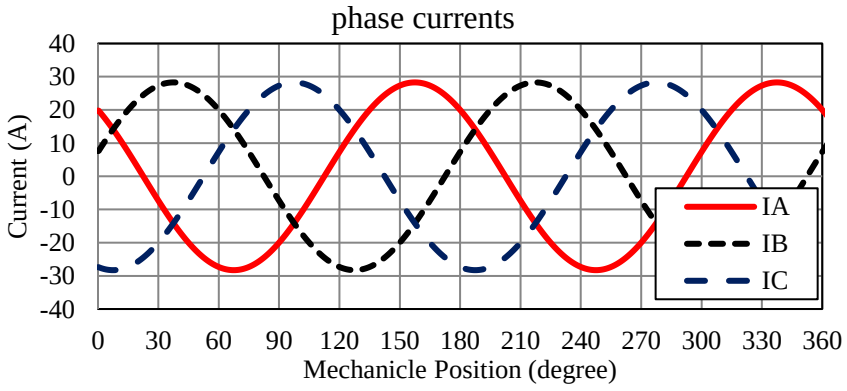

Figure 5.30. Ideal optimal sinusoidal phase currents for TSRMs.

Table 5-XII TSRM torque comparison with optimal sinusoidal phase currents.

	Analytical Model	Matlab Model
Average Torque(Nm)	0.0485	0.0473
Torque Ripples (%)	0	37.22

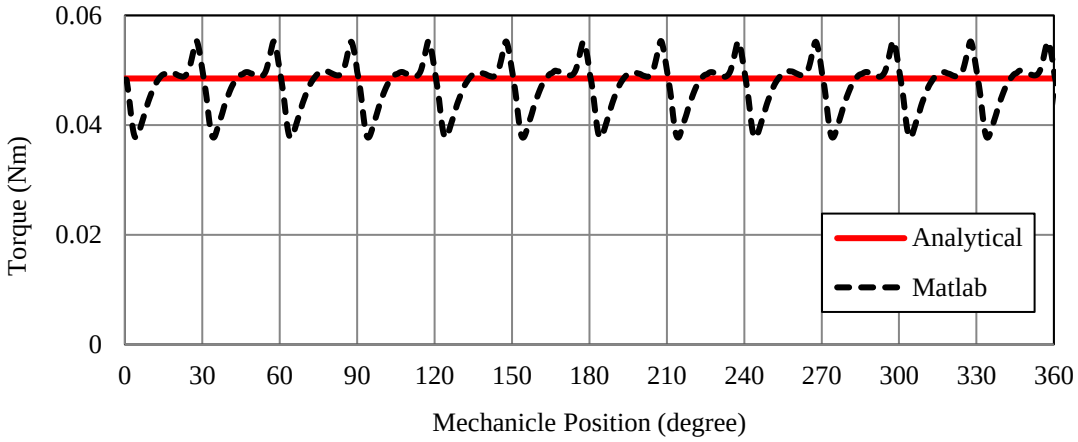

Figure 5.31. TSRM torque waveform comparison with optimal sinusoidal phase currents.

5.6.2. Hysteresis and SVPWM current control.

Hysteresis control is one of the most popular current control schemes, which has a fast dynamic response and model independency. However, it suffers from variable switching frequency and high sampling frequency. And, Hysteresis control also introduces extra torque ripple and acoustical noise because of the current chopping.

Voltage source inverters with pulse width modulation (SVPWM) are also widely spread in systems of electrical and electromechanical energy conversion. It overcomes hysteresis control's drawbacks. Its fixed switching frequency also makes electromagnetic interference filter design easier. Properly choosing its switching frequency can avoid the

SRM natural resonate frequency, which is essentially important for noise reduction in SRM development.

The dynamic performance of the resized TSRM will be studied and compared with these two control schemes in the section at a different speed.

As for the half-bridge inverter, there is a conversion between the line to line voltage and actual phase voltage. In the meantime, it concludes that the DC bus voltage demand with three-phase half-bridge inverter should be $\sqrt{3}$ time that of the 12-switch full-bridge one. Thus, DC bus voltage is modification based on this conversion. All simulation follows the constraints in Table 5-XIII.

Table 5-XIII Constraints of the Hysteresis and SVPWM controls in simulation.

DC voltage	=21V
Peak phase current	=24A
Current band	=1A
Simulation sample rate	=1MHz
Switching frequency	100kHz

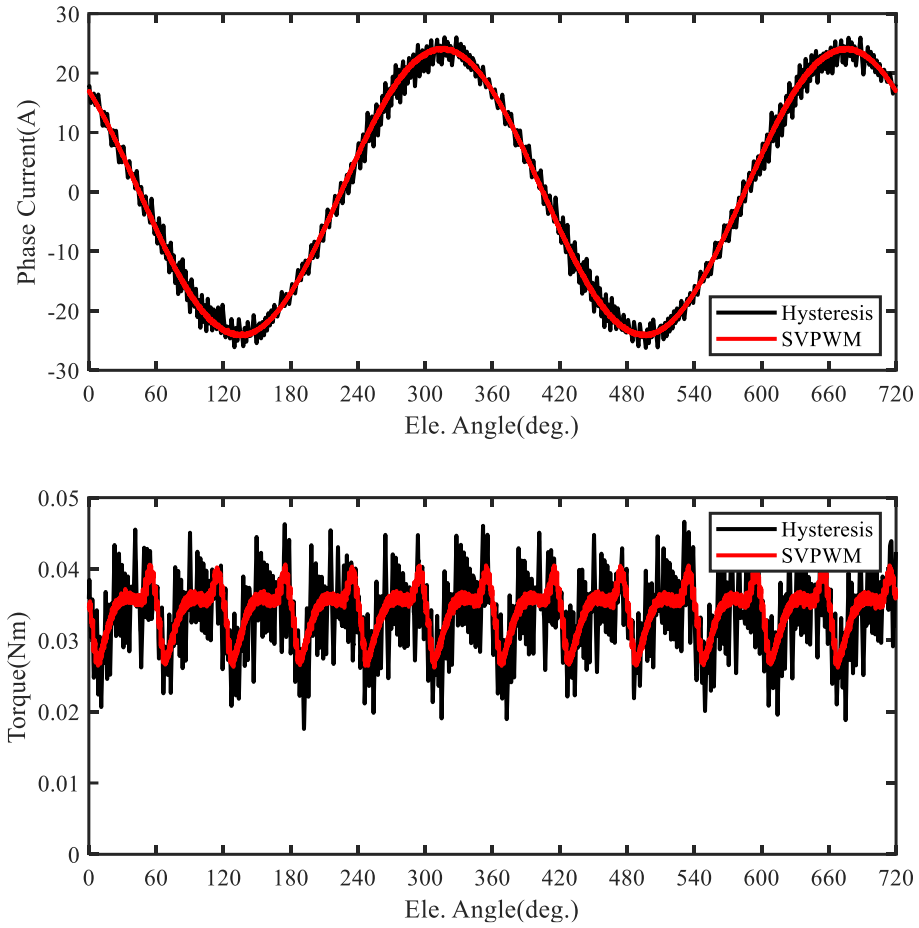

Figure 5.32. Resized TSRM phase current and torque waveform comparison at 10,000 rpm.

Both hysteresis control and SVPWM works well on the TSRMs at 10,000 rpm. As can be seen in the current waveforms in Figure 5.32, the current is very sinusoidal despite the switching ripples. It also indicates that hysteresis control has larger current ripples at lower speed which brings higher torque ripples.

Resized TSRM controlled by the half-bridge inverter is compared against CSRM and resized TSRM with the full-bridge inverter. A higher DC bus voltage and higher peak phase current are needed. In the meantime, sinusoidal current control has lower torque

ripples and lower iron losses than full-bridge inverter controlled TSRM as shown in Table 5-XIV.

Table 5-XIV Dynamic performance comparison at 10,000 rpm.

	CSRM	Resized TSRM		
Inverter/Controller	Asymetrix	Full-bridge	Hysteresis	SVPWM
DC voltage(V)	12	12	21	21
Peak current(A)	20	17	24	24
Control Angle	Commutation angle (mech. deg.)		Advance Angle (ele. deg.)	
	45 to 77	-24	45	
Average torque(mNm)	25.17	34.10	33.46	34.21
Torque ripple (%)	136.95	135.96	85.79	42.30
Copper losses (W)	11.66	11.21	13.01	13.28
Iron losses (W)	2.80	6.20	2.91	1.58
Motor efficiency (%)	64.57	67.22	68.76	70.68

*All the iron losses are estimated by FEA based on simulation phase currents.

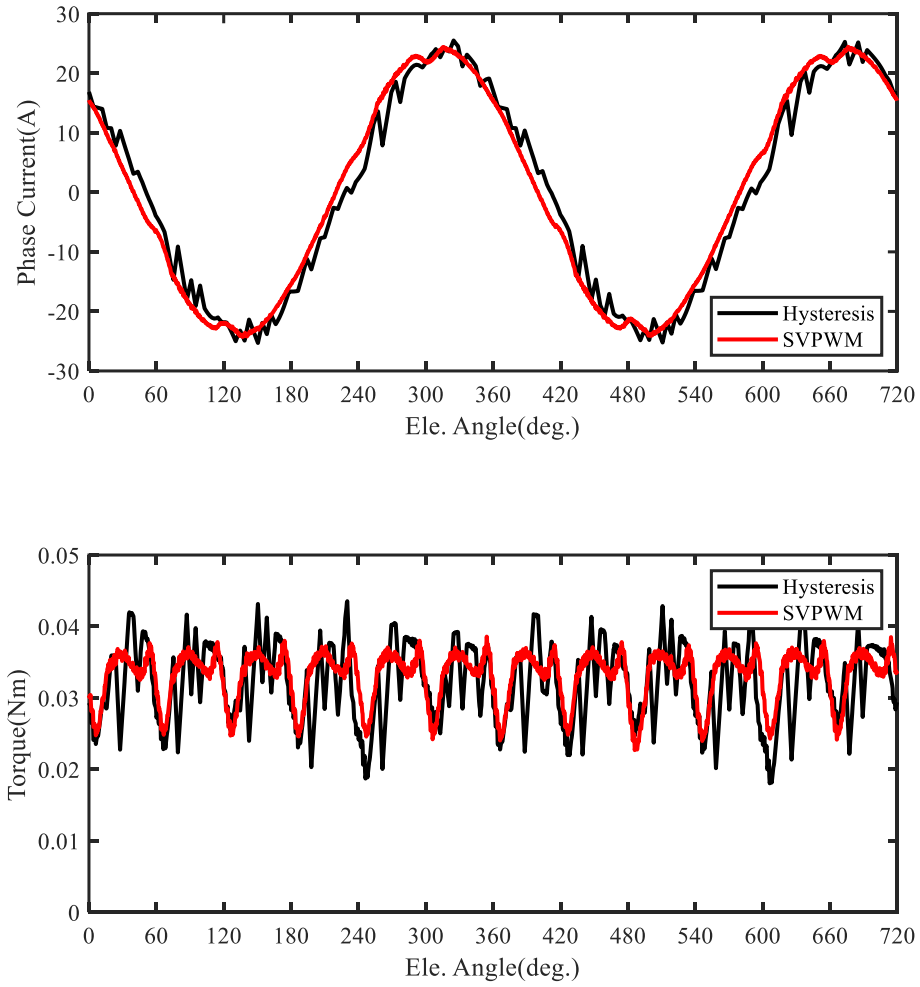

Figure 5.33. Resized TSRM phase current and torque waveform comparison at 30,000 rpm.

As shown in Figure 5.33, the current control is not dropped with speed increase mainly caused by the limited DC bus voltage and switching frequency. The performance appears more different between hysteresis control and SVPWM. In Table 5-XV, it also shows a similar output torque of TSRM with different control. However, the sinusoidal current control introduces more copper losses. In addition, because of the high current ripples in

hysteresis control, there are higher iron losses too. Overall, the resize TSRM performs well with all the three control methods compared to CSRM regarding the output torque and efficiency at 30,000 rpm.

Table 5-XV Dynamic performance comparison at 30,000 rpm.

	CSRM	Resized TSRM		
Inverter/Controller	Asymetrix	Full-bridge	Hysteresis	SVPWM
DC voltage(V)	12	12	21	21
Peak current(A)	20	17	24	24
Control Angle	Commutation angle (mech. deg.)		Advance Angle (ele. deg.)	
	45 to 78	-14	45	50
Average torque(mNm)	24.50	31.80	32.27	33.18
Torque ripple (%)	77.35	123.34	76.92	43.33
Copper losses (W)	11.74	10.53	12.71	13.06
Iron losses (W)	4.30	8.07	11.36	7.66
Motor efficiency (%)	82.75	84.30	80.81	83.42

*All the iron losses are estimated by FEA based on simulation phase currents.

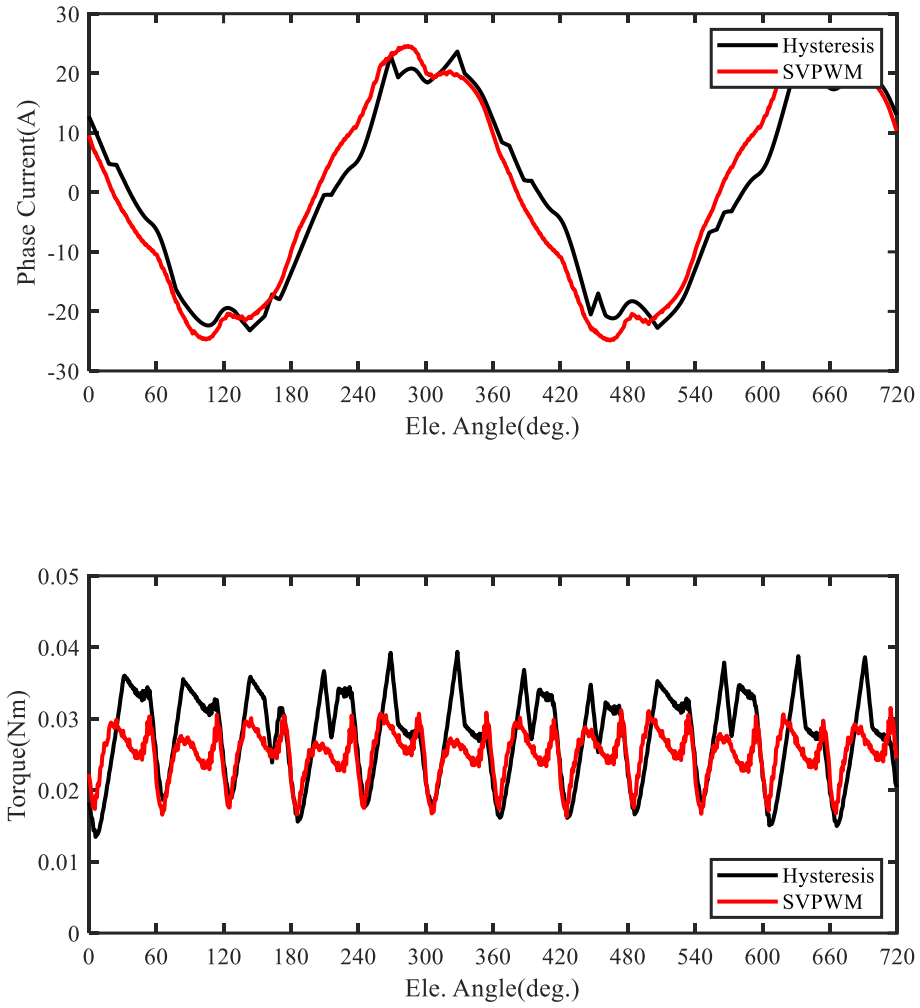

Figure 5.34. Resized TSRM phase current and torque waveform comparison at 50,000 rpm.

The control capability is dropped more at 50,000 rpm, as shown in Figure 5.34. There is deformity in the current waveform. For this reason, the torque fluctuates more. In Table 5-XVI, it shows that the sinusoidal current-controlled TSRM produce even more copper and iron losses. But they also generate more output torque with lower torque ripple.

Table 5-XVI Dynamic performance comparison at 50,000 rpm.

	CSRM	Resized TSRM		
Inverter/Controller	Asymetrix	Full-bridge	Hysteresis	SVPWM
DC voltage(V)	12	12	21	21
Peak current(A)	20	19	24	24
Control Angle	Commutation angle (mech. deg.)		Advance Angle (ele. deg.)	
	38 to 85	-6	58	68
Average torque(mNm)	21.42	24.05	29.10	25.29
Torque ripple (%)	77.41	141.83	89.22	57.83
Copper losses (W)	11.69	10.75	11.65	12.47
Iron losses (W)	8.51	11.01	16.81	14.59
Motor efficiency (%)	84.74	85.27	84.26	83.03

*All the iron losses are estimated by FEA based on simulation phase currents.

5.6.3. Conclusions on Sinusoidal Current Control with Conventional Half-Bridge Inverters.

It shows that TSRM with 12-switch full-bridge inverter has better utilization of DC voltage than sinusoidal excited TSRM with 6-switch half-bridge inverter. Because the maximal phase voltage through half-bridge inverter will only be $1/\sqrt{3}$ of the DC voltage

while it utilizes full DC voltage with the full-bridge inverter. Since the phase voltage is the main issue limit current response and as a sequence it limits torque output, the full-bridge inverter has better performance at a higher speed. In the meantime, as copper losses are controlled the same, which is the main constraint on torque performance at lower speed, TSRM performs similarly regarding output average torque. However, the torque ripple is smallest with SVPWM, and then hysteresis control.

The comparison among hysteresis current control and SVPWM shows that SVPWM has better performance with torque ripple control. However, since it responds slower than hysteresis control, hysteresis control has better current control performance at a higher speed compared to SVPWM. In the meantime, hysteresis control has lower switching losses at higher speed since overshooting doesn't happen with the limited phase voltage. However, the SVPWM switching frequency doesn't change accordingly.

5.7. Conclusions.

In this chapter, a CSRM is optimized and proposed for high-speed operation. The most popular three-phase six-stator-pole four-rotor-pole topology is selected considering its preeminent performance as well as the relatively lower operating frequency. To achieve a consistent comparison, the TSRM stator pole height is reduced of 2mm to achieve the same envelope dimension as CSRM. Because of the resizing of TSRM stator, TSRM weights 55g lighter than CSRM.

The static profiles comparison among the CSRM and TSRM indicated they are able to produce a similar magnetic field and static torque. However, it's observed that TSRMs have relatively higher flux localization. Thus, it is more sensitive to saturation and is at the risk of high iron losses. In addition, because of the decentralization of the magneto-motive force in TSRMs, it has more flux leakage. Those flux leakage function as cancellation on TSRM torque generation. However, considering the superiority of lower copper losses, TSRM could handle higher current. This will compensate the torque drops.

Their dynamic performance is evaluated via Matlab/Simulink with inductance profiles calculated in FEA. The models have been validated by FEA. CSRM is controlled with an asymmetric inverter by angular position control during the simulation. TSRM is first simulated with 12-switch full-bridge inverter and square current waveform and then with half-bridge inverter and sinusoidal current waveform. They are all able to generate 0.02Nm for speed up to 50,000 rpm with the restrained copper losses of 13W. However, the comparison also indicates the TSRM has a better overall performance at lower speed since the output torque is purely limited by the copper losses. However, with the speed increase, TSRM torque is more sensitive to the DC voltage and switching frequency. Moreover, since TSRM has higher iron losses and iron losses' holds more effect on the overall performance. The comparison between full-bridge inverter and half-bridge inverter on TSRMs suggest half-bridge inverter requires higher DC bus voltage and peak phase current but with only half power electronic components. The sinusoidal current control produces torque with much lower torque ripple. However, because the current waveform deformity at higher speed, the TSRM with half-bridge inverter and sinusoidal

current control yield higher copper and iron losses than TSRM controlled by full-bridge inverter.

Overall, the dynamic simulation indicates that all the machines can produce average torque above 0.02Nm with copper losses below 13W for speed up to 50,000 rpm. The efficiency of all the machines is over 83% at 50,000 rpm.

Chapter 6 Prototype and Experimental Validations

6.1. Prototype Motor Mechanical Realization.

In this chapter, the resized single layer TSRM is built and tested against the original-sized CSRM. Compared with CSRM, the envelope dimension of TSRM is enlarged since the windings are wounded outside the lamination. To make the same volumetric comparison between CSRM and TSRM more consistent, the stator pole height of TSRM is reduced by 2 mm. But the other dimensions, like the stator yoke thickness, stay the same. That's to say, the lamination outer diameter reduces 4 mm, leaving space for the toroidal winding outside the stator yoke. This can achieve the same envelope dimension between CSRM and TSRM.

6.1.1. Stator/Rotor Assembly.

Lamination is made via laser cut and weld together. Both stators have six weld points, and rotors each have four weld point. During the prototype, both stators have six extra parts outside for the purpose of easy assemble, which have no influence on machine electromagnetic performance. All those outer parts share the same diameter, which allows the two machines to use the same housing. M3 screws are used to hold stator, which has been treated with insulation spray to avoid extra iron losses. They share the same rotors as shown in Figure 6.1.

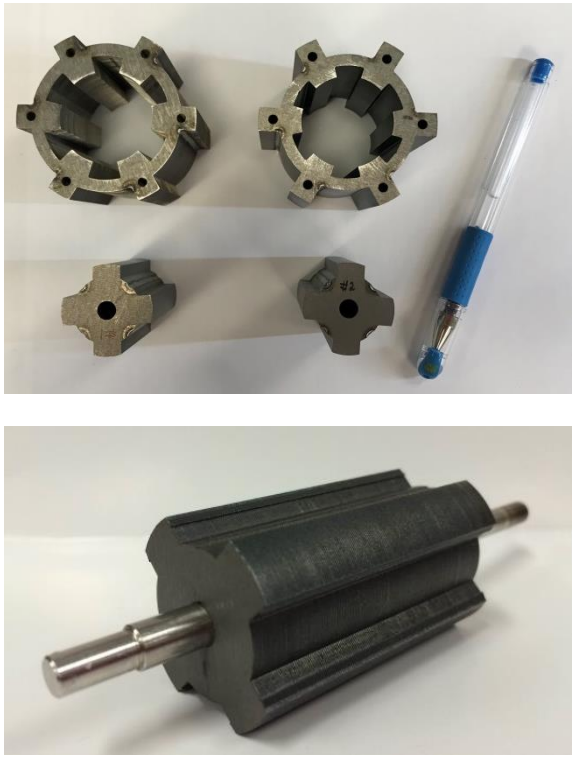

Figure 6.1 Lamination stacks, up left: CSRM; upright: resized TSRM, bottom: the assembled rotor.

6.1.2. Stator Test before Full Assembly.

During prototyping, hand-wound is applied. As for the high-speed machine, thinner wire with more strands will benefit for lower AC losses at high frequency. However, a high-strands number will reduce the filling factor, and as a result, lead to higher DC copper losses. Taking both into consideration, the prototype machines winding parameters have been presented in Table 6-I

Table 6-I Winding comparison during prototyping.

	CSRM	Resized TSRM
AWG	23	22
Bare copper wire OD (mm)	0.5740	0.6426
Strands	4	4
Number of turns per coil	6	6
Coil per slot	2	1
Estimated filing factor (%)	25.79	24.01
Estimated Coil Resistance (mΩ)	13.46	9.72
Measured Average Coil Resistance (mΩ)	18	11

But the copper is slightly heavier because of the coil connection is not considered during the simulation process. After hand winding, additional insulation treatment, Epoxy resin sealant is used to improve winding performance. Moreover, the resin has improved the heat-conductive coefficient to 1.5W/m/K and structural winding support.

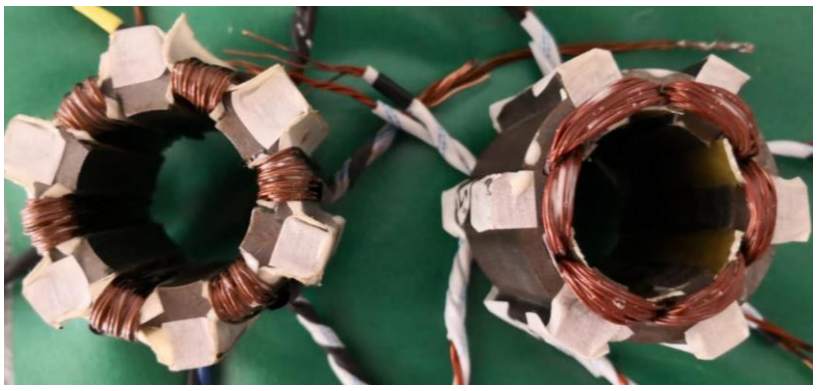

(a) (b)

Figure 6.2 Stator build process: (a) toriodal winding; (b)conventional winding.

Because additional volumes are added for structural purpose, the active stator core weight is normalized, stated in Table 6-II. The weight shows good agreement with design parameters. In other word, the stacking factor has been well kept during the lamination stacking process. It shows the lamination weight is very close to the simulation results. The weight comparison shows that CSRM is heavier because of its larger stator core size.

Table 6-II Active parts weight comparison during prototyping.

Stator Core Length	CSRM	Resized TSRM
Rotor Core	185	186
Stator Core	333	269
Total	577	523

6.2. Static Characterization.

6.2.1. DC Resistance Comparison.

Table 6-III Phase resistance measurement (Room temperature = 28°C).

	CSRM		Resized TSRM	
	Resistance (mΩ)	Difference	Resistance (mΩ)	Difference
Phase A	37	33%	22	10%
Phase B	35	26%	25	25%
Phase C	37	33%	20	0%

The difference is evaluated with the analytical resistance model with the updated winding parameters as stated in Table 6-I. Because the prototypes are built by hands, the filling factor has dropped around 25% from the designed 30%. In addition, the connection wire among the coils also increases the resistance of the prototyped machine. Compared

against Table 5-IV, CSRM has resistance increases by 60%, while TSRM increases by 46%. Thus, with the same phase currents, the maximal copper losses must be increased.

6.2.2. Flux linkage/Inductance & Static Torque Profiles.

Flux-linkage and static torque profiles are of the most important characteristics describing a designed machine. The FEA results are already presented in Chapter 6. To verify the analysis, it's necessary to check these static profiles before the dynamic test. The static test bench is shown in Figure 6.3. The aligned position is first decided as via injecting DC current into these two machines. The position is then controlled accurately via the position holder on the left. Through this set-up, static torque and inductance at different positions are measured and compared against FEA.

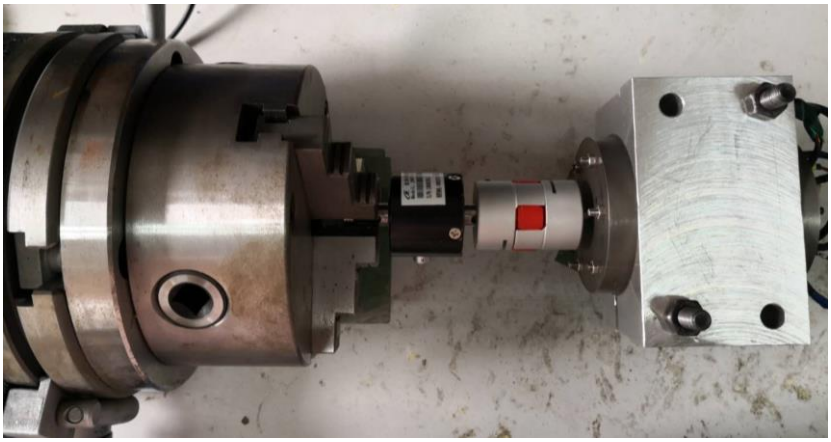

Figure 6.3 Static characterization test setup: left to right: rotor position holder; static torque sensor; coupling; electric machine.

- ***Inductance Profiles***

It should be the same rotor position and locked. And increasing voltage will be applied to phase A, and its reaction current will be recorded together with the phase voltages of the other two phases. A voltage pulse is applied on a single phase. Then the corresponding current is measured and plotted.

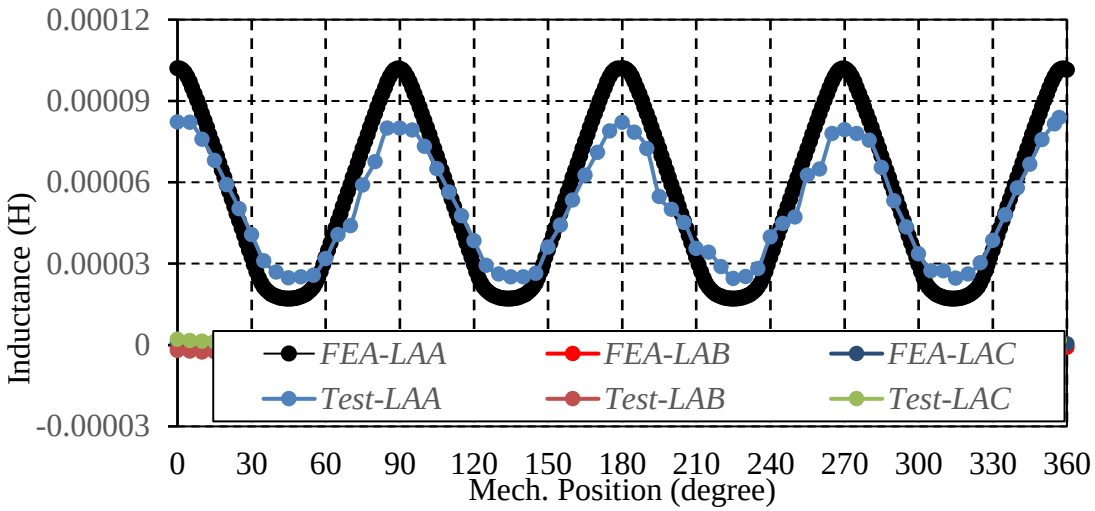

Figure 6.4 CSRM inductance profile validation and comparison.

Table 6-IV CSRM inductance difference during Prototyping.

Parameters	FEA	Prototype	Difference
Aligned inductance (μH)	102.19	83.97	-17.83%
Unaligned inductance (μH)	17.15	24.64	43.69%
Inductance variation (μH)	85.04	59.33	-30.23

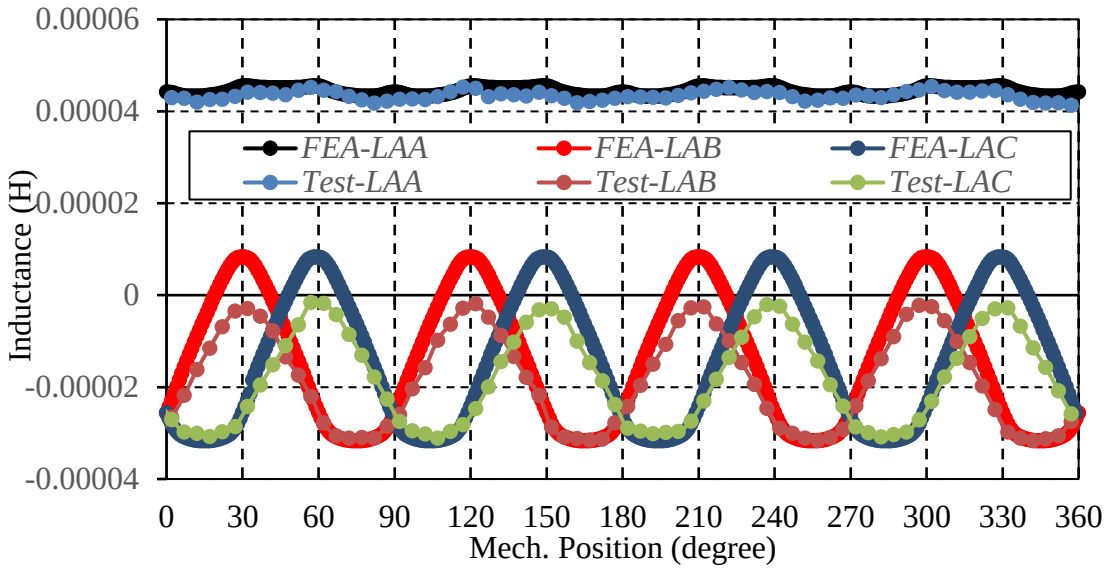

Figure 6.5 TSRM inductance profile validation and comparison.

Table 6-V TSRM inductance difference during prototyping.

Parameters	FEA	Prototype	Difference
Self-inductance – 0^{th} Order(μH)	44.356	43.425	-2.10%
Mutual-inductance – 0^{th} Order(μH)	14.023	18.529	32.13%
Mutual-inductance – 4^{th} Order(μH)	20.219	14.582	-27.88%

As known zero-order inductance, no matter self or mutual, has no contribution to torque generation in the reluctance motor. Such a reduction in 4^{th}-order mutual inductance will result in a proportional drop in TSRM torque generation.

As one of the possible manufactory error for the SRM prototype is eccentric between the stator and rotor. The flux linkage profiles of two aligned positions are checked in Figure 6.6. To verify the concentricity, the two flux linkage curves match with each other very well. That is to say, the inductances at different aligned positions are the same, which

mean the air gaps are constant at the aligned position. The flux linkage profiles for the three phases are also measured in Figure 6.7. The consistency between them shows that the winding balance and mechanical symmetry can be guaranteed. This is considerably important to avoid vibration and noise during the operation.

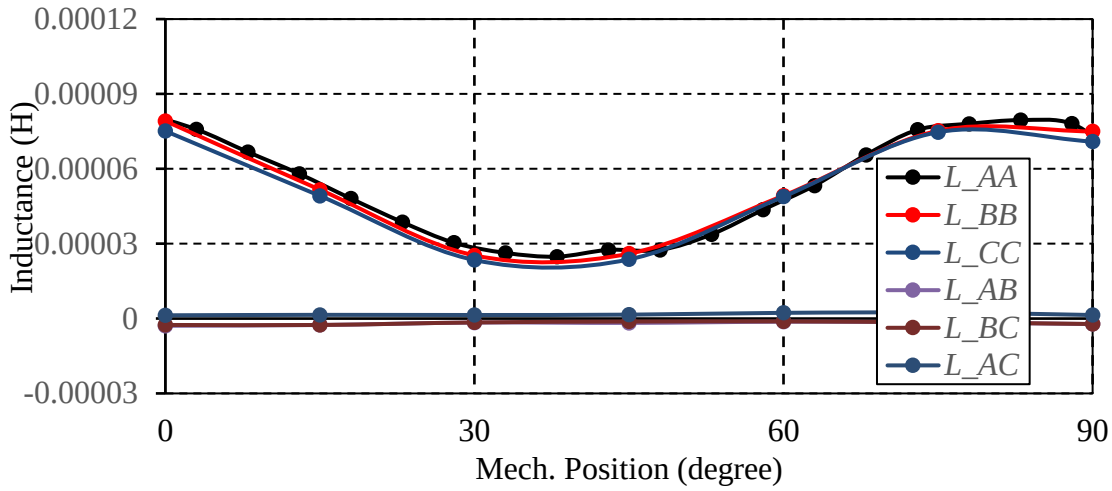

Figure 6.6 Three-phase inductance comparison in prototyped CSRM – phase B shifted 30°; phase C shifted 60°.

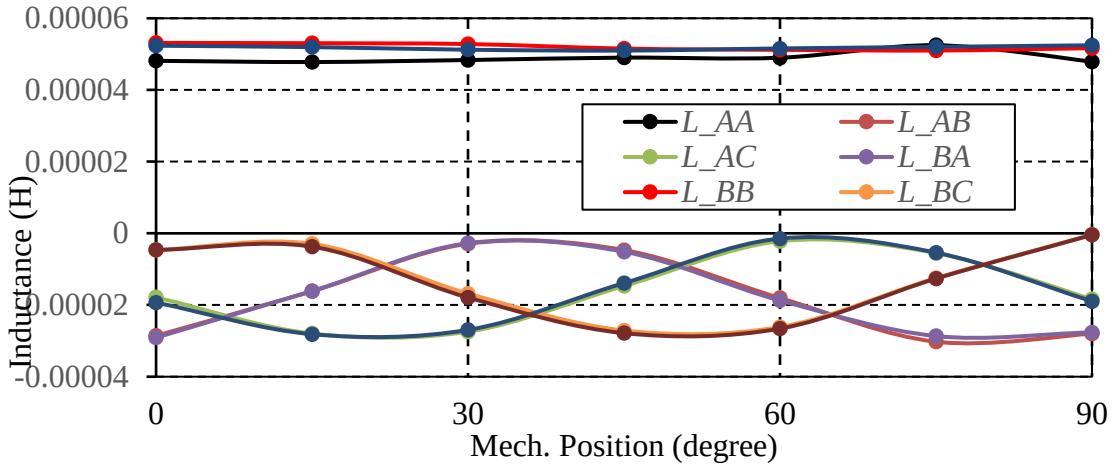

Figure 6.7 Three-phase inductance comparison in prototyped TSRM.

- ***Torque Profiles***

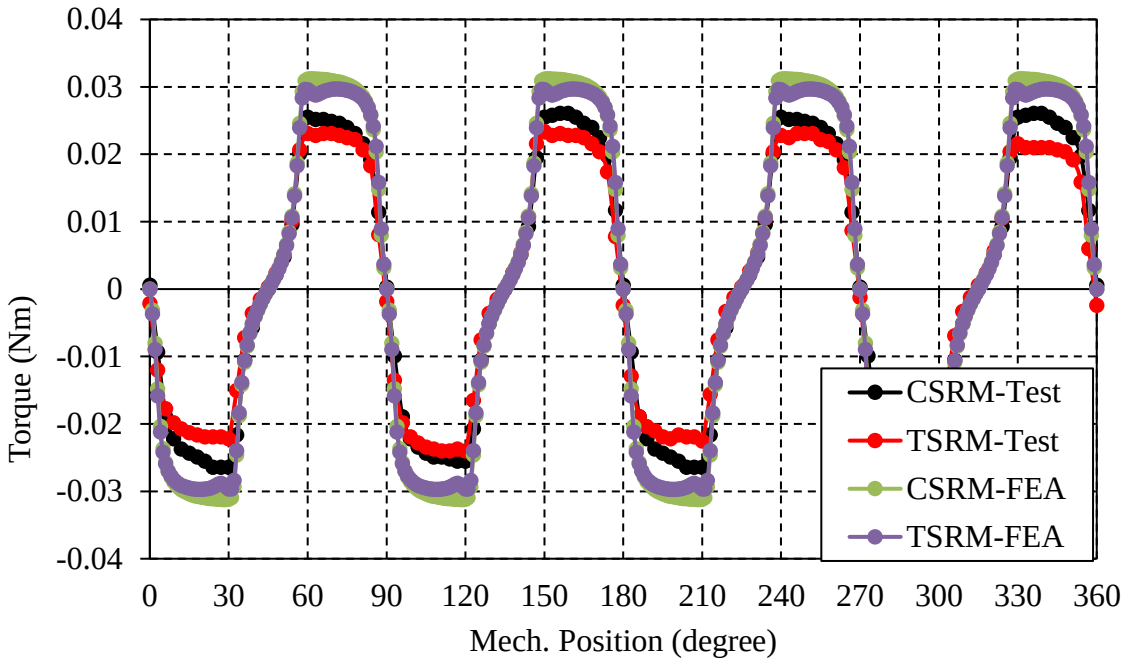

Figure 6.8 Static torque validation and comparison during prototyping.

Table 6-VI Average static torque (from unaligned to aligned position) comparison.

Machine	FEA	Prototype	Difference
CSRM	0.0219	0.0164	-25%
TSRM	0.0218	0.0157	-28%

It shows that there is a similar amount of static torque drop compared to the inductance variation reduction in Table 6-V. The agreement between these two validated the measurement accuracy. The most important reason for this is the material property difference between the FEA and actual prototype. To firmly confirm this, the material test is necessary for future work.

6.3. Friction Losses Measurement.

In the high-speed electric machine, the friction losses are significant since friction losses are generally proportional to the cube of speed. The wind resistance from the salient rotor pole structure, together with the bearing friction will be measured through this test.

Every SRM with all three phases open is driven by the DC motor at a different speed. Their friction torques are measured through the torque sensor in the middle. Mechanically, there is no difference between CTSRM and TSRM-1 as they two are only electrically re-wounded on the stator. Thus, the friction coefficients are calculated for all these machines. This value will also be used for higher speed.

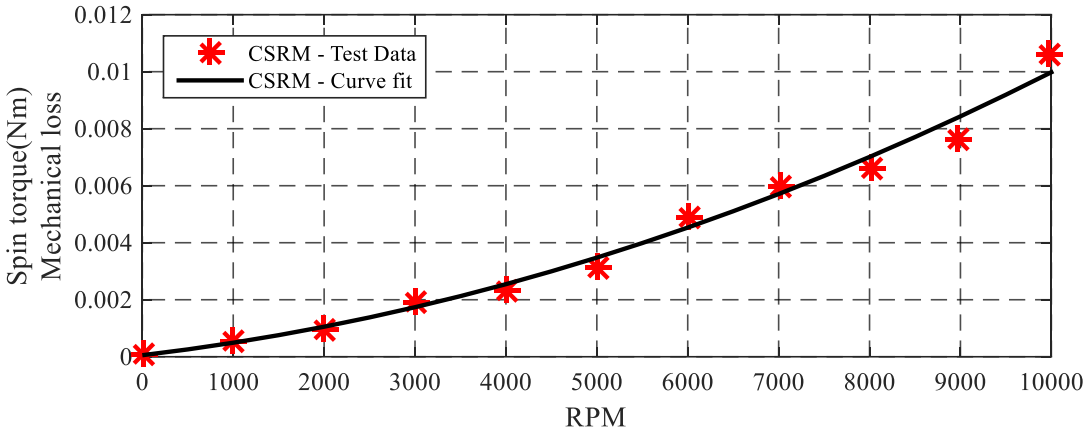

(a)

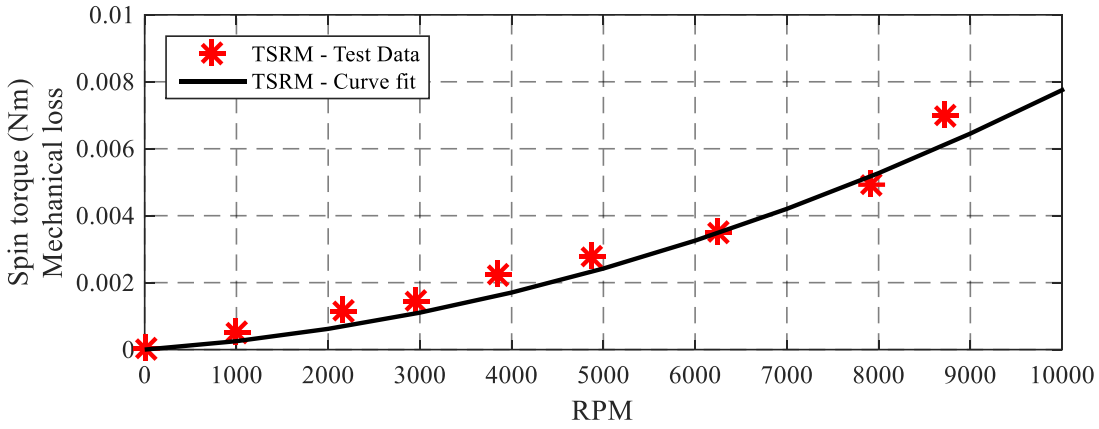

(b)

Figure 6.9 Curve fitting for friction losses analysis: (a) CSRM, (b) TSRM.

$$T_{fric} = k_{fric1} \cdot rpm^2 + k_{fric2} \cdot rpm + DC\_offset \qquad \text{Equation 6-1}$$

Table 6-VII Friction torque measurement at different speeds (Temperature = 26°C).

	CSRM	Resized TSRM
Kfric1	$6.16e\times10^{-11}$	5.815×10^{-11}
Kfric2	3.766×10^{-7}	1.936×10^{-7}

Since torque sensor used can only handle speed below 10,000 rpm. Spin torque above will be estimated based on Equation 6-1 and the coefficients in Table 6-VII. Based on spin torque measurement, it shows the two machines have almost the same coefficients while that of CSRM is slightly higher because the two rotors are the same in geometry. However, resulting from the manufacture difference, they cannot be exactly the same.

In the future, the rotor dynamic will be more studied with efforts to reduce air resistance by fill the rotor to a cylinder using light and non-magnetic material.

6.4. Static Thermal Characteristics.

The toroidal winding benefits machine thermal performance as the winding is directly exposed. This characteristic has been validated. Since the iron losses need more analysis, which also depends on stacking technology. It will be the focus of future work. In this part, only the effect of winding location and copper losses are studied. The motor copper losses are controlled to be constant and the same between two motors. Different DC currents, as shown in Table 6-VIII have been injected to all three phases. Air cooling is applied, and fan location and power is controlled the same among the two motor test. Two thermocouples have been glued on each of the two SRMs: one on the winding, and the other on stator core. The results are shown in Figure 6.10. The temperature is updated every second and recorded for half an hour when it reaches stable. Clearly shown that, when only copper losses are considered in the test, TSRM wire has better heat radiation, and the stable temperature is about 7°C lower than that of CSRM. As for the core temperature, they are more relayed on iron losses which are not the focus of this section. The core temperatures are almost the same between two motors.

Table 6-VIII DC phase current for copper losses of 21W (Ambient Temperature = 28°C).

	CSRM	Resized TSRM
DC Phase Current	14A	18A

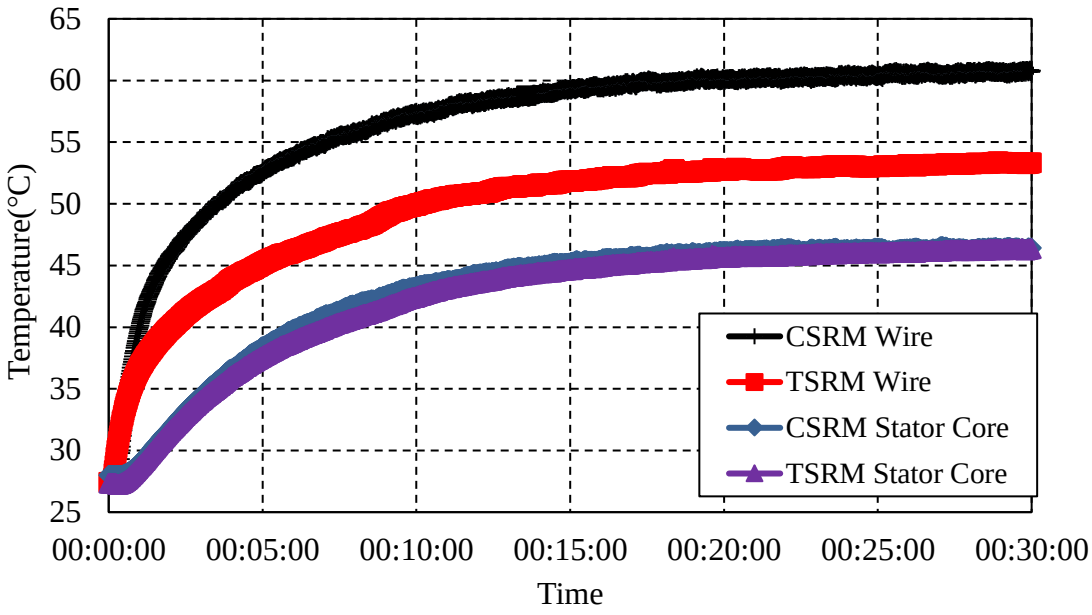

Figure 6.10 Temperature variation comparison between CSRM and TSRM with constant phase currents in Table 6-VIII.

6.5. Dynamic Torque-Speed Performances.

For this high-speed machine test, one of its difficulty is that rare torque measurement unit with proper accuracy and range, are capable of handling speed up to 50,000 rpm. Thus, in this chapter, the test bench has been modified for speed below and above 10,000 rpm, as shown in Figure 6.11. Torque is measured only for lower speed because of the torque sensor has maximal allowance speed of 10,000 rpm.

In both CSRM and TSRM, a 360-step (8.5 bit) high-speed magnetic position sensor, AMS AS5132, is used for position measurement. Quadrature A/B mode is selected for the input of the micro-computer unit on the PCB. Regarding control method, PWM is used on both CSRM and TSRM. Moreover, angular position control is applied on CSRM for

phase turn on and off. As PWM modulation comparison is not a focus of this thesis, only SVPWM as a popular modulation method of three-phase machine is used on TSRM. Three thermocouples have been put on each stator. Two of them are on copper wires of two different phases. The other is used to measure stator core temperature. An oscilloscope is used for current and voltage recording.

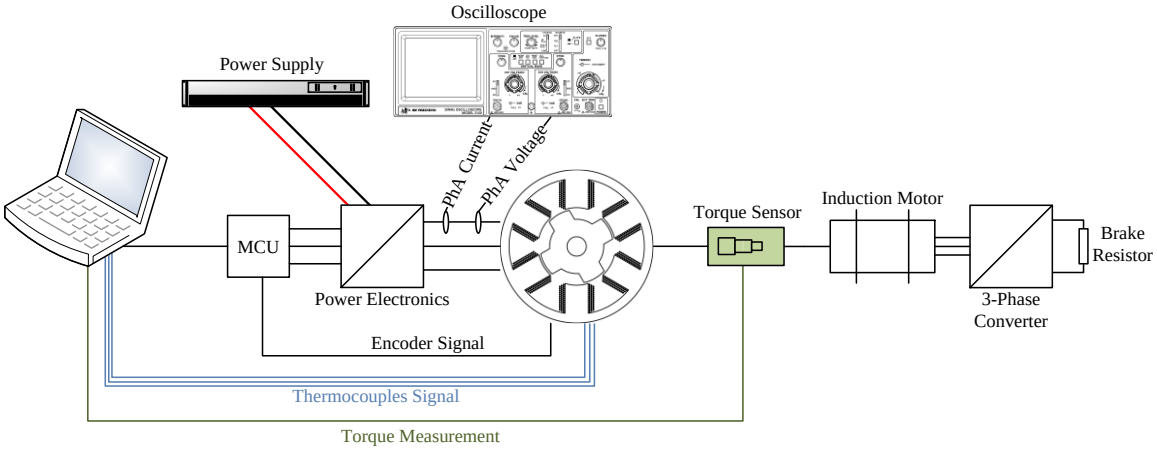

(a)

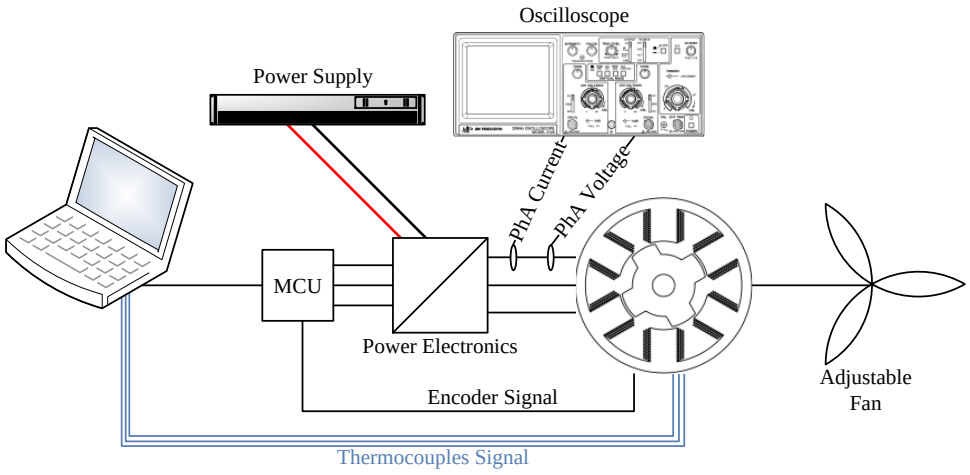

(b)

Figure 6.11 Test bench sketches: (a) below 10,000 rpm, (b) above 10,000 rpm.

During the dynamic tests under speeds of 10,000 rpm, the induction motor is controlled by its converter at a constant speed, while the drive unit, either CSRM or TSRM, operates at a torque mode whose currents are controlled via its controller and converter. As a result, the CSRM/TSRM operates at motoring mode, but the induction machine is at generator mode. Thus, a brake resistor is used for energy consuming. The induction machine load system, together with the torque measurement unit, is removed at higher-speed operation because of their maximal allowance speed is 10,000 rpm. They are replaced by an adjustable fan. The fan blade size can be changed at different speed to allow the system maintaining at different steady state. Motor performance is estimated via its recorded current and voltage waveform.

The author tries to make a consistent comparison between these two prototyped SRMs. However, there are still things which are out of the author's controllability. To avoid confusion, they are clarified here first.

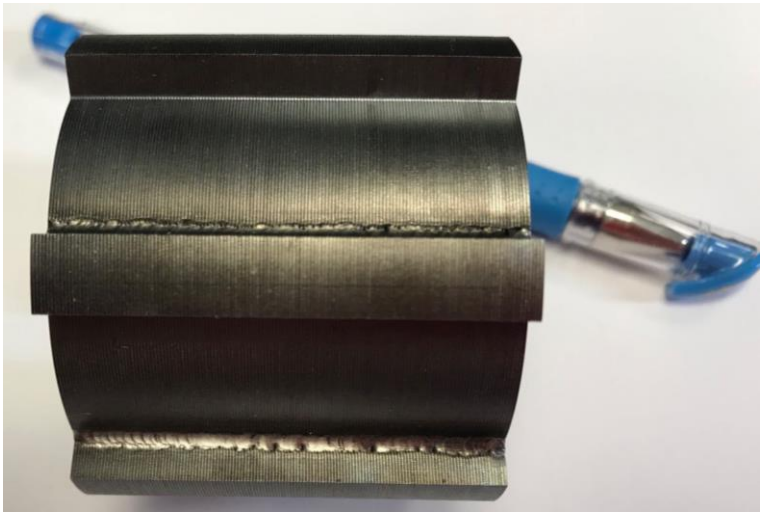

Figure 6.12 Welded stator during prototype.

- During the prototyping, copper resistance has been well controlled via the copper wire used and the number of turns wounded. However, their iron losses and magnetic performance are highly dependent on the material used and the machining technologies used during prototyping. It is widely known that the cutting process of a small stator core and the welding step, as shown in Figure 6.12 afterward led to a significant change in the material properties, resulting in increased iron. It in terms of modifications of the BH hysteresis loops and the resulting iron losses increases and magnetic property deteriorates.
- The same position encoder is applied to the two SRMs. However, there is an unavoidable error which could be introduced during the installation process. And those errors could potentially affect machine performance, especially at high-speed operation.
- Because of the characteristic differences between the two SRMs, different control methods are applied. PI controller and DQ model is used on TSRM, while they both increase the control difficulties of TSRM.
- Because of the limitation of power electronic hardware, CSRM is controlled with switching frequency of 100 kHz while TSRM is tested under 30 kHz via a three-phase commercial PMSM converter is used instead of building a 12-switch converter. A three-phase asymmetric inverter is applied for CSRM.
- Because of the limitation of test equipment, only torque below 10krpm is measured. For the test above this speed, phase current and voltage are measured. The two machines are compared with the same load and copper losses.

6.5.1. Dynamic Tests at Speeds of up to 10,000 rpm.

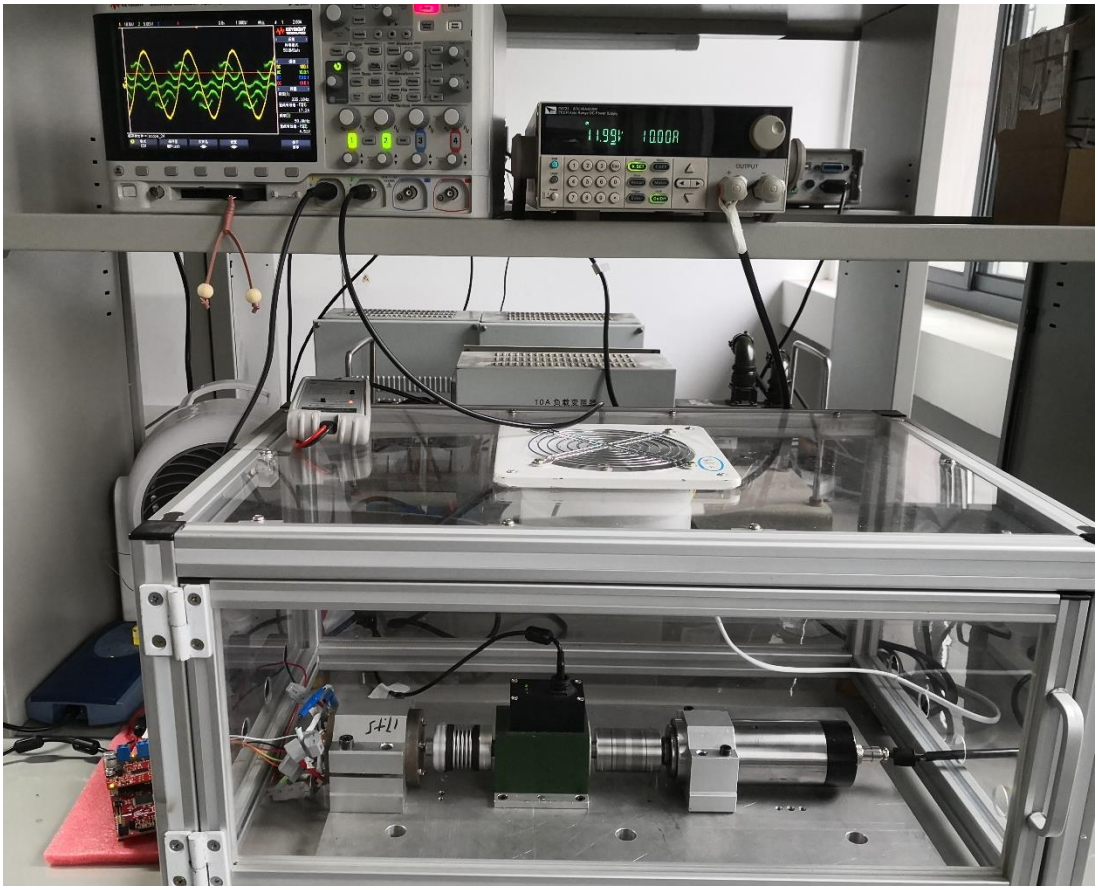

Figure 6.13 Test bench with torque measurement unit and induction machine as load.

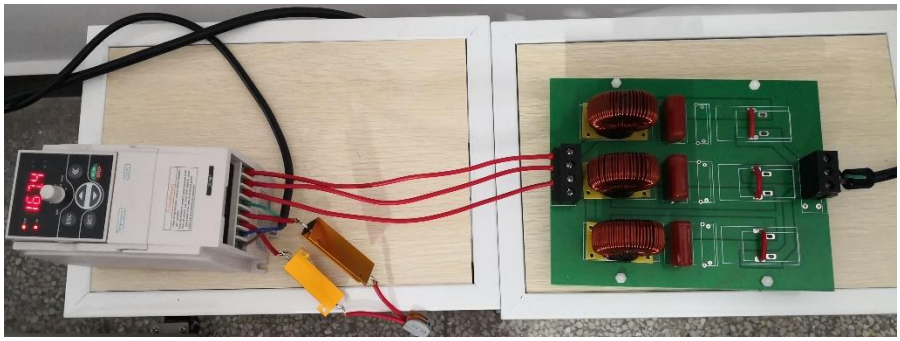

Figure 6.14 Induction-motor converter with filter.

- ***CSRM***

PWM control is used for current limitation. The switching frequencies are at 100 kHz. Copper losses are controlled by limiting phase current via tuning both commutation angle and PWM duty cycle. During the dynamic test, the system is first driven to a certain speed by the induction machine. Based on the encoder position signal, the micro-computer unit of CSRM turns on/off phases through MOSFETs.

Mechanical torque is measured via the torque sensor in the middle. Its values have been calibrated by adding spin losses on. Current and voltage of phase are recorded for phase A. Through it, CSRM electrical input power is calculated. DC copper losses are estimated via phase current time resistance at its operating temperature. All the rest is considered as iron losses.

Since the system operates at low speed. No advance commutation angle is needed. Thus, the control is adjusted only by tuning its PWM duty cycle, while the commutation angle is shown in Table 6-IX. As shown in Table 6-X, large PWM duty cycle will introduce higher phase current, which will lead to higher torque generation. However, it also results in higher copper and iron losses. In Table 6-XI, at higher speed, larger PWM cycle is needed to overcome the proportionally increased phase impedance and reach refine torque output.

Table 6-IX Control parameters during low-speed CSRM tests.

DC voltage	Operation Temperature	Turn-on Angle	Turn-off Angle
12V	38°C	45°	80°

Table 6-X CSRM test data at a reference speed of 10,000 rpm.

Duty Cycle	Actual Speed	Torque	Power Input	Mech. Power	Copper Loss	Iron Loss	Motor Eff.
⁄400	rpm	Nm	Watts				%
160	10075.4	0.0184	47.08	19.37	15.66	12.06	41.13
170	10084.8	0.0218	51.92	23.02	17.48	11.42	44.34
180	10102.3	0.0244	57.2	25.84	18.5	12.86	45.18
190	10107.4	0.0256	64.19	27.09	20.46	16.64	42.20
200	10118.6	0.0258	71.7	27.30	22.3	22.10	38.07
210	10130.6	0.0306	77.44	32.47	23.16	21.81	41.93
220	10144.8	0.0282	84.69	29.97	26.49	28.22	35.39

Table 6-XI CSRM test data at reference speeds of 5,000 to 10,000 rpm.

Ref. Speed	Duty Cycle	Actual Speed	Torque	Power Input	Mech. Power	Cu. Loss	Fe. Loss	Motor Eff.
rpm	⁄400	rpm	Nm	Watts				%
5000	140	5146.4	0.0253	40.15	13.56	19.93	6.67	33.33
6000	150	6251.2	0.0282	51.59	18.47	23.49	9.64	35.80
7000	160	7149.0	0.0282	58.79	21.12	22.98	14.69	35.92
8000	170	8147.4	0.0267	61.46	22.79	22.57	16.09	37.09
9000	180	9093.3	0.0253	63.22	24.13	21.97	17.13	38.16
10000	190	10107.4	0.0256	64.19	27.09	20.46	16.64	42.20

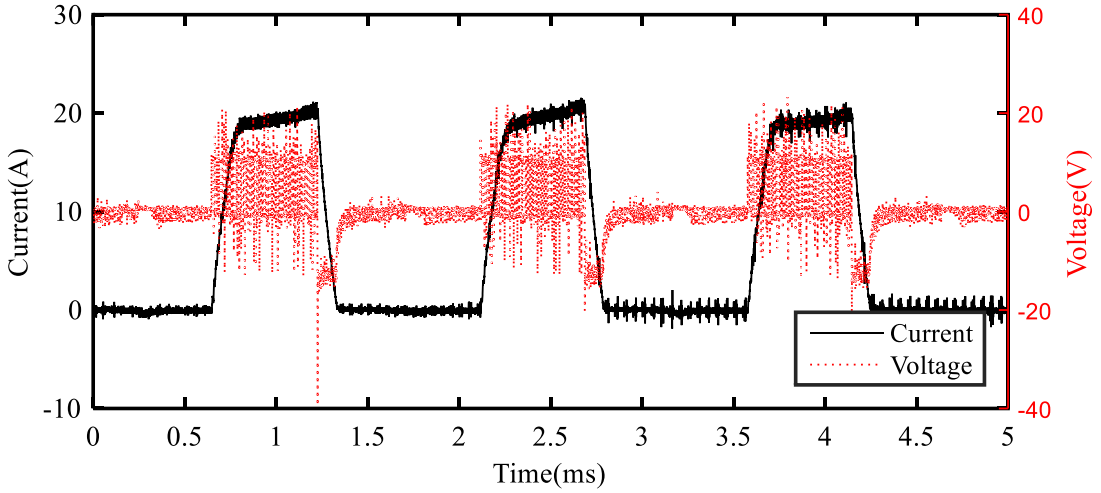
Current(A)
Voltage(V)
Time(ms)
Current
Voltage
30
20
10
0
-10
40
20
0
-20
-40
0
0.5
1
1.5
2
2.5
3
3.5
4
4.5
5

(a)

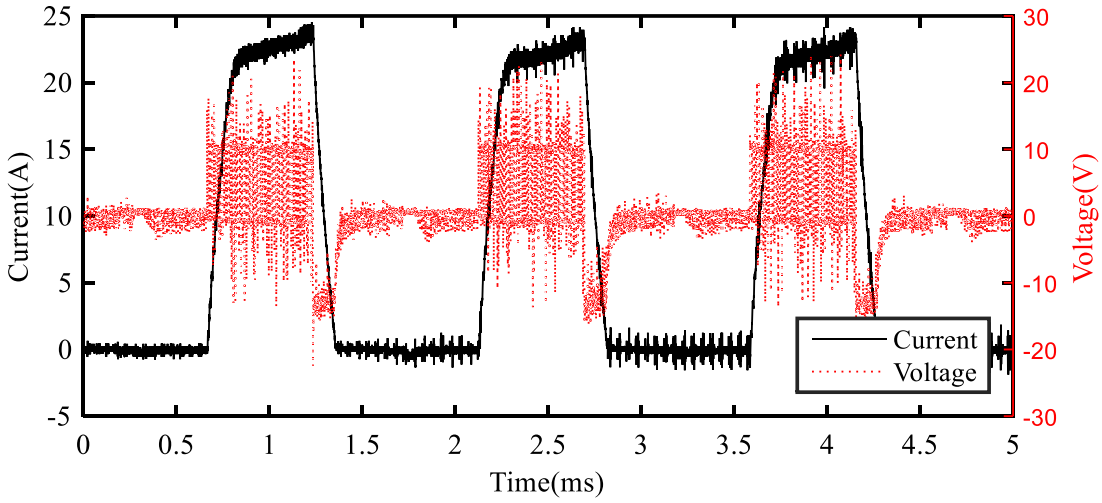
Current(A)
Voltage(V)
Time(ms)
Current
Voltage
25
20
15
10
5
0
-5
30
20
10
0
-10
-20
-30
0
0.5
1
1.5
2
2.5
3
3.5
4
4.5
5

(b)

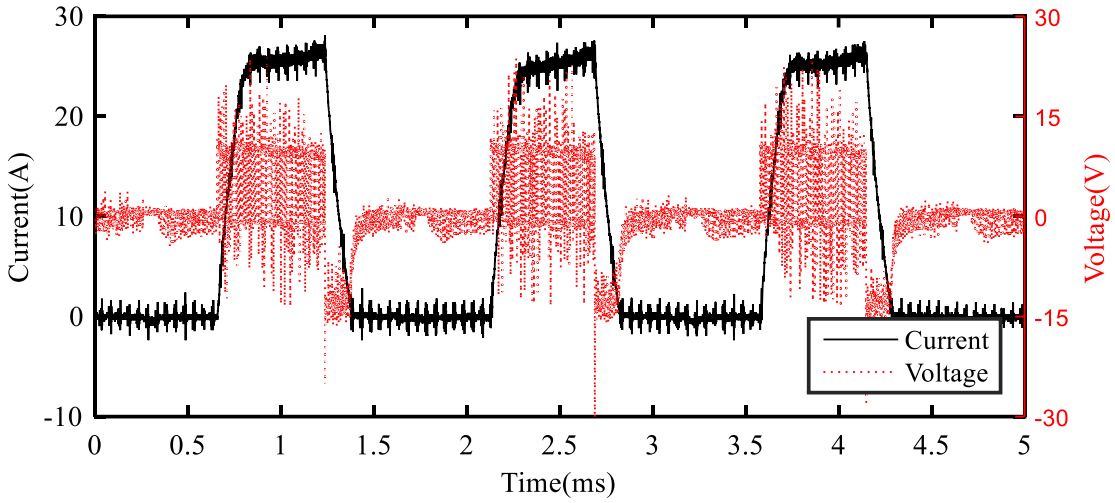

(c)

Figure 6.15 CSRM phase current and voltage waveform at 10,000 rpm validation test(Turn-on/off = 45°/80°): (a) duty cycle = 160/400; (b) duty cycle = 190/400; (c) duty cycle = 220/400.

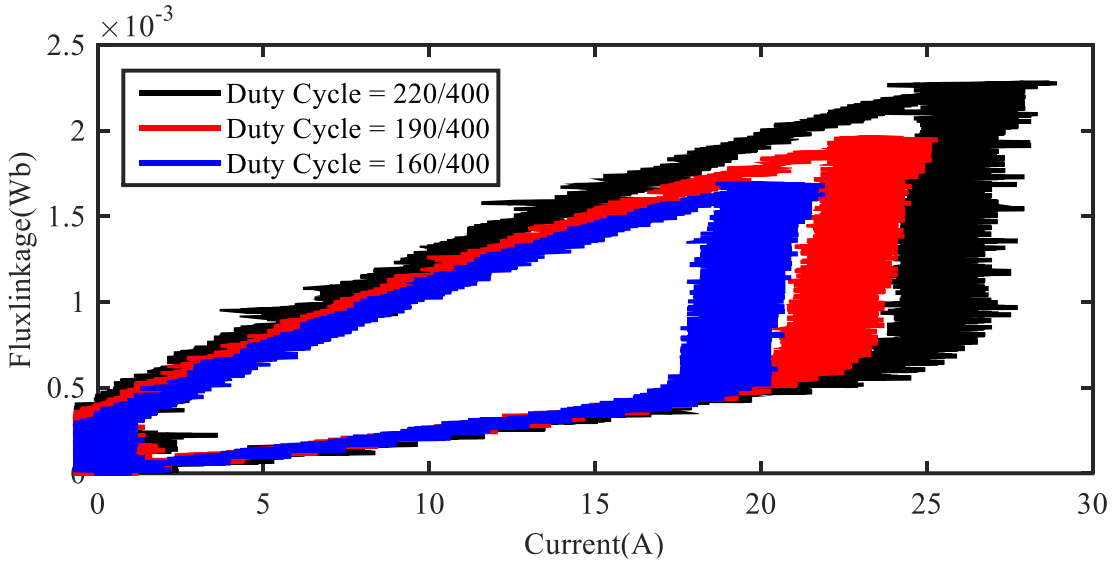

Figure 6.16 CSRM energy conversion curve during the validation test at a speed of 10,000 rpm.

- ***TSRM***

Commercial TI TMS320F28069 Launchpad together with TI DRV8301 BoosterPack is used as TSRM driver. The switching frequencies are limited by the hardware, at 30 kHz for all these tests. This is much lower than that of the CSRM test, which is 100 kHz. Conventional PI control is used for the current regulator. PWM duty cycle is automatically calculated and updated during the test. Since the temperature rise is slower than the CSRM test, all the TSRM low-speed tests are conducted with a controlled winding temperature of 36°C instead of 38°C. Optimal commutation angle requires equal I_d and I_q. An advance angle is not necessary at low speed. The control setting is shown in Table 6-XII.

Table 6-XII Control parameters during low-speed TSRM tests.

DC voltage	Operation Temperature	Peak Phase Current	Commutation Angle
12V	36°C	24A	45° (I_d=I_q)

Table 6-XIII TSRM test data at reference speeds of 5,000 to 10,000 rpm.

Ref. Speed	Actual Speed	Torque	Power Input	Mech. Power	Cu. Loss	Fe. Loss	Motor Eff.
rpm	rpm	Nm	Watts				%
5000	5280.0	0.0236	59.50	13.06	21.77	24.67	21.96
6000	6231.2	0.0232	63.90	15.13	21.61	27.16	23.67
7000	7332.2	0.0232	69.68	17.82	21.39	30.47	25.57
8000	8078.8	0.0223	73.54	18.83	21.36	33.35	25.61
9000	9095.2	0.0218	82.21	20.77	21.59	39.85	25.27
10000	10098.2	0.0250	86.76	26.45	21.19	30.79	40.09

Table 6-XIV. TSRM test data with different peak currents at a speed of 10,000 rpm.

Actual Speed	Phase I_{peak}	Torque	Power Input	Mech. Power	Cu. Loss	Fe. Loss	Motor Eff.
rpm	A	Nm	Watts				%
9995.0	6	0.0016	12.05	1.62	1.31	9.12	13.46
10018.6	12	0.0069	22.02	7.24	5.38	9.40	32.87
10056.2	18	0.0129	49.63	13.61	12.08	23.94	27.42
10098.2	24	0.0250	86.76	26.45	21.19	30.79	40.09

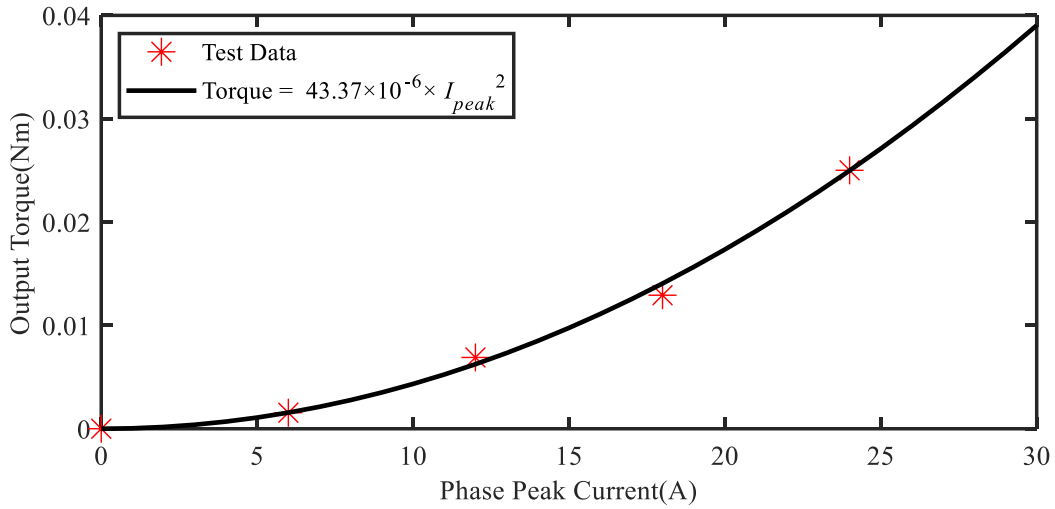

Figure 6.17 Relationship between output torque and peak phase current at low-speed.

Table 6-XV TSRM test data with different advancing angles at a reference speed of 10,000 rpm.

Excitation Angle	Actual Speed	Torque	Power Input	Mech. Power	Copper Loss	Iron Loss	Motor Eff.
Ele. Deg.	rpm	Nm	Watts				%
36	10080.3	0.0220	80.06	23.17	20.44	36.45	28.94
39	10089.4	0.0229	83.37	24.16	20.77	38.44	28.99
42	10094.7	0.0239	84.29	25.24	21.07	37.98	29.94
45	10098.2	0.0250	86.76	26.45	21.19	39.13	30.48
48	10101.0	0.0234	86.63	24.73	21.30	40.61	28.54
51	10101.9	0.0236	87.24	25.00	21.30	40.93	28.66
54	10102.5	0.0233	86.93	24.65	21.32	40.97	28.36
57	10100.1	0.0233	86.03	24.68	21.13	40.22	28.69
60	10096.5	0.0229	85.43	24.26	21.19	39.97	28.40

In the scoped phase voltages and currents presented Figure 6.18, the current values at zero show the difference of the advance angle. And their energy conversion curves are also compared and stated in Figure 6.19. It shows a bare difference at such a low-speed condition for this non-magnet reluctance motor.

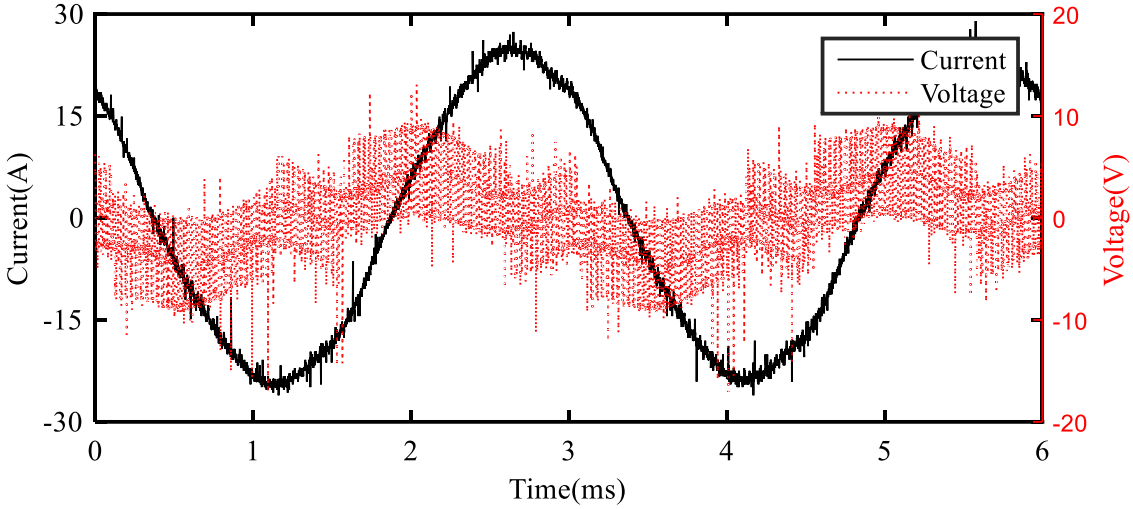
Current
Voltage
Current(A)
Voltage(V)
Time(ms)
30
15
0
-15
-30
20
10
0
-10
-20
0
1
2
3
4
5
6

(a)

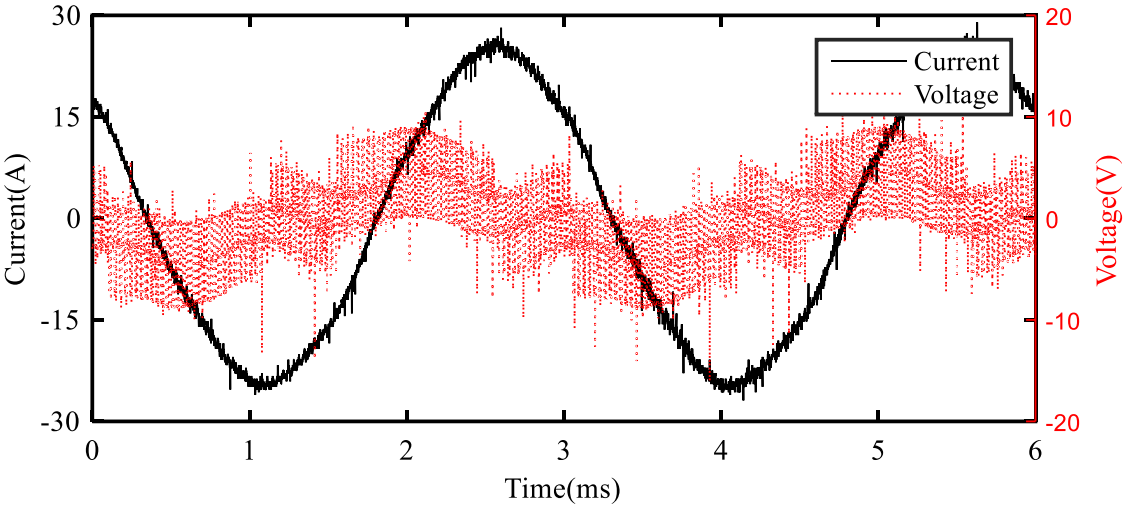
Current
Voltage
Current(A)
Voltage(V)
Time(ms)
30
15
0
-15
-30
20
10
0
-10
-20
0
1
2
3
4
5
6

(b)

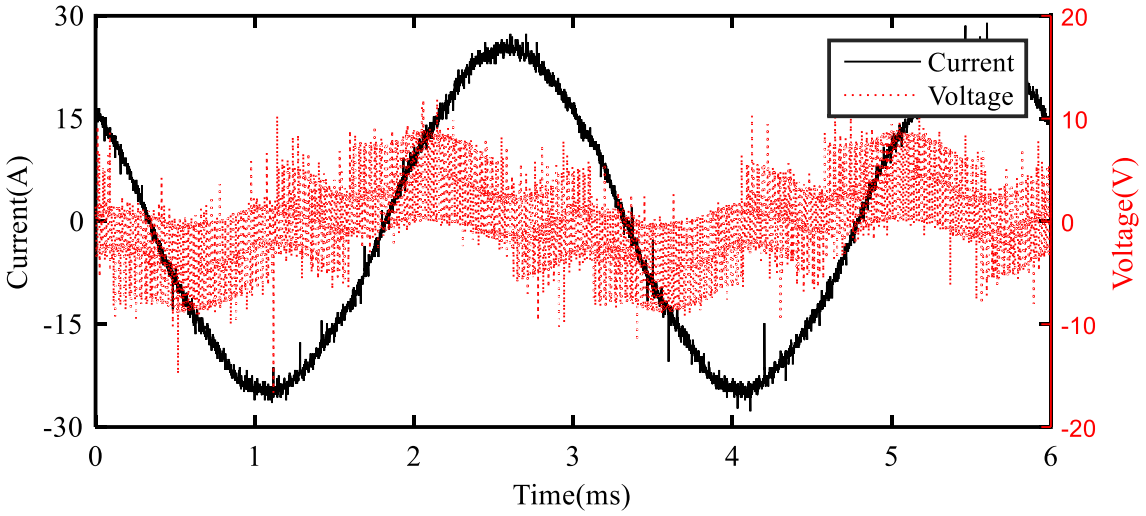

(c)

Figure 6.18 TSRM phase current and voltage waveform at 10,000 rpm validation test: (a) advance angle = 36°; (b) advance angle = 45°; (c) advance angle = 49°.

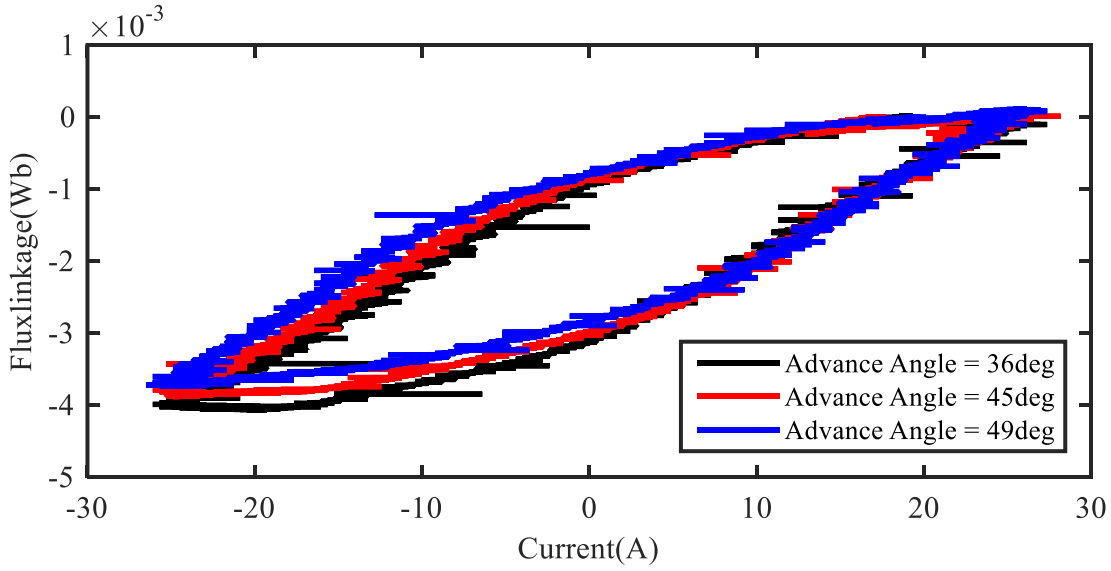

Figure 6.19 TSRM energy conversion curve during the validation test at a speed of 10,000 rpm.

6.5.2. Torque Estimation Model based on Current/Voltage Measurement and Measured Static Inductance/Resistance Profiles.

Torque output is one of the most important criteria to compare these two motors. However, torque measurement for such high speed is very difficult and cost intensive. With the current test environment, the dynamic torque is only measured for speed up to 10,000 rpm. However, as both machines have been characterized during the static test, their dynamic torque could be estimated based on that. Thus, the static inductance profiles of the two machines have been used for the dynamic torque estimation. The torque measurements obtained at speed up to 10,000 rpm are used to validate the estimation model's accuracy.

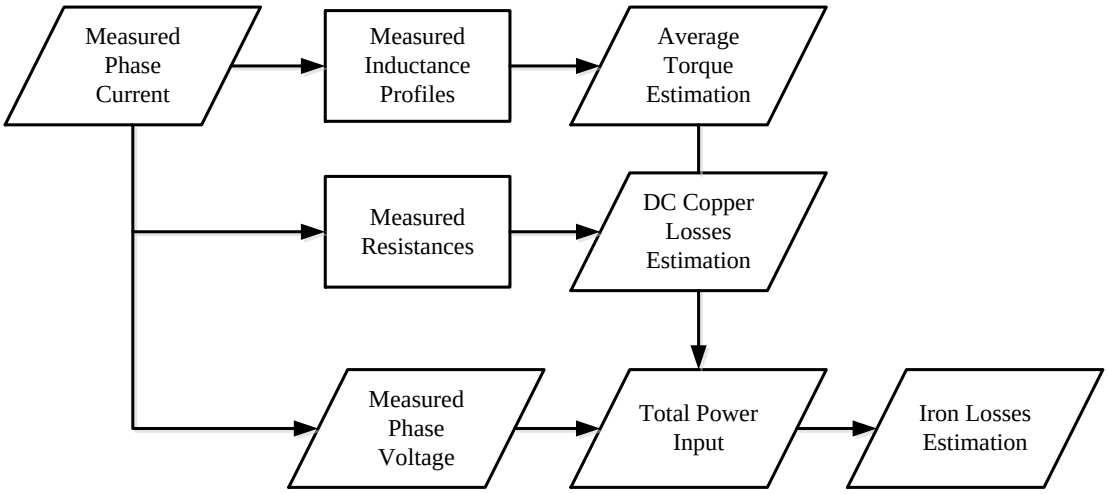

Figure 6.20 Torque estimation flowchart based on dynamic current/voltage measurements.

- ***CSRM***

Table 6-XVI CSRM test and estimation torque comparison.

Duty Cycle	Actual Speed	Measured Torque	Estimated Torque	Difference
⁄400	rpm	Nm	Nm	%
160	10075.4	0.0184	0.0175	4.8948
170	10084.8	0.0218	0.0199	9.5257
180	10102.3	0.0244	0.0223	9.5415
190	10107.4	0.0256	0.0248	3.1953
200	10118.6	0.0258	0.0276	-6.6613
210	10130.6	0.0306	0.0305	0.3549
220	10144.8	0.0282	0.0306	-7.7961

In Table 6-XVI, CSRM torque estimation model is validated compared to the tested data around 10,000 rpm with different duty cycle. All the test is conducted with V_{dc} = 12V, turn-on angle = 45°, and turn-off angle = 80°. The operation temperature is updated based on the test record. In the meantime, the voltage drops on switches/diode together with the wire connection has been considered in the estimation. From the comparison, all the difference is within 10%, which is an acceptable error. Thus, for the test above 10,000 rpm, this torque estimation model will be used to get an idea of the CSRM torque generation when torque measurement is not available.

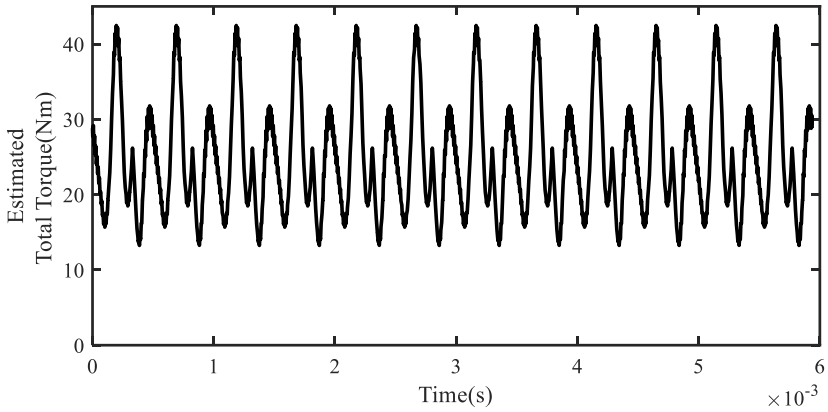

Figure 6.21 Estimated CSRM dynamic torque at 10,107rpm: V_{dc} = 12V, Turn-on/off = 45°/80°, PWM duty cycle = 190/400.

Table 6-XVII CSRM test performance comparison around 10,000 rpm.

	Updated Simulation	Test
DC voltage(V)	12	
Peak current(A)	24	
Control Angle	Turn-on/off = 45°/80° Duty cycle = 190/400	
Average torque(mNm)	25.21	25.6
Torque ripple (%)	117.6	NA
Copper losses (W)	20.9	20.46
Iron losses (W)	3.36	16.64
Motor efficiency (%)	55.8	42.2

Simulation iron losses are calculated via FEA with simulation three-phase currents as input.

- ***TSRM***

Table 6-XVIII TSRM test and estimation torque comparison.

Excitation Angle	Actual Speed	Measured Torque	Estimated Torque	Difference
ele. deg	rpm	Nm	Nm	%
36	10080.3	0.02195	0.02383	-7.88
39	10089.4	0.02287	0.02451	-6.68
42	10094.7	0.02387	0.02492	-4.19
45	10098.2	0.02501	0.02506	-0.18
48	10101	0.02338	0.02492	-6.19
51	10101.9	0.02364	0.02451	-3.56
54	10102.5	0.0233	0.02383	-2.22
57	10100.1	0.02333	0.02289	1.93
60	10096.5	0.02295	0.0217	5.76

As seen in Table 6-XVIII, the updated torque estimation model has been validated for TSRM at 10,000 rpm with different excitation angles. All the difference is within 10%. Thus, it will be used for average torque estimation for TSRM tested over 10,000 rpm. The model can also get an insight of the torque ripple as shown in Figure 6.22.

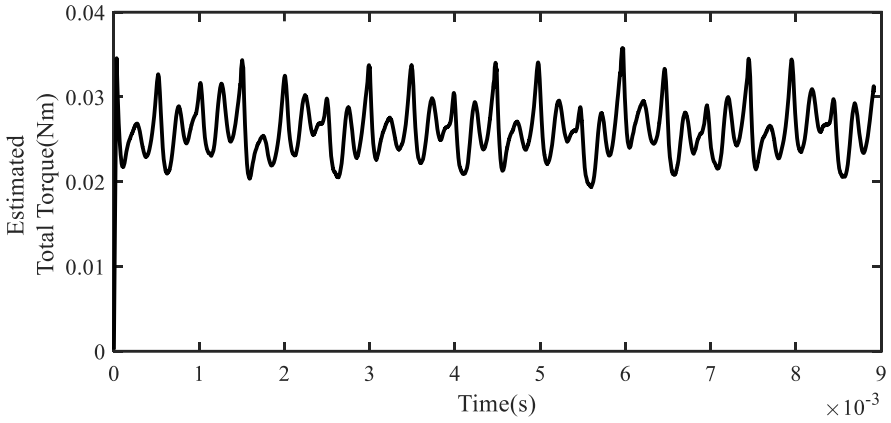

Figure 6.22 Estimated TSRM dynamic torque at 10,098rpm: V_{dc} = 12V, excitation angle = 45°, I_{peak} = 24A.

Table 6-XIX TSRM test performance comparison at 10,098rpm.

	Updated Simulation	Test
DC voltage(V)	12	
Peak current(A)	24	
Control Angle	45	
Average torque(mNm)	25.06	25.01
Torque ripple (%)	62.85	NA
Copper losses (W)	20.90	21.19
Iron losses (W)	6.20	39.13
Motor efficiency (%)	49.38	30.48

Simulation iron losses are calculated via FEA with simulated three-phase currents as input.

In the updated simulation model, the copper losses are calculated with the measured DC copper resistance, average torque is estimated with the static inductance profile as obtained in 6.2.2, but simulation iron losses is still based on original FEA model in Chapter 5. As seen that, the estimated test iron losses have been much higher than FEA simulation. There could be two reasons causing this difference. One reason is that the material difference and prototype issue lead to higher iron losses. The other reason is that AC copper losses are also added in as iron losses in Table 6-XVII and Table 6-XIX. The iron losses are the sum of iron losses and AC copper losses. Thus, it should be called AC losses.

Table 6-XX CSRM and TSRM test performance comparison at 10,000 rpm.

	CSRM	TSRM
DC voltage(V)	12	12
Peak current(A)	24	24
Average torque(mNm)	25.6	25.0
DC Copper losses (W)	20.46	21.19
AC losses (W)	16.64	39.13
Motor efficiency (%)	42.2	30.48

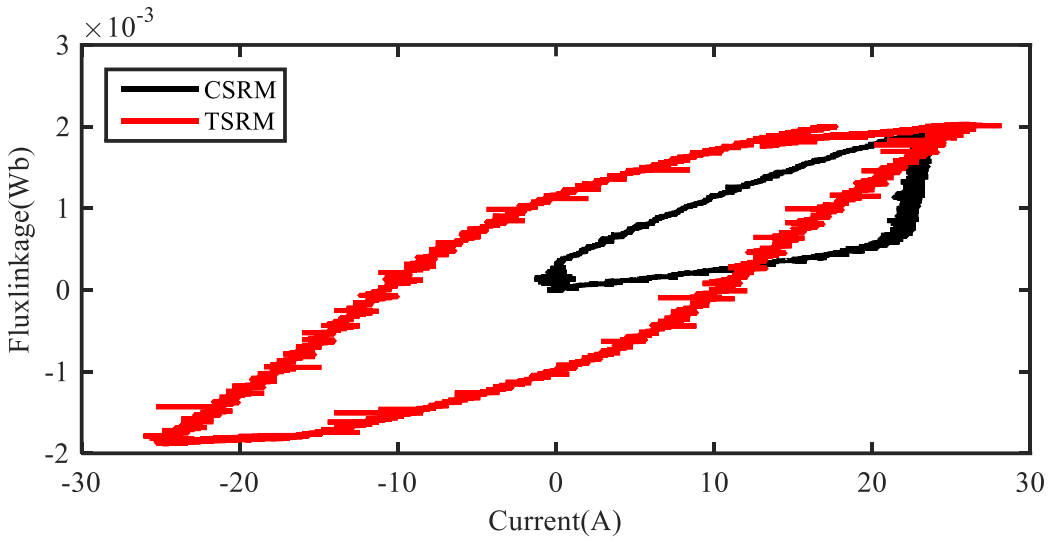

Figure 6.23 CSRM and TSRM energy conversion comparison at 10,000 rpm.

In Table 6-XX and Figure 6.23, it shows that for the two porotype CSRM and TSRM, they produce about the same torque at the same DC copper losses. However, TSRM produces almost double the iron losses of CSRM.

6.5.3. Dynamic Tests at Speeds of up to 30,000 rpm.

As indicated before, because of the limitation of torque sensor speed range, the test bench has been modified for a test at speed above 10,000 rpm. The comparison between CSRM and TSRM is through the same load condition, as shown in Figure 6.24.

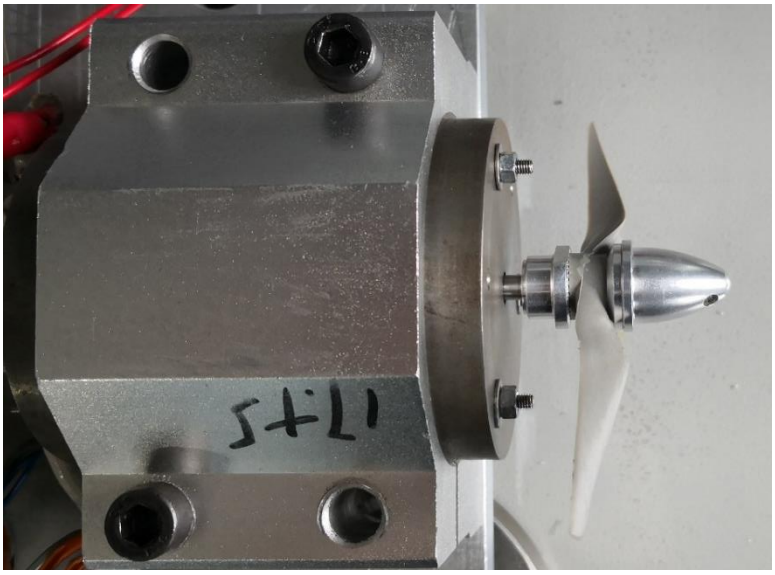

(a)

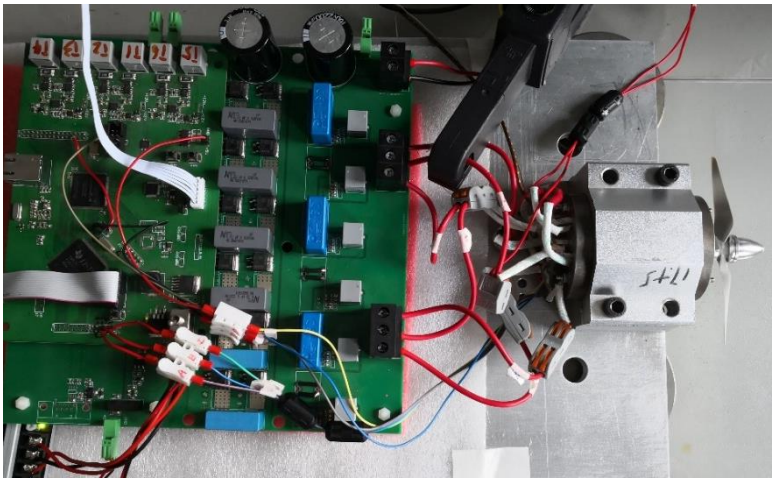

(b)

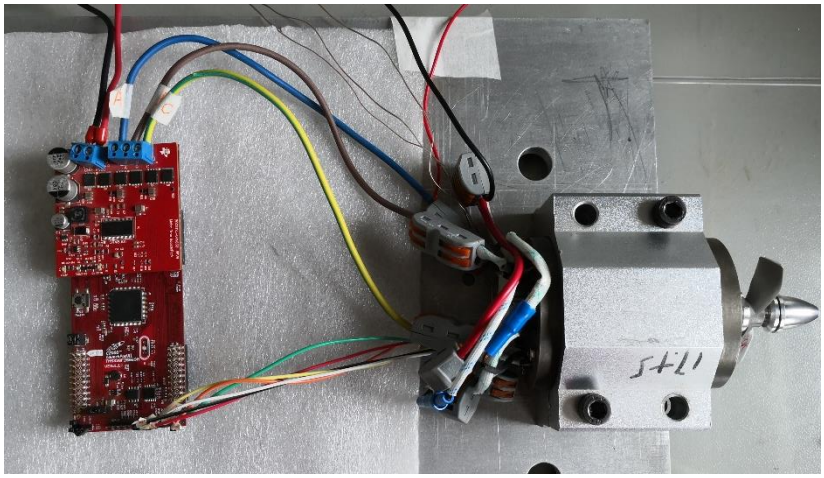

(c)

Figure 6.24 Test Bench with an adjustable fan as the load: (a) test motor with fan. (b) CSRM with the converter, (c) TSRM with the converter.

As noticed during the test at 10,000 rpm, the voltage drop on power electronic is significant for this low-voltage high-current system. Such a voltage drop is even more obvious at a higher speed. So to compensate this, the switch/diode resistance is checked, and 2Vdc is added to DC bus voltage. The latest control parameters are presented in Table 6-XXI.

Table 6-XXI Control parameters during fan blade size tuning.

DC voltage	Operation Temperature	Turn-on Angle	Turn-off Angle	Duty Cycle
14V	38°C	45°	80°	0.8

The load is controlled through the fan blade size. The fan size is first tuned during the CSRM test as shown in Figure 6.25 to make it stable at required speed with demand

resistance torque. Then the selected fan blade radius is $R = 26mm$, which is also used also for TSRM test. Through such load control, their performance is checked and compared.

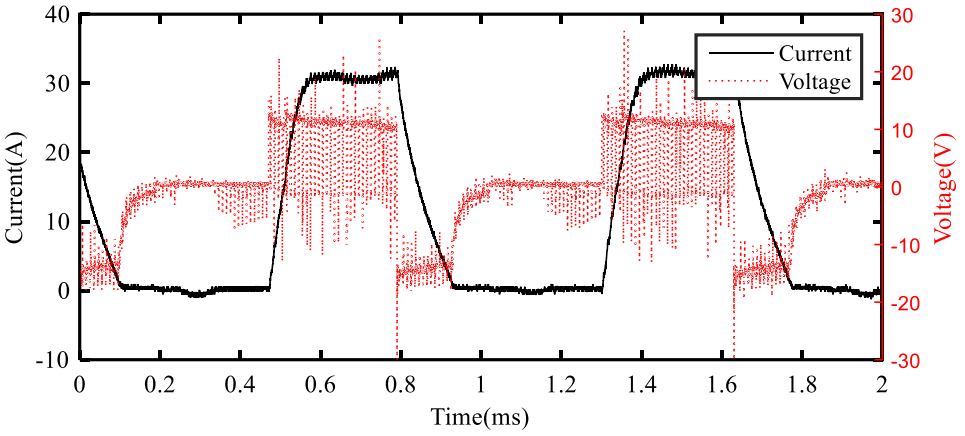

(a)

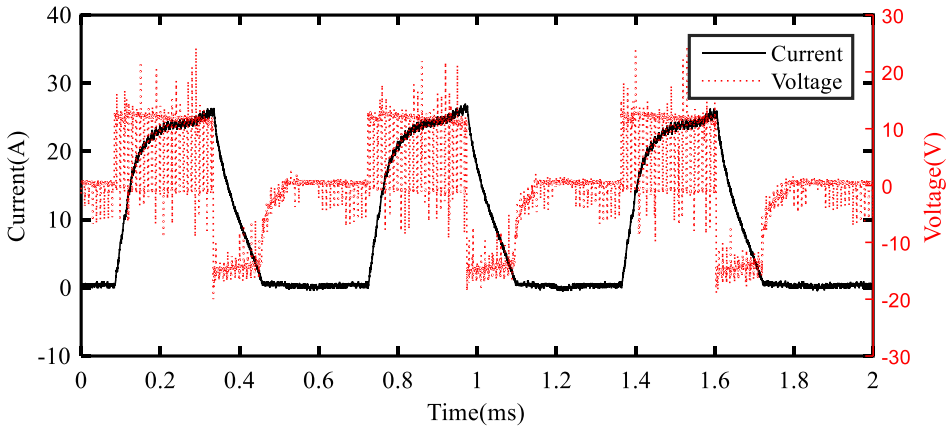

(b)

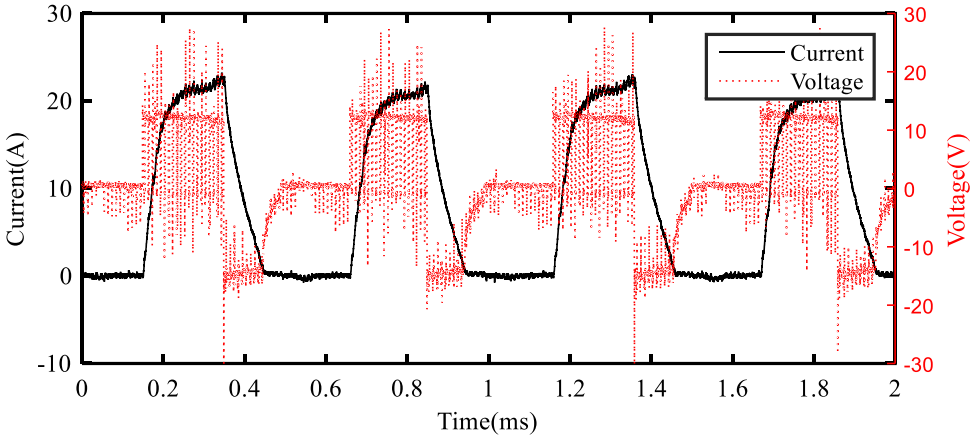
Current
Voltage
Current(A)
Voltage(V)
Time(ms)
30
20
10
0
-10
-20
-30
0
0.2
0.4
0.6
0.8
1
1.2
1.4
1.6
1.8
2

(c)

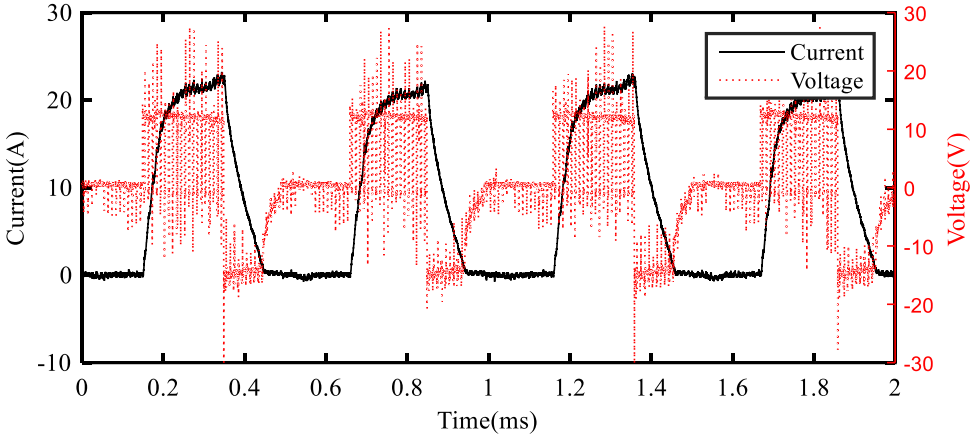
Current
Voltage
Current(A)
Voltage(V)
Time(ms)
30
20
10
0
-10
-20
-30
0
0.2
0.4
0.6
0.8
1
1.2
1.4
1.6
1.8
2

(d)

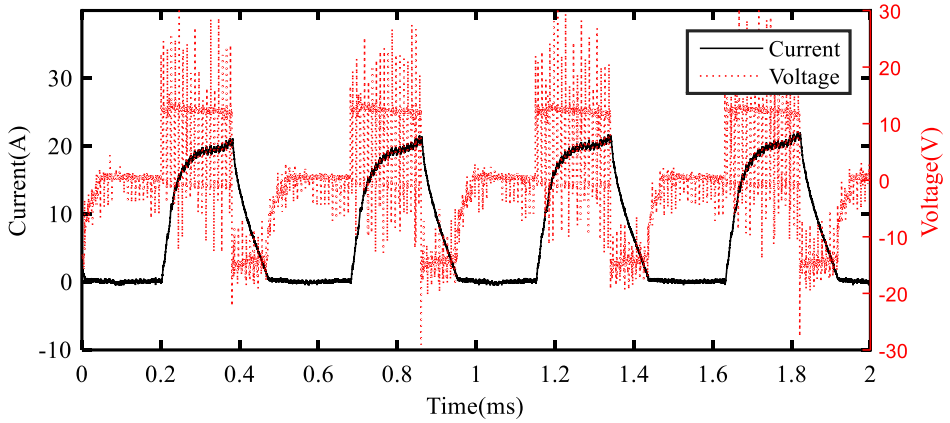

(e)

Figure 6.25 CSRM current and voltage waveform with different fan blade radius: (a)blade=60mm; (b)blade = 35mm; (c)blade = 29mm, (d)blade = 26mm, and (e)blade = 24mm.

- ***CSRM***

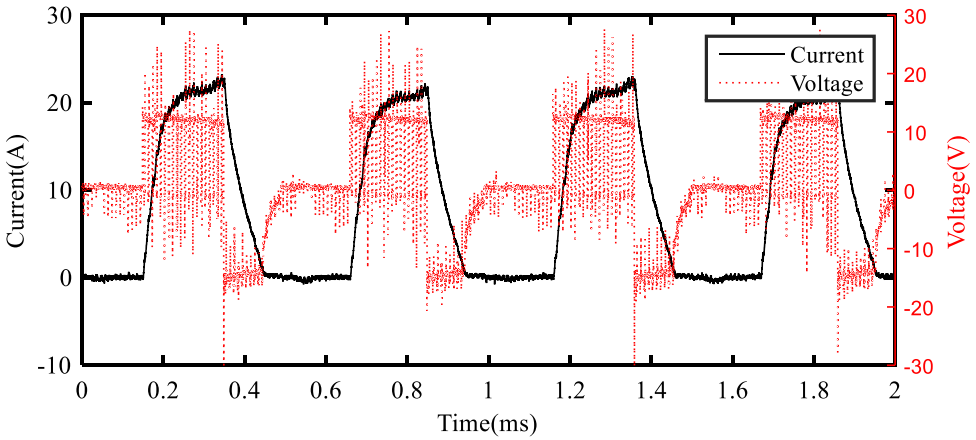

(a)

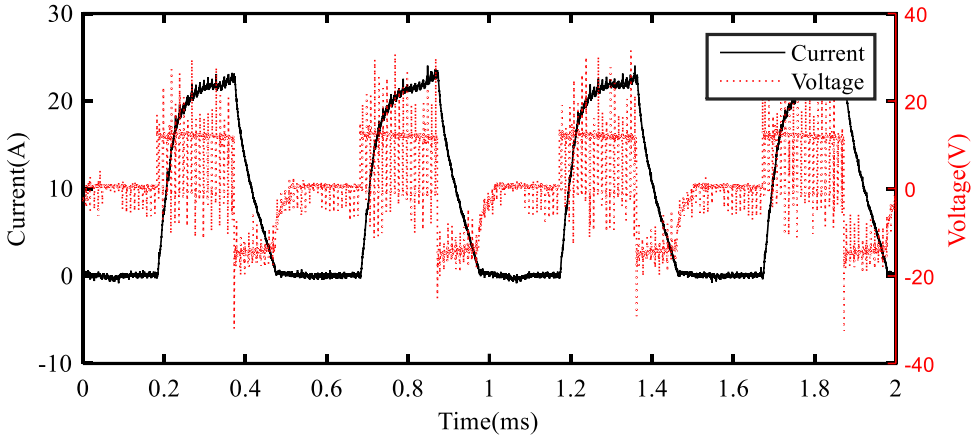

(b)

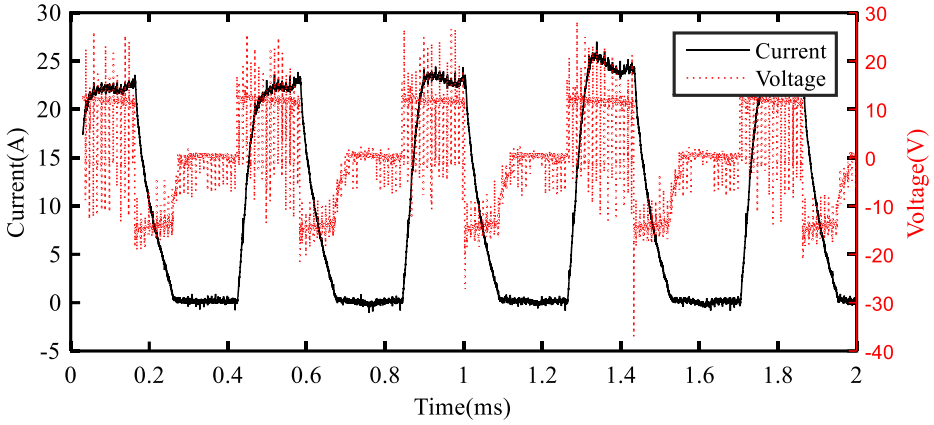

(c)

Figure 6.26 CSRM current and voltage waveform with different duty cycle(fan blade radius = 26mm): (a)duty cycle = 0.8; (b)duty cycle = 0.85; (c) duty cycle = 0.9.

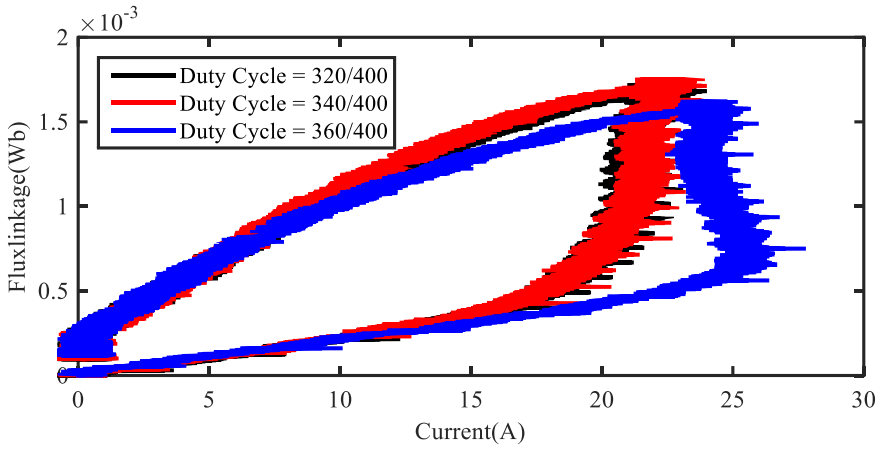

Figure 6.27 CSRM energy conversion curves with different duty cycles at speeds around 30,000 rpm, with fan blade radius = 26mm.

Table 6-XXII CSRM dynamic performance at 30,000 rpm with fan blade radius 0f 26mm.

DC voltage(V)	14		
DC current(A)	11.14	12.25	16.01
Phase peak current(A)	23.216	24.05	24.422
Control Angle	Turn-on/off = 45°/80°		
PWM duty cycle	0.8	0.85	0.9
Speed (RPM)	29696	30150	34905
Motor input power (W)	93.086	120.7	146.25
Copper losses (W)	17.586	20.23	23.523

During the test, different PWM duty cycles are tuned to get the demand speed of 30,000 rpm. Obviously in Table 6-XXII, a higher duty cycle leads to higher phase current, which could potentially increase the electromagnetic torque. For a fixed blade size, a raised output torque means a higher stable maximal speed. But all this is at the expense of higher copper losses.

- ***TSRMs***

The same fan is used for TSRM test. The test is first conducted with the same DC bus voltage of 14V as shown in Table 6-XXIII and Figure 6.28. To clarify, the peak phase current is set to 20A, because that it cannot reach higher with V_{dc} of 14V. In Figure 6.28, the time is set the same, by counting the number of periods; it shows a clue for the speed difference. Another difference is the current shape at different speeds. With the speed increase, the voltage has difficulty to control proper sinusoidal phase currents.

Table 6-XXIII TSRM control parameters with different excitation angles around 30,000 rpm.

DC voltage	Operation Temperature	Phase peak current peak
14V	38°C	20A

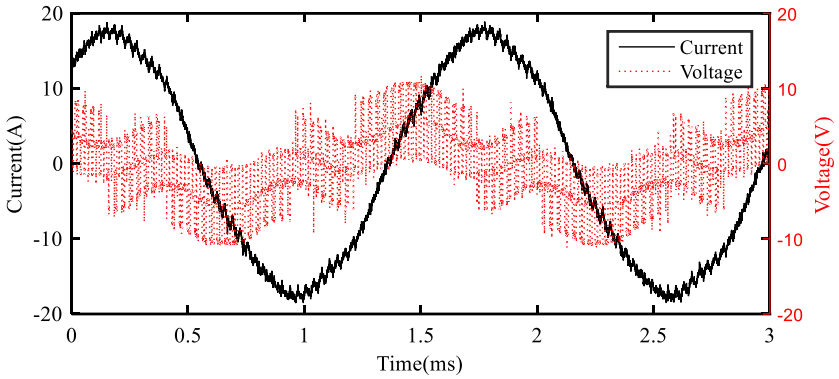
Current
Voltage
Current(A)
Voltage(V)
Time(ms)
20
10
0
-10
-20
0
0.5
1
1.5
2
2.5
3

(a)

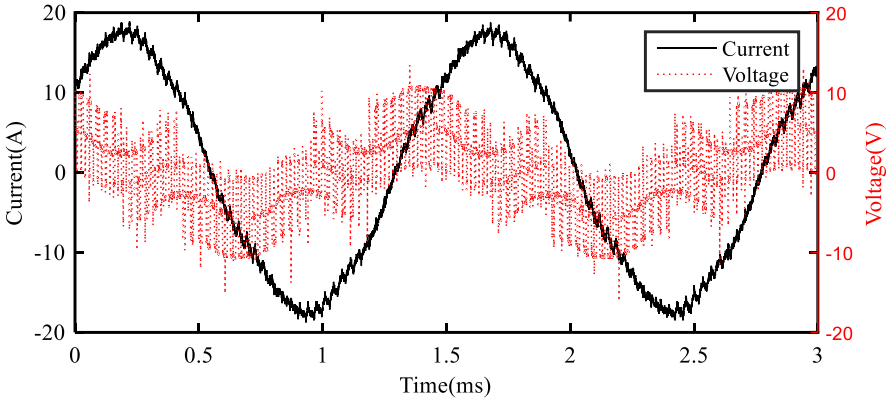
Current
Voltage
Current(A)
Voltage(V)
Time(ms)
20
10
0
-10
-20
0
0.5
1
1.5
2
2.5
3

(b)

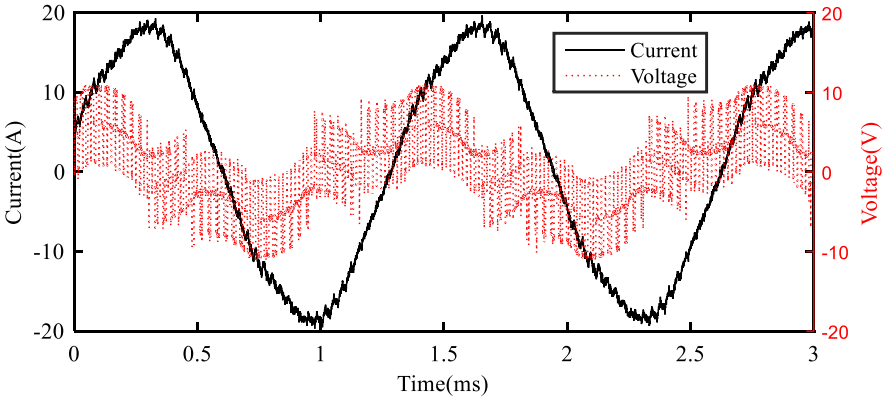
Current
Voltage
Current(A)
Voltage(V)
Time(ms)
20
10
0
-10
-20
0
0.5
1
1.5
2
2.5
3

(c)

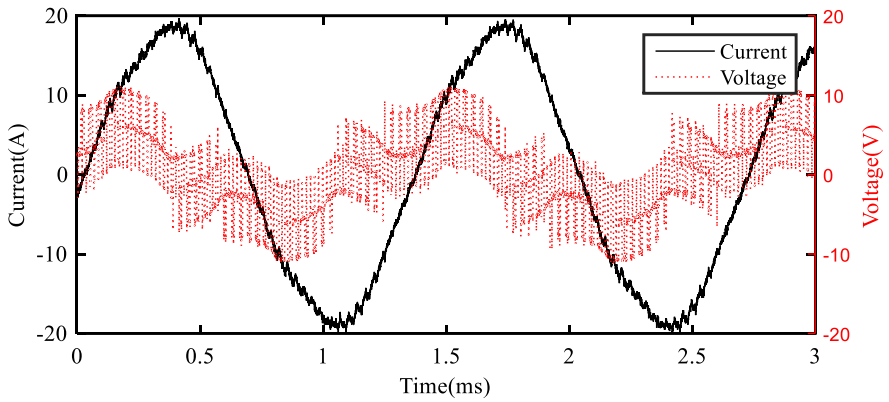

(d)

Figure 6.28 TSRM current and voltage waveform with different commutation anlges(fan blade radius = 26mm, *Vdc* = 14V): (a) φ=45°; (b) φ=55°; (c) φ=75°; (c) φ=95°.

Table 6-XXIV TSRM dynamic performance between speeds of 10,000 and 30,000 rpm with a fan blade radius of 26mm, *Vdc* = 14V.

DC current(A)	5.97	7.02	7.23	7.2
Phase peak current(A)	18.89	18.89	19.70	19.70
Commutation angle (ele. deg.)	45	55	75	95
Speed (RPM)	18611	20190	22335	22167
Motor input power (W)	62.78	69.64	81.35	82.23
Copper losses (W)	10.44	10.22	11.27	11.82

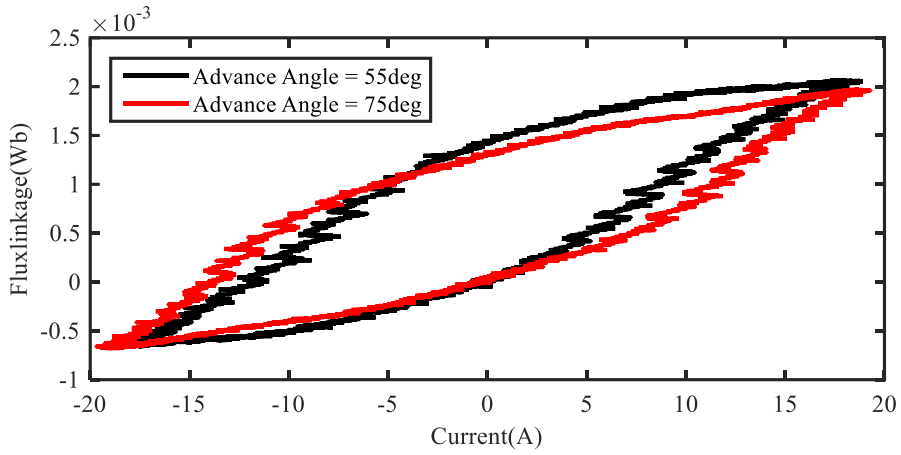

Figure 6.29 TSRM energy conversion curve around 30,000 rpm validation test with fan blade radius = 26mm, *Vdc* = 14V.

As shown in Table 6-XXIV, a higher excitation angle can result in better utilize of DC bus voltage. There will be a larger energy conversion curve, as shown in Figure 6.29. This leads to higher output torque. The reason is that inductance is different in d-axis and q-axis. However, the maximal speed is only 22.3krpm. The reason is mainly caused by the DC bus voltage limitation. Because of that the wire connection and control during the validation test, the same DC bus voltage will result in different phase voltage in the two prototyped machine. Since the switching frequency of TSRM is limited to 30kHz because of its hardware, and switch frequency of CSRM is 100kHz. In the control of TSRM, it maximal phase voltage is set as Equation 6-3. $\frac{1}{\sqrt{3}}$ is for the conversion between phase voltage and line voltage. And 0.8 is to compensate for the hardware control limitation of TSRM.

$$V_{saturation} = 0.8 \times \frac{V_{dc}}{\sqrt{3}} \qquad \text{Equation 6-2}$$

However, because of that the wire connection and control during the validation test, the same DC bus voltage will result in different phase voltage in the two prototyped machine. Since the switching frequency of TSRM is limited to 30kHz because of its hardware, and switch frequency of CSRM is 100kHz. In the control of TSRM, it maximal phase voltage is set as Equation 6-3. $\frac{1}{\sqrt{3}}$ is for the conversion between phase voltage and line voltage. And 0.8 is to compensate for the hardware control limitation of TSRM. For the consistent maximal phase voltage, the DC bus voltage of TSRM should be at least 30V. With a DC bus voltage of 24V, TSRM can reach up to 30,000 rpm as shown in Figure 6.28 by tuning the commutation angle, loaded by fan blade radius of 26mm. A higher DC voltage will achieve even higher speed as shown Figure 6.31. Their energy conversion curves are compared in Figure 6.32.

$$V_{saturation} = 0.8 \times \frac{V_{dc}}{\sqrt{3}} \qquad \text{Equation 6-3}$$

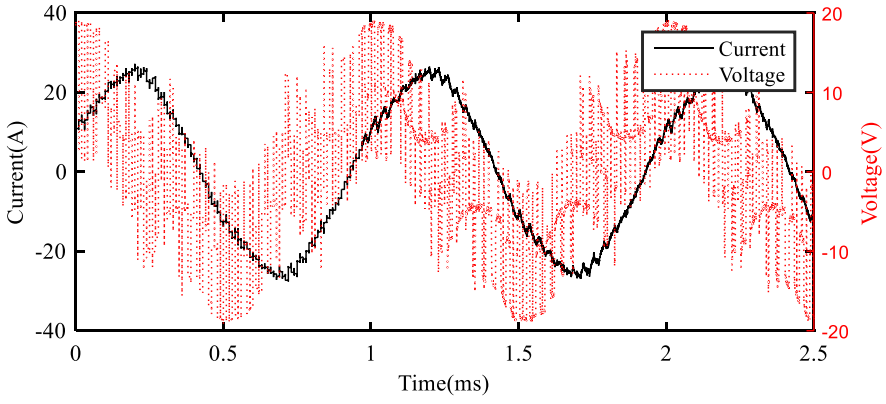

Figure 6.30 TSRM current and voltage waveforms at 29,998rpm with fan blade radius = 26mm, V_{dc} = 24V, I_{ss} = 24A, φ= 63°.

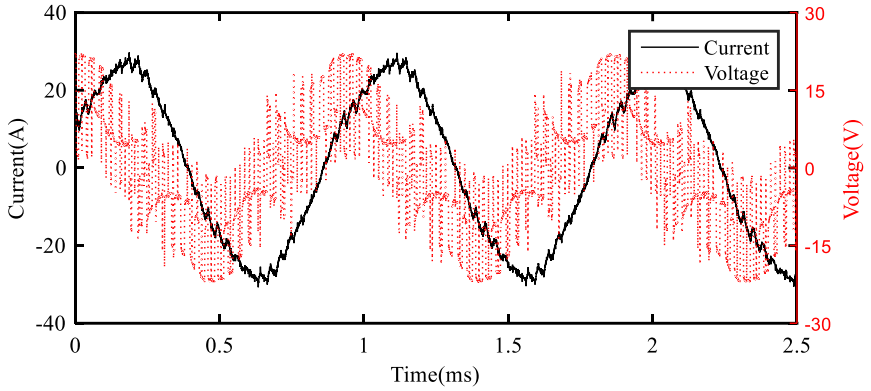

Figure 6.31 TSRM current and voltage waveforms at 32,370rpm with fan blade radius = 26mm, Vdc = 28V, Iss = 24A, φ= 57°.

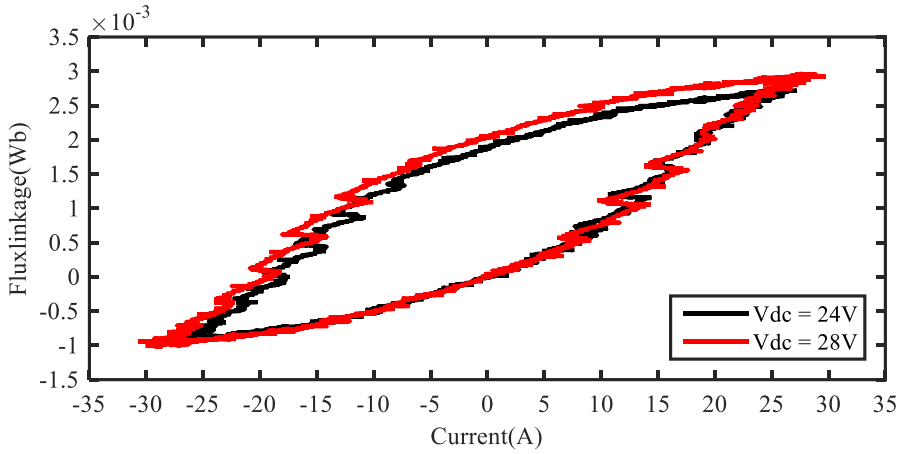

Figure 6.32 TSRM energy conversion curves at 30,000 rpm with unequal id & iq, different DC voltage, fan blade radius = 26mm.

Table 6-XXV TSRM dynamic performance comparison with different DC bus voltage at speed around 30,000 rpm, fan blade radius = 26mm.

DC voltage(V)	24	28
Angle (ele. Deg.)	63	57
DC current(A)	10.1	10
Phase peak current(A)	27.22	29.75
Speed (RPM)	29,998	32,370
Motor input power (W)	207.66	254.48
Copper losses (W)	21.20	25.32

As shown in Table 6-XXV, higher DC bus voltage will introduce more input power, and therefore result in larger torque output. With a fixed fan load, it will reach higher maximal speed.

With the same fan load, CSRM and TSRM are compared at the speed of 30,000 rpm as their energy conversion curves shown in Figure 6.35. And dynamic current/voltage waveform previously presented in Figure 6.33(a) and Figure 6.34. They are also controlled with similar DC copper losses. It shows to produce a similar output torque and with a similar amount of DC copper losses, TSRM requires much higher electric input power.

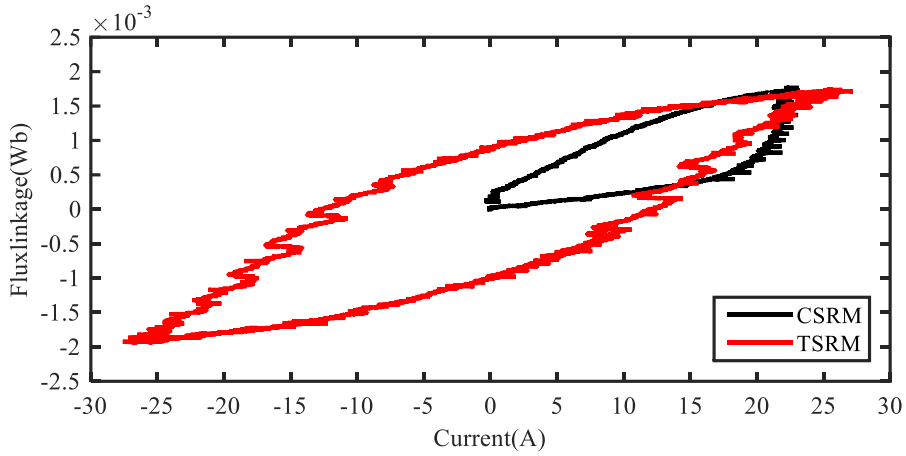

Figure 6.35 CSRM and TSRM energy conversion comparison at 30,000 rpm validation test.

With the dynamic current and voltage waveform recorded during the test, the electric input power and DC copper losses can be easily calculated. Based on the torque estimation model obtained in Section 6.5.2, their dynamic torques are estimated based on the measured dynamic phase currents.

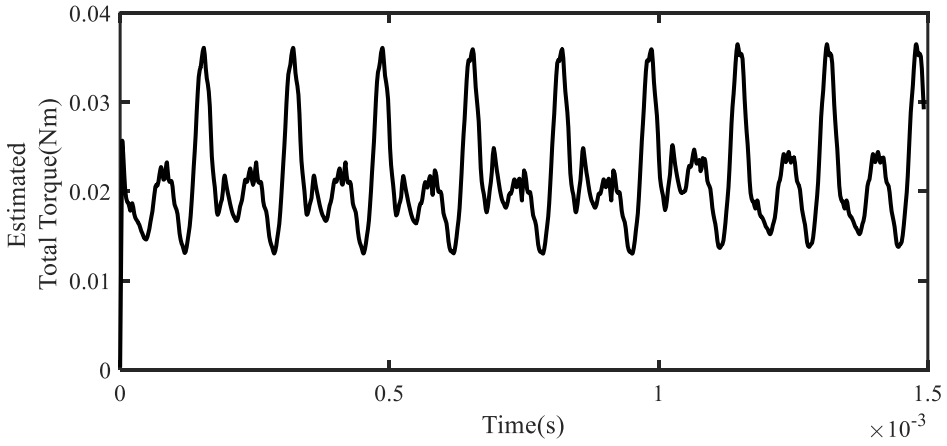

(a)

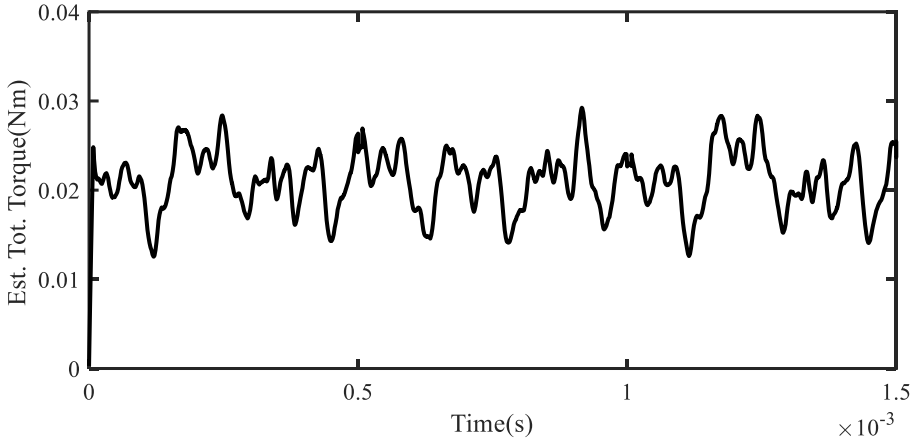

(b)

Figure 6.36 Estimated dynamic torque based on record dynamic current at 30,000 rpm with detail presented Table 6-XXIX: (a) CSRM, (b) TSRM.

Table 6-XXVI CSRM and TSRM test performance comparison at 30,000 rpm with fan blade radius of 26mm.

	CSRM	TSRM
RPM	30150	29998
DC voltage(V)	14	24
Ref. peak current(A)	24	24
Control Angle	45° to 80°, mech. Angle, duty cycle = 0.8	63° ele. angle
Input power(W)	120.7	207.66
Copper losses (W)	20.23	21.20
Est. Ave. Torq. (mNm)	21.71	21.69
Est. Torq. Ripple(%)	108.14	74.19
Est. AC losses(W)	31.92	118.32
Eff.(%)	56.79	32.81

The test in Table 6-XXIX is under the same fan condition. The very similar maximal speed indicates the very close output torque with similar DC copper losses. This is validated by the estimated average torque of 21.7mNm. In the meantime, the estimated dynamic torque based on recorded phase current and measured inductance/resistance profile also suggest that CSRM yields higher torque ripples that TSRM. However, TSRM

suffers almost four times AC losses compared to CSRM. Because of the significant AC losses, the efficiency of TSRM is much lower than that of CSRM.

6.5.4. Dynamic Test for Speeds of up to 50,000 rpm.

In the prototyped machine, there is significant windage and friction torque. However, they are still part of the electromagnet output torque. With further mechanical improvement, they could be much better controlled, which is not the focus of this thesis. In the dynamic test of the two machines up to the speed of 50,000 rpm, they are both without any extra load. The fan has been removed from the shaft.

- ***CSRMs***

To reach the demand speed, the PWM duty cycle is first tuned. But the commutation angles are still controlled as turn-on angle = 45°, and turn-off angle = 80°. The dynamic current/voltage waveforms are recorded and presented in Figure 6.37. And their energy conversion curves are drawn in Figure 6.38. Accordingly, a high PWM duty cycle leads to higher phase current; and therefore produce more output torque. However, with the fix DC bus voltage for a higher speed up to 50,000, the current variation is limited. Thus, even with a 100% duty cycle, CSRM can only reach a peak current of 20A and maximal speed of 44,800rpm, with detail presented in Table 6-XXVII.

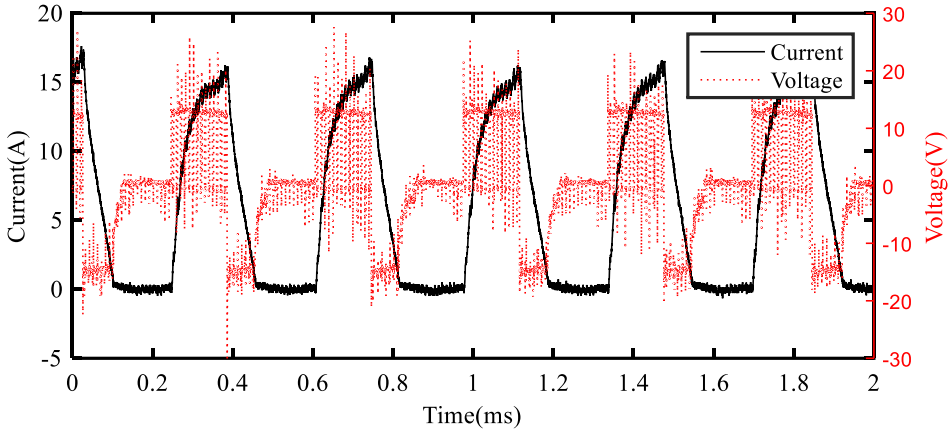

(a)

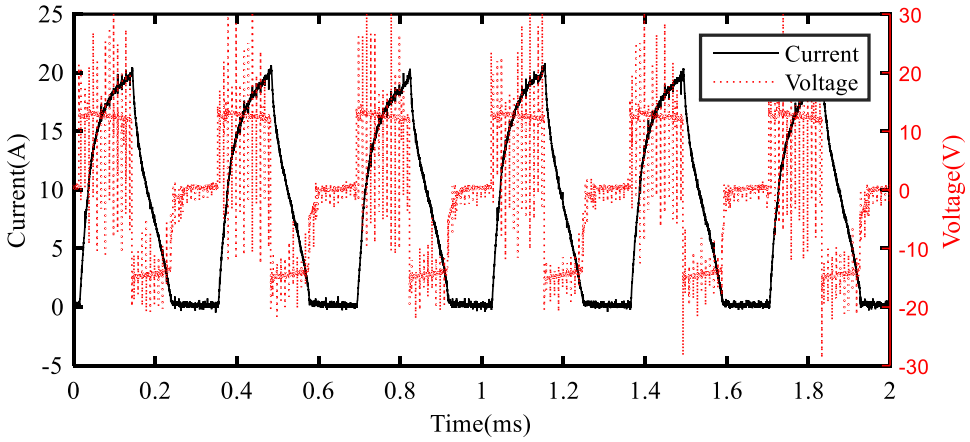

(b)

Figure 6.37 CSRM current and voltage waveform without extra load– turn on = 45°; turn-off = 80°: (a)duty cycle = 0.6; (b)duty cycle = 1.0.

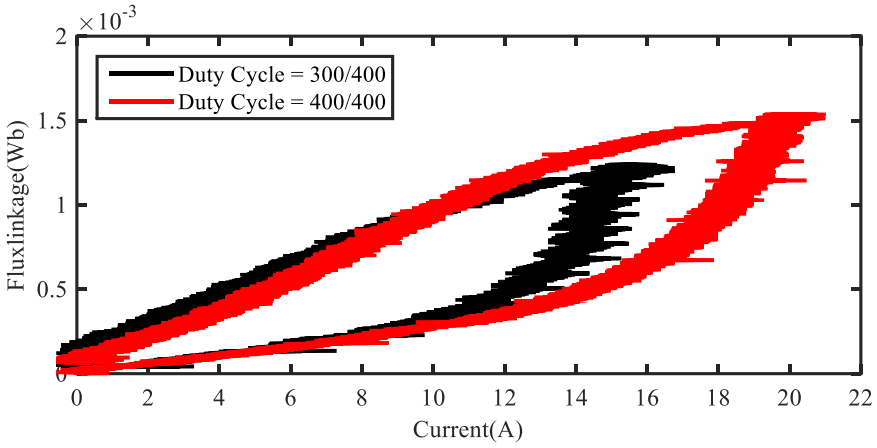

Figure 6.38 CSRM energy conversion curve around 50,000 rpm validation test– turn on = 45°; turn-off = 80°.

Table 6-XXVII CSRM dynamic performances with different duty cycle at 50,000 rpm without the extra load.

DC voltage(V)	14	
Phase peak current(A)	16.80	20.83
Commutation angle (mech. deg.)	45°-80°	
PWM duty cycle	0.6	1.0
Speed (RPM)	42700	44800
Motor input power (W)	64.87	102.36
Copper losses (W)	8.70	14.20

Considering the high speed, an advanced angle of 5 mechanical degrees is added to the control. With a full duty cycle, CSRM without extra load can reach a maximal speed of 52,000 rpm as its current/voltage waveform shown in Figure 6.39.

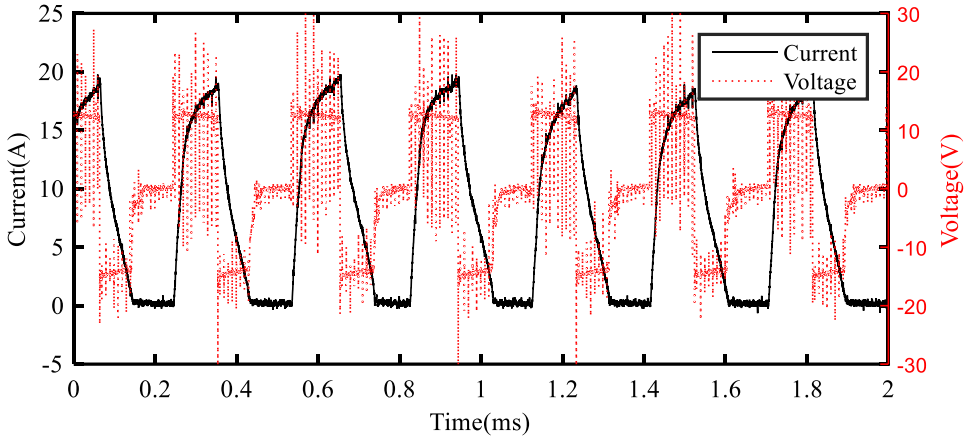

(a)

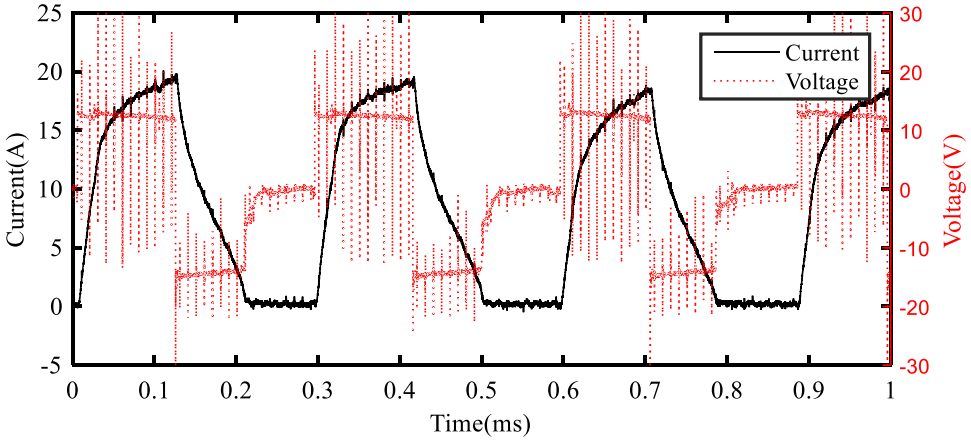

(b)

Figure 6.39 CSRM current and voltage waveform with advanced commutation angle around 50,000 rpm validation test– turn on = 40°; turn-off = 75°:(a) two-cycles; (b) one-cycle.

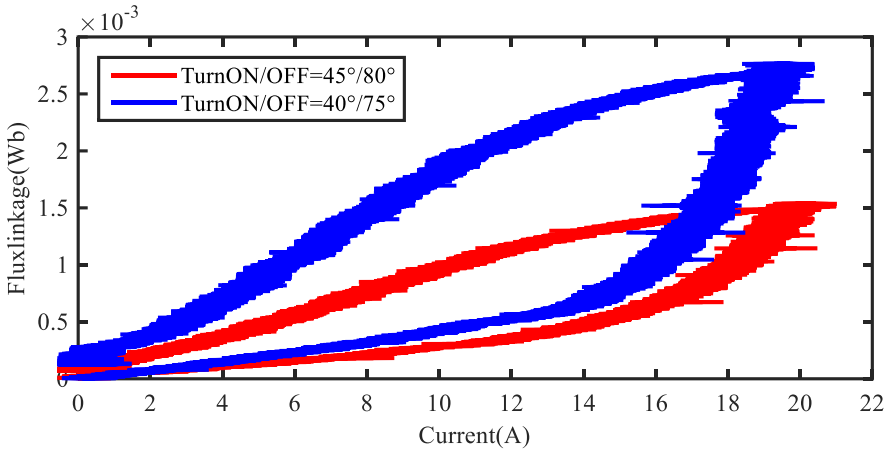

Figure 6.40 CSRM energy conversion curve with different commutation angle around 50,000 rpm validation test - PWM duty cycle = 1.0.

Table 6-XXVIII CSRM dynamic performance with different commutation angle at 50,000 rpm without the extra load.

DC voltage(V)	14	
Phase peak current(A)	20.83	19.81
PWM duty cycle	1.0	
Commutation angle (mech. deg.)	45-80	40-75
Speed (RPM)	44800	52000
Motor input power (W)	102.36	114.9
Copper losses (W)	14.20	13.82

As shown in Figure 6.40, an advanced commutation angle will introduce an earlier current rising and convert more electrical power to mechanical power. The detail performance difference between different commutation angle is presented in Table 6-XXVIII.

- ***TSRMs***

First of all, different peak phase current is studied. To be able to reach the demanded current, higher DC bus voltage is used for a higher phase current. The comparison between these two tests has been presented in Figure 6.41 and Figure 6.42. From Figure 6.41, it shows that the system control ability is much reduced with higher voltage at higher speed since the switching frequency is only 30 kHz in TSRM compared to 100kHz in CSRM. In Figure 6.42, it shows a higher phase current/voltage could introduce more energy conversion during its rotation.

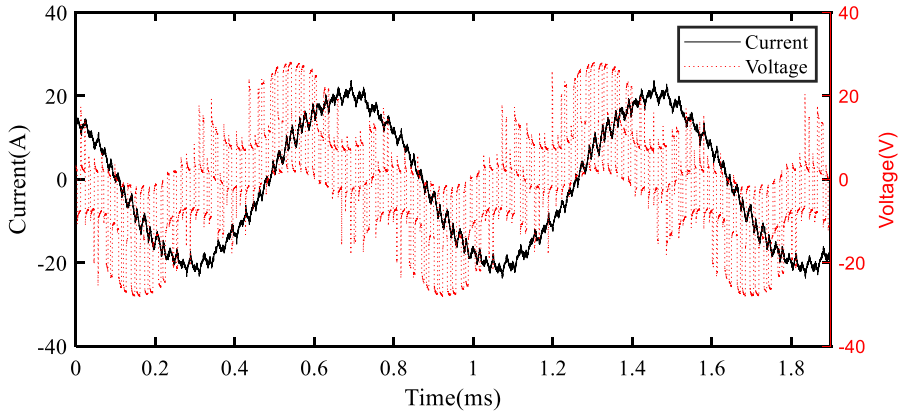

(a)

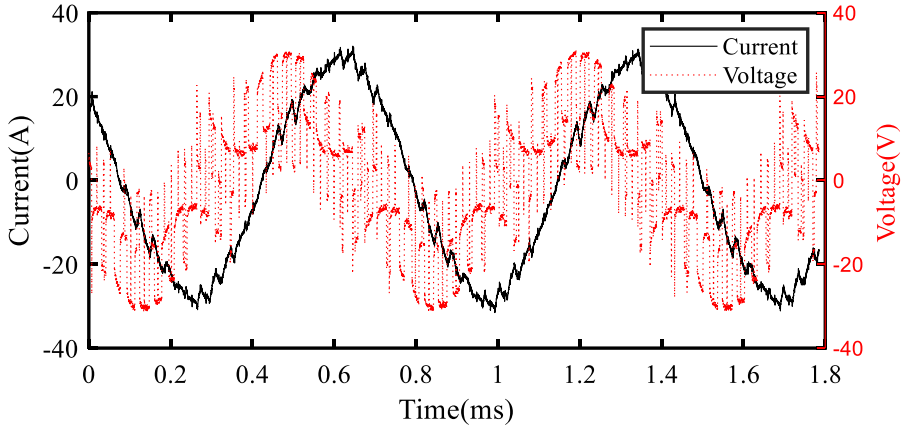

(b)

Figure 6.41 TSRM current and voltage waveform without extra load– advance angle = 45°:(a) Vdc = 36V; Ipk = 20A; (b) Vdc = 38V; Ipk = 24A.

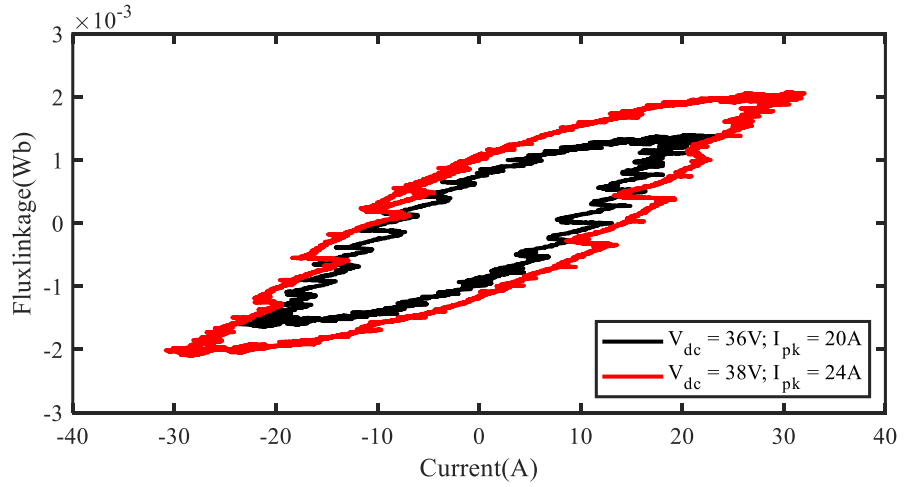

Figure 6.42 TSRM energy conversion curve without extra load with different DC voltage and peak phase current.

Their electromagnetic torque is estimated through the model presented in Section 6.5.2, with estimated results stated in Table 6-XXIX. Accordingly, the maximal speed is higher with a higher phase current. However, there is significant power consuming. It shows that

the speed gets 8% higher with a rise of 105% more power input. With a relatively low DC copper resistance change, most of the losses go as iron losses and AC copper losses, which is highly dependent on frequency.

Table 6-XXIX. TSRM dynamic performance with different peak phase current and DC voltage around maximal speed without the extra load.

DC voltage(V)	36	38
Ref. Phase peak current(A)	20	24
Excitation angle (ele. deg.)	45	
Speed (RPM)	38919	42018
Motor input power (W)	175.94	361.32
DC Copper losses (W)	14.43	27.66

Different excitation angles are also studied with results presented in Figure 6.44 and Figure 6.44. A larger excitation angle could better use the voltage and leads to higher phase current. Therefore, higher energy conversion can be achieved. However, as shown in Table 6-XXX, all those small speed rising results in significant power losses increase.

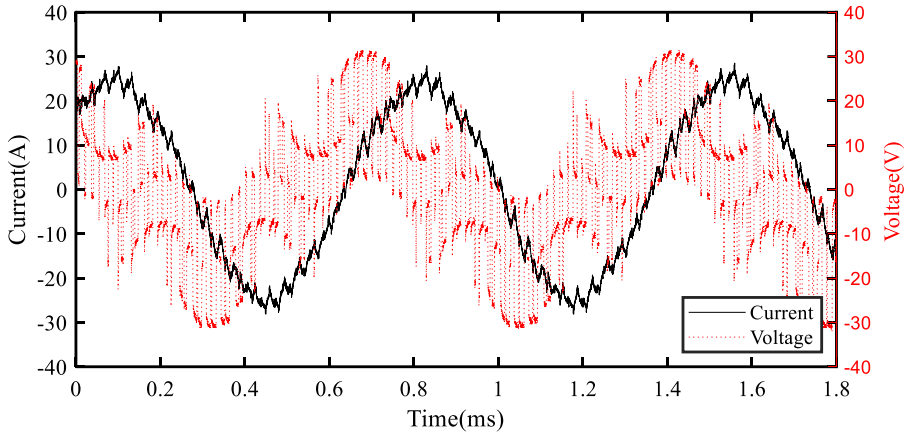

(a)

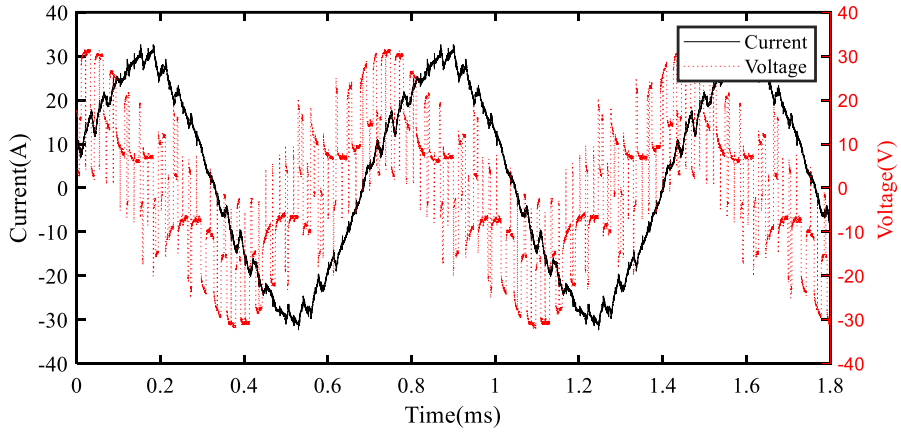

(b)

Figure 6.43 TSRM current and voltage waveform without extra load– V_{dc} = 39V:(a) advance angle = 45°; (b) advance angle = 63°.

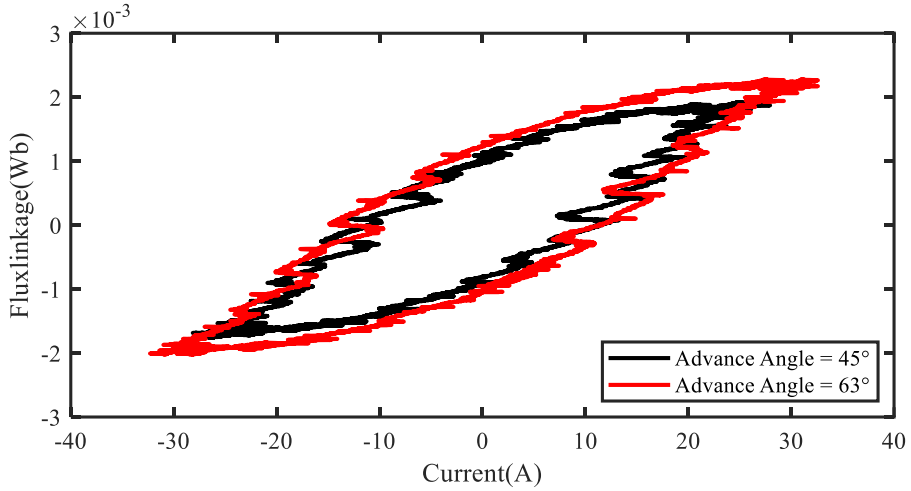

Figure 6.44 TSRM energy conversion curve without extra load with different advance angle.

Table 6-XXX TSRM dynamic performance with different Advance Angle around maximal speed without the extra load.

DC voltage(V)	39	
DC current(A)	10.55	11.14
Excitation Angle (ele. deg.)	45	63
Speed (RPM)	41000	41850
Motor input power (W)	255.67	368.99
Copper losses (W)	20.94	28.96

Considering significant power losses, especially iron losses, increase in TSRM at speed over 40,000 rpm, TSRM is suggested to operate below 40krpm. For the same DC copper losses, CSRM and TSRM are compared in Table 6-XXXI.

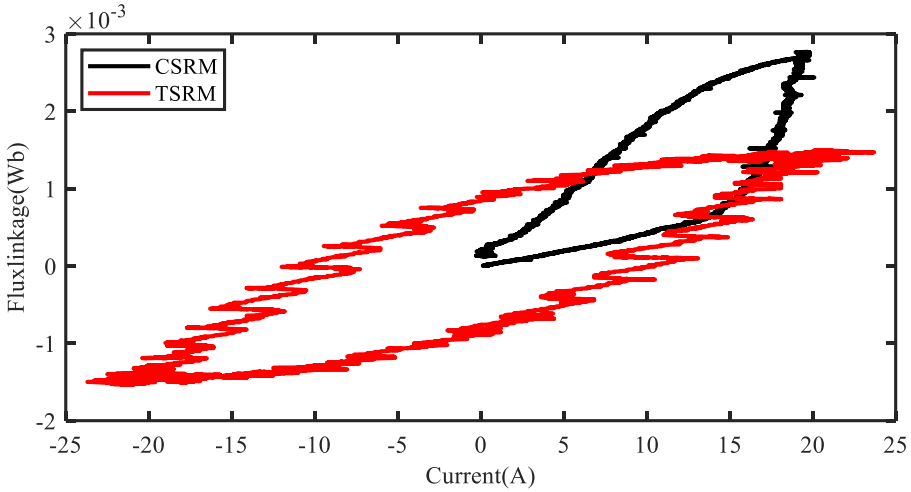

Figure 6.45 CSRM and TSRM energy conversion comparison at maximal speed without extra load – the same copper losses are controlled as Table 6-XXXI.

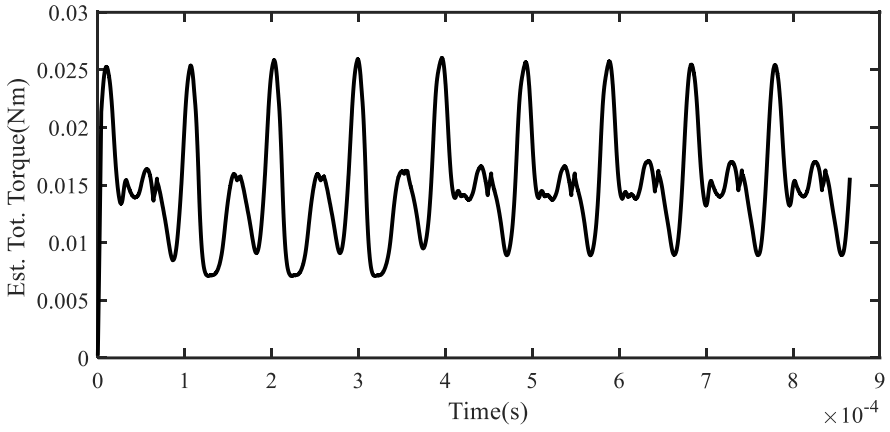

(a) CSRM

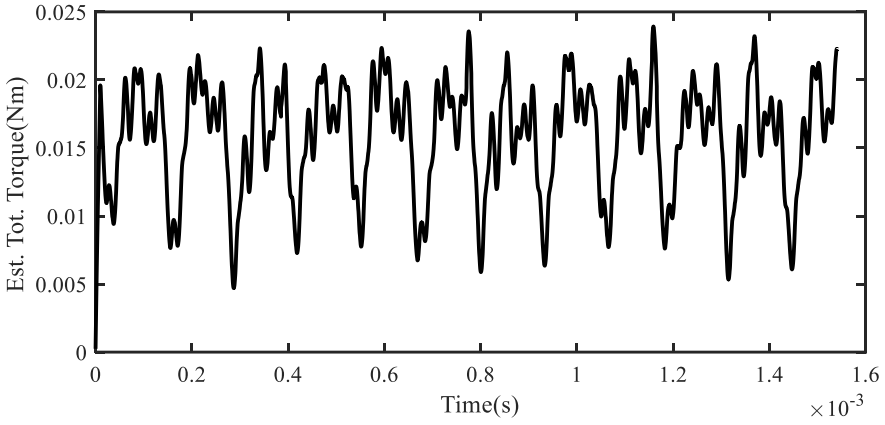

(b) TSRM

Figure 6.46 Estimated CSRM and TSRM torque performance as detail stated Table 6-XXXI.

Table 6-XXXI CSRM and TSRM test performance comparison at maximal speed without the extra load

	CSRM	TSRM
DC voltage(V)	14	36
Phase peak current(A)	19.81	23.72
Angle Shift(deg.)	40-75	45
Speed (RPM)	52000	38919
Motor input power (W)	114.9	175.94
Copper losses (W)	13.82	14.43
Est. Ave. Torq. (mNm)	15.38	15.86
Est. Torq. Ripple(%)	123.16	117.16
Est. AC losses(W)	17.35	96.87
Eff.(%)	72.87	36.74

In Table 6-XXXI, it shows the CSRM and TSRM has about the same DC copper losses and torque performance. However, the maximal rotation speed is different from the same test bench setting. The reason could be a different bearing friction/windage resistance torque in the TSRM after a long-time operation at higher bearing temperature.

As for the AC losses, TSRM generates almost 5 times iron losses than TSRM. Such a high core loss will increase core material temperature rise. Higher temperature increases

the permeability decrease in a rotated magnetic domain. This behavior leads in general to smaller magnetic saturation levels when the temperature rises. Such a characteristic will also reduce TSRM's output torque.

Considering all the above, CSRM is a better candidate for high-speed operation compared to TSRM.

6.6. Summaries.

The author tries to make a consistent comparison between these two prototyped SRMs. However, there are still things which are out of the author's controllability. To avoid confusion, they are clarified here first.

- During the prototyping, copper resistance has been well controlled via the copper wire used and the number of turns wounded. However, their iron losses and magnetic performance are highly dependent on the material used and the machining technologies used during prototyping. It is widely known that the cutting process of a small stator core and the welding step afterward led to a significant change in the material properties, resulting in increased iron. It in terms of modifications of the BH hysteresis loops and the resulting iron losses increases and magnetic property deteriorates.
- The same position encoder is applied to the two SRMs. However, there is an unavoidable error which could be introduced during the installation process. And

those errors could potentially affect machine performance, especially at high-speed operation.

- Because of the characteristic difference between the two SRMs, different control methods are applied. PI controller and DQ model are used on TSRM, while they both increase the control difficulties of TSRM.
- Because of the limitation of power electronic hardware, CSRM is controlled with switching frequency of 100 kHz while TSRM is tested under 30 kHz via a three-phase commercial PMSM converter is used instead of building a 12-switch converter. A three-phase asymmetric inverter is applied for CSRM.
- Because of the limitation of test equipment, only torque below 10krpm is measured. For the test above this speed, phase current and voltage are measured. The two machines are compared with the same load and copper losses.

Here are some conclusions, drawn from the prototyped machine and their test results:

- Toroidal winding is much easier for hand-winding during prototyping.
- The active part of TSRM is about 10% lighter than CSRM.
- Phase resistance of TSRM is about 37% lower than that of CSRM.
- With the same copper losses of 21W (DC current injected), temperature rising of TSRM is about 7.5 degrees lower than CSRM.
- Inductance variation of prototypes is reduced by 30% for both motors because of the prototyping technique. Static torque is reduced by 30% for both motors.
- CSRM is tested up to 52,000 rpm; and TSRM 42,000 rpm.

- Iron losses are much higher than simulation results because of the applied material property and welding technique. TSRM has much higher iron losses than CSRM.
- For CSRM with three-phase asymmetric inverter and TSRM with commercial three-phase half-bridge, higher DC voltage is required for TSRM.
- TSRM has better torque output at the lower speed because copper losses are dominant. CSRM has more advantages at a higher speed because of its lower iron losses and lower DC voltage requirement.

Chapter 7 Conclusions and Future Research

7.1. Conclusions.

The thesis has studied the application of SRMs for high-speed vacuum cleaners. Besides the conventional SRM winding, a toroidal winding is introduced and compared against CSRM. The operation principles of both these motors have been studied in detail, especially focusing on the induction and torque generation profiles.

Based on the analysis, a three-phase six-stator-pole, four-rotor-pole CSRM was designed and optimized with a speed of up to 50,000 rpm. A TSRM was resized based on CSRM to achieve the same envelope dimension. The static analysis shows that TSRMs have relatively higher flux localization and are more sensitive to magnetic saturation. Moreover, TSRMs are at risk of high iron losses. Furthermore, because of the decentralization of the magneto-motive force in TSRMs, they have more flux leakage. This flux leakage results in torque cancellations in TSRM. However, considering TSRM's advantage of reduced copper losses, it is still attractive.

The conventional asymmetric inverter, together with angular position control, was applied to CSRM. Two 12-switch inverter topologies were proposed for TSRMs to achieve the equivalent dynamic magnetic field as that of a CSRM. In addition, the commercial three-phase half-bridge inverter with sinusoidal was also proposed as a solution to drive TSRMs. The dynamic performance was evaluated and compared between CSRM and TSRM using Matlab/Simulink models with inductance/torque profiles calculated from FEA.

Following the comparative analysis, CSRM and TSRM are both prototyped and tested. However, because of the limitation of power electronic hardware, TSRM was only tested via a three-phase commercial PMSM converter instead of building a 12-switch converter. A three-phase asymmetric inverter is applied for CSRM and controlled with a switching frequency of 100 kHz while the switching frequency of the half-bridge inverter is only 30 kHz for TSRM. The following conclusions can be drawn based on the results of this research.

The active part of the TSRM is about 10% lighter than that of the CSRM because of the stator size reduction. Toroidal winding is easier for hand-winding during prototyping. The prototyped phase resistance of the TSRM is about 37% lower than that of the CSRM. Because of the reduced filling factor and additional connection wire among coils, the phase resistance of both SRMs is higher than analytical value. It is 60% higher for the CSRM and 46% higher for the TSRM. The resistance comparison indicates thermal performance variation between CSRM and TSRM, from the heat generation point of view. In addition, their heat radiation also differs because of the distinct wire locations. With the same copper losses of 21W, the temperature increase of the TSRM is about 7.5 degrees lower than that of the CSRM. Inductance variation of prototypes is reduced by 30% for both CSRM and TSRM. As a result of the inductance change, the static torque is also reduced by 30% for both motors. The potential reason for this is the material difference between the simulation datasheet and actual lamination sheet.

The CSRM was tested for speeds of up to 52,000 rpm and the TSRM for speeds of up to 42,000 rpm. In case of the CSRM with three-phase asymmetric inverter and the TSRM

with a commercial three-phase half-bridge, higher DC voltage is required for the TSRM. Tested iron losses of both motors are much higher than those during their simulation. Because the applied material is different from that used during analysis and the welding technique also significantly increases iron losses in the prototyped motors. Moreover, the comparison shows TSRM has much higher iron losses than CSRM.

Given the above, both CSRM and TSRM were prototyped and tested for speed above 40,000 rpm with promising output torque. At lower speeds, TSRM has better torque performance, because copper losses are dominant. At higher speeds, CSRM has more advantages, because of its lower iron losses and lower DC voltage requirement.

7.2. Future Research.

In future research, the author will focus on an iron losses reduction analysis, which will include an accurate iron losses estimation model, a material property test, and a lower phase/pole number SRM design. Following that, a comprehensive thermal comparison between CSRM and TSRM is necessary. In addition to this, it has been found that the position accuracy plays an important role in a high-speed SRM drive. Considering the cost and performance of position sensors at high speeds, sensorless control on high-speed CSRM and TSRM will be another focus of the author's future work.

7.3. Publications in Print and Planned

[1] **J. Lin**, "Axial Flux Switched Reluctance Machines" in *Switched Reluctance Motor Drives: Fundamentals to Applications*: CRC Press, 2018, Ch. 15, pp. 735-755.

[2] J. Dong, B. Howey, B. Danen, **J. Lin**, J. W. Jiang, B. Bilgin and A. Emadi, "Advanced dynamic modeling of the three-phase mutually-coupled switched reluctance machine", *IEEE Transactions on Energy Conversion*, vol. 33, no. 1, pp. 146-154, July 2017.

[3] S.M. Castano, B. Bilgin, **J. Lin**, and A. Emadi, "Radial forces and vibration analysis in an external-rotor switched reluctance machine," *IET Electric Power Application*, vol. 11, no. 2, pp 252 – 259, Feb. 2017.

[4] **J. Lin**, T. Lambert, Y. Yang, B. Bilgin, R. Lankin, A. Emadi, "A novel axial flux switched reluctance motor with multi-level air gap geometry," accepted to present at 2016 *IEEE Electrical Power and Energy Conference*, Ottawa, Canada, 2016.

[5] **J. Lin**, P. Suntharalingam, N. Schofield, and A. Emadi, "Comparison of high-speed switched reluctance machines with conventional and toroidal windings," *in Proc. 2016 IEEE Transportation Electrification Conference and Expo*, Dearborn, MI, 2016, pp. 1-6.

[6] F. Peng, **J. Lin**, J. Ye, and A. Emadi, “Optimal calculation method for control of switched reluctance motor,” *in Proc. 2015 IEEE Transportation Electrification Conference and Expo*, Dearborn, MI, 2015, pp. 1-6.

[7] **J. Lin**, P. Suntharalingam, N. Schofield, and A. Emadi, “High-speed switched reluctance machine design with toroidal-windings,” *in Proc. 2015 Energy Conversion Congress and Exposition*, Montreal, Canada, 2015, pp. 1789–1794

[8] **J. Lin**, N. Schofield, and A. Emadi, "External-rotor 6–10 switched reluctance motor for an electric bicycle", *IEEE Transactions on Transportation Electrification*, vol.1,no.4,pp. 348-356, Dec.2015.

References

[1] A. De Almeida, P. Fonseca, B. Schlomann, and N. Feilberg, "Characterization of the household electricity consumption in the EU, potential energy savings and specific policy recommendations," *Energy Build.*, vol. 43, no. 8, pp. 1884–1894, 2011.

[2] H. Kawaguchi and T. Oikawa, "High-efficiency motors for air-conditioner compressors," *Mitsubishi Electr. Adv.*, vol. 103, pp. 2–4, 2003.

[3] "Best selling vacuum cleaners," *allergy buyers club*. [Online]. Available: https://www.allergybuyersclub.com/best-selling-vacuum-cleaners.html. [Accessed: 08-Aug-2019].

[4] B. S. Yoon and A. J. Jetter, "Investigation of different perspectives between developers and customers : robotic vacuum cleaners," in *Proceedings of PICMET '14 Conference: Portland International Center for Management of Engineering and Technology; Infrastructure and Service Integration*, 2014, pp. 2307–2313.

[5] L. Stinson, "Dyson aims for a cordless revolution with tiny 120,000 rpm motor," 2014. [Online]. Available: available: http://www.wired.com/2014/01/dysons-new-vacuum-motor-spur-cordless-revolution. [Accessed: 08-Aug-2019].

[6] "Vacuum cleaner motor," *CHIAPHUA COMPONENTS*. [Online]. Available:

http://www.cclmotors.com/website/eng/product-list?cat=11. [Accessed: 08-Aug-2019].

[7] B. Steve, "Dyson vacuums 104,000 rpm brushless DC technology," *Electronics Weekly.com*, 2009. [Online]. Available: https://www.electronicsweekly.com/market-sectors/power/dyson-vacuums-104000 rpm-brushless-dc-technology-2009-06/. [Accessed: 08-Aug-2019].

[8] J. Lee, K. B. Jang, S. H. Won, and T. H. Kim, "Starting and high-speed driving of single-phase flux-reversal motor for vacuum cleaner," *IEEE Trans. Magn.*, vol. 41, no. 10, pp. 3967–3969, 2005.

[9] A. L. Sebok, "Simplified air density correction of vacuum cleaner performance data," *IEEE Trans. Ind. Gen. Appl.*, vol. IGA-6, no. 1, pp. 88–94, 1970.

[10] Z. Kolondzovski, A. Arkkio, J. Larjola, and P. Sallinen, "Power limits of high-speed permanent-magnet electrical machines for compressor applications," *IEEE Trans. Energy Convers.*, vol. 26, no. 1, pp. 73–82, 2011.

[11] C. Bailey, D. M. Saban, and P. Guedes-Pinto, "Design of high-speed direct-connected permanent-magnet motors and generators for the petrochemical industry," *IEEE Trans. Ind. Appl.*, vol. 45, no. 3, pp. 1159–1165, 2009.

[12] N. Bianchi, S. Bolognani, and F. Luise, "Potentials and limits of high-speed PM motors," *IEEE Trans. Ind. Appl.*, vol. 40, no. 6, pp. 1570–1578, 2004.

[13] M. A. Rahman, A. Chiba, and T. Fukao, “Super high speed electrical machines - summary,” in *IEEE Power Engineering Society General Meeting, 2004.*, 2004, vol. 2, no. iii, pp. 1272–1275.

[14] A. Binder and T. Schneider, “High-speed inverter-fed AC drives,” in *International Aegean Conference on Electrical Machines and Power Electronics and Electromotion ACEMP’07 and Electromotion’07 Joint Conference*, 2007, pp. 9–16.

[15] D. Gerada, A. Mebarki, N. L. Brown, C. Gerada, A. Cavagnino, and A. Boglietti, “High-speed electrical machines: technologies, trends, and developments,” *IEEE Trans. Ind. Electron.*, vol. 61, no. 6, pp. 2946–2959, 2014.

[16] D. Fodorean, “Study of a high-speed motorization with improved performances dedicated for an electric vehicle,” *IEEE Trans. Magn.*, vol. 50, no. 2, pp. 921–924, 2014.

[17] E. Gouda, S. Mezani, L. Baghli, and A. Rezzoug, “Comparative study between mechanical and magnetic planetary gears,” *IEEE Trans. Magn.*, vol. 47, no. 2, pp. 439–450, Feb. 2011.

[18] J. F. Gieras and J. Saari, “Performance calculation for a high-speed solid-rotor induction motor,” *IEEE Trans. Ind. Electron.*, vol. 59, no. 6, pp. 2689–2700, Jun. 2012.

[19] J. Lou, W. Ding, and L. Liu, “Design and control of a high-speed switched reluctance machine with conical magnetic bearings for aircraft application,” *IET*

Electr. Power Appl., vol. 7, no. 3, pp. 179–190, Mar. 2013.

[20] A. Boglietti, A. Cavagnino, A. Tenconi, and S. Vaschetto, "Key design aspects of electrical machines for high-speed spindle applications," in *IECON 2010 - 36th Annual Conference on IEEE Industrial Electronics Society*, 2010, pp. 1735–1740.

[21] J. B. Danilevich, I. Y. Kruchinina, V. N. Antipov, Y. P. Khozikov, and A. V Ivanova, "Some problems of the high-speed permanent magnet miniturbogenerators development," in *2008 18th International Conference on Electrical Machines*, 2008, pp. 1–4.

[22] D.-K. Hong, B.-C. Woo, J.-Y. Lee, and D.-H. Koo, "Ultra high speed motor supported by air foil bearings for air blower cooling fuel cells," *IEEE Trans. Magn.*, vol. 48, no. 2, pp. 871–874, Feb. 2012.

[23] A. Boglietti, R. I. Bojoi, A. Cavagnino, P. Guglielmi, and A. Miotto, "Analysis and modeling of rotor slot enclosure effects in high-speed induction motors," *IEEE Trans. Ind. Appl.*, vol. 48, no. 4, pp. 1279–1287, Jul. 2012.

[24] X. Jannot, J.-C. Vannier, C. Marchand, M. Gabsi, J. Saint-Michel, and D. Sadarnac, "Multiphysic modeling of a high-speed interior permanent-magnet synchronous machine for a multiobjective optimal design," *IEEE Trans. Energy Convers.*, vol. 26, no. 2, pp. 457–467, Jun. 2011.

[25] D. Gerada, A. Mebarki, N. L. Brown, K. J. Bradley, and C. Gerada, "Design aspects of high-speed high-power-density laminated-rotor induction machines,"

IEEE Trans. Ind. Electron., vol. 58, no. 9, pp. 4039–4047, Sep. 2011.

[26] J. Rowlatt, "Rare earths: Neither rare, nor earths," *BBC World Service*, 2014. [Online]. Available: https://www.bbc.com/news/magazine-26687605. [Accessed: 08-Aug-2019].

[27] "Neodynium and Praseodymium Oxide Price in China," *Investing News Network*. [Online]. Available: https://investingnews.com/company-profiles/medallion-resources-rare-earth-magnets-monazite/. [Accessed: 08-Aug-2019].

[28] J. Ahn, S. H. Won, and J. Lee, "The high-speed operation of single phase switched reluctance motor considering magnetic saturation," *J. Appl. Phys.*, vol. 99, no. 8, p. 08S103, 2006.

[29] J. L. Neto, R. Andrade, L. G. B. Rolim, A. C. Ferreira, G. G. Sotelo, and W. Suemitsu, "Experimental validation of a dynamic model of a SRM used in superconducting bearing flywheel energy storage system," in *2006 IEEE International Symposium on Industrial Electronics*, 2006, pp. 2492–2497.

[30] V. Fernandez, "Rare-earth elements market: A historical and financial perspective," *Resour. Policy*, vol. 53, no. March, pp. 26–45, 2017.

[31] Y. Takano *et al.*, "Design and analysis of a switched reluctance motor for next generation hybrid vehicle without PM materials," *2010 Int. Power Electron. Conf. - ECCE ASIA -*, no. c, pp. 1801–1806, Jun. 2010.

[32] M. Besharati, G. Atkinson, J. D. Widmer, V. Pickert, and K. R. Pullen, "Investigation of the mechanical constraints on the design of a super-high-speed switched reluctance motor for automotive traction," in *7th IET International Conference on Power Electronics, Machines and Drives (PEMD 2014)*, 2014, pp. 2.5.04-2.5.04.

[33] "Adura's MESA Electric Powertrain Combines Controls, Switched Reluctance Traction Motor and MicroTurbine," *Green Car Congress*, 2009. [Online]. Available: https://www.greencarcongress.com/2009/04/adura-20090420.html. [Accessed: 08-Aug-2019].

[34] "What Do Deere and LeTourneau Have in Common?," *Engineering News-Record*, 2011. [Online]. Available: https://www.enr.com/blogs/13-critical-path/post/15743-what-do-deere-and-letourneau-have-in-common. [Accessed: 08-Aug-2019].

[35] T. Nakamichi, "Nidec Shows Off Switched Reluctance Motor for EVs, HEVs," *Nikkei Electronics*, 2012. [Online]. Available: https://tech.nikkeibp.co.jp/dm/english/NEWS_EN/20120123/203839/. [Accessed: 08-Aug-2019].

[36] T. J. E. Miller, "Optimal design of switched reluctance motors," *IEEE Trans. Ind. Electron.*, vol. 49, no. 1, pp. 15–27, 2002.

[37] F. Sahin, H. B. Ertan, and K. Leblebicioglu, "Optimum geometry for torque ripple minimization of switched reluctance motors," *IEEE Trans. Energy Convers.*, vol.

15, no. 1, pp. 30–39, Mar. 2000.

[38] M. Balaji, S. Ramkumar, and V. Kamaraj, “Sensitivity analysis of geometrical parameters of a switched reluctance motor with modified pole shapes,” *J. Electr. Eng. Technol.*, vol. 9, no. 1, pp. 136–142, Jan. 2014.

[39] J. Faiz, F. Tahvilipour, and G. Shahgholian, “Performance improvement of a switched reluctance motor,” in *PIERS Proceedings*, 2012, pp. 728–732.

[40] M. Kim, H. Lee, H. Kim, and J. Byun, “A new unified design environment for optimization of electric machines based on continuum sensitivity and B-spline parametrization,” *J. Electr. Eng. Technol.*, vol. 6, no. 4, pp. 513–518, 2011.

[41] J. W. Jiang, B. Bilgin, B. Howey, and A. Emadi, “Design optimization of switched reluctance machine using genetic algorithm,” in *Proceedings - 2015 IEEE International Electric Machines and Drives Conference, IEMDC 2015*, 2016, pp. 1671–1677.

[42] J. W. Jiang, B. Bilgin, and A. Emadi, “Three-phase 24/16 switched reluctance machine for a hybrid electric powertrain,” *IEEE Trans. Transp. Electrif.*, vol. 3, no. 1, pp. 76–85, 2017.

[43] J. Lee and N. Kikuchi, “Structural topology optimization of electrical machinery to maximize stiffness with body force distribution,” *IEEE Trans. Magn.*, vol. 46, no. 10, pp. 3790–3794, Oct. 2010.

[44] J. S. Ryu, Y. Yao, C. S. Koh, S. Yun, and D. S. Kim, "Optimal shape design of 3-D nonlinear electromagnetic devices using parameterized design sensitivity analysis," *IEEE Trans. Magn.*, vol. 41, no. 5, pp. 1792–1795, May 2005.

[45] M. Balaji and V. Kamaraj, "Design optimization of switched reluctance machine using particle swarm optimization," in *2011 1st International Conference on Electrical Energy Systems*, 2011, no. 1, pp. 164–169.

[46] M. Balaji and V. Kamaraj, "Particle swarm optimization approach for optimal design of switched reluctance machine," *Am. J. Appl. Sci.*, vol. 8, no. 4, pp. 374–381, 2011.

[47] A. Kechroud, J. J. H. Paulides, and E. a. Lomonova, "B-spline neural network approach to inverse problems in switched reluctance motor optimal design," *IEEE Trans. Magn.*, vol. 47, no. 10, pp. 4179–4182, Oct. 2011.

[48] H. Zhang, W. Xu, S. Wang, Y. Huangfu, G. Wang, and J. Zhu, "Optimum design of rotor for high-speed switched reluctance motor using level det method," *IEEE Trans. Magn.*, vol. 50, no. 2, pp. 765–768, Feb. 2014.

[49] ShyShenq P. Liou and Jim Ye, "Flux distribution and core losses of switched reluctance motors," in *Proceedings of 1996 Canadian Conference on Electrical and Computer Engineering*, 1996, vol. 2, pp. 935–938.

[50] L. Morel, H. Fayard, H. Vives Fos, A. Galindo, and G. Abba, "Study of ultra high speed switched reluctance motor drive," in *Conference Record of the 2000 IEEE*

Industry Applications Conference. Thirty-Fifth IAS Annual Meeting and World Conference on Industrial Applications of Electrical Energy (Cat. No.00CH37129), 2000, vol. 1, pp. 87–92.

[51] J. M. Silveyra, a. M. Leary, V. DeGeorge, S. Simizu, and M. E. McHenry, "High speed electric motors based on high performance novel soft magnets," *J. Appl. Phys.*, vol. 115, no. 17, p. 17A319, May 2014.

[52] R. Kolano, K. Krykowski, A. Kolano-Burian, M. Polak, J. Szynowski, and P. Zackiewicz, "Amorphous soft magnetic materials for the stator of a novel high-speed PMBLDC motor," *IEEE Trans. Magn.*, vol. 49, no. 4, pp. 1367–1371, Apr. 2013.

[53] D. A. Gonzalez and D. M. Saban, "Study of the copper losses in a high-speed permanent-magnet machine with form-wound windings," *IEEE Trans. Ind. Electron.*, vol. 61, no. 6, pp. 3038–3045, 2014.

[54] E. Fairall, "Design considerations for high surface-speed and high-load switched reluctance machines," McMaster University, Hamilton, ON, Canada, 2017.

[55] S. D. Calverley, G. W. Jewell, and R. J. Saunders, "Aerodynamic losses in switched reluctance machines," *IEE Proc. - Electr. Power Appl.*, vol. 147, no. 6, p. 443, 2000.

[56] H. Yang, Y. Lim, and H. Kim, "Acoustic noise/vibration reduction of a single-phase sRM using skewed stator and rotor," *IEEE Trans. Ind. Electron.*, vol. 60, no.

10, pp. 4292–4300, Oct. 2013.

[57] J. Dong *et al.*, "Advanced dynamic modeling of three-phase mutually coupled switched reluctance machine," *IEEE Trans. Energy Convers.*, vol. 33, no. 1, pp. 146–154, 2018.

[58] B. C. Mecrow, "New winding configurations for doubly salient reluctance machines," *IEEE Trans. Ind. Appl.*, vol. 32, no. 6, pp. 1348–1356, 1996.

[59] X. Y. Ma, G. J. Li, G. W. Jewell, Z. Q. Zhu, and H. L. Zhan, "Performance comparison of doubly salient reluctance machine topologies supplied by sinewave currents," *IEEE Trans. Ind. Electron.*, vol. 63, no. 7, pp. 4086–4096, Jul. 2016.

[60] G. Li, J. Ojeda, S. Hlioui, E. Hoang, M. Lecrivain, and M. Gabsi, "Modification in rotor pole geometry of mutually coupled switched reluctance machine for torque ripple mitigating," *IEEE Trans. Magn.*, vol. 48, no. 6, pp. 2025–2034, 2012.

[61] G. J. Li, J. Ojeda, E. Hoang, M. Lecrivain, and M. Gabsi, "Comparative studies between classical and mutually coupled switched reluctance motors using thermal-electromagnetic analysis for driving cycles," *IEEE Trans. Magn.*, vol. 47, no. 4, pp. 839–847, 2011.

[62] X. Liang, G. Li, J. Ojeda, M. Gabsi, and Z. Ren, "Comparative study of classical and mutually coupled switched reluctance motors using multiphysics finite-element modeling," *IEEE Trans. Ind. Electron.*, vol. 61, no. 9, pp. 5066–5074, 2014.

[63] B. C. Mecrow, “Fully pitched-winding switched-reluctance and stepping-motor arrangements,” *IEE Proc. B Electr. Power Appl.*, vol. 140, no. 1, p. 61, 1993.

[64] R. Marlow, N. Schofield, and A. Emadi, “A continuous toroidal winding SRM with 6- or 12-switch DC converter,” *IEEE Trans. Ind. Appl.*, vol. 52, no. 1, pp. 189–198, 2016.

[65] R. Hoshi, K. Kiyota, A. Chiba, K. Nakamura, and M. Nagano, “Consideration of the winding structure of the toroidal winding switched reluctance motors,” in *19th International Conference on Electrical Machines and Systems, ICEMS 2016*, 2017, vol. 4, pp. 1–6.

[66] Ji-Young Lee, Byoung-Kuk Lee, Jung-Jong Lee, and Jung-Pyo Hong, “A comparative study of switched reluctance motors with conventional and toroidal windings,” in *IEEE International Conference on Electric Machines and Drives, 2005.*, 2005, vol. 2, pp. 1675–1680.

[67] Ji-Young Lee, Byoung-Kuk Lee, Tao Sun, Jung-Pyo Hong, and Woo-Taik Lee, “Dynamic analysis of toroidal winding switched reluctance motor driven by 6-switch converter,” *IEEE Trans. Magn.*, vol. 42, no. 4, pp. 1275–1278, 2006.

[68] J. Lin, P. Suntharalingam, F. Peng, N. Schofield, and A. Emadi, “High-speed switched reluctance machine design with toroidal-windings,” in *2015 IEEE Energy Conversion Congress and Exposition (ECCE)*, 2015, pp. 1789–1794.

[69] R. Krishnan, *Switched reluctance motor drives: Modeling, simulation, analysis,*

design, and applications. Boca Raton London New York Washington, D.C.: CRC Press, 2017.

[70] T. J. E. Miller, *Switched Reluctance Motors and Their Control*. New York, NY, USA: Oxford University Press, 1993.

[71] M. Ilic'-Spong, R. Marino, S. Peresada, and D. Taylor, "Feedback linearizing control of switched reluctance motors," *IEEE Trans. Automat. Contr.*, vol. 32, no. 5, pp. 371–379, May 1987.

[72] W. Perruquetti, *Sliding mode control in engineering*. New York, NY, USA, 2002.

[73] S. Mir, M. E. Elbuluk, and I. Husain, "Torque-ripple minimization in switched reluctance motors using adaptive fuzzy control," *IEEE Trans. Ind. Appl.*, vol. 35, no. 2, pp. 461–468, 1999.

[74] D. S. Reay, T. C. Green, and B. W. Williams, "Neural networks used for torque ripple minimisation from a switched reluctance motor," in *Power Electronics Specialists Conference*, 1993, pp. 1–6 vol.6.

[75] J. G. O'Donovan, P. J. Roche, R. C. Kavanagh, M. G. Egan, and J. M. D. Murphy, "Neural network based torque ripple minimisation in a switched reluctance motor," in *Proceedings of IECON'94 - 20th Annual Conference of IEEE Industrial Electronics*, 1994, vol. 2, pp. 1226–1231.

[76] J. Lin, "External-rotor 6/10 switched reluctance motor for an rlectric bicycle,"

McMaster University, Hamilton, ON, Canada, 2013.

[77] S. Mulder, “Power ferrite loss formulas for transformer design,” *Power Convers. Intell. Motion*, vol. 21, no. 7, pp. 22–31, 1995.

[78] E. C. Snelling, *Soft ferrites: properties and applications*. London ; Boston: Butterworths, 1988.

[79] C. P. Steinmetz, “On the Law of Hysteresis,” *Trans. Am. Inst. Electr. Eng.*, vol. IX, no. 1, pp. 1–64, 2010.

[80] T. A. Lipo, *Introduction to AC machine design*. Hoboken, New Jersey & Canada: Wiley-IEEE Press, 2017.